Adhesion Characteristics of Fuel Spray Impinging on Flat Wall for Gasoline Engine

(平板壁面に衝突するガソリン噴霧の液膜形成に関する研究)

By

駱洪亮 (Hongliang LUO)

Dissertation

Submitted to the Graduate School of Engineering

of Hiroshima University

in Partial Fulfillment of the Requirements

for the Degree of

Doctor of Engineering

Hiroshima University

September, 2018

ABSTRACT

Spray-wall impingement is a widespread phenomenon applied in many fields, inlcuding spray-wall cooling precess, spray coating process and fuel spray atomization in internal combustion engines. Although the spray impingement has been investigated for decades, the mechanisms of the interaction between spray and wall are still far from being fully understood. Recently, with the development of the visual technology, a range of interesting behaviors can be observed. However, researches on impinging spray are not enough, and the mechanisms of fuel adheison formation are not clear, especailly for gasoline engine. In gasoline direct injection (GDI), it is difficult to avoid the fuel adhesion on the piston and sylinder surfaces. The wet wall caused by impingement affects the air-fuel mixture formation process, which is a possible source of unburned hydrocarbons (UHC) and particulate matters (PM), making it difficult for direct injection spark ignition (DISI) engines to meeting the future requirements of particle number (PN) regulations.

The novelty of this study lies in the correlation between the impinging spray and fuel adheion formation together to better understand the spray-wall impingement in gasoline engine. The high-speed video observation method (Mie scattering technique) was applied to visualize the spray evolution and impingement processes inside a high-pressure and high-temperture constant chamber. Meanwhile, the adhered fuel on the wall was measured by refrective index matching (RIM) under non-evaporation and evaporation conditions considering the effects of different injection pressures, ambient pressrues, impingement distances, nozzle hole diameters and ambient temperatures in experiments.

Furthermore, the microscopic characteristics of impinging spray were investigated using particle image analysis (PIA). The droplet size and number were compared before and after impingement. Moreover, the relationship between droplets behaviors and fuel adhesion on the wall was discussed under the same conditions. Additionally, the spray-wall impingement model and droplet breakup/ coalescence model were discussed deeply as well.

TABLE OF CONTENTS

NOMENCLATURES

ASOI	After start of injection
AEOI	After end of injection
BTDC	Before top dead center
$C_{droplet}$	Perimeter of droplet
CCD	Charge-coupled device
CGR	Charged gasoline injection
CFD	Computational fluid dynamics
D	Nozzle hole diameter
D_{area}	Area diameter
D_{32}	Sauter mean diameter
DI	Direct injection
DISI	Direct injection spark ignition
d_{in}	Incident droplet diameter
d_{out}	Out droplet diameter
d_{fl}	Film thickness
D_{imp}	Impingement distance (mm)
ECU	Electronic control unit
EOI	End of injection
EGR	Exhaust gas recirculation
$f_M(h)$	Probability of fuel mass
fps	Frames per second
HC	Hydrocarbon
H_i	Impinging spray height (mm)
H_v	Impinging vortex height (mm)
$h(x, y)$	Fuel adhesion thickness (μm)
$I_{wet}(x, y)$	Light intensity of the fuel deposit
$I_{ref}(x, y)$	Light intensity of the dry image
IC	Internal combustion
ICCD	Intensified charge-coupled device
GDI	Gasoline direct injection

L_x	Distance to wall (mm)
L_r	Radial distance (mm)
L/D	Length to diameter
LCV	Light commercial vehicles
LDA	Laser doppler anemometer
LIF	Laser induced fluorescence
M_{inj}	Injection mass (mg)
M(h)	Fuel adhesion mass in the thickness (mg)
NO_x	Oxides of nitrogen
Oh	Ohnesorge number
PIA	Particle image analysis
P_{inj}	Injection pressure (MPa)
P_{amb}	Ambient pressure (MPa)
PFI	Port fuel injection
PN	Particle number
PDA	Phase doppler anemometry
PDPA	Phase doppler particle analysis
PIA	Particle image analysis
PM	Particulate matters
Ra	Arithmetical mean deviation of the profile
Re	Reynolds number
R_s	Impinging spray radius (mm)
RIM	Refractive index matching
S	Spray tip penetration
$S_{droplet}$	Area of droplet
SI	Spark ignition
SMD	Sauter mean diameter
SOI	Start of injection
T_{sat}	Saturated temperature of fuel droplet
T_l	Temperature of impinging droplet (K)
T_w	Wall surface temperature (K)
T_{PA}	Pure adhesion temperature (K)

T_{PR}	Pure rebound temperature (K)
T_N	Nakayama temperature (K)
T_{Leid}	Leidenfrost temperature (K)
T_{amb}	Ambient temperature (K)
t_d	Injection duration (ms)
TDC	Top dead center
UHC	Unburned hydrocarbon
We	Weber number
θ_{imp}	Impingement angle (deg)
ΔP	Difference of injection pressure and the ambient pressure (MPa)
$\Delta I\ (x, y)$	Reduction of the scattered light
3-D	Three dimensional

CHAPTER 1 INTRODUCTION

1.1 BACKGROUND AND MOTIVATION

1.1.1 Automobiles Development and Environment Issues

The Austrian inventor, firstly put a liquid-fuel internal combustion engine on a simple handcart which made him the first man to propel a vehicle by means of gasoline. Today, this car is known as "the first Marcus car". As one of the most important inventions in 19th century, almost all technological innovations of internal combustion engines are promoting human progress in the modern history of mankind. Due to its unique high thermal efficiency, wide output and high speed, high reliability and flexibility, internal combustion engines are the most widely used power machinery in industrial, agricultural production and transportation [Haworth, 2005]. The commercial production in automobile began in France in 1890, and it was almost equal to that of United States. One historian said that the cars free common people from the limitations of their geography, and they create mobility in human lifestyles. With the development in the economy of the world, the passenger cars are becoming more and more popular in the world.

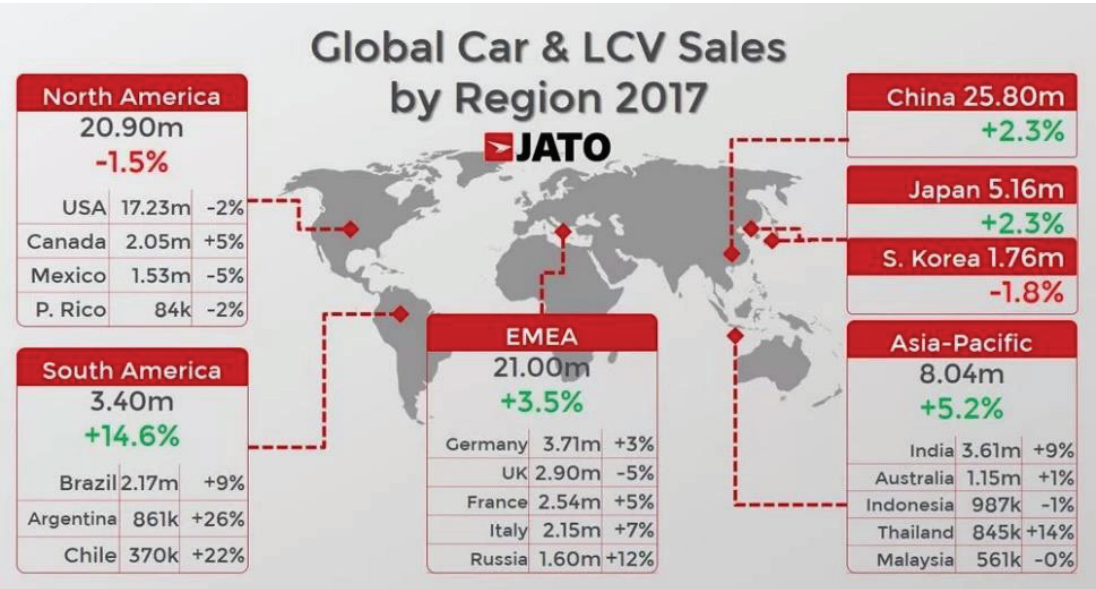

Figure 1.1 Worldwide car sales in 2017 [JATO Dynamics, 2017]

In 2017, worldwide sales of passenger cars and light commercial vehicles (LCV) increased 2.4%, based on the research from JATO Dynamics. Slightly more than 2 million additional

vehicle sales compared to 2016 make for a new total of 86.05 million global car sales. Passenger car sales were up 2.3% to 82 million and LCV sales were up 4.4% to 4.05 million vehicles. As shown in Figure 1.1, China remains the largest single market with 25.8 million sales despite reporting the slowest growth rate in more than a decade. Only North American (although Canada +5%) and S. Korea car sales decreased in the world. Growth in China slowed to just 2.3% from 17% in contrast to 2016. India and Brazil are other engines of growth, as the great increase in the economy and population in these countries.

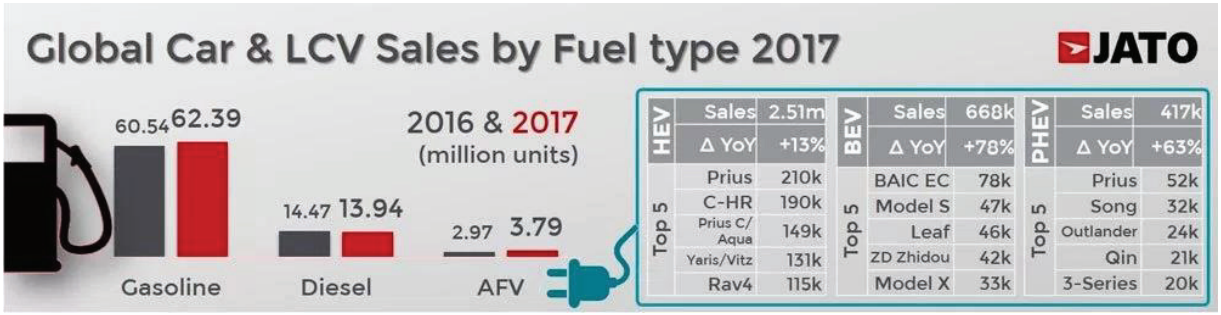

Figure 1.2 Global car sales by fuel type in 2017 [JATO Dynamics, 2017]

Figure 1.2 shows the fuel type of global car in 2017. Among these, gasoline power vehicles increased to 623.9 million, that occupies the biggest of the market share. According to JATO's calculations, although the alternative fuel vehicles increase rapidly, the share is quite smaller (about 5%) compared to gasoline and diesel cars. As a result, it is still very important to develop and investigate on the internal combustion (IC) engines (both gasoline and diesel engines) in the world.

Predicted demand rate of diesel fuel / gasoline (Shown as how many increased times compared with current rate)		**Future**		
		2035	**2040**	**2050**
Saudi ARAMCO 2015 SAE GCI Symposium	**Transport (Tollway Scenario)**	**1.9**	**2.4**	**3.9**
	Transport (Freeway Scenario)	**1.4**	**1.9**	**2.5**
OPEC World Oil Outlook 2014	**Global product demand**	**–**	**1.20**	**–**
ExxonMobil The Outlook for Energy	**Transportation**	**–**	**1.62**	**–**
IEA World Energy Outlook 2013	**Road-transport**	**1.35**	**–**	**–**

Figure 1.3 Demand rate of diesel fuel / gasoline forecast [Hitomi M, 2017]

However, due to the rapid development of IC engines, as the planet on which humankind depends, its resources such as oil, gas and coal decrease irreparably as they are non-renewable energy source in the earth. Energy consumption leads to a series of problems, and fossil fuels are considered overuse. Because the mainly energy is still acquired from coal and oil in the future decades, although the renewable energy and clear energy is expected to be developed further and more. Therefore, the energy crisis threatens the development of mankind. Many researchers have spared no effort to find new ways to solve this imminent danger. Especially, this demand will continue to increase. Figure 1.3 describes that future demand rate of diesel fuel / gasoline is increasing due to the transportation consumption. Even in 2050, the demand will be more than 3 times compared with current rate due to the booming of the population.

Moreover, while enjoying the development and achievements brought from the IC engine technology, humans have to face the negative issues such as environmental deterioration and pollutions. The traditional IC engines discharge harmful emissions into the environment to provide inexhaustible power. As a result, environmental health and safety are a major issue in the development of human society. In the next half century, it will be the common problem power facing all the humanity beings.

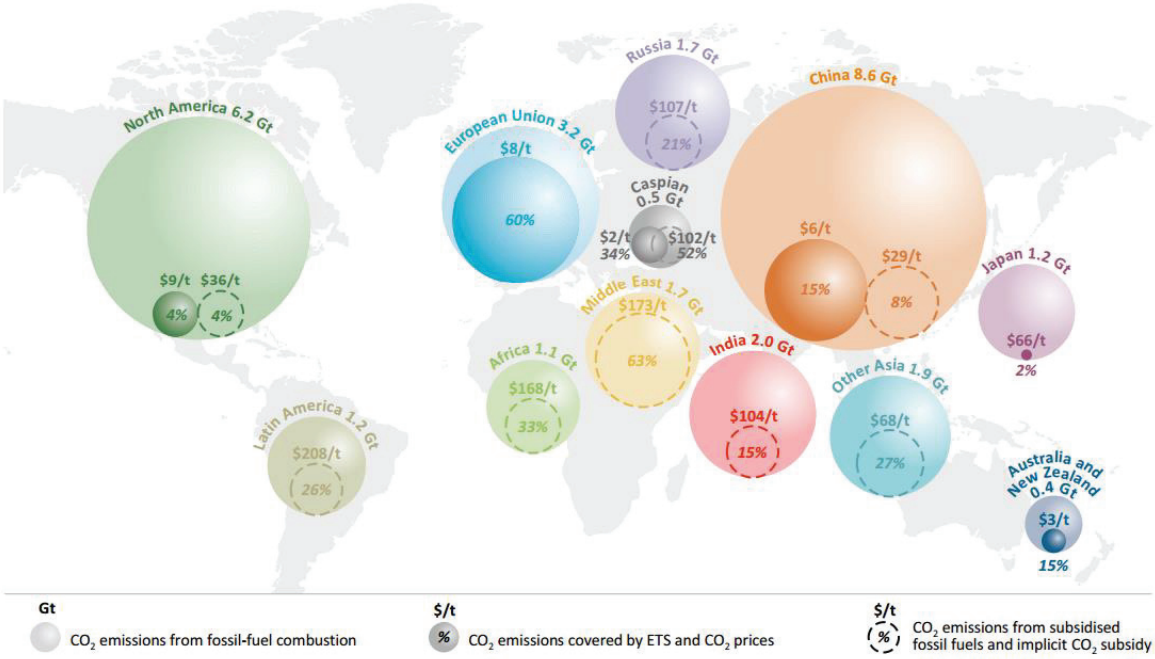

Notes: The implicit CO_2 subsidy is calculated as the ratio of the economic value of those subsidies to the CO_2 emissions released from subsidised energy consumption. ETS = emissions trading scheme.

Figure 1.4 Energy-related CO_2 emissions in selected regions [Maria H, 2015]

Recently, as the climate change, more and more attentions are paid to environmental protection. In fact, the consumption of the fossil fuel is one of the main indisputable sources of the pollutions, which causes up the climate warming, fog, and haze. Dillon et al. [2010] and Lacis et al. [2013] have demonstrated that the greenhouse gas emission is the immediate reason of the world warming. The greenhouse and harmful gases pollute the earth, threatening the eco-system and the health of human beings. The energy related CO_2 emissions, especially caused by the fossil-fuel combustion in 2014 all around the world is published by International Energy Agency and shown in Figure 1.4 [Maria van der Hoeven, 2015]. It can be seen that China, North America, and European Union are the three largest carbon markets in the world. Hence, the improved technology and method, such as optimizing combustion, enhancing the energy efficiency, and reducing emission substantially, become very important subject for the sustainable development of the world.

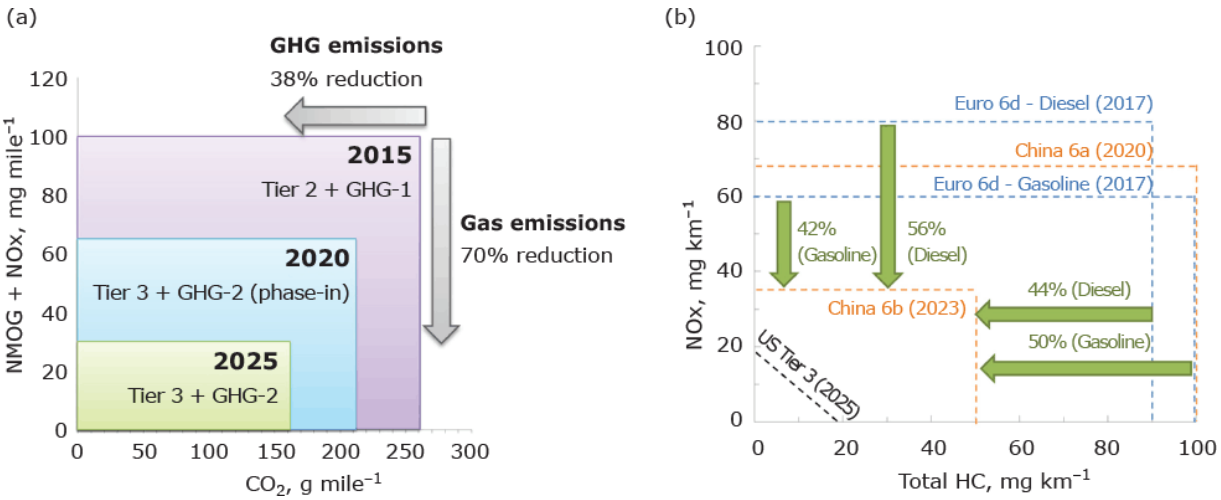

Figure 1.5 Light-duty regulations for tailpipe emissions in major markets: (a) the concurrent tightening of criteria pollutant and CO2 emission limits in the USA; (b) by 2023, the proposed limits in China will be tighter than those in Europe [Joshi A, 2017]

What comes with pollutions is the increasingly stringent emission standards. Increasingly stringent emission standards have been introduced to reduce gasoline automotive emissions such as NO_X, particulates, CO_2, in the world. The light-duty regulation for emissions in major markets for gasoline car is exhibited in Figure 1.5.

1.1.2 Direct-injection Spark Ignition (DISI) Engines

As shown in Figure 1.6, the development of injection system from carburetor to port fuel injection (PFI) to direct injection (DI) system.

In early gasoline engines, the mixture formation was created by an aid of a carburetor, which causes a worse engine-out emissions and fuel consumption. Thereafter, the PFI system was introduced into gasoline engines with the development of electrical controlling. Although PFI engines can ensure the equivalence ratio Φ=1.0 in chamber, which is required to the work of three-way oxidation/reduction catalysts, they still have several disadvantages. The relative low-pressure fuel injector installed in the intake port may cause fuel adhesions on the port walls, even on the intake valves during cold start (excess of fuel requires to form favorable fuel vapor mixing in cylinder for robust ignition). Large-scale swirl and tumble flow induced by the intake movement leads to intense turbulent flows in cylinder, thus decreasing cycle-to-cycle variability owing to the distortion of flame kernel formation. For preventing the in-cylinder knocking, the compression ratio is limited to 10:1. Furthermore, a decrease in fuel economy at part load occurs in the consequence of the pumping (throttling) losses [Maly RR,1994; Drake et al., 2007].

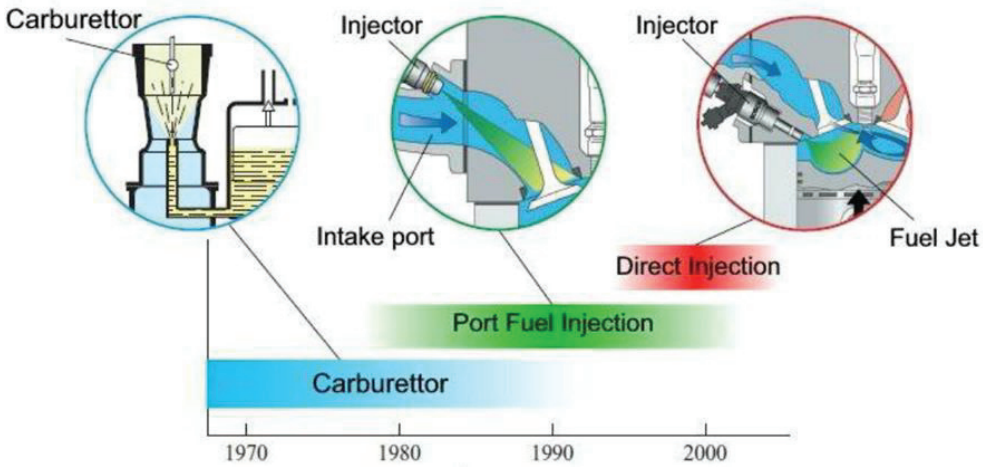

Figure 1.6 The development of fuel injection system [Romain N, 2013]

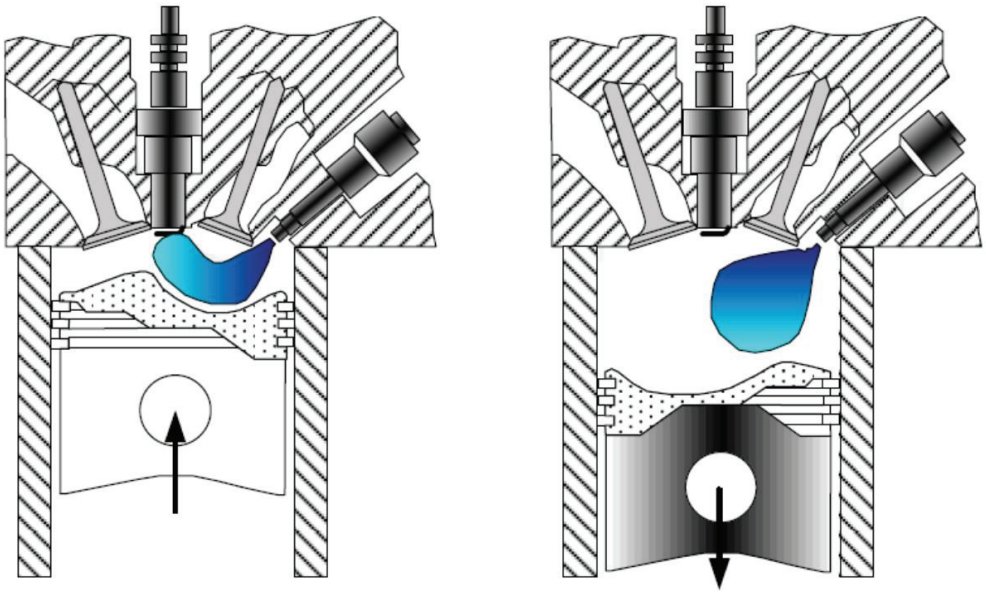

(a) Stratified charge (b) Homogeneous charge

Figure 1.7 Homogeneous and stratified-charge modes of DISI engine [Suresh et al., 2015]

Therefore, direct-injection spark ignition (DISI) engines as a greatly potential alternative to conventional PFI gasoline engines become more and more widely used for their significant advantages: (1) volumetric efficiency, because of the decrease in in-cylinder temperature induced by fuel direct injection; (2) enhanced thermal efficiency due to less pumping losses during intake stroke; (3) increased specific output at part load owing to stratified mixture formation and combustion in cylinder; (4) improved fuel economy throughout precise fuel injection in transient response. [Zhao et al., 1999; Moreira et al., 2010; He et al., 2012].

Meanwhile, two basic charge modes are implemented in the DISI engines: homogeneous and stratified charge homogeneous charge mode, as shown in Figure 1.7 [Suresh et al., 2015].

The homogeneous charge is used at full loads. In that case the fuel is injected during intake stroke so that the early injection timing allows for a homogeneous mixture forming throughout the cylinder [Kume et al., 1996]. In homogeneous charge condition the managing of engine load is by throttling while in stratified charge condition it is by air-fuel equivalence ratio [Spicher et al., 2000].

The stratified charge is used at partial loads. It occurs when fuel is injected late in the cycle (0-90 degrees BTDC) creating a non-homogeneous mixture of air, fuel and exhaust gas

recirculation (EGR). Due to the late injection timing, the injected fuel remains close to the spark plug and does not penetrate the cylinder as far as in homogeneous combustion. This creates a stratified mixture of fuel and air with a high air-fuel ratio at the spark plug electrode. The result is a local ignitable mixture near the spark plug with a globally lean air-fuel mixture in the rest of the cylinder. It allows for the injection of the minimal amount of fuel required to achieve a power output or engine speed. Due to this reason, stratified combustion is usually applied for idle, low engine loads and speeds, and transition from these points to higher loads and speeds [Peery, 1975].

In stratified mode, three combustion processes are used to form ignitable mixture. These are spray guided, wall guided and air guided combustion processes as shown in Figure 1.8.

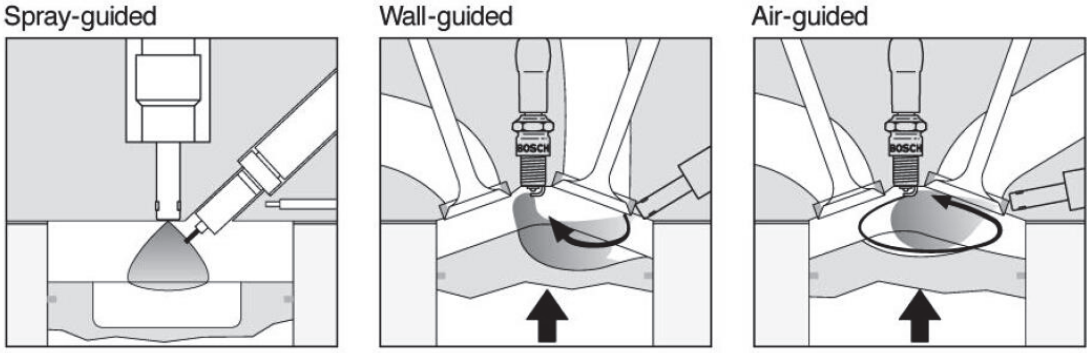

Figure 1.8 Classification of the GDI combustion systems [Preussner C, 2006]

Spray guided combustion process: Here the fuel is injected near the spark plug where it evaporates. The spray guided combustion theoretically has highest efficiency. This process requires advanced injection systems. The spray guided combustion has the following advantages. These include less wall wetting, large stratified operation region, reduced emissions, and less sensitive to cylinder to cylinder variation and in-cylinder air flow. Recognized limitations include high sensitivity to changes in injection and ignition timing and spark plug reliability [Cathcart et al., 2001]. Mercedes-Benz devised a sophisticated spray guided combustion system. It is a stratified charged gasoline injection (CGI) engine with piezo injection technology. The spray guided injection achieves better efficiency than the conventional wall guided injection process. The advantage of CGI engine is attained at the stratified operating mode. In this mode the engine runs with excess air hence high fuel efficiency is obtained. High rpm and higher loads can be driven using multiple injections. During each and every compression stroke a series of

injections takes place space a fraction of seconds apart. This permits good mixture formation, good combustion and low fuel consumption [Baumgarten C, 2006].

Wall guided combustion process: In this case a specially designed piston will be used to transfer the fuel to the spark plug. The fuel will not evaporate completely because the fuel is injected on the surface of the piston resulting in high emissions and fuel consumption. Usually this system will be used along with air guided combustion process [Anon et al., 2002].

Air guided combustion process: The fuel is injected onto the flow of air which moves the fuel sprayed near the spark plug. With a special shape the inlet ports provide the air flow and the speed of the air is controlled using air perplexes in the manifold. Here the fuel does not wet the piston and the cylinder. Most of the CGI DISI engines use a large scale of air motion as well as specially shaped piston to keep the fuel spray compact and to move it to the spark plug [Park et al., 2012]. In air guided and wall guided combustion systems the injector is isolated to the spark plug. Volkswagen DISI system is a combination of two systems. The resulting system is less sensitive against the cyclic variations of airflow. As shown in Figure 1.8 (b), injector is placed intake-side. The fuel is injected into the chamber but onto the piston with a specific angle. Piston has two bowls; fuel bowl and air bowl. The fuel bowl is on the intake valve side and air bowl is on the exhaust valve side. Tumble or swirl flow is obtained by special shaped intake port [Kim et al., 2008; Alkidas et al., 2007]. The fuel is guided simultaneously via air and fuel bowl to spark plug.

1.1.3 Impinging Spray in DISI Engines

Owing to the short impingement distance and high injection pressure, spray impingement on the combustion chamber wall and piston head in gasoline engine is quite difficult to avoid at both stratified charge and homogeneous charge conditons. However, the impingement affects the fuel-air mixture prior to combustion, which is a possible source for unburned hydrocarbon(UHC) and particulate matters [Kalantari and Tropea, 2007]. Although it has been demonstrated that the port-injection generally produces a thicker fuel adhesion than DI owing to the lower injection pressure and ambient temperature when compared to DI engines [Zhao et al., 1999], it is also suggested that the soot emissions of DI engines is more strongly dependent on the fuel adhesion on the wall, especially considering the future regulatory requirements regarding the particle number (PN) [Moreira et al., 2010; He et al., 2012]. Tanaka et al., [2017] showed the

relationship between the deterioration ratio of engine our PN emissions and fuel adhesion volume, indicating that PN emissions increases with the increasing of fuel adhesion on the wall, as shown in Figure 1.9.

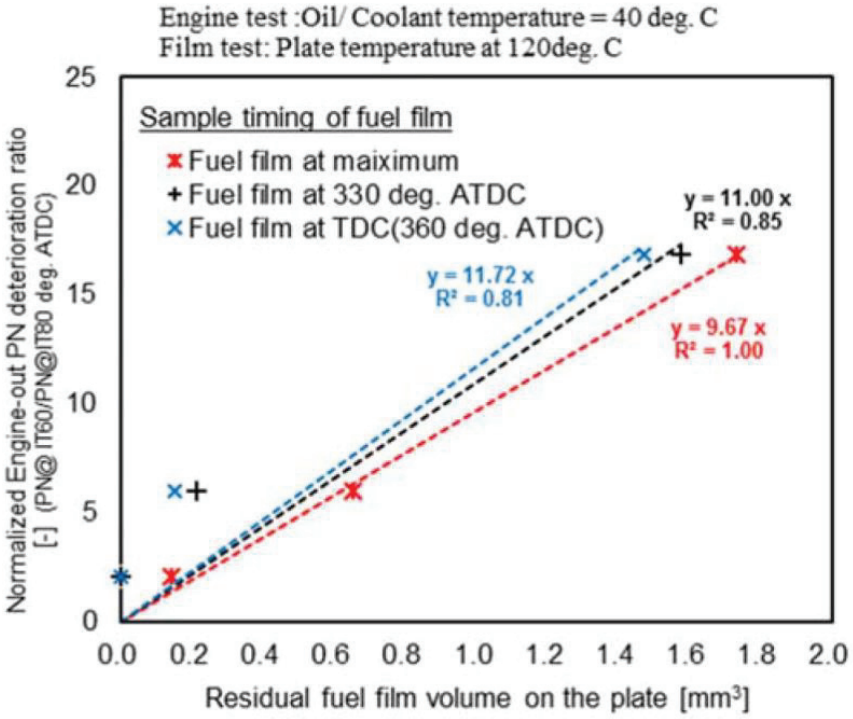

Figure 1.9 Relationship between PN emission and fuel adhesion on the wall [Tanaka et al., 2017]

The stratified charge DISI engines increases high fuel efficiency at part load, but have some problems to create the proper stratified-charge fuel distribution to ensure reliable ignition, proper combustion phasing, and minimum engine emissions. During this process, the fuel sprays impact the piston and form adhesions of liquid fuel on the wall [Drake et al., 2003]. The fuel adhesion formation and evaporation, which results in cylinder pool fires, unburned hydrocarbon and smoke emissions, have been studied extensively experimentally and computationally, but many questions remain [Oh et al., 2010]. For homogeneous charge DISI engines, an optimization of injector spray pattern can reduce liner and piston wetting which leads to a reduction in oil dilution. It also reduces soot emissions over a wide window of fuel injection timing, however, the soot emission problem is still serious [Lai et al., 2011]. As a result, it is important to get a deeper understanding on the fuel adhesion formation along with the impinging spray characteristics.

1.2 OBJECTIVES AND APPROACHES

The target of this study is to investigate the characteristics of gasoline spray impingement and fuel adhesion formation experimentally. The specific objectives of this study are shown as follows:

Analyze the impinging spray evolution characteristics which belongs to the single-hole nozzle under the non-evaporation and evaporation conditions.

Illustrate the influence of dynamic factors (injection pressure and injection quantity), geometrical factor (hole diameter) and impingement factor (impingement distance and roughness of wall surface) on the difference in the spray behaviors and fuel adhesion formation.

Model the fuel adhesion formation under the non-evaporation and evaporation conditions to provide an insightful understanding of the interaction between spray and wall.

Focus on the droplets diameter and velocity before and after impingement to characterize the microscopic spray under different injection and ambient pressure.

Correlate the spray evolution and fuel adhesion results with droplets behaviors under gasoline engine like condition.

In this study, the Mie Scattering technique was implemented to obtain the observations of gasoline spray emerging from single hole injector under the different condition. In addition, the refractive index matching (RIM) technique was adopted to analyze the formation process of fuel adhesion on the wall qualitatively and quantitatively under both non-evaporation the evaporation condition. Moreover, the microscopic characteristics of impinging spray were obtained using particle image analysis (PIA) to investigate the influences of breakup and coalescence on the droplet behavior.

1.3 OUTLINES

To present this work, the thesis is organized as follows: First of all, a review of previous works on the development of DISI engines, impinging spray and fuel adhesion formation as well as its relative experimental methods are presented in Chapter 1. Chapter 2 introduces the experimental apparatus implemented in this study, such as constant high-pressure chamber, electrical control system, impingement system and the observation techniques applied in this investigation. The spray characteristics and fuel adhesion evolution are experimentally investigated under non-

evaporation conditions in Chapter 3. The effect of pressure, roughness of the wall surface, impingement distances are tested in this chapter. After that, the evaporation conditions are considered in Chapter 4, and the effects of ambient temperatures and hole diameters on the spray impingement and fuel adhesion formation are studied. Furthermore, the different mechanisms in fuel adhesion formation will be discussed in this chapter. To correlate the spray behaviors with the fuel adhesion, Chapter 5 illuminates the microscopic characteristics of impinging spray under different conditions, then, the droplets diameter and velocity will be reported before and after impingement. Finally, the relationships between droplets and fuel adhesion are summarized and compared with the single droplets behavior in this chapter.

1.4 STUDIES REVIEW

1.4.1 Spray-Wall Interaction

A schematic description of a full-cone high-pressure spray is given in Figure 1.10. The graphic shows the lower part of an injection nozzle with needle, sac hole, and injection hole. Modern injectors for passenger cars have hole diameters of about 0.18 mm and less, while the length of the injection holes is about 1 mm.

Immediately after leaving the nozzle hole, the spray jet starts to break up into a conical spray. This first break-up of the liquid is called primary break-up and results in large ligaments and droplets that form the dense spray near the nozzle. In case of high-pressure injection, cavitation and turbulence, which are generated inside the injection holes, are the main break-up mechanisms. The subsequent break-up processes of already existing droplets into smaller ones are called secondary break-up and are due to aerodynamic forces caused by the relative velocity between droplets and surrounding gas. The aerodynamic forces decelerate the droplets. The drops at the spray tip experience the strongest drag force and are much more decelerated than droplets that follow in their wake.

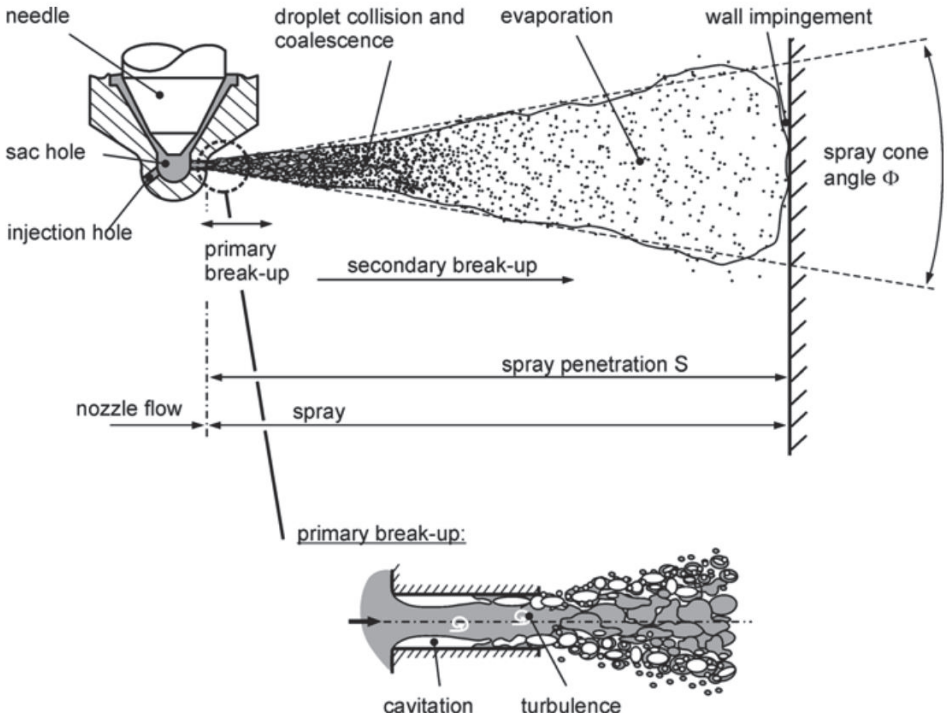

Figure 1.10 Typical schematic of spray structure [Baumgarten C, 2006]

During the secondary break-up, the more and more liquid droplets are formed and move towards downstream of the spray. The droplets at spray tip also lost their momentum gradually, then the following droplets with higher momentum probably purse the precedent ones and push them forward. Therefore, the spray propagates continuously downwards, and the large ambient gas vortex is induced by the spray plumes which further enhances the spray atomization. However, the droplet collide with each other can produce the droplet coalescence effect and result in a formation of larger droplet. The liquid fuel at the downstream spray is mainly influenced by the ambient gas conditions, such as pressure, temperature and density. When the ambient temperature increases over the room temperature, the liquid droplet set out to vaporize. In the well-used DISI engines of the wall-guided concept, when the gasoline is lately injected into the wall to form the stratified mixture, it is inevitable that a fraction of fuel would impinge on the piston crown and probably form a fuel film on that wall. This would cause an inferior UHC and soot emission as describe above. Therefore, the interaction of liquid droplet and piston wall needs to be investigated to reduce the impact of the spray impingement.

With the great progress on the optical diagnostic technique, it is possible to study the spray break-up and evolution more intuitively by the high-speed imaging. The characteristics of spray, such as spray morphology, droplet's size distribution and equivalence ratio distribution have been studied aggressively, and numerous semi-empirical equations and theories also have been summarized. The spray tip penetration of the spray was examined by Hiroyasu et.al [1990]. They separated the spray evolution into two aspects. First, the penetration length is proportion to the time as the liquid core region moves without break-up. Second, during the spray evolution, the momentum of liquid droplet is influenced by the surrounding gas in the result of the slower droplets at the tip region. The equations which describe these two regimes can be summarized as follows:

$$S = 0.39 \cdot \left(\frac{2\Delta P}{\rho_f} \right)^{0.5} \cdot t \tag{1-1}$$

$$S = 2.95 \cdot \left(\frac{\Delta P}{\rho_a} \right)^{0.5} \cdot (D \cdot t)^{0.5} \tag{1-2}$$

$$t_{break} = \frac{28.65 \cdot \rho_f \cdot D}{(\rho_a \cdot \Delta P)^{0.5}} \tag{1-3}$$

Where ΔP is the pressure drop at the nozzle hole exit [Pa], ρ_f is the liquid density [kg/m^3], D is the nozzle hole diameter [m]. The influence of the ambient temperature T_{amb} was taken into consideration and the increase in the ambient gas temperature can reduce the length of the spray penetration. The improved equation is shown as:

$$S = 3.07 \cdot \left(\frac{\Delta P}{\rho_a} \right)^{0.25} \cdot (D \cdot t)^{0.5} \cdot \left(\frac{294}{T_{amb}} \right)^{0.25} \tag{1-4}$$

The sauter mean diameter (SMD) is usually used to quantitatively characterize the droplet size apart from the spray tip penetration. It is defined as the diameter of a sphere that has the same volume/surface area ratio as a particle of interest [Wang et al., 2013]. The definition of SMD is described as follow.

$$SMD = \frac{\sum_{i=1}^{n} d_i^3}{\sum_{i=1}^{n} d_i^2} \tag{1-5}$$

The semi-empirical equation of SMD also was presented by Hiroyasu et al. [1990] as below:

$$\frac{SMD}{D} = 0.38 \cdot Re^{0.25} \cdot We_l^{-0.32} \cdot \left(\frac{\mu_l}{\mu_a}\right)^{0.37} \cdot \left(\frac{\rho_l}{\rho_a}\right)^{-0.47} \tag{1-6}$$

Moreover, other researchers also pointed their models, such as Wakuri et al. [1957], Narber and Siebers 1996].

Although the characteristics about spray have been well studied, the interactions between wall and spray are seldom considered. Recently the combustion chamber in a gasoline engine tends to be small in order to reduce fuel consumption, and injection pressure tends to increase as compared with a conventional engine. Wall impingement of the spray might occur due to downsizing of the engine and high pressure of fuel injection, and injected fuel was adhered on the wall of cavity. The impingement spray causes the emission of hydrocarbon (HC) and soot from the diesel engine. Therefore, it is important to understand the spray-wall interaction and adhesion characteristics of impinging spray.

Spray-wall interactions occur if a spray penetrating into a gaseous atmosphere impacts a wall, which can be the backside of the intake valve or the wall of the combustion chamber in case of a direct injection engine. Two main physical processes can be involved: wall-spray development and wall adhesion evolution. Both processes may strongly influence combustion efficiency and the formation of pollutants. Whether wall impingement occurs or not depends on the penetration length of the spray and on the distance between injection nozzle and wall. High injection pressures as well as low gas densities and temperatures increase penetration and the possibility of wall impact.

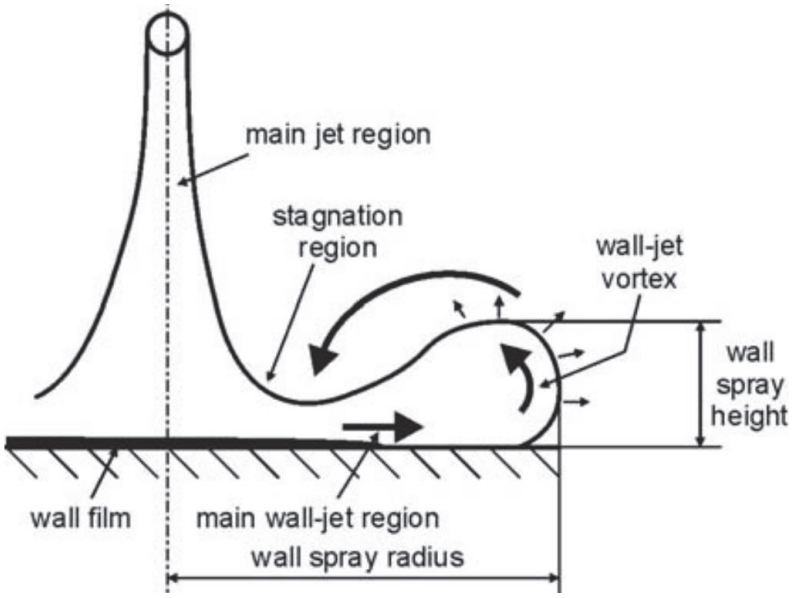

Figure 1.11 Typical schematic of impinging spray [Heil et al., 2001]

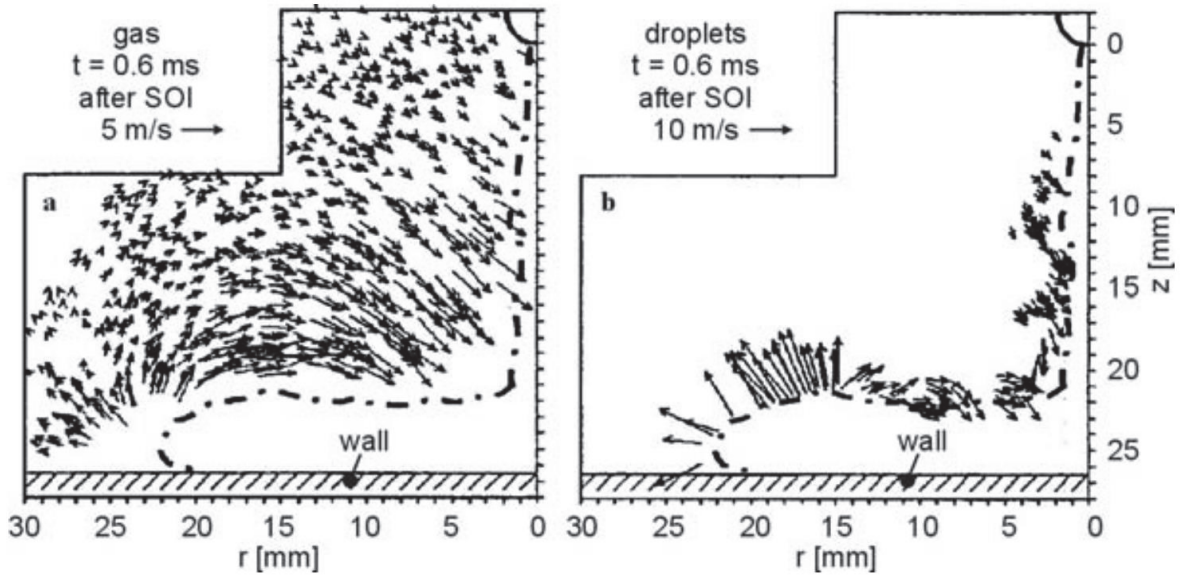

Figure 1.12 Typical flow around the impinging spray [Heil et al., 2001]

Figures 1.11 and 1.12 illustrate the schematic of imping spray and a typical gas flow field around the spray. When the fuel jet impinged on the wall, a large number of droplets is formed at the periphery of the spray tip, which develops along the wall. Whether the drops stick to the wall and continue to evaporate, spread out to form a liquid film, reflect, or break up into smaller droplets, depends on the kinetic energy of the incident drops and on the wall temperature, A

large-scale vortex is formed around the wall spray entraining a considerable amount of hot gas into the spray. In the case, the velocities of droplets and air are changed by the vortex.

Depending on wall temperature and the amount of liquid deposited on the wall, spray-wall interaction can have both negative and positive effects. In the case of low wall temperature, under cold starting conditions for instance, the formation of a liquid wall adhesion can significantly increase the unburned hydrocarbon and soot emissions because of partial burning due to the very slow evaporation of the wall adhesion. On the other hand, shattering of droplets at the wall may intensify droplet disintegration and increase the total spray surface. The formation of a large-scale gas vortex near the wall may also promote air entrainment and enhance mixture formation. Furthermore, contact with a hot wall intensifies evaporation. In some DI engines, the fuel spray has been intentionally impinged on a surface as a method to control combustion.

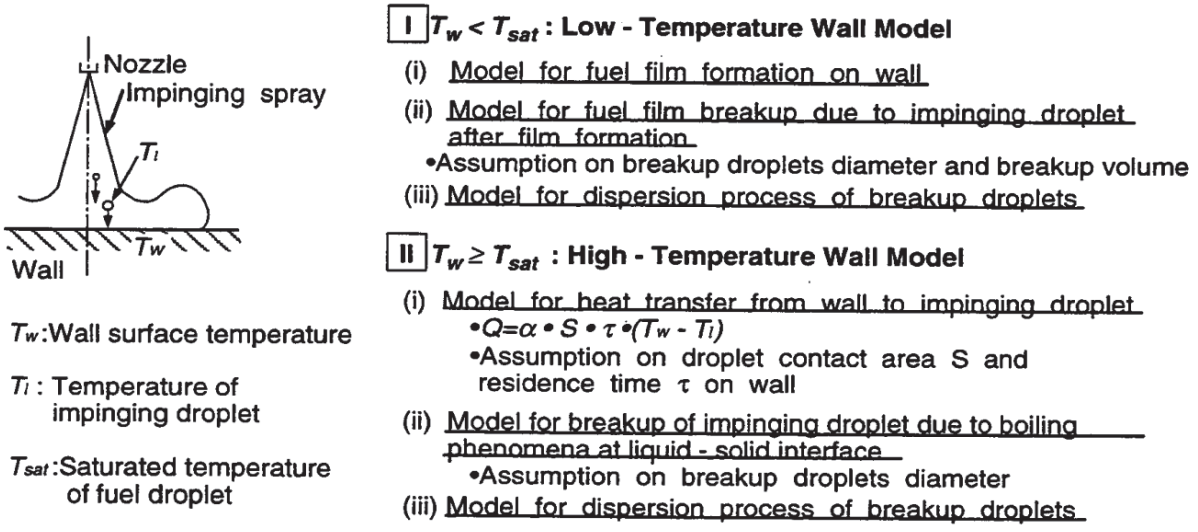

Figure 1.13 Typical flow around the impinging spray [Senda et al., 1997]

Senda et al. [1997] proposed a new model for spray-wall interaction by consider the saturated temperature of the fuel and wall surface temperature, see in Figure 1.13. In the case of $T_w < T_{sat}$, fuel film breakup process and dispersion of the droplets are considered. At the start of spray impingement, a fuel film is formed in the impingement region by the impinging droplets. Here, it is assumed that all impinging droplets spread as a radial film and they remain on the surface, until a wall wetting film as a pool is formed on the wall. After the fuel film is

completely formed in the whole impingement region as a pool, the film is disintegrated into droplets with simple model as splash process by further impingement of droplets on the film. Then, the newly formed droplets disperse in a calculated direction, based on the assumption that mass and momentum of the impinging droplet is conserved during the film breakup process. In the case of $T_w \geqslant T_{sat}$, sub-model for heat transfer process from the wall surface to the droplets, the breakup, process of impinging droplets due to the boiling phenomena and dispersion process of droplets are considered on the basis of previous experimental results [Senda et al., 1982; 1988; 1994]. Thus, droplets impinging on the hot surface breakup into small droplets due to dynamic unbalance and vapor formed at the liquid-solid interface; then, they disperse and evaporate. In this case, the droplets just disperse on the wall with the velocity estimated from his previous experimental data [Senda et al., 1982]. And, during the residence time on the surface, heat is transferred from the surface to the impinging droplet. They can even estimate the spray dispersion for the case of high T_w, such as heavy load operation in engines, using this model.

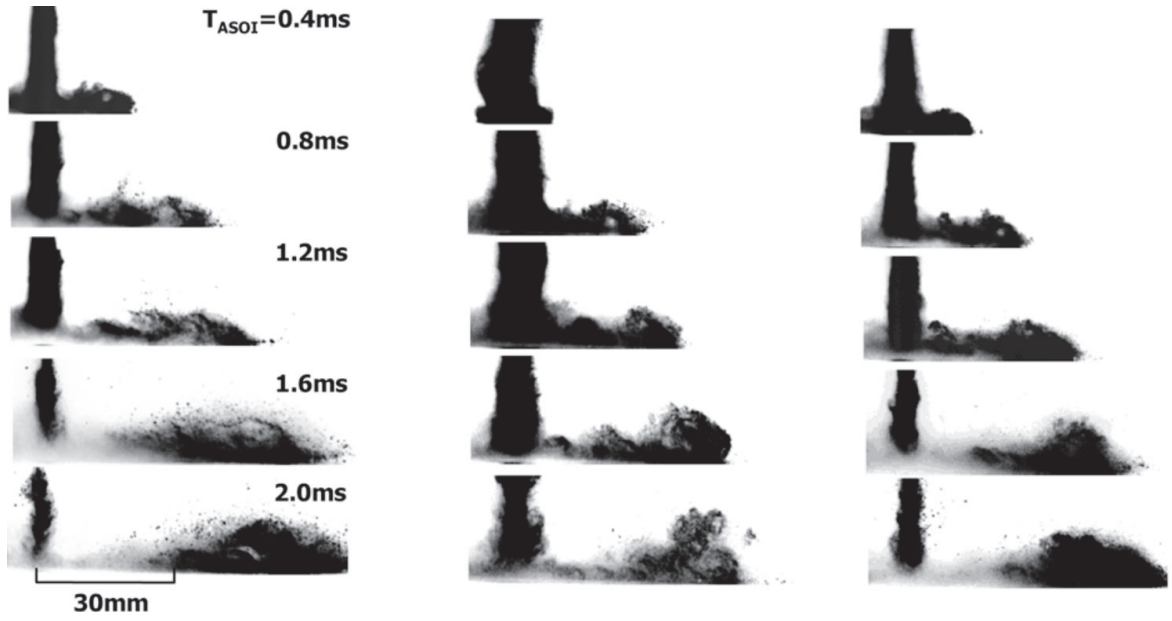

Figure 1.14 Structure of the spray impinged on the wall [Park et al., 2004]

Recently, researchers were interested in the observation of impinging spray to characterize it. An experimental study was performed to investigate the macroscopic behavior and atomization characteristics by Park et al. [2004] using the spray visualization system composed of a Nd: YAG laser and an intensified charge-coupled device (ICCD) camera. Figure 1.14

depicts the structures of spray impinged on the wall. He reported that the radial penetration of the impinged spray has the longer radial penetration at higher injection pressures, shorter wall distances from the injector, and smaller angles of wall inclination. However, the radial penetration decreases with the increase in ambient pressure. The effect of wall temperature on the radial penetration is negligible in comparison to the effects of other parameters. Alger et al. [2001], Andreassi et al. [2007] and Schulz et al. [2014] did the similar research on impinging spray.

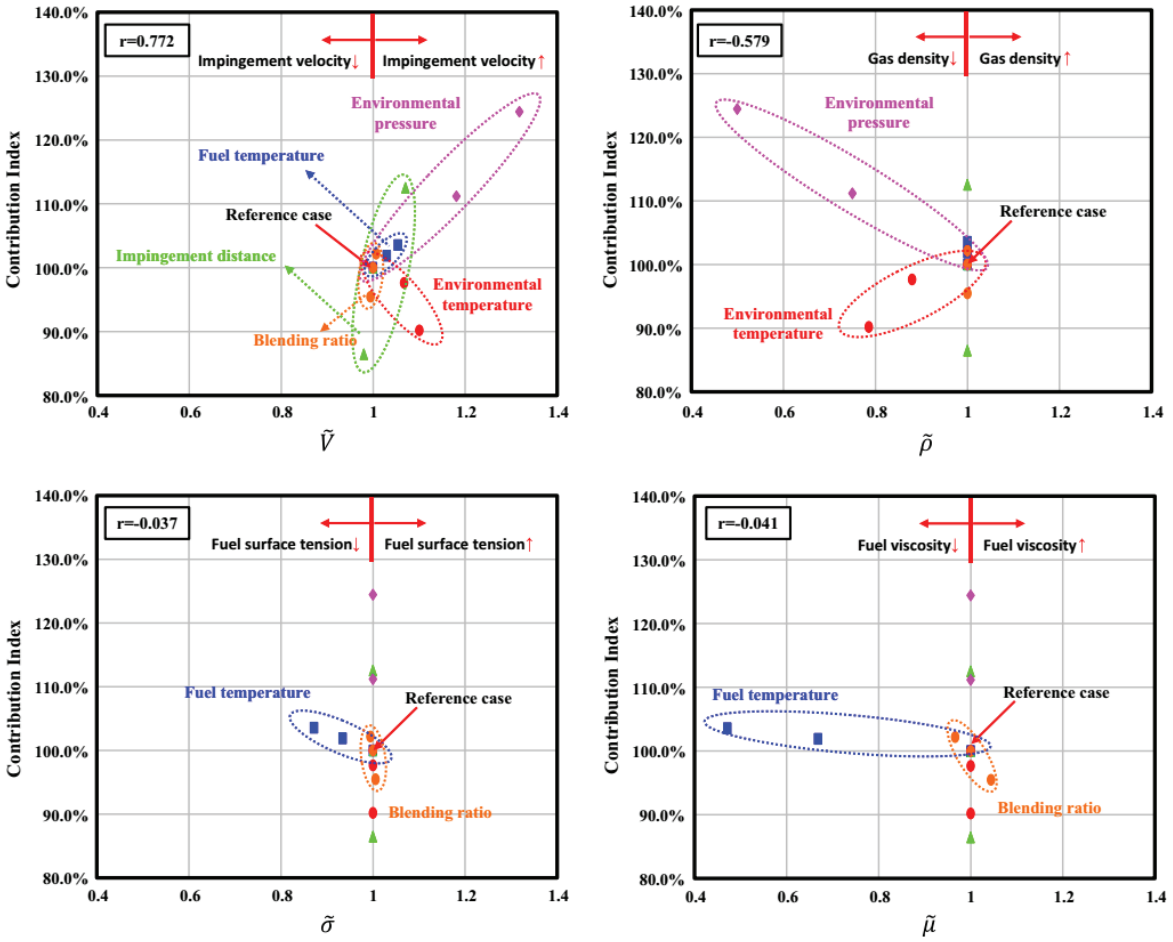

Figure 1.15 The contribution of each dimensionless number to the R_w variation [Yu et al., 2004]

As shown in Figure 1.15, Yu et al. [2016] investigated the spray-wall impingement characteristics by testing different fuels. The impingement spray radius (R_w) and height (H_w) were obtained experimentally so as to evaluate the impingement characteristics. Results showed that the spray impingement momentum had the greatest effect on R_w, followed by air entrainment,

while the impact of the fuel viscosity and surface tension (or spreading resistance) were limited. Lahane et al. [2014] also studied the wall impingement for biodiesel-diesel blend.

Du et al. [2018] studied the different phase on the spray structure after wall impingement by obtaining the behavior of liquid and vapor phase impingement spray, respectively. Figure 1.16 shows the processing method for liquid and vapor image. Results show that higher injection pressures cause higher liquid-phase spray diffusion rates after wall impingement.

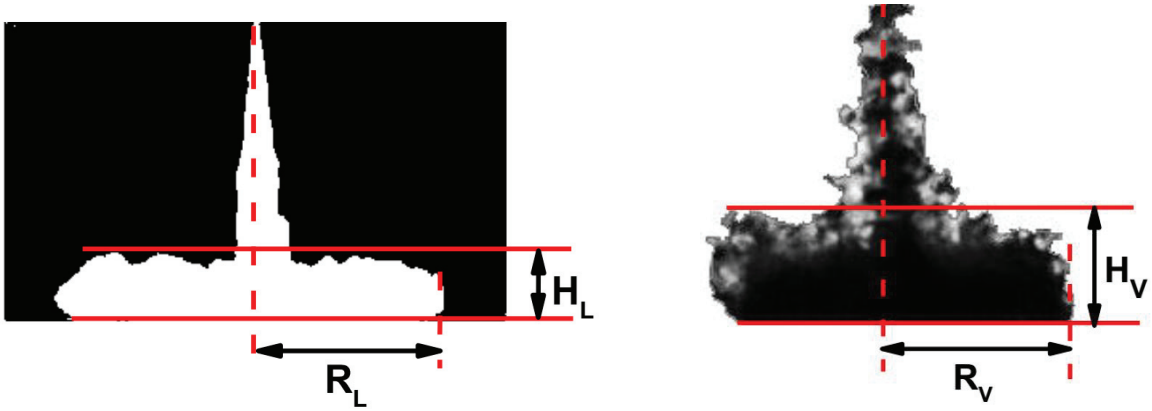

(a) Liquid phase (b) Vapor phase

Figure 1.16 Processed image of impinging spray [Du et al., 2018]

Liu et al. [2018] studied the spray-wall impingement with different wall temperatures and heat transition of the spray, as shown in Figure 1.17. Results show that the liquid phases of the spray do not reach the wall except in the condition of low wall temperature and high injection pressure. With the decrease of wall temperatures, the high-concentration regions are enlarged at the near wall regions. However, at the injection pressure of 1600 bar, the influence of wall temperatures on the equivalence ratio is small. The decreasing wall temperature deteriorates the mixing process of the fuel and ambient gas, but the effect is weakened with the increase of injection pressure. Arcoumanis et al. [1993;1998], Panao et al. [2009] and Zhou et al. [2018] did the similar work to study the heat transfer of spray impingement on piston surface.

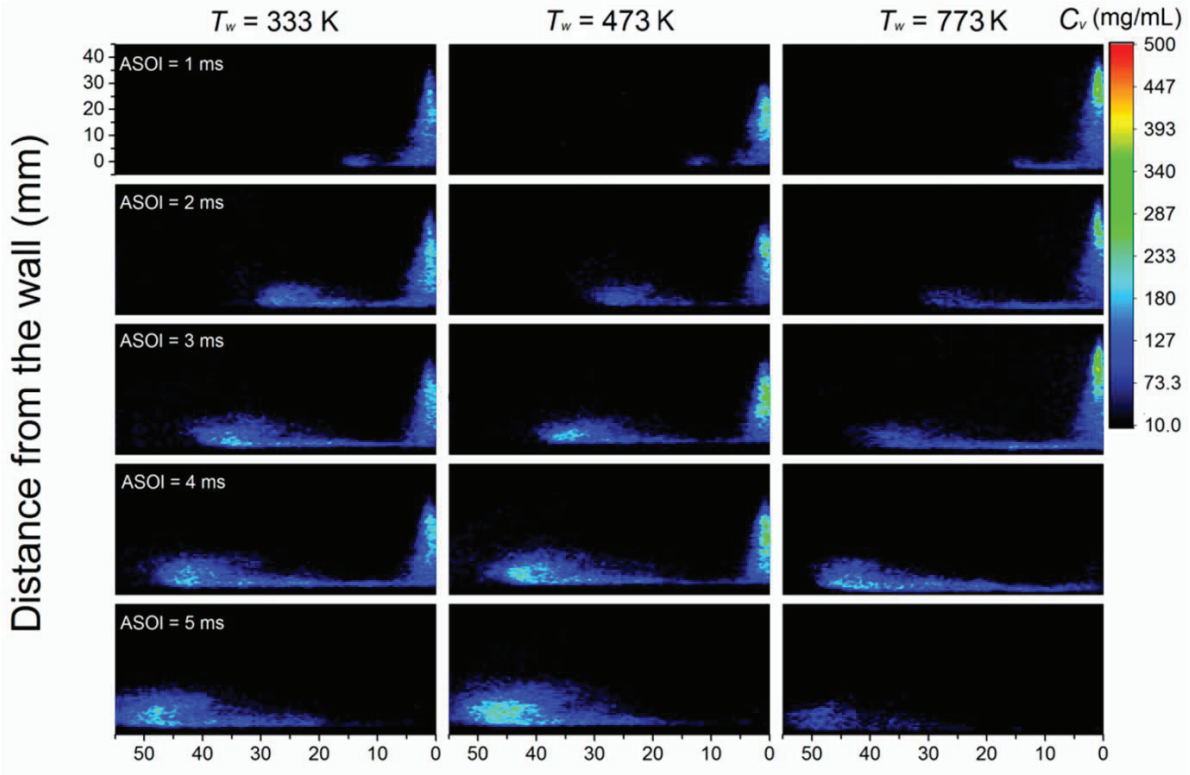

Figure 1.17 Typical flow around the impinging spray [Liu et al., 2018]

Pizziol et al. [2018] tested the multiple impinging jet atomization in Figure 1.18. In multiple impinging jets sprays, considering 2-,3-and 4-jets, the air flow rate assisting atomization allows some control over the average droplet size.

The researches above focus on the flat wall impinging spray, however, Zhang et al. [2018] investigated the corner angle of the expanding corner on the evolution of the impinging spray and found that the expanding corner angle remarkably affects the impinging spray structure. Figure 1.19 shows the spray structures. Ko et al. [2003] did the similar work before. The spray-wall interaction has been widely investigated, however, the research correlation the spray behavior and fuel adhesion together is seldom reported in the literatures. Besides, more studies should be done for the mechanisms of impinging spray.

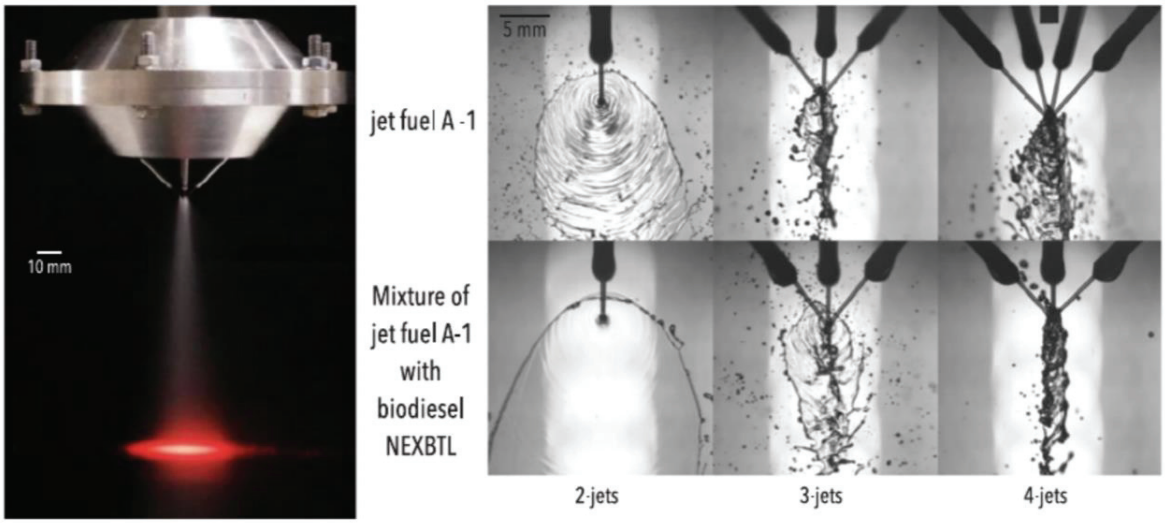

Figure 1.18 Injector and spray produced by the multiple impinging jets atomizer [Pizziol et al., 2018]

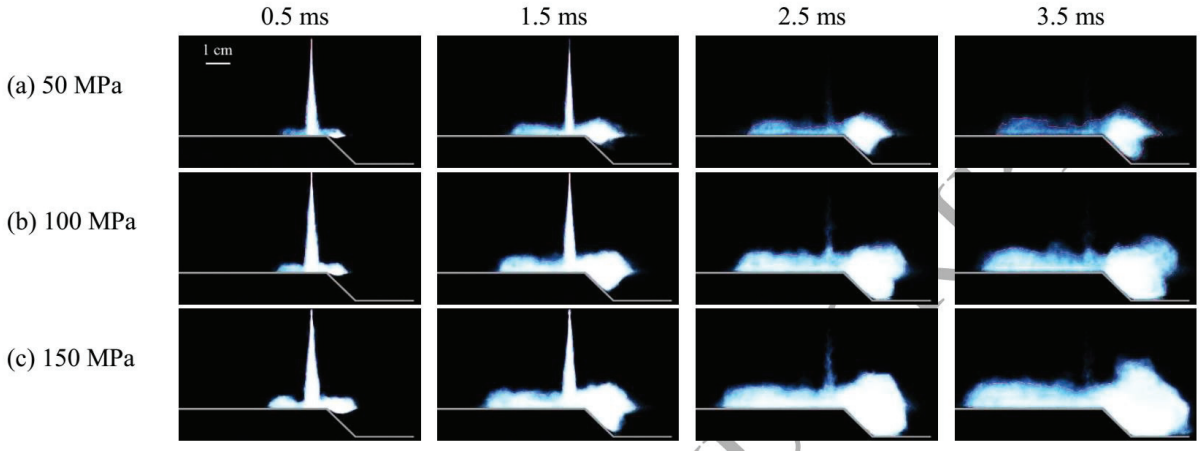

(a) $\theta_c = 45^\circ$

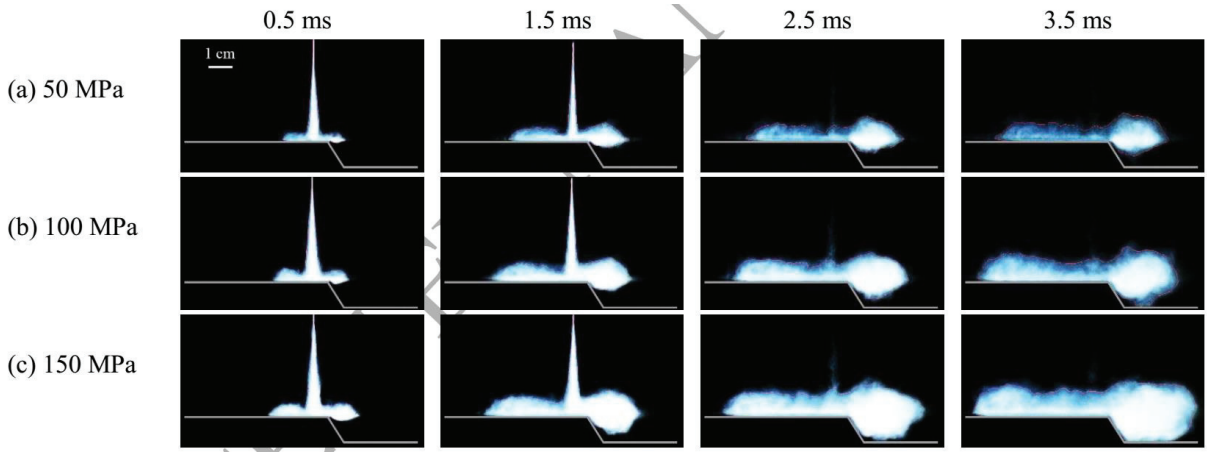

(b) $\theta_c = 60^\circ$

Figure 1.19 Image of the impinging spray under different corner angles [Zhang et al., 2018]

1.4.2 Microscopic characteristics of Spray and Droplet Behaviors

It is well known that the microscopic characteristics of fuel spray are very important for atomization and mixture formation. The droplet size and number distributions reveal the quality of spray and atomization, which affects the subsequent combustion and emissions characteristics [Guan et al., 2015]. In the near spray region, the transition from the injector flow to the fully developed spray is modeled as a three-step mechanism, see Figure 1.20, consisting of film formation, sheet break-up, and, final disintegration into droplets.

Figure 1.20 Break-up of the liquid sheet into ligaments and droplets [Baumgarten C, 2006]

Comprehensive experimental investigations have been carried out to deeper understand the microscopic spray characteristics. Both Payri et al. [1996] and Lacoste et al. [2003] discussed the shear force and coalescence behavior of droplets in diesel free spray. Manin et al. [2014] reported direct observations of the liquid structures or droplets in the near-nozzle region of a single-hole injector, as shown in Figure 1.21. Their observations showed that the surface tension of high-grade n-dodecane fuel was evident when fuel was injected into a low-ambient pressure condition, whereas the surface tension decreased significantly under higher ambient-pressure condition as fuel ligaments and droplets breakup. Lee et al. [2014] focused on the spray breakup and atomization processes of GDI injectors. Their results showed that an increase in injection pressure led to a decrease in Sauter mean diameter (SMD, also known as D_{32}), but there is a limitation on droplet breakup up to 20 MPa. Guan et al. [2015] examined the effect of different fuels on the microscopic spray characteristic during free spray. They reported that lower viscosity and surface tension improved the spray characteristics by comparisons of droplet number density and droplets size distribution. Wang et al. [2015] investigated the microscopic characteristics of split injection spray, and their results showed that higher injection pressure led to better dispersion and atomization. Moreover, the strong collision between split injection caused larger droplets than those obtained with single injection. Crua et al. [2015] used long-range microscopy to investigate the primary atomization of diesel, biodiesel and kerosene fuels in the near-nozzle region, both at atmospheric and realistic engine conditions. Their findings confirm that fuel can remain trapped in the injector holes after the end of injection. Although we could not measure the hydrocarbon content of the trapped vapourised fluid, we observed that its density was lower than that of the liquid fuel, but higher than that of the in-cylinder gas, as shown in Figure 1.22.

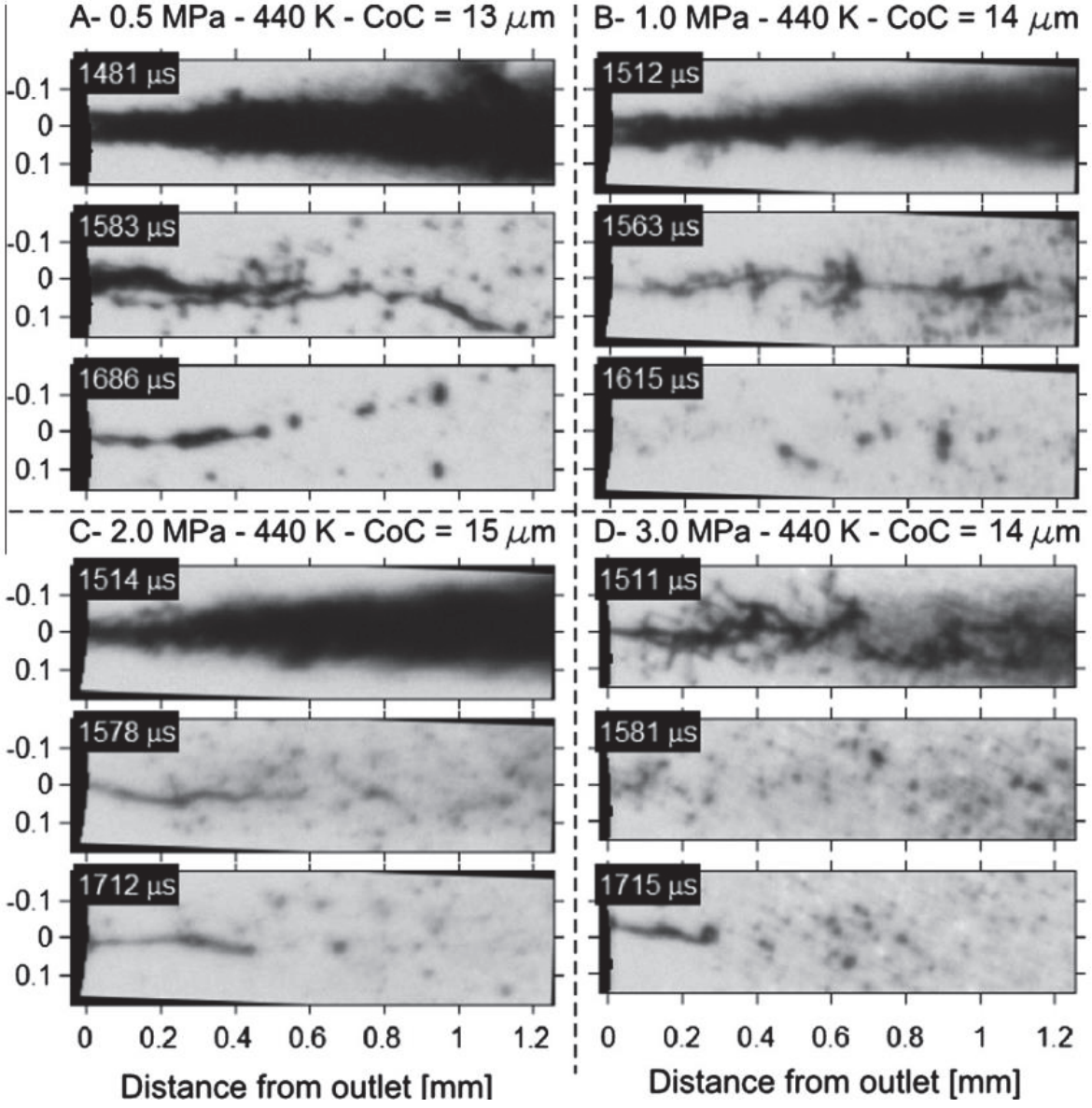

Figure 1.21 The liquid structures or droplets in the near-nozzle region [Manin et al., 2014]

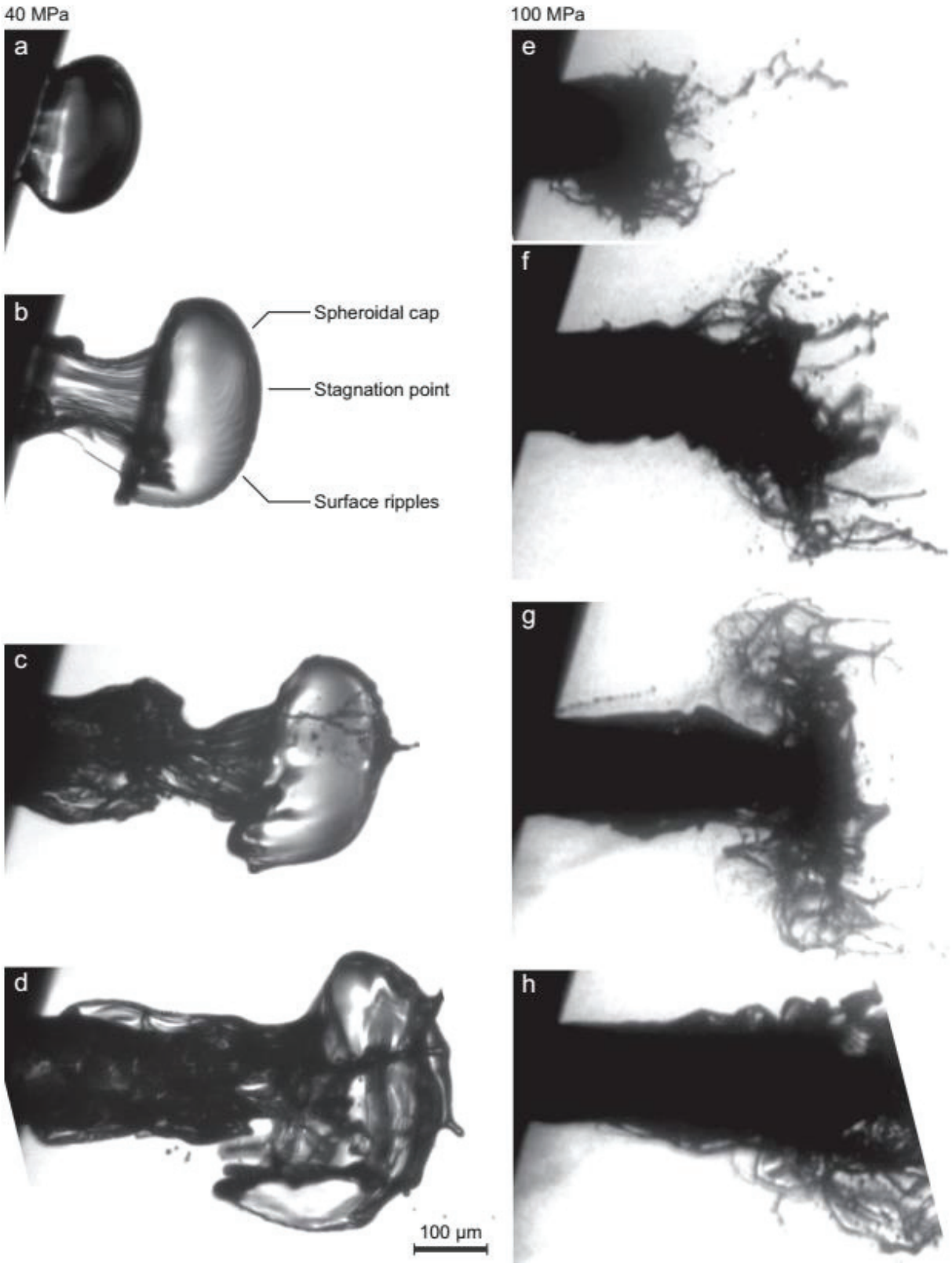

Figure 1.22 Effect of injection pressure on the initial stage of spray [Crua et al., 2015]

Feng et al. [2016] experimentally studied the spray and atomization characteristics of fuels blends in common rail injection system. They found that the droplet size decreased as gasoline blending ratio increased in diesel fuel, indicating that the spray atomization was promoted. Guo et al. [2017] visualized the gasoline microscopic spray under idle and wide-open throttle conditions in GDI engine. It was revealed that the SMD decreased on increasing the fuel temperature from 20 to 60 °C, and the reduction in viscosity and surface tension should be the main reasons for that. Liu et al. [2017] reported on the droplet characteristics of gasoline spray under high-temperature (up to 376 °C). They found that the droplet size dropped significantly when the fuel temperature approximated the critical point (278 °C), and that large droplets disappeared when the temperature exceeded 173 °C. Jing et al. [2017] investigated the spray characteristics of dieseline fuel. Macroscopic spray characteristics in terms of spray morphology and penetration were investigated in a constant volume vessel under elevated ambient pressures using high-speed imaging system, while the microscopic spray characteristics including droplet size and velocity distribution were measured at atmospheric condition using Phase Doppler Particle Analyzer (PDPA) system. The results have shown that the gasoline/diesel blending ratio played an important role in affecting the spray atomization process, as shown in Figure 1.23.

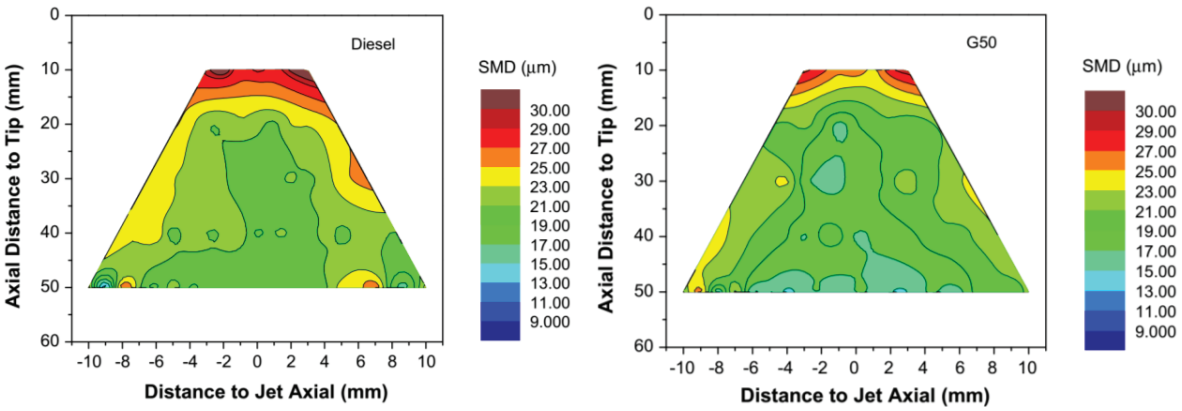

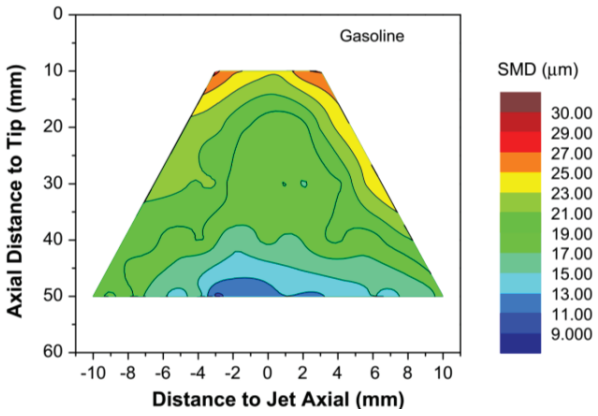

Figure 1.23 Droplet size distribution of gasoline [Jing et al., 2017]

A series of studies have been extensively conducted in terms of free spray processes under different pressures, temperatures and test fuels. However, wall-impingement behavior has not been sufficiently studied. After impingement, the fuel spray velocity changes significantly, and the energy interaction between the fuel and air becomes more violent, resulting in the mechanism of spray and atomization becoming more complicated, especially under high ambient and injection pressures. Therefore, more researches are required to clarify the mechanism of wall-impinging spray. First, the single droplets experiment was done by Mundo et al. [1995], he observed the droplets depositing on the wall and splashing off the wall, then gave the schematics of both, see Figure 1.24 and 1.25.

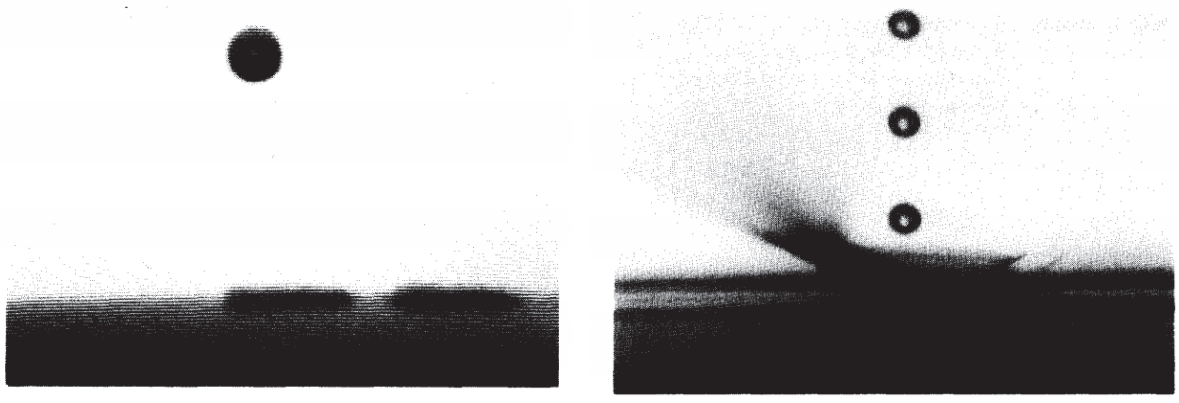

(a) Deposition (b) Splashing

Figure 1.24 Imping droplets behaviors [Mundo et al.,1995]

Bai et al. [2002] proposed the Bai-Gosman model considers four impingement regimes: stick, rebound, spread and splash, shown schematically in Figure 1.26. They identify the various impingement regimes that an impinging droplet may undergo under different conditions as listed:

"Stick" — in which the impinging droplet adheres to the wall in nearly spherical form. This occurs when the impact energy is very low and the wall temperature T_w is below T_{PA} (pure adhesion temperature, below it adhesion occurs at low impact energy).

"Spread" — where the droplet impacts with a moderate velocity onto a dry or wetted wall and spreads out to form a wall film for a dry wall, or merges with the pre-existing liquid film for a wetted wall.

"Rebound" — in which the impinging droplet bounces off the wall after impact. This regime is observed for two cases: (1) on a dry wall when $T_w \geqslant T_{PR}$, (pure rebound temperature, above which bounce occurs at low impact energy), in this case contact between the liquid droplet and the hot surface is prevented by the intervening vapor film; (2) on a wetted wall, when the impact energy is low, and the air film trapped between the droplet and the liquid film causes low energy loss and results in bouncing.

"Rebound with break-up" — where the droplet bounces off a hot surface ($T_w < T_{PR}$), accompanied by breakup into two or three droplets.

"Boiling-induced breakup" — in which the droplet, even at very low collision energy, disintegrates due to rapid liquid boiling on a hot wall whose temperature lies near the Nakayama temperature T_N (is the Nakayama temperature at which a droplet reaches its maximum evaporation rate).

"Break-up" —where the droplet first undergoes a large deformation to form a radial film on the 'hot' surface ($T_w > T_{PA}$), then the thermo-induced instability within the film causes the fragmentation of the liquid film in a random manner.

"Splash" —in which, following the collision of a droplet with a surface at a very high impact energy, a crown is formed, jets develop on the periphery of the crown and the jets become unstable and break up into many fragments.

The existence of these impingement regimes is governed by a number of parameters characterizing the impingement conditions. These include incident droplet velocity, size, temperature, incidence angle, fluid properties such as viscosity, surface tension, wall temperature, surface roughness, and if present wall film thickness and gas boundary layer characteristics in the near-wall region. Quantitative criteria for the regime transitions for both the dry- and wet-wall situations at sub-boiling temperatures derived from the earlier study Bai and Gosman [1995] and refined in the present work are presented in Figure 1.27 and Table 1.1.

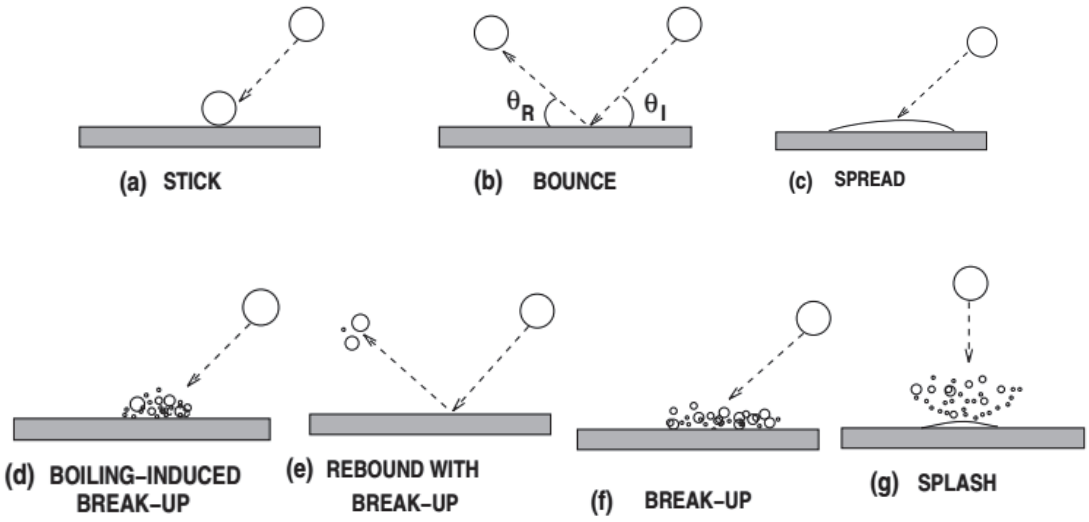

Figure 1.26 Schematics of different impact regimes [Bai et al., 2002]

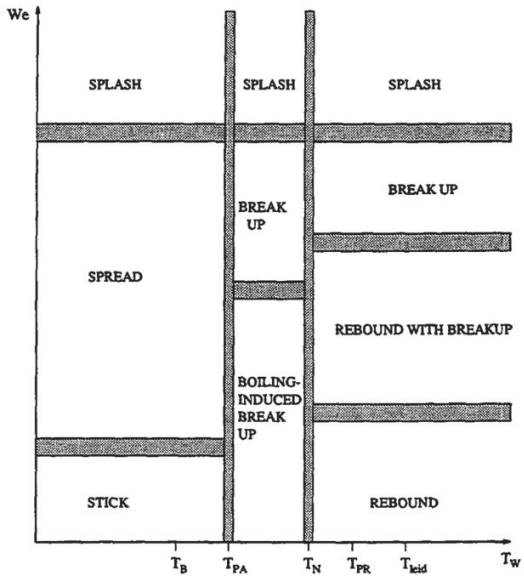

$T_B < T_{PA} < T_N < T_{PR} < T_{leid}$

T_B is the liquid boiling temperature;

T_N is the Nakayama temperature at which a droplets reaches its maximum evaporation rate;

T_{leid} is the Leidenfrost temperature or the minimum evaporation temperature;

T_{PA} is the pure adhesion temperature, below which adhesion occurs at low impact energy;

T_{PR} is the pure rebound temperature, above which bounce occurs at low impact energy.

Figure 1.27 Regime transition conditions [Bai et al., 1995]

Table 1.1 Regime transition conditions [Bai et al., 2002]

Wall status	Regime transition state	Critical Weber number
Dry	Adhesion(Stick/Spread) → Splash	$We_c \approx 2630 La^{-0.183}$
Wetted	Stick → Rebound	$We_c \approx 2$
	Rebound → Spread	$We_c \approx 20$
	Spread → Splash	$We_c \approx 1320 La^{-0.183}$

Senda et al. [1997] divided the impact model into three parts by considering the ratio of out droplets diameter to incident droplets diameter and the ratio of film thickness to incident droplets diameter, as shown in Figure 1.28. Thus, the breakup form was classified into 3 types: Rim type breakup, Cluster type breakup and Column type breakup with their probability. Briefly, these breakup modes for impingement onto a liquid film included breakup or droplet ejection of one or a few droplets at the outer edge of the film (Rim type). Breakup into clusters of many small droplets (Cluster type). And breakup into one or a few droplets from a column of fluid at the center of the spreading droplet resulting from the surface waves reflecting back to their source (Column type). Moreover, he also pointed out that the spray impingement model on high temperature wall and droplets life time on the wall with consideration of the superheat, shown in Figures 1.29 and 1.30.

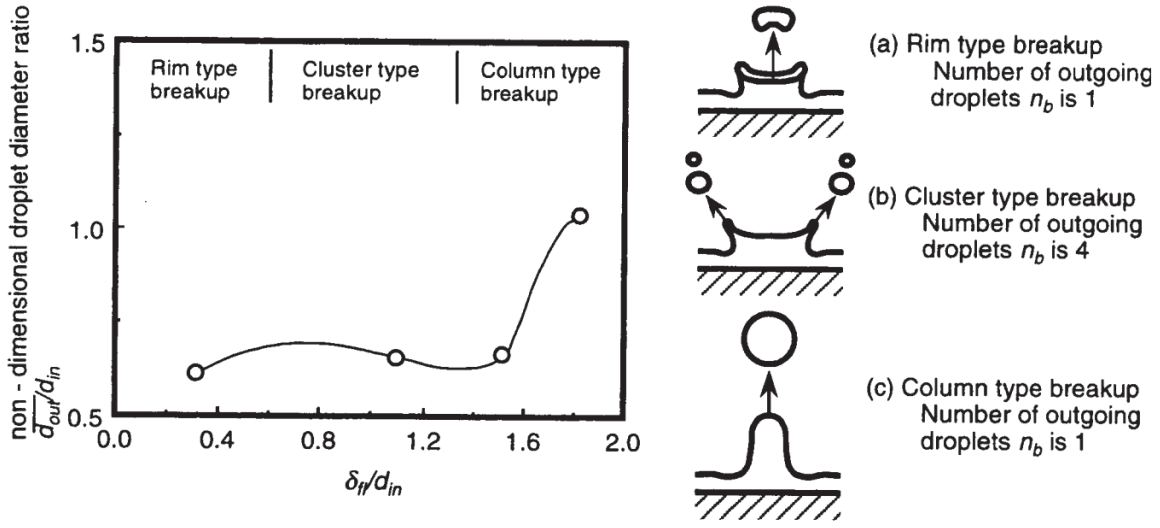

Figure 1.28 Change in non-dimentional droplet diameter ratio d_{out}/d_i with non-dimentional film thickness d_{fl}/d_{in} [Senda et al., 1997]

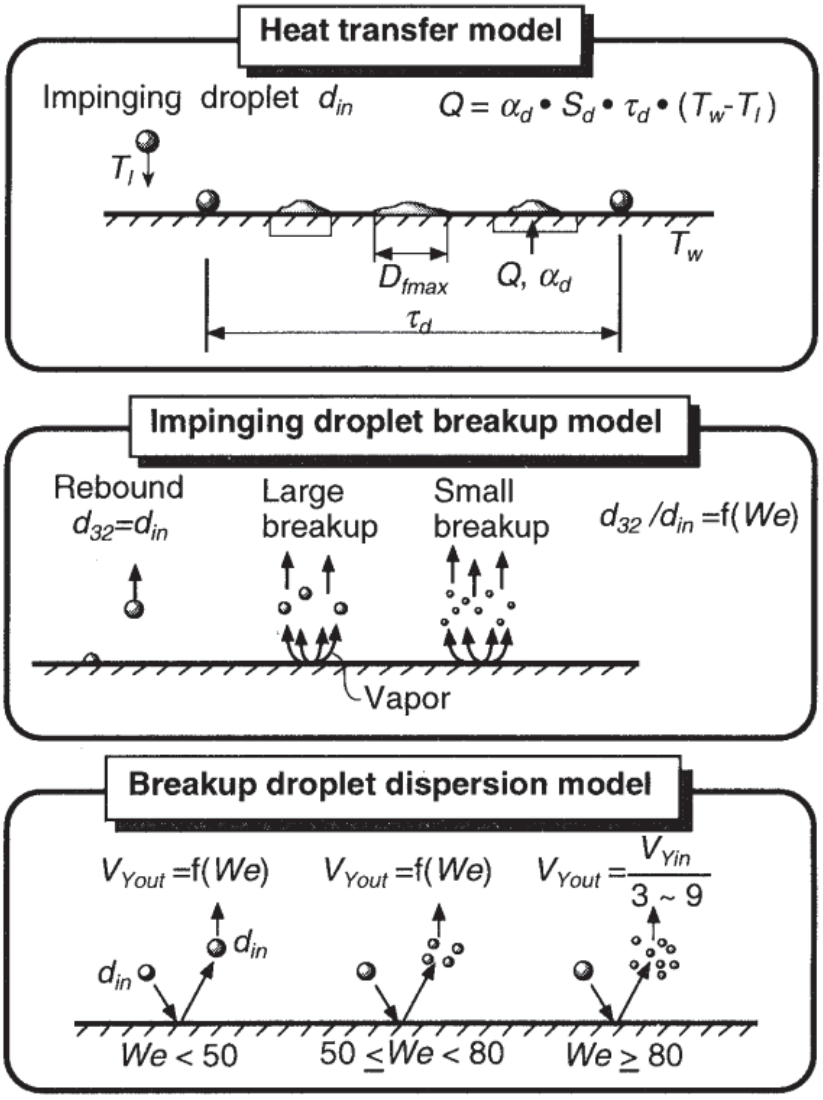

Figure 1.29 Spray impingement model on high temperature wall [Senda et al., 1994]

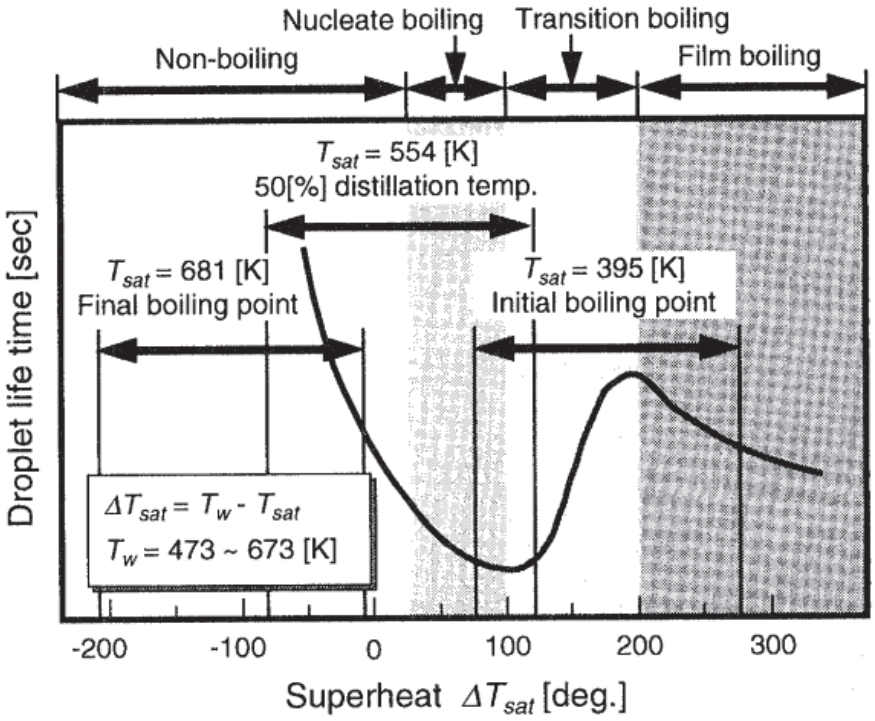

Figure 1.30 Droplet life time with superheat [Senda et al., 1994]

Papers in the current literature mainly focus on experimental work, although a few numerical works have also been conducted. Allocca et al. [2016] described the spatial and temporal evolution of liquid and vapor phases on a heated wall of GDI spray to investigate the structure of spray–wall interaction. Montanaro et al. [2016] studied the spray-wall impact of both GDI multi-hole spray and a single-hole spray over a cold and hot wall to evaluate the droplet behavior after impingement. Piazzullo et al. [2017] investigated the heat transfer effect on wall–film formation in GDI spray, and a good agreement was obtained between the experimental and numerical results. Zhao et al. [2017] studied the spray morphology before and after impingement of spray, and showed that the larger droplets tend to contribute to the fuel film formation more than the smaller ones. Cen et al. [2018] studied the dynamic of jet breakup on the wall with heat transfer. The droplet falling height was set from 1 cm to 9 cm with interval of 0.5 cm, with corresponded Weber number around from 6.94 to 102.12, as shown in Figure 1.31.

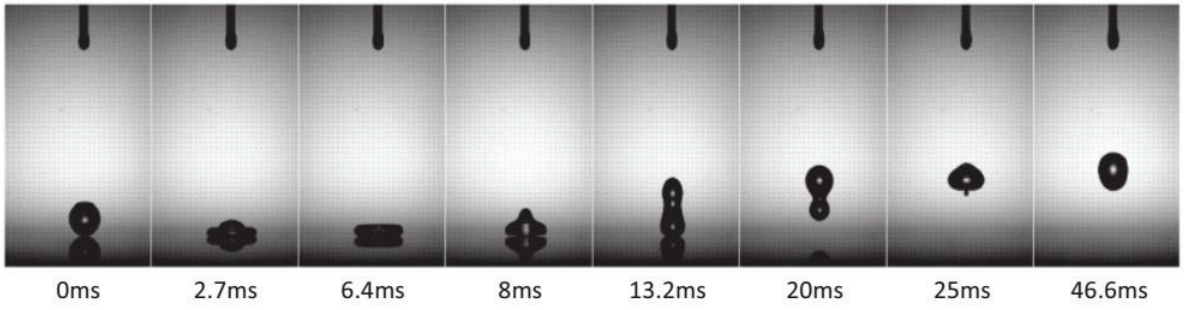

(a) At the height of 1.0 cm

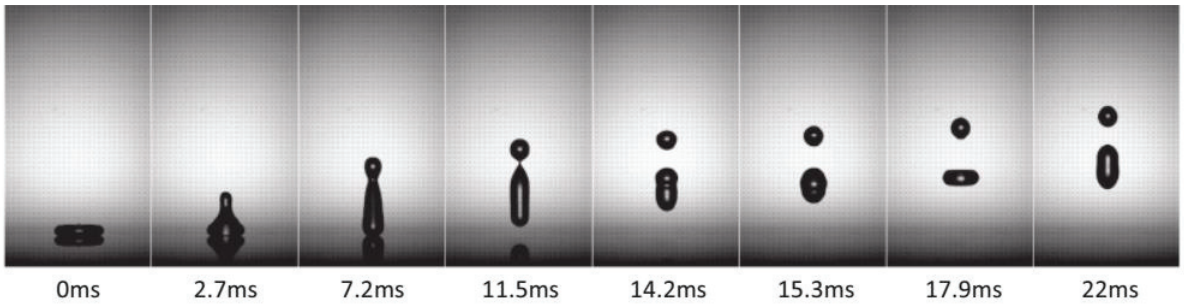

(b) At the height of 1.5 cm

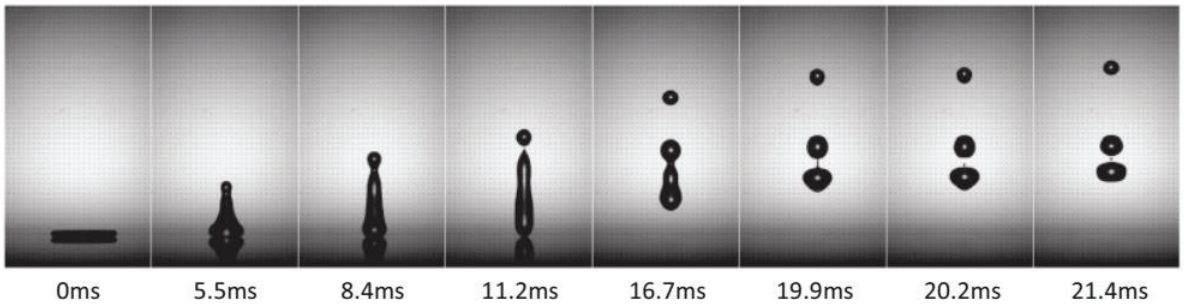

(c) At the height of 2.0 cm

Figure 1.31 Phenomenon of jet breakup [Cen et al., 2018]

1.4.3 Evolution of Fuel Adhesion on the Wall

Fuel droplets tend to get deposited on the wall, resulting in “wet wall” on the piston head and cylinder wall [Yu et al., 2017; Gold et al., 2001]. This affects the air–fuel mixture formation process, which is a major source of excessive soot and unburned hydrocarbons (UHC), making it difficult for DISI engines to meet the subsequent requirements of particle number (PN) regulations [Montanaro et al., 2012; Zhao et al., 1999; He et al., 2012]. In particular, the tendency of reduction in engine size and increase in rail pressure makes it increasingly difficult

to prevent the occurrence of adhered fuel. Therefore, it is essential to understand the impingement behavior and formation of fuel adhesion to improve the performance of gasoline engine and make it more environmentally friendly [Schulz et al., 2017].

However, since it is hard to measure fuel adhesion in a real working engine, comprehensive experimental investigations have been carried out in a constant volume chamber. Specific quantitative studies were performed on fuel adhesion, out of which mainly three methods are summarized. Akop et al. [2013;2013;2014;2014] and Yu et al. [2017] calculated the mass of fuel adhered to an impingement disk wall under different conditions. This method is limited to characterization of the total fuel adhesion mass, not the evolution and thickness of adhesion, as shown in Figures 1.32 and 1.33.

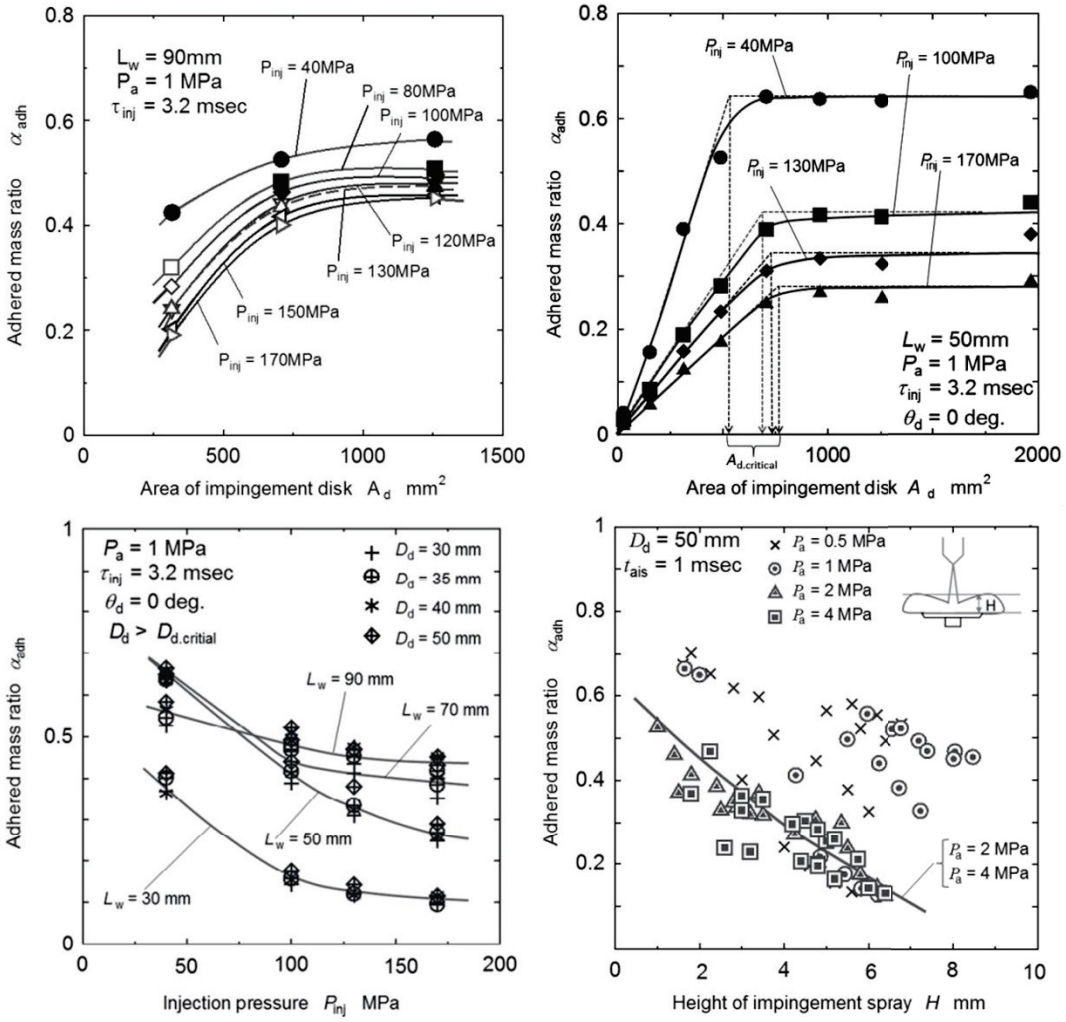

Figure 1.32 Adhered mass characteristics [Akop et al., 2013;2014]

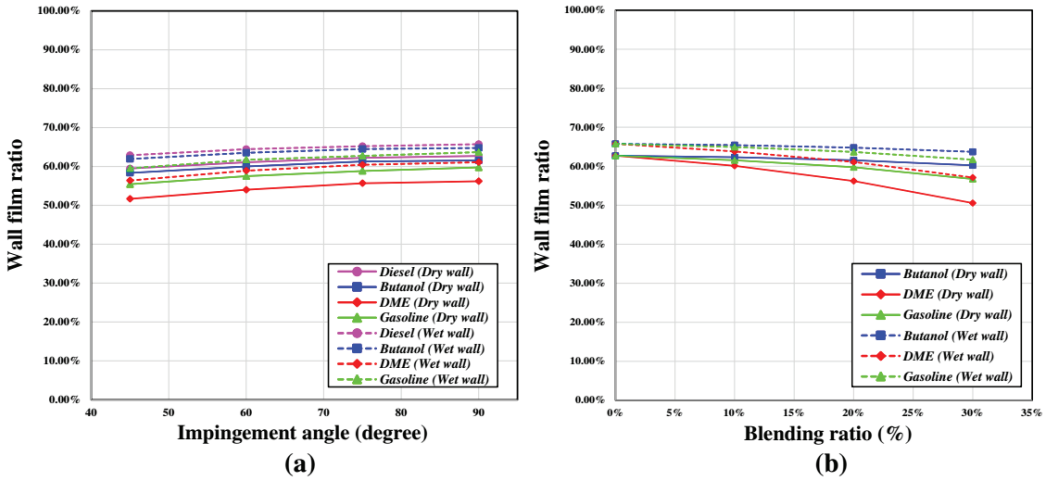

Figure 1.33 Wall film ratio under conditions [Yu et al., 2017]

In the laser-induced fluorescence (LIF) technique, a fluorescent tracer is adjusted to a certain concentration with a given quantum yield and a molar absorption coefficient, and it is excited with a predefined radiation. The adhesion thickness is then determined by measuring the fluorescence intensity. The spatial distribution of fuel adhesion was captured by Senda et al. [1999], Okamoto et al. [2012], Cheng et al. [2010], and Schulz et al. [2015; 2016; 2017]. Especially, Schulz et al. [2016;2017] not only measure the fuel film of the single hole, but multiple holes. And some results are shown in Figure 1.34. However, this method is limited to a perfectly smooth impinging wall, which differs from the real roughness of an engine piston, especially one with carbon depositing after combustion.

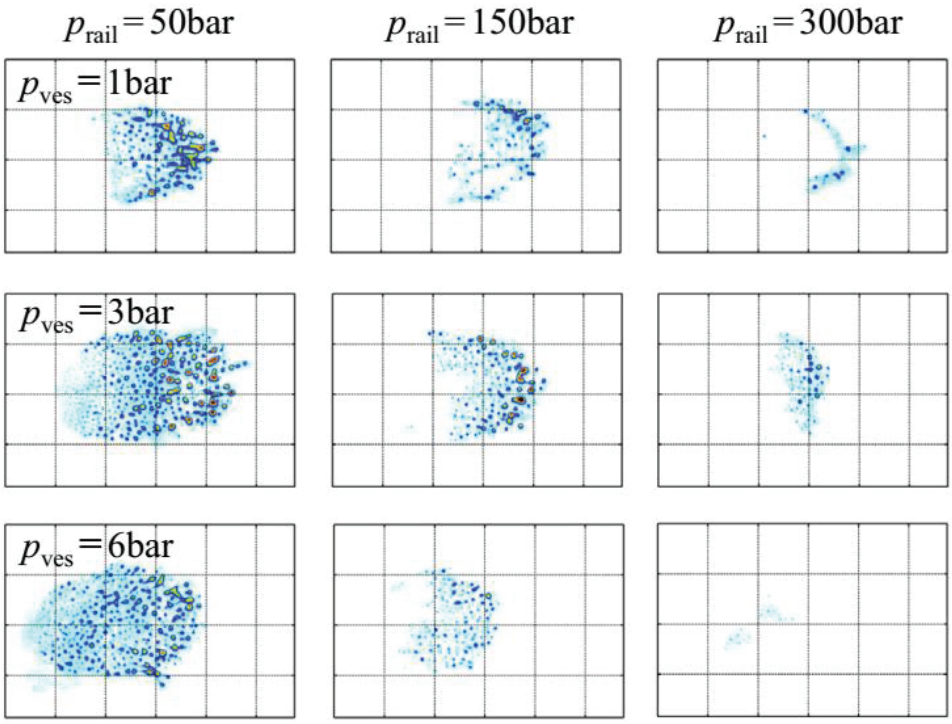

(a) Single fuel adhesion

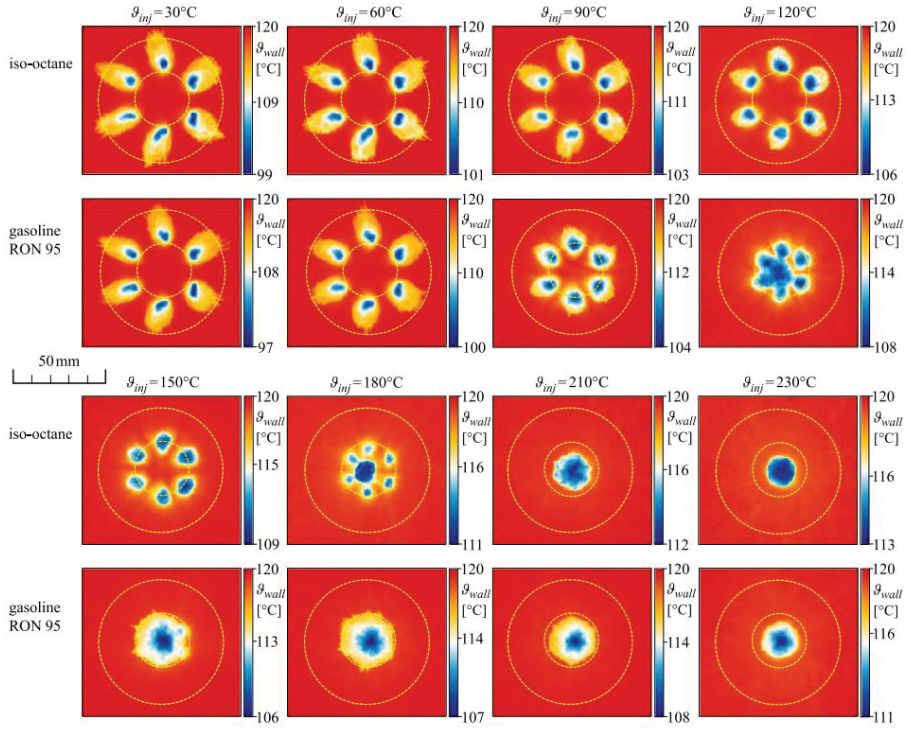

(a) Multiple fuel adhesion

Figure 1.34 Wall adhesion evolution [Schulz et al., 2016; 2017]

A more widespread and well-observed technique for measuring the fuel adhesion on a flat wall with roughness similar to that of a real engine piston is the refractive index matching (RIM) method. Drake et al. [2002; 2003; 2007] developed this optical technique, which was then used by Yang and Ghandhi [2007], Maligne and Bruneaux [2011], Zheng et al. [2012], Henkel et al. [2016], and Luo et al. [2017; 2018] to measure the fuel adhesion under different impingement conditions. In recent times, Ding et al. [2018] has also used the RIM method to measure fuel adhesion in a stratified-charge SI engine, some results from them are shown in Figure 1.35.

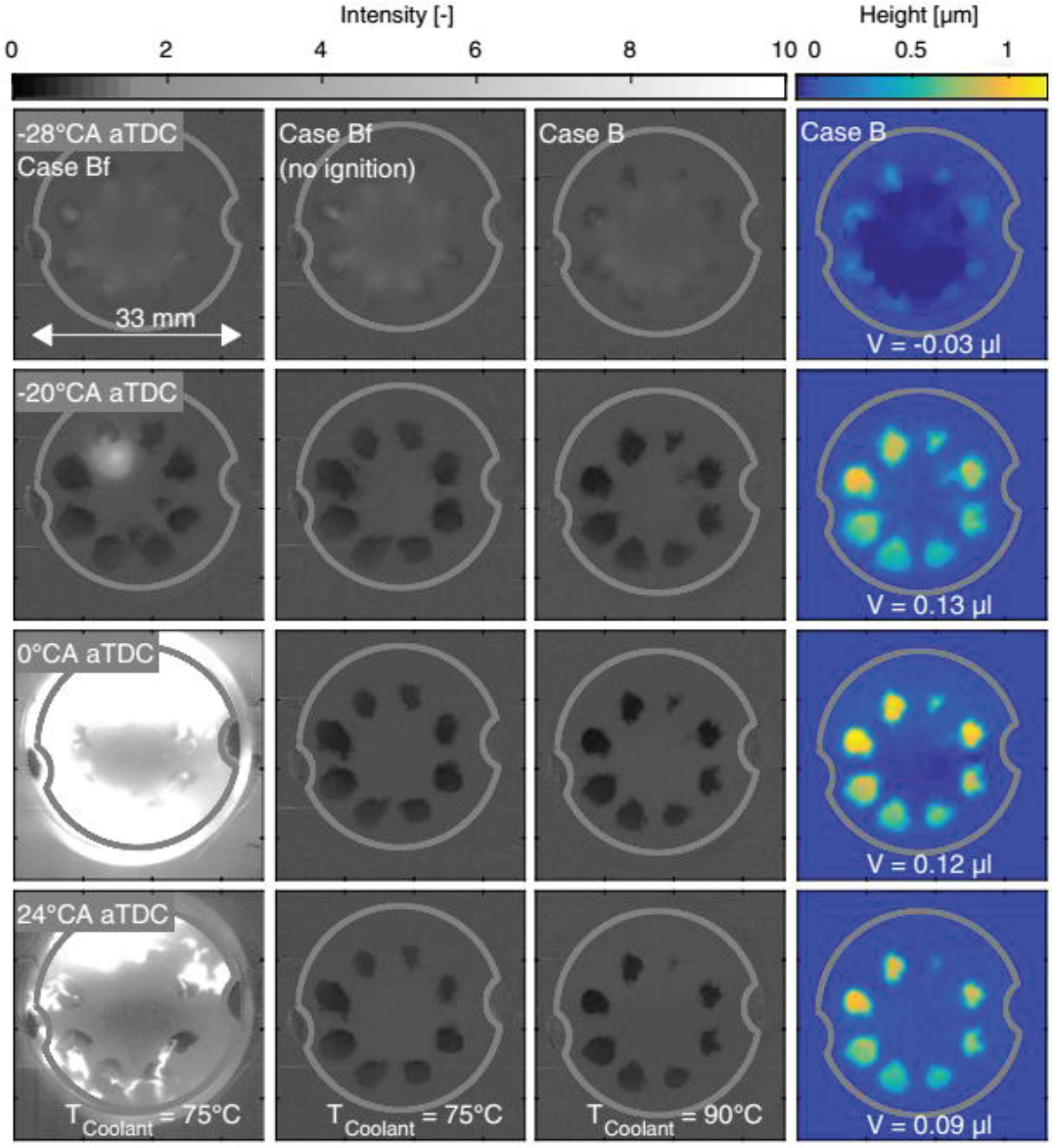

Figure 1.35 Normalized adhesion images of selected cycles [Ding et al., 2018]

A series of extensive studies have been conducted on fuel adhesion characteristics under non-evaporation conditions. However, the air temperature in a real engine during operation is quite high, especially when the engine is under high load. Maligne and Bruneaux [2011] observed “discrete pocket” areas of the gasoline fuel that evaporate faster than areas of “continuous film”. Zheng et al. [2012] studied the mass and area of gasoline fuel adhesion under conditions of high temperature of the air–fuel mixture, and compared the results with computational fluid dynamics (CFD) calculations. Schulz et al. [2017] investigated the effect of flash-boiling on fuel adhesion formation using a multi-hole gasoline injector, and discovered that increasing the fuel temperature to a certain value does not lead to a constant reduction in the adhered fuel on the wall owing to the collapse of spray jets and fuel accumulation in a single region. Piazzullo et al. [2017] compared the gasoline footprint at the wall between measured and simulated results under evaporation condition by evaluating the fuel mass adhering to the wall and the wall heat flux. Until now, the formation of fuel adhesion on the wall is still ambiguous and requires more research.

1.4.4 Optical Diagnostic Technique in DISI Engines Conditions

In order to get thorough understand of the impinging sprays, the optical diagnostic techniques have been widely applied in the study. Most of the techniques have already been summarized excellently by Zhao and Ladommatos [2001].

1.4.4.1 Spray observation

In this section, some typical spray visualization diagnostic techniques will be reviewed briefly based on their work introduced in Part 1.4.3, and Table 1.2 shows the list of these techniques.

Table 1.2 Summary of optical techniques for spray evolution measurement

Technique	Applications	Advantages	Limitations
Mie Scattering	Liquid fuel distribution	Simple setup	Sensitive to large droplets
Schlieren and Shadowgraph	Observation of overall spray	Simple setup	Sensitive to both liquid and vapor phases

Because of the simplicity and explicitness of Mie scattering method, shown in Figure 1.36 (a), it is mainly applied to detect the spray liquid phase. According to the Lorenz-Mie theory, when the droplets are spherical and their diameter is larger than 1 μm, the scattering intensity is mainly determined by the droplets concentration and the square of droplet diameter [Kim et al., 2002]. Hodges et al., [1991] applied ensemble-scattering polarization ratio method, based on the Mie scattering, to measure the droplet size and concentration. One year after that, the spray fuel concentration was measured by Kosaka et al., [1992] quantitatively by applying a 2-D Mie scattering technique. However, compared with recently developed techniques, the accuracy of the droplet diameter concentration measured from the Mie scattering experiment is not high enough. As a result, this technic is usually applied to detect the spray structure [Gulder et al., 1992] and the liquid phase penetration [Siebers DL, 1998].

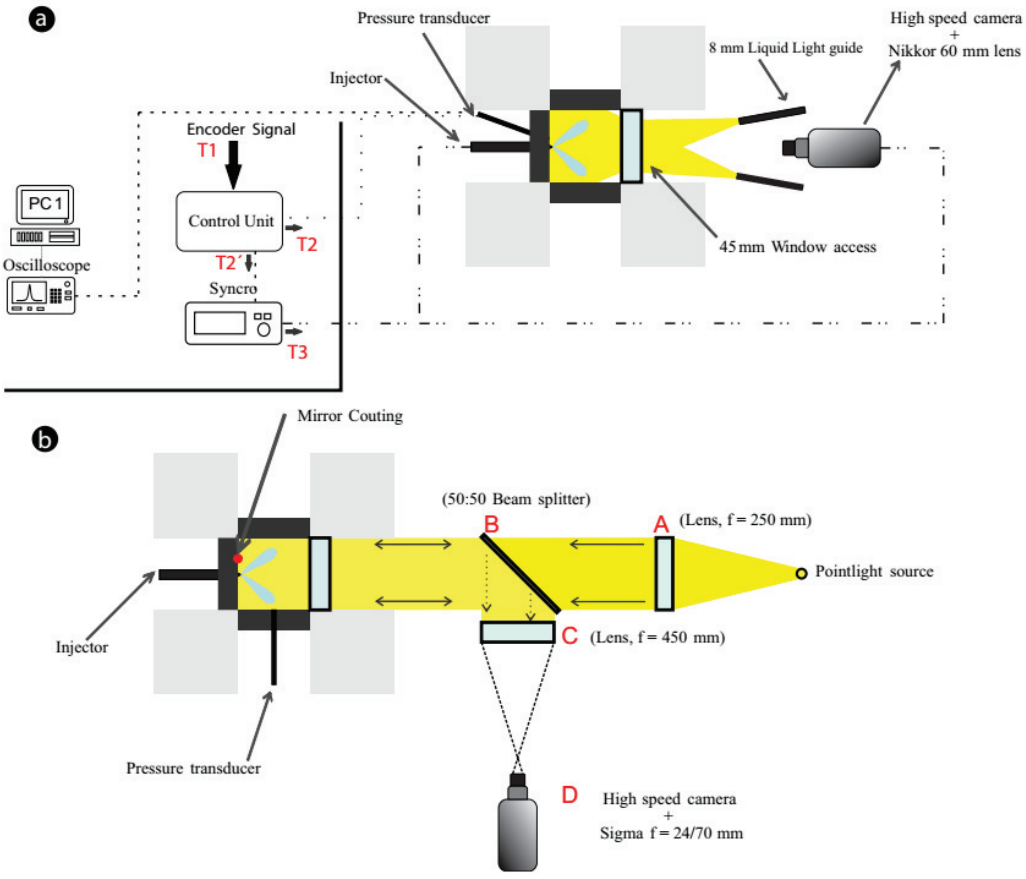

Figure 1.36 Sketch of optical techniques arrangement. (a) Mie scattering for liquid length measurements and (b) focused shadowgraph for vapor penetration measurements [Pastor et al., 2011]

As two of the earliest optical diagnostics Schlieren (shown in Figure 1.37) and shadowgraph (shown in Figure 1.36 (b)) can be used to observe the spray liquid and vapor phase, simultaneously. Normally, they are also usually adopted to measure the spray structure, because of the limitation of quantitative analysis. However, compared with Mie scattering method, their superiority is that they can not only detect the spray liquid phase but also distinguish the vapor phase. Furthermore, the interface between liquid and vapor phase can be evaluated through the gradient of intensity roughly. As a result, it also has been used to identify the evaporating spray boundary [Siebers, 1998; Pickett et al., 2009].

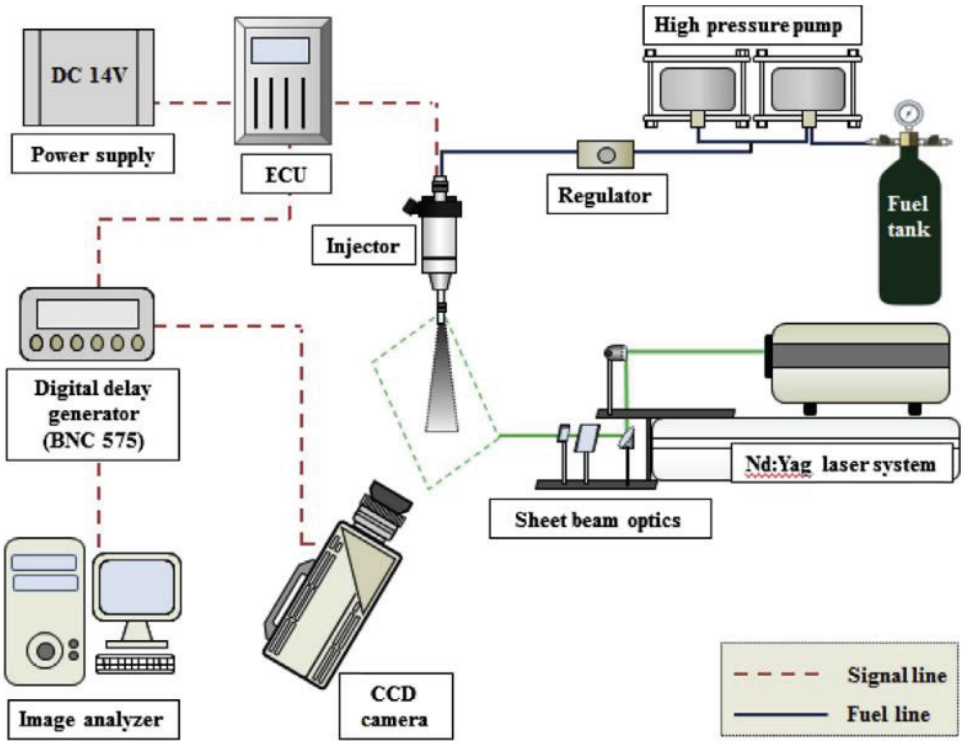

Figure 1.37 Sketch of optical techniques arrangement for Schlieren [Lee et al., 2014]

1.4.4.2 Droplets detection

For droplets velocity and diameter measurement, two methods are widely used: PDPA and PIA, as summarized in Table 1.3.

The Laser doppler velocimetry has been widely applied and well developed, including the Laser Doppler Anemometer (LDA) and Phase Doppler Anemometry (PDA), which is also known as the name of Phase Doppler Particle Analysis (PDPA) techniques. Based on the

Doppler shift of the laser light, which is scattered from the small particles within the moving fluid, LDA is usually applied to measure the particle size and velocity. Figure 1.38 shows the PDPA system including an argon ion laser, a beam separator, a Fiber Flow transmitting optics, a Fiber PDA receiving optics, a photoelectric converter, a BSA P80 doppler signal analyzer with 180 MHz frequency and a 3-D motion traverse system. Laser power used in this study was 1300 mW and lase wave length ranged from 488 nm to 514. 5 nm. The focal lengths of transmitter and receiving optics were both 500 mm and they were installed in an L-type 3-D motion traverse system to achieve stable light path. The measuring range of droplet size was set from 0 μm to 236 μm with resolution of ±0.05 μm. Meanwhile, droplet velocity measuring range was set from 151.95 m/s to 238.77 m/s.

Table 1.3 Summary of optical techniques for droplets measurement

Technique	Applications	Advantages	Limitations
PDPA	Droplets velocity and diameter	Time-resolved data	Complex setup
PIA	Droplets velocity and diameter	Simple setup	Single shot data

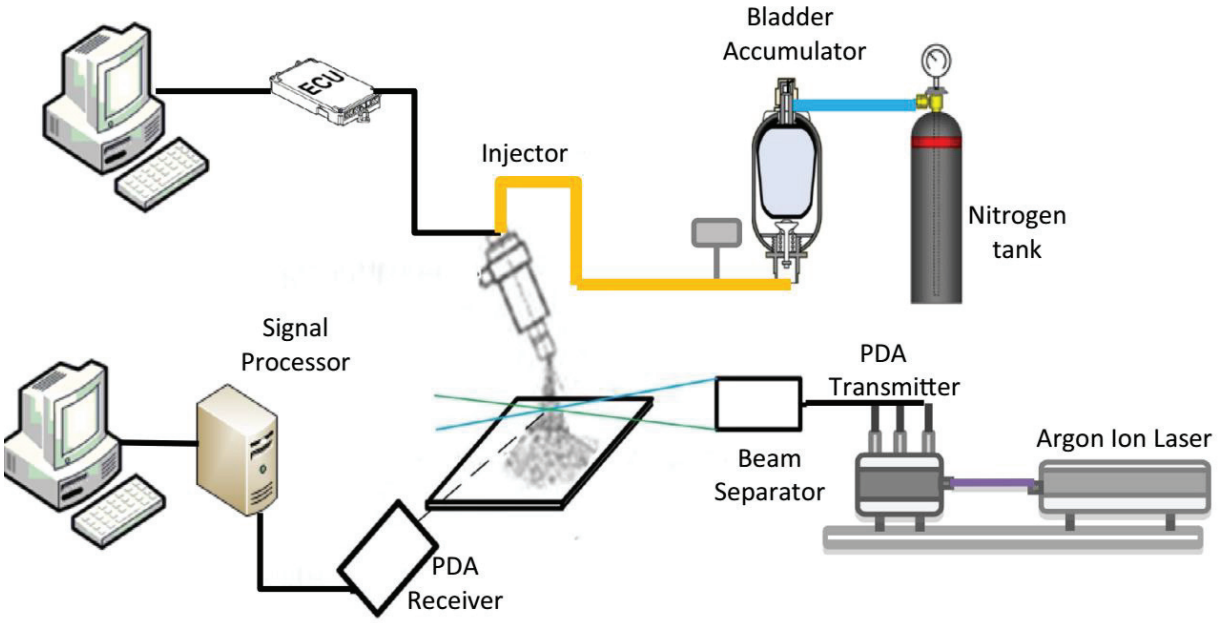

Figure 1.38 Typical PDPA system for analyzing droplets size and velocity [Pei et al., 2017].

Previously, Kashdan et al. [2007] and Berg et al. [2006] compared the PIA technique with the well-established technique PDPA and the results show that PIA is a reliable technique to measure the size of spherical and non-spherical droplets. Hence Guan et al. [2015] employed the PIA system to investigate the microscopic spray characteristics, shown in Figure 1.39. An Nd: YAG laser with the wavelength of 532 nm, along with a diffusor attachment, was employed for the homogeneous illumination. The diameter of the lens at the head of the diffusor is 120 mm, which is larger than the window of the chamber, to ensure the homogeneous illumination of the spray flow field. CCD camera (ImagerProSX 5M) connected with a long-distance microscope (Queststar QM1) and a magnifying lens with an amplification factor of 2 was used to capture the droplets. The camera and microscope were mounted on an electric positioner MC600. The precise displacement control (1 μm) ensures the accurate scanning of the measurement position. The calibration was carried out via a scaling plate with minimum scale of 25 μm.

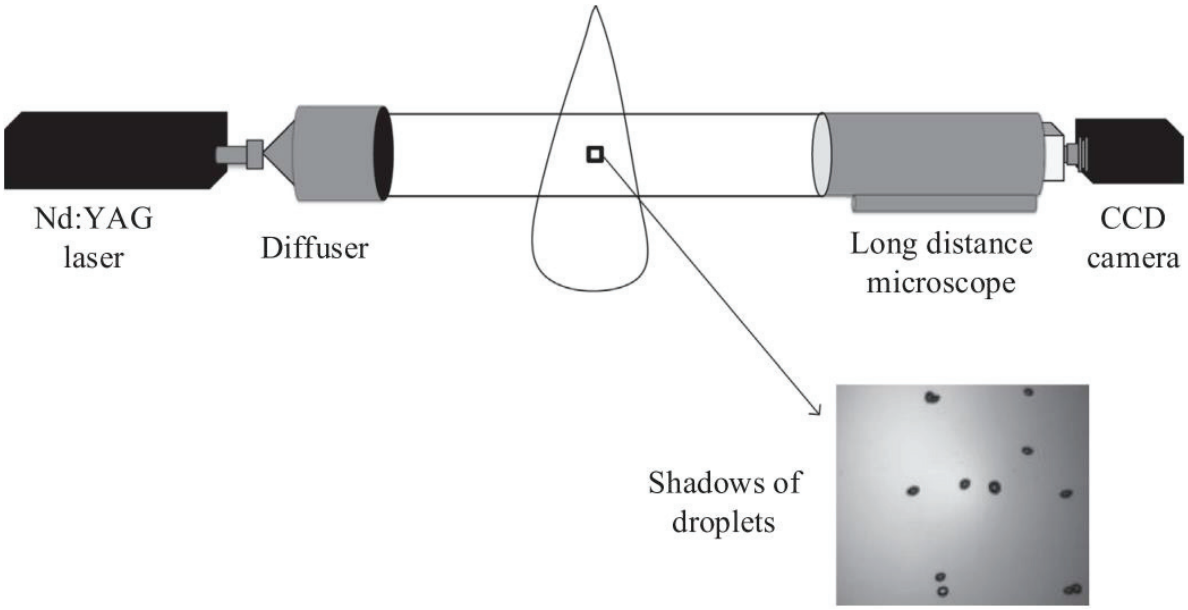

Figure 1.39 The sketch of PIA system [Guan et al., 2017].

1.4.4.3 Fuel adhesion measurement

As I introduced in Part 1.4.3, Specific quantitative studies were performed on fuel adhesion, out of which mainly three methods are summarized: Weighting; LIF and RIM, as summarized in Table 1.4.

Table 1.4 Summary of optical techniques for fuel adhesion measurement

Technique	Applications	Advantages	Limitations
Weighting	Liquid fuel adhesion	Simple setup	Measure the mass only
LIF	Liquid fuel adhesion	Simple setup; Thickness distribution	Difficult to calibrate; Flat-wall must be smooth
RIM	Liquid fuel adhesion	Simple setup; Thickness distribution; Different roughness of the wall can be used	Difficult to calibrate;

The procedure for measurement of adhering fuel mass is illustrated in Figure 1.40. The mass of the dry impingement disk was measured before fuel injection. Then, the impingement disk was set normally to the injector. After spray impinged on the disk, the disk was removed from the high-pressure vessel and adhered fuel mass was measured together with the mass of disk by using a precision balance with sensitivity of 0.01 mg. Adhered fuel mass was derived by the difference of the disk masses of before and after impingement

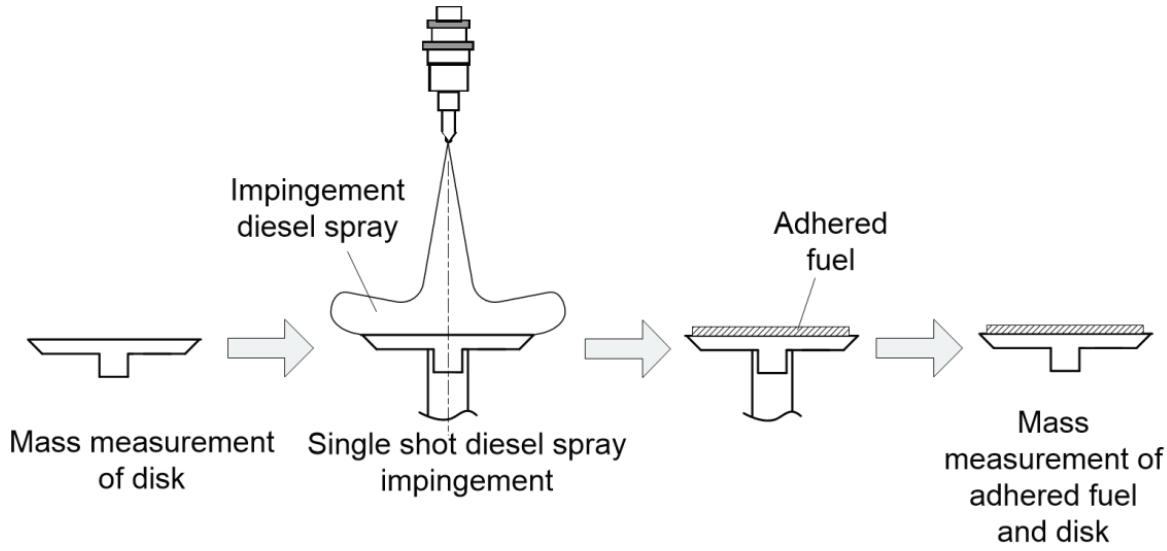

Figure 1.40 Measurement procedure for weighting adhesion [Akop et al., 2013]

Laser Induced Fluorescence (LIF) method has been applied for measuring temperature, thin film thickness, concentration and so on using the changes of fluorescence lifetime and intensity. An explanation of LIF is shown in Figure 1.41. LIF uses an electronic absorption and emission

process which can produce relatively strong signal with high spatial resolution [Andresen et al., 1990]. When the atom or molecule absorbs the specified laser energy, the electronic state energy is excited to an upper level. Because of the instability, the electronic goes back to state ground immediately accompanied with the emission light, which is usually called as fluorescence. Therefore, the fluorescence intensity can be used to estimate the fuel concentration because it is proportional to the molecular density. As a result, LIF is widely used to measure mass distribution [Yeh et al., 1994; Bruneaux, 2002]. However, fluorescence intensity is very sensitive to the quenching effect, and the impingement plat must be smooth, which is different with the real roughness of the piston head in the engine.

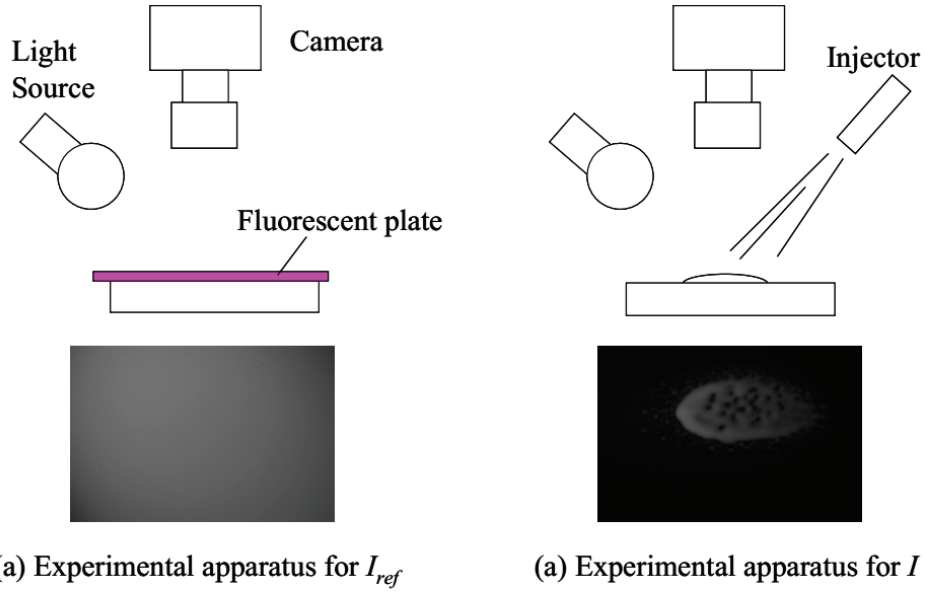

(a) Experimental apparatus for I_{ref} (a) Experimental apparatus for I

Figure 1.41 Typical LIF system for fuel adhesion [Okamoto et al., 2012]

Drake et al. [2002; 2003; 2007] developed an optical method to quantitatively investigate the fuel film on the piston of a direct-injection gasoline engine, as shown in Figure 1.42. The technique is based on the variation of light scattered from a roughened surface when a liquid of refractive index that matches the window is in contact with the surface. This method enabled time-resolved quantitative information to be derived from the entire fuel film under vaporizing conditions with high spatial and temporal resolution. Their experimental results showed that liquid fuel film volumes were approximately 1% of the injected fuel for a hollow-cone swirl injector and only 0.1% for a multi-hole injector. The liquid fuel films, with gasoline fuel, were observed to have a maximum local film thickness of around 3 μm and area-average film

thickness of around 1 μm. These results were found to correlate very well with engine-out smoke emissions from an optimized wall-controlled SIDI gasoline engine under warmed-up stratified-charge operating conditions.

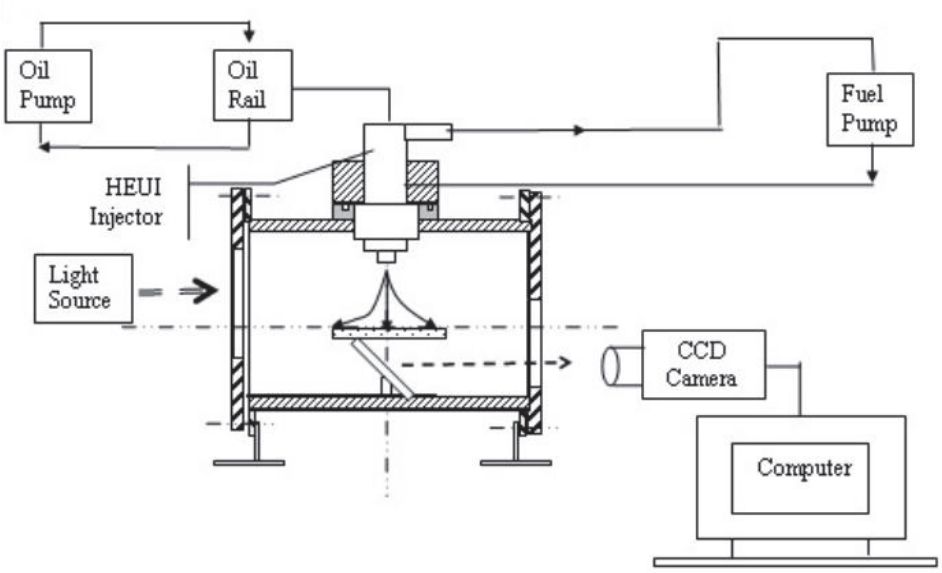

Figure 1.42 Typical RIM system for fuel adhesion [Drake et al., 2007]

1.5 SUMMARY

In this chapter, the background and motivation of this study is introduced firstly. After that, the outline is shown before a series of study review. From the spray-wall interaction to droplets behaviors and fuel adhesion formation, a lot of classic theories developed form experimental and numerical researches were described in detail. After that, the corresponding technical approaches were also introduced one by one.

Based on the review of previous study about the gasoline spray system, impinging spray for gasoline was well investigated under high injection pressure conditions. However, the research on fuel adhesion is not enough, especially for the formation of fuel adhesion on the wall. Therefore, a single-hole nozzle is originally applied in the fundamental research to provide insights into the spray characteristics and fuel adhesion in this study. Meanwhile, previous research has also shown some interesting report about droplets, but most of them focused on the free spray. The microscopic of impinging spray is necessary to study, and correlation between

the droplets characteristics and fuel adhesion can give us a clear understanding about fuel adhesion formation.

In the following chapters, the experimental investigations method applied in this study and the results about the impinging spray under non-evaporation and evaporation conditions will be presented.

CHAPTER 2 EXPERIMENTAL APPARATUS AND MEASUREMENT METHODS

2.1 CONSTANT HIGH-PRESSURE CHAMBER

In order to acquire the engine-like ambient condition and high quality of visualization of spray evolution, a special high pressure and high temperature chamber was applied.

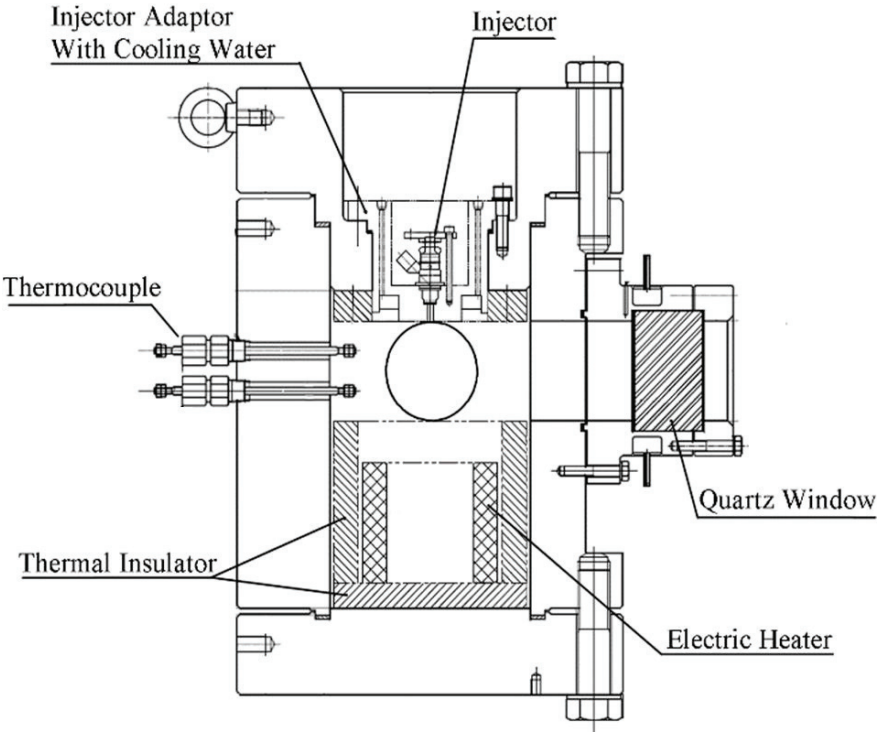

Figure 2.1 Schematic of the high-pressure chamber

As shown in Figure 2.1, it has four available windows, and according to the specific experiment the utilized window was variable. The quartz glass with diameter of 100 mm was mounted in the utilized window adaptor. Two thermocouples were fixed by the thermocouple adaptor, which can detect the ambient temperature and the near wall temperature. A kanthal alloy heating unit was placed inside the chamber to produce the engine like high temperature and high temperature condition as high as 500 K. The internal and external surfaces of the chamber are covered by the thermal insulator to avoid the heat conduction and maintain the stable environment. There were cooling water circulations inside the injector adaptor to avoid

overheating. The high-pressure condition inside the chamber was produced by applying a gas cylinder, which can increase the chamber pressure to above 1.5 MPa.

2.2 ELECTRICAL CONTROLLING SYSTEM

In the experiments, the injection timing, imaging timing, and laser induced timing are all controlled by the electrical controlling system. Specifically, the injector was controlled by the injector electronic control unit (ECU). Injection timing, injected mass and image taken timing were controlled by a delay pulse generator (Stanford Inc., DG 535 or DG645). The basic information of the signal for injector, camera is shown in Figure 2.2.

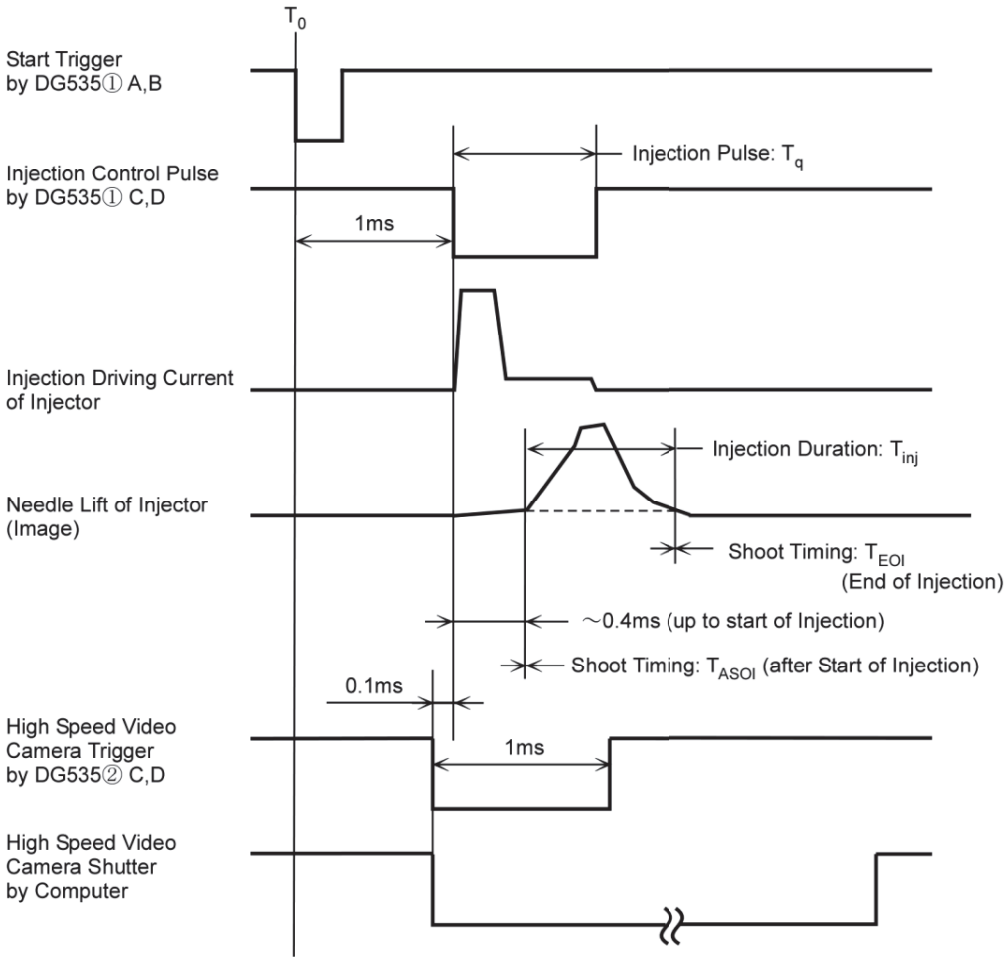

Figure 2.2 Timing chart of signal

However, it can be seen that there is a delay between the injection signal and the fuel injection, which can cause the difficulties in deciding the start of injection and time after start of injection by the high-speed images. In order to find the start of injection timing as accurately as

possible, the injection delay measurement was conducted by comparing the pulse signal and the injection rate signal during the injection rate measurement experiments. The imaging time of the camera and laser induced setting are changing according to the injection delay variation.

2.3 IMPINGEMENT SYSTEM

As shown in Figure 2.3, a quartz glass (Sigma Koki, DFSQ1-50CO2) with a diameter of 50 mm and thickness of 2 mm, was set under the injector as the flat wall. The impingement angle was 45° and the impingement distance was 22 mm from the nozzle exit to the impingement point of the flat wall along the spray axis. The coordinate system is defined, and the intersection point o of the nozzle center axis and the wall is determined as the impingement point. The positive *y* axis is along the lateral direction of the spray after impingement, and the positive *z* axis is parallel to the injector axis, and the *x* axis is perpendicular to the *yz* plane, pointing out of the figure. Moreover, the surface roughness was measured by a portable high-performance surface roughness and waviness measuring instrument (Kosaka Laboratory Ltd., SE300), whose resolution is 0.0064 μm.

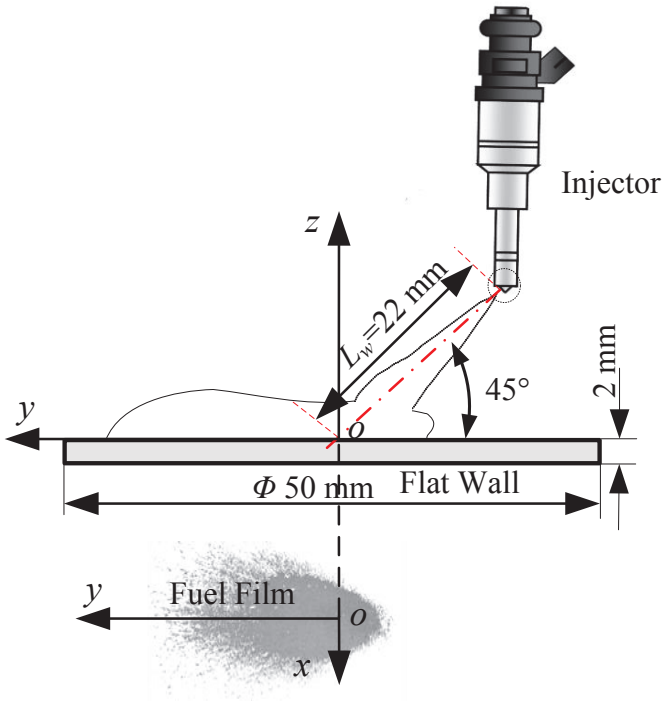

Figure 2.3 Schematic of injector and flat wall

2.4 OPTICAL MEASUREMENT SYSTEMS

2.4.1 Mie Scattering Method

2.4.1.1 Experiment apparatus

In order to observe the spray development process, a Mie scatting experiment was performed using a single-hole injector, and the specific experimental apparatus are shown in Figure 2.4. It consists of a constant high-pressure chamber, an injection system, and an optical system. Toluene fuel was directed into the mini sac injector by a high-pressure injection system. A high-speed video camera (Photron FASTCAM SA-Z) was utilized to observe the spray and was set at a frame rate of 20000 frames per second (fps) and at a frame size of 512 × 512 pixels. A xenon lamp (Ushio SX-131 UID501XAMQ) was set in a direction perpendicular to the camera to illuminate the spray, and both were in the same plane. The injector and camera were synchronized by a delay generator. Two windows of the constant volume chamber were used. The layout of the lamp and the camera is shown in Figure 2.4 (b).

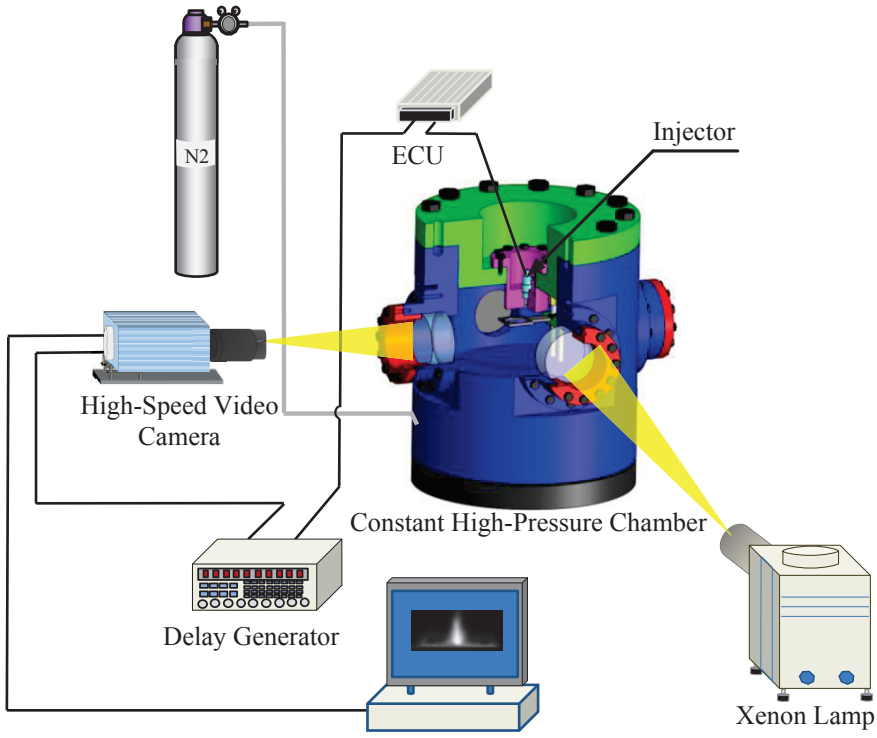

(a) Front view

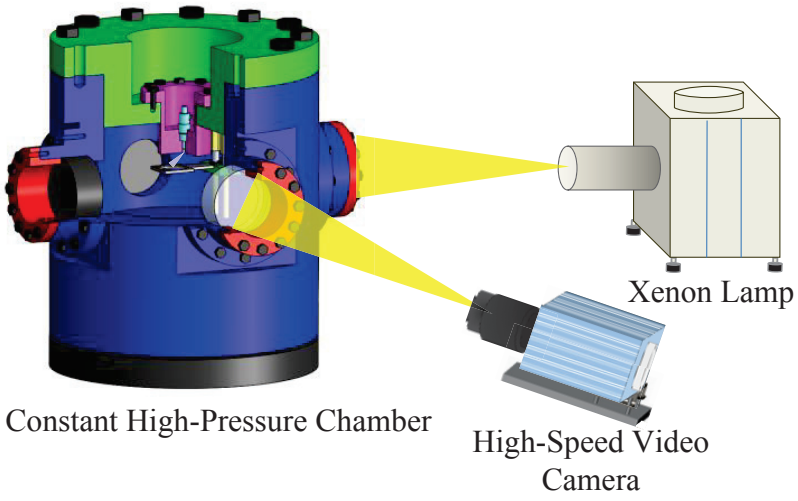

(b) Side view

Figure 2.4 Experimental apparatus for spray observation.

2.4.1.2 Image processing method

The parameters such as impinging spray radius (R_s), impinging vortex height (H_v), spray tip penetration (S) and impinging spray height (H_i) are widely used to investigate the characteristics of the spray-wall impingement (Park and Lee, 2004; Andreassi et al., 2007; Zhang et al., 2014; Yu et al., 2016). These values were experimentally obtained from raw images by determining the edge of the impinging spray using inhouse code created by ourselves in MATLAB software as shown in Figure 2.5.

The dotted line in Figure 2.5 represents the wall surface. The focus of the front and side views is on the impingement point plane and spray axis plane, respectively. R_s and H_v are defined from the front view. R_s is the maximum horizontal distance from the spray center to the furthest edge of the spray. H_v is the maximum distance from the wall surface to the edge of the spray vortex. S and H_i are defined from the side view. The spray tip penetration is defined as the distance from the nozzle exit to the spray tip (Guo et al., 2015). Generally, before impingement, the spray tip penetration is just the distance from the nozzle exit to the spray tip. However, after wall impingement, the penetration is not only the distance from the nozzle to the wall, but also the radial distance (Yu et al., 2012; Guo et al., 2016). Thus, the spray tip penetration S is defined as the sum of the distance to wall L_x and the radial distance L_r,. The impinging spray height H_i is

the maximum distance from the wall surface to the edge of the impinging spray. Results of the front and side views were obtained from a clear spray by binarizing the images. The fuel adhesion data were obtained from the bottom view. All the results were calculated three times under each specific set of experimental conditions, and the average values were presented.

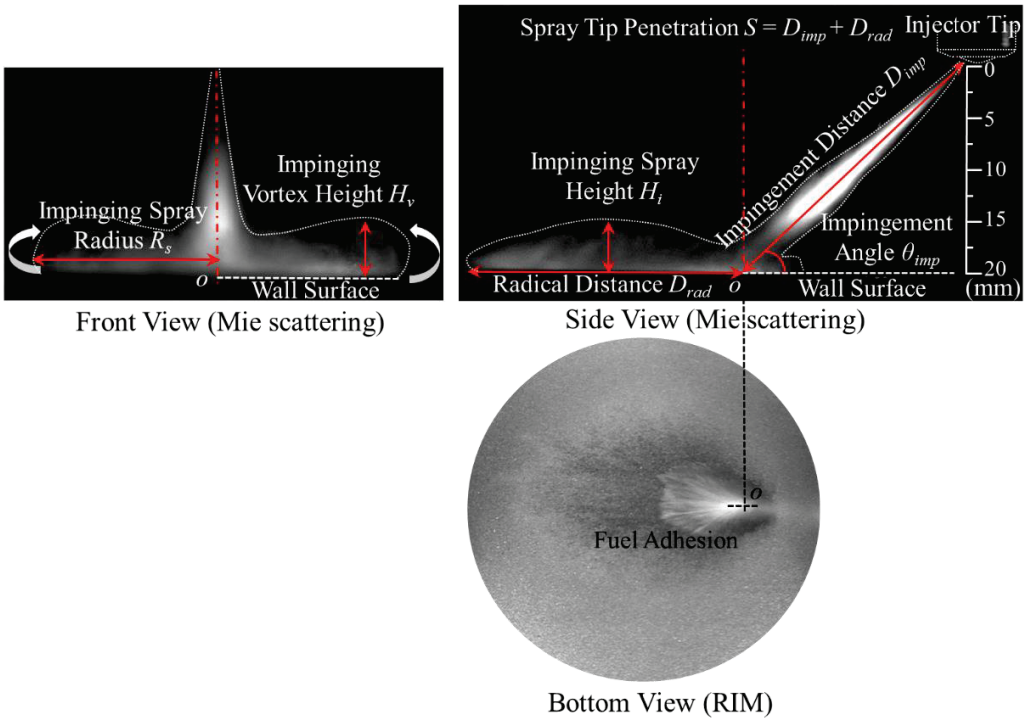

Figure 2.5 Experimental extraction of R_s, H_v, S and H_i

2.4.2 Refractive Index Matching (RIM) Method

2.4.2.1 Experiment apparatus

The RIM experimental equipment in the current study is shown in Figure 2.6. The high-pressure constant volume chamber and injection system were the same as those for the Mie scattering experiment. Only the optical system had some differences. The xenon lamp was positioned at the side window to emit continuous and high intensity light that passed through the window of the chamber with an incident angle about 5°. A reflection mirror was placed directly beneath the impingement surface. Fuel adhesion images were captured with a high-speed video camera through the mirror, as shown in Figure 2.6 (b). Further, the high-speed video camera was set at a frame rate of 10,000 fps and at a frame size of 512 × 512 pixels. The layout of the lamp and the camera is shown in Figure 2.6 (c).

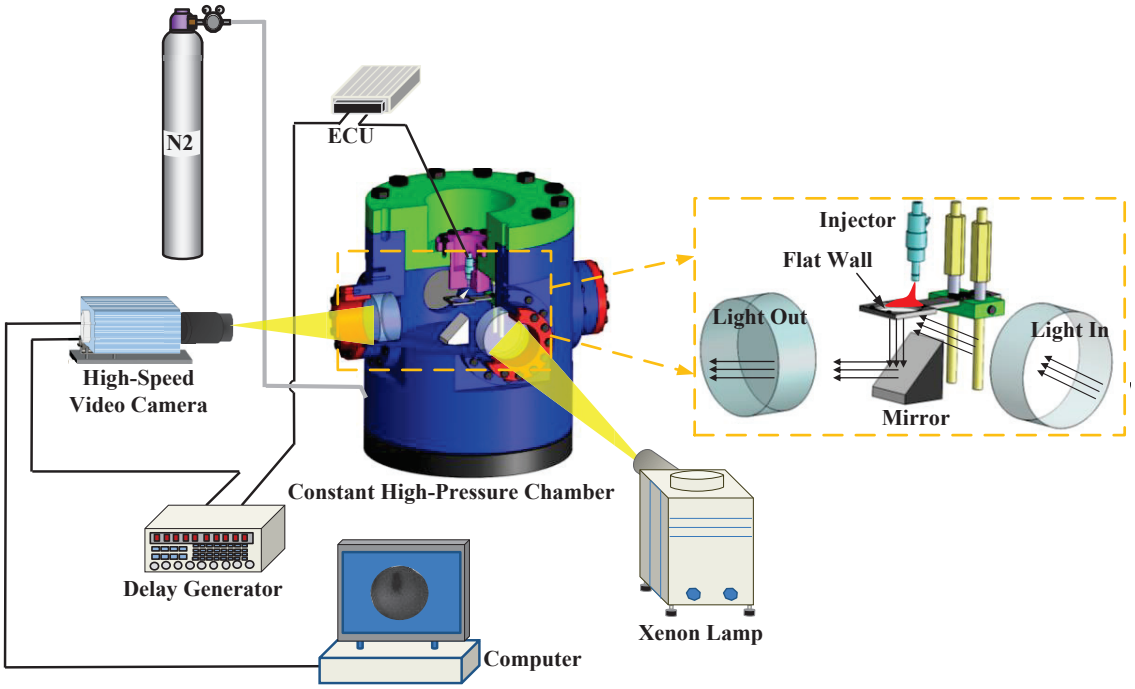

(a) RIM experiment setup (b) Internal structure

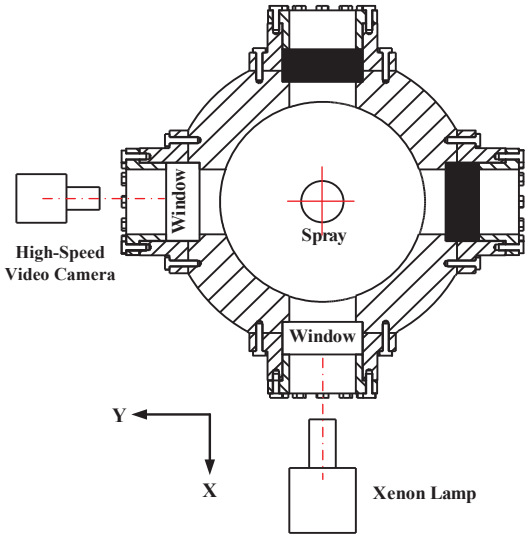

(c) Optical arrangement

Figure 2.6 Experimental setup for fuel adhesion measurement

2.4.2.2 Image processing method

The RIM technique measures the spatial distribution of the fuel adhesion thickness, from which the adhered adhesion area and mass can be calculated. In this method, the difference in refractive index between the quartz glass and air results in the scattering of light from the roughened

surface that is modified by the presence of the fuel closely matching the refractive index of the impingement glass.

Figure 2.7 describes the light transfer in the quartz glass without and with fuel adhesion on the wall. When fuel adheres on the wall, the transmitted light becomes strong, while the diffused reflection light becomes weak, which results the reduction in the light from the fuel image.

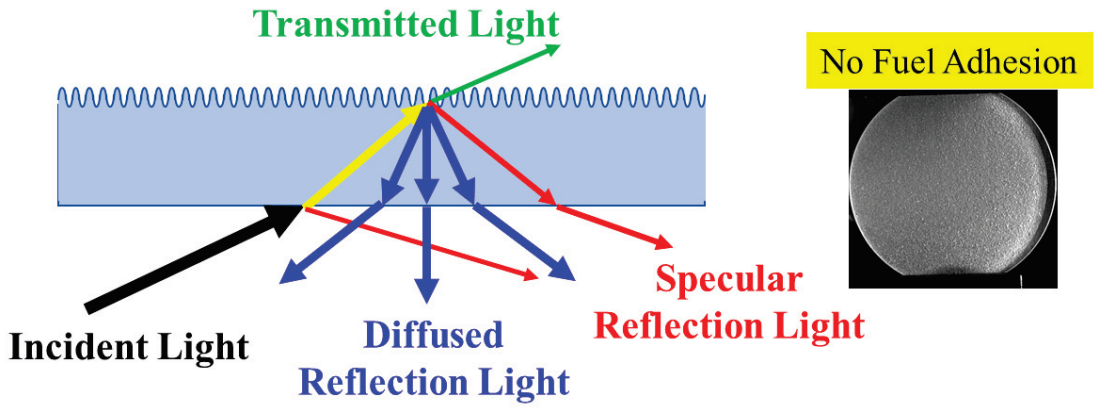

(a) Without fuel adhesion

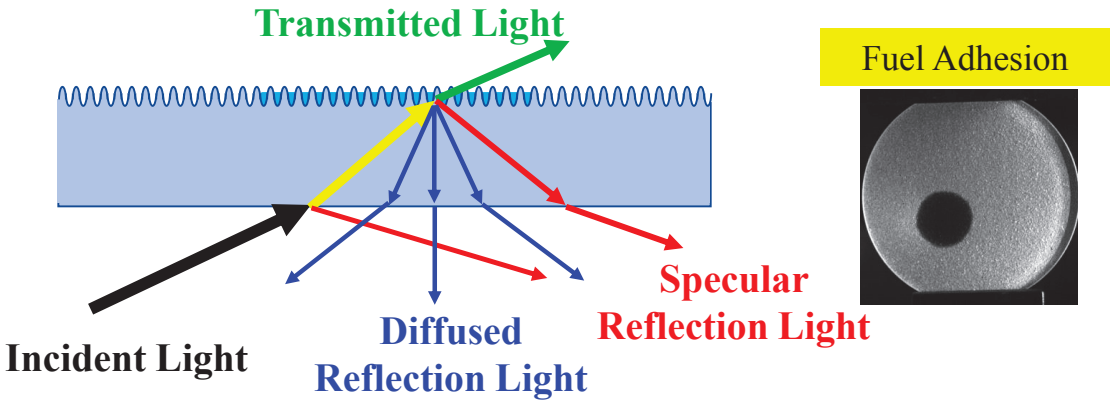

(b) With fuel adhesion on the wall

Figure 2.7 The schematics of light transfer in the quartz glass

Drake et al. (2002) showed the relation between the fuel adhesion thickness $h(x, y)$ and the intensity reduction of the scattered light $\Delta I(x, y)$. The reduction through the glass is written as follows:

$$\Delta I(x,y) = 1 - \frac{I_{wet}(x,y)}{I_{ref}(x,y)} \tag{2.1}$$

where $I_{ref}(x,y)$ is the intensity of the scattered light in the dry image at the location of (x, y), and $I_{wet}(x,y)$ is the intensity of the fuel deposit at the location of (x, y).

After the calibration, a function that is the correlation between $h(x,y)$ and $\Delta I(x,y)$can be built:

$$h(x,y) = f(\Delta I) \tag{2.2}$$

To obtain the calibration curves, a calibration experiment was carried out under atmospheric conditions without the injection system. Two different fuels were selected because tridecane has low volatility and high viscidity, but toluene has high volatility and low viscidity. Moreover, their refractive index is similar to that of the quartz glass. A much thinner thickness of fuel adhesion can be obtained with a liquid mixture of these fuels. The characteristics of the fuels and quartz glass are summarized in Table 2.1.

Table 2.1 Characteristics of fuels and quartz glass

Parameter	Refractive Index	Density (kg/m^3)	Boiling Point (K)	Kinematic Viscosity (10^{-6} m^2/s)	Surface Tension (N/m)
Toluene	1.49	866	382.75	0.68	0.0285
Tridecane	1.43	756	507.58	2.35	0.0303
Gasoline	1.42	737	-	0.46	0.022
Quartz Glass	1.46	-	-	-	-

A mixture (10% volume of tridecane and 90% volume of toluene) was used for the calibration procedure. The fuel mixture was dripped on the dry window by means of a syringe and the reduction in scattering light increased from 0 to the maximum value. After a certain volume of the mixture was dripped on the rough quartz, the droplet rapidly expanded, and the area of fuel increased rapidly. During this time, toluene, which is the high volatility component, quickly evaporated; however, there was only a slight increase in the scattered light. Once the adhesion area reached a certain value, tridecane, which is the low volatility component, begins to

evaporate, and the scattered light changed significantly. There are two hypotheses in this case: one stating that all the toluene has evaporated, but all the tridecane has not yet evaporated; another stating that the thickness of fuel adhesion is uniform. Thus, $h(x,y)$ can be calculated because the tridecane volume was calculated as 10% of the mixture, and the averaged reference dry image was obtained before the liquid deposited on the glass. Then $\Delta I(x,y)$ can be calculated using Equation (2.1). Eventually, one point with $h(x,y)$ and $\Delta I(x,y)$ was obtained. By varying the mixture volume from 0.1 μL to 10 μL, the calibration curve was acquired by Equation (2.1). The calibration curves are plotted in Figure 2.8. The horizontal axis is the reduction in scattered light, and the vertical axis is fuel adhesion thickness. Although it is difficult to calibrate the fuel adhesion thickness below 0.2 μm and above 1.4 μm owing to the limitations of the experimental instruments, extrapolation was applied to calculate the fuel adhesion thickness in the full range with acceptable accuracy (Drake and Haworth, 2007; Zheng et al., 2012).

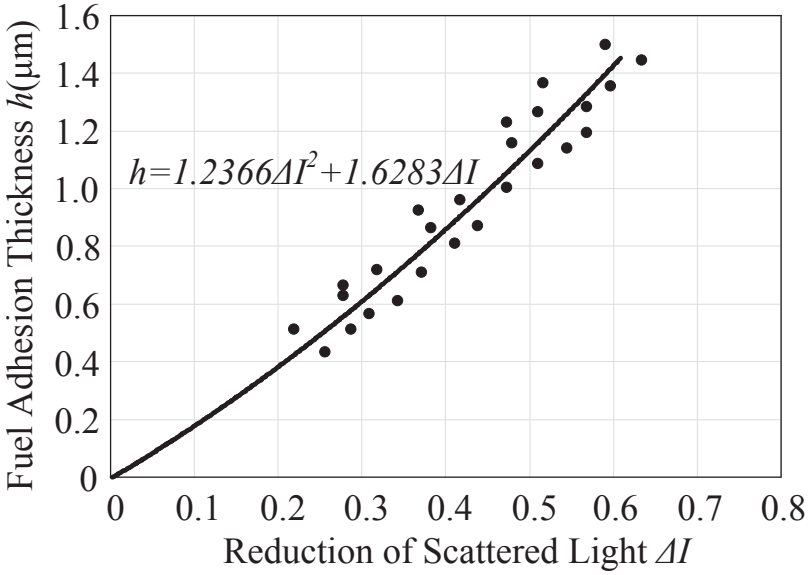

Figure 2.8 Calibration curve.

After the calibration calculation, the fuel adhesion thickness can be measured through the RIM method. The image processing of the RIM experiment is shown in Figure 2.9. First, a dry image was acquired. Then, it was subtracted by the wet image to obtain only the adhered fuel image, and the $\Delta I(x,y)$ can be obtained by this image. Finally, the thickness distribution was calculated through the calibration curve. The adhered fuel area and mass can also be integrated

from the pixels of each thickness. Additional details about RIM method can be found in our previous studies (Luo et al., 2017; 2018).

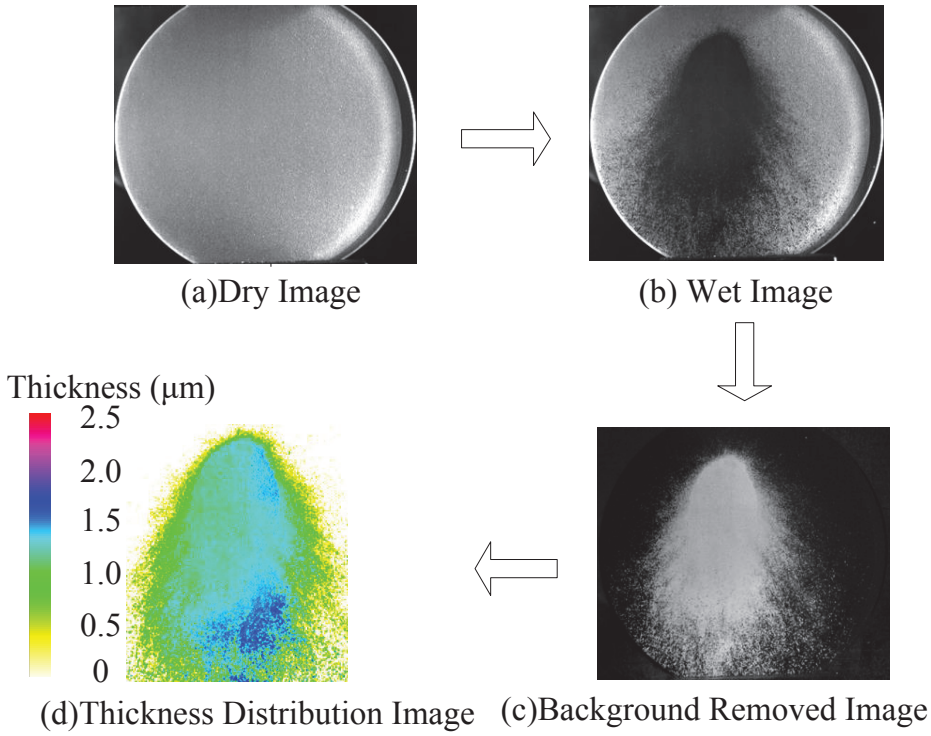

Figure 2.9 Image processing

2.4.3 Particle Image Analysis (PIA)

2.4.3.1 Experiment apparatus

Previously, both Berg et al. (2006) and Kashdan et al. (2006) certified that particle image analysis (PIA) was a reliable technique to measure the size of spherical and non-spherical droplets. Hence the PIA system was employed to investigate the microscopic spray characteristics. The experimental equipment is shown in Figure 2.10. It consisted of a constant-volume chamber, an injection system, and an optical system. Toluene fuel was directed into the mini-sac injector by a high-pressure injection system. An Nd: YAG laser with a wavelength of 532 nm was used as the light source. The energy of the laser pulse was in the order of 10 mJ, and a duration of approximate 6 ns. The light beam was expanded from 8 to 100 mm to provide homogeneous illumination over a sufficiently large area. A charge-coupled device (CCD) camera (Flowtech Research Inc., FtrNPC) with a long-distance microscope was employed to visualize the spray structure. As shown in Figure 2.9, two teleconverters (Kenko Tokina, N-AF 1.4X

TELEPLUS MC4) were connected with the CCD camera by a bellows to enlarge the spray image. The camera location was collinear with the laser axis. The image was captured at 1200 μs and 900 μs after the start of injection under P_{inj} = 10 and 20 MPa, respectively, when the spray showed the quasi-steady state period. Guan et al. (2014) and Feng et al. (2016) selected similar periods for image taking in their work. The resolution was approximately 2.008 μm per pixel, and the frame size was 1600 × 1200 pixels.

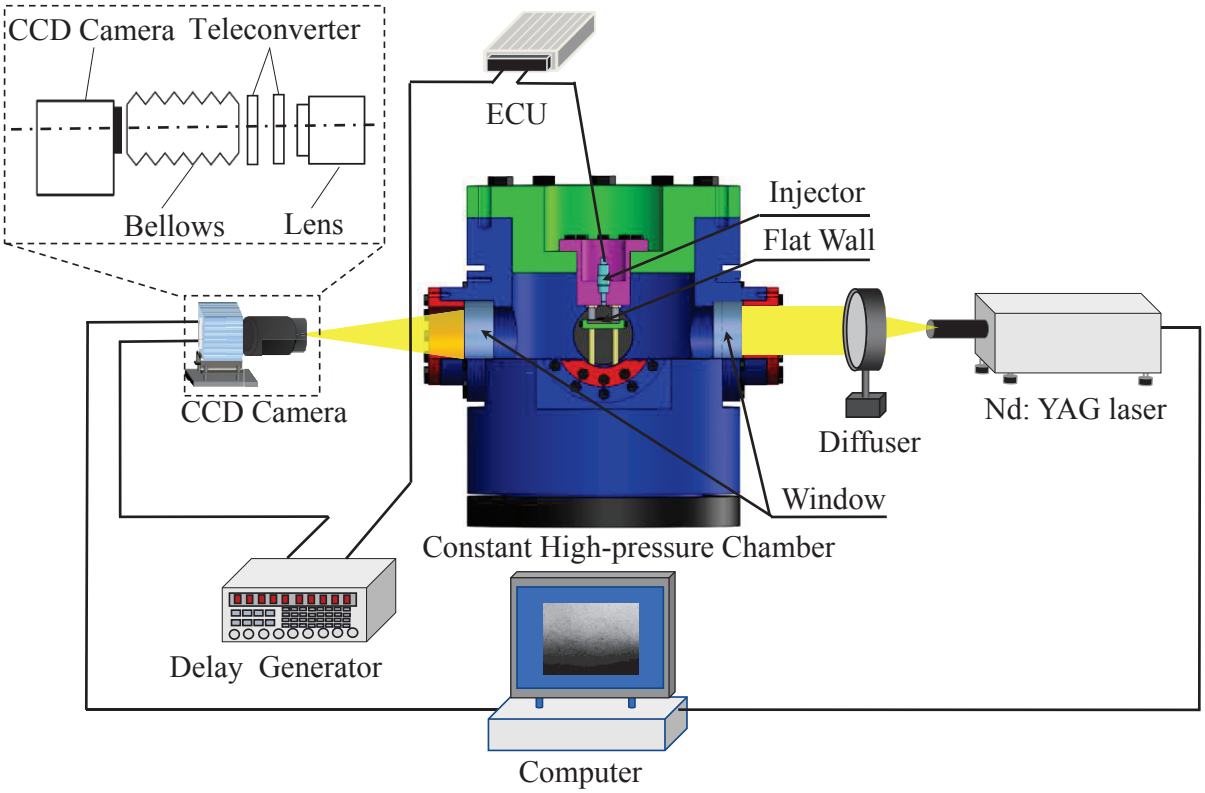

Figure 2.10 PIA experimental setup.

The measurement regions and coordinate system are shown in Figure 2.11. The field of view is 3.2 × 2.4 mm^2. The exit of the nozzle was defined as the origin point. The positive x-axis is along the lateral direction of the spray after impingement, and the positive y-axis is the vertical direction along the injector axis. There are many droplets in the impingement region, thus making it difficult to recognize droplets in the dense area. The regions before and after impingement are selected near the real impingement region, whose center point coordinates are (10,10) and (22,14) mm. The solid line represents the surface of the wall after impingement. In

Chapter 5, all results are calculated for these two regions under different conditions to compare the microscopic behaviors before and after impingement on the wall.

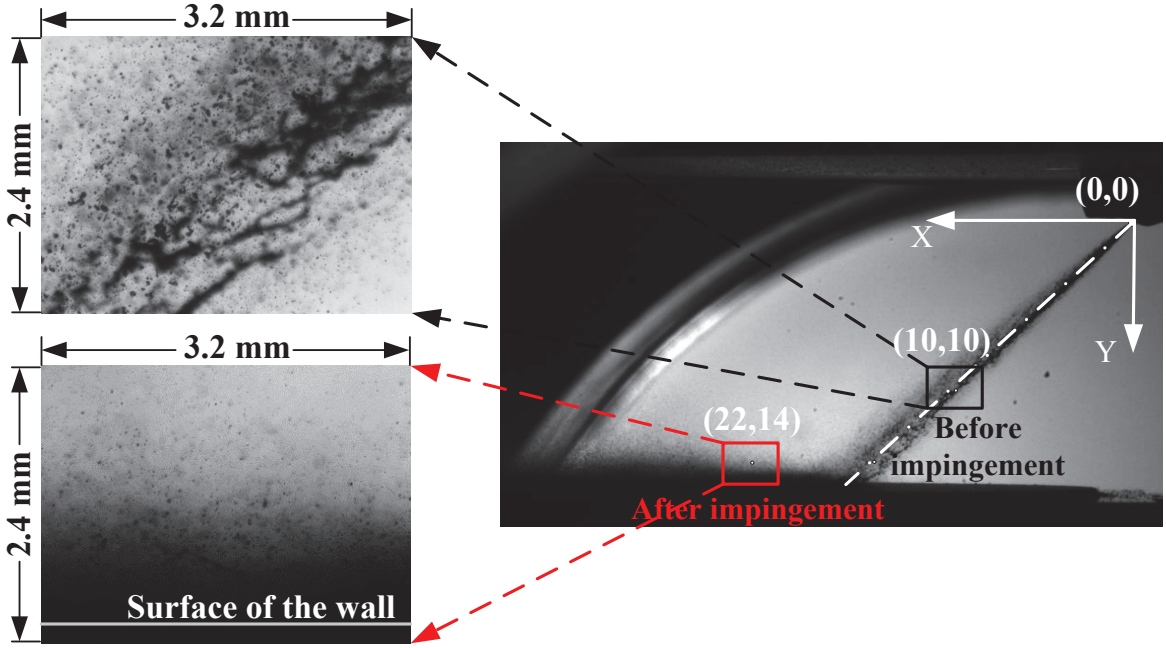

Figure 2.11 Definition of before and after impingement

2.4.3.2 Image processing method

Twenty injection events under each condition were recorded to detect more than 10,000 validated particles. To detect the droplets correctly, refined criteria were used. Droplets appear sharp on the focal plane and others that are away from the focal plane appear blurred. The threshold was set at 25/255 (10% of the maximum pixel intensity), and all pixels whose intensities are above 25 can be detected. Droplets with pixel numbers less than 4 are rejected, thereby requiring droplets to consist of at least four pixels for detection.

Moreover, the roundness of the droplets was defined as follows:

$$Roundness = \frac{4\pi \cdot S_{droplet}}{C_{droplet}^2} \times 100 \tag{2.3}$$

where $S_{droplet}$ and $C_{droplet}$ are the area and perimeter of the droplet. A roundness value of 100 implies that the droplet has a spherical shape. The roundness of the droplet was set from 80 to

100 to ensure that all the selected droplets were nearly round. More detailed algorithms of the droplet sizing can be found in a previous paper (Fujimoto et al., 2008; Luo et al., 2018).

The area diameter D_{area} of the droplets was defined as follows:

$$D_{area} = \sqrt{\frac{4 \times S_{droplet}}{\pi}} \tag{2.4}$$

Droplets with the pixel numbers less than 4 are rejected, such that detected droplets consists of at least 4 pixels. With a resolution of 2.008 μm/pixel, the pixel number was set from 4 to 2500; as a result, the area diameter of droplets was limited to 100 μm, as discussed in the next section. The refined criteria are presented in Table 2.2.

Table 2.2 Refined criteria.

Threshold Value	25/255
Roundness	80 – 100
Pixel Number	4 – 2500
Area Diameter	4 – 100 μm

Figure 2.12 illustrates the droplet detection procedure. A commercial software package, FtrPIA-Cruise, was used to process the shadow images. Before impingement, all the droplets were above the wall. First, the raw image was acquired using the CCD camera. The grayscale image was then inverted for better recognition. Using the refined criteria listed in Table 2.2, the droplets were filtered, as indicated by red points in Figure 2.12. However, after impingement, in order to ensure that the surface of the wall is taken in the image, the image necessarily includes a region of high droplet density near the wall. It is difficult to correctly distinguish the droplets in this region, such that only the droplets at least 0.6 mm from the surface of the wall can be detected. Moreover, the dense region is limited, and we are confident that the specific spray region after impingement is sufficient and meaningful for discussion in Chapter 5.

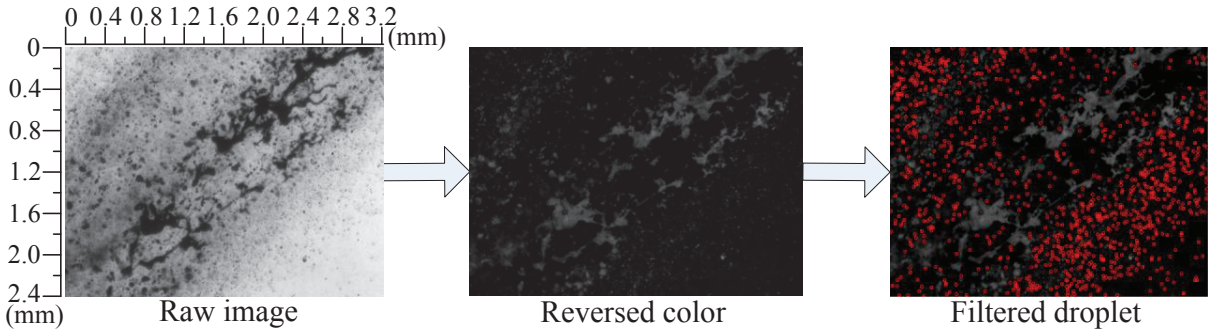

(a) Before impingement

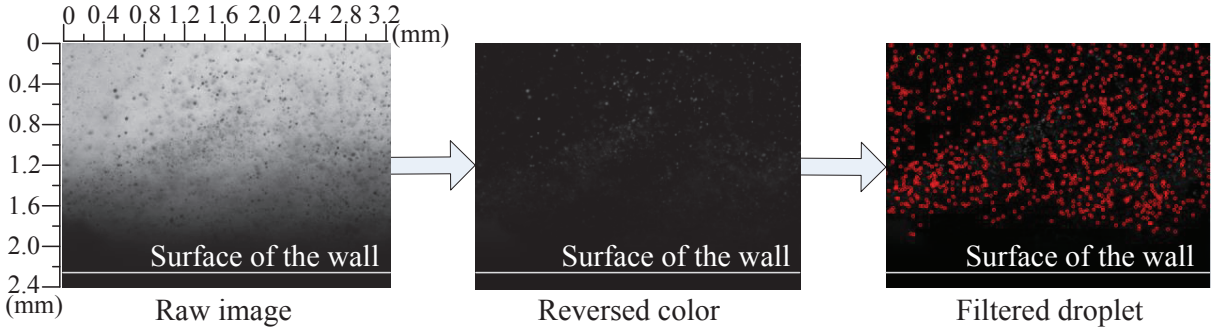

(b) After impingement

Figure 2.12 Droplet detection procedure

2.5 SUMMARY

In this chapter, the experimental apparatus applied in this dissertation are introduced in detail, for example, high-pressure and high-temperature ambient condition acquiring system, electrical controlling system and so on. Moreover, the measurement technology, including the Mie scattering, RIM and PIA technical methods, which are corresponding to the non-evaporation and evaporation condition measurements, respectively, are also introduced in this chapter. All the apparatus and technic introduced here will be applied to investigate the spray evolution and fuel adhesion formation processes inside the chamber. In next chapter, the detailed results obtained by these measurements in this study will be discussed.

CHAPTER 3 FUEL ADHEISON FORMATION UNDER NON-EVAPORATION

3.1 EFFECT OF INJECTION AND AMBIENT PRESSURE

3.1.1 Experimental Conditions

The experimental conditions, shown in Table 3.1, were determined in consideration of the real operating conditions of passenger car gasoline engines.

Table 3.1 Experimental conditions

Injection Conditions	
Fuel	Toluene
Injection Mass (M_{inj})	3.0 mg
Injection Pressure (P_{inj})	10, 20, 30 MPa
Injector Type	Mini-Sac, Single-Hole
Nozzle Hole Diameter (d)	0.135 mm
Injection Duration (t_d)	2.4, 1.65, 1.36 ms
Ambient Conditions	
Ambient Gas	Nitrogen
Ambient Pressure (P_{amb})	0.1, 1.0 MPa
Ambient Temperature (T_{amb})	300 K
Impingement Conditions	
Impingement Plate	Quartz Glass
Impingement Distance (L_x)	22 mm
Impingement Angle	45 deg
Surface Roughness	Ra7.5 μm

The ambient pressures ranged between 0.1 and 1.0 MPa, and the injection pressures varied from 10 to 30 MPa. The experiments were carried out under room temperature with nitrogen. A mini-sac injector with a nozzle hole of 0.135 mm diameter was used, and toluene was employed as a surrogate fuel for gasoline. The injection mass was kept constant at 3.0 mg with different conditions, resulting in the different injection durations of 2.4, 1.65 and 1.36 ms at different

injection pressures. The impingement angle was 45 deg and the impingement distance was 22 mm from the nozzle exit to the impingement point of the quartz glass along the spray axis. Glass plates with surface roughness of Ra7.5 μm, was investigated in this study.

3.1.2 Spray Impingement Characteristics

Figure 3.1 shows spray tip penetrations under three conditions. The horizontal axis is the time after start of injection, and the vertical axis is spray tip penetration *S*. For all conditions, the spray development can be divided into two stages. It increases almost linearly before impingement, and the gradient of *S* decreases after spray impingement. The splashing due to the wall impingement, drag force from the wall and ambient gas can be regarded as the main reasons for this phenomenon. More importantly, under different ambient pressures, *S* of 0.1 MPa is larger than that of 1.0 MPa, and impingement time of 0.1 MPa is earlier than 1.0 MPa. It can be expected that higher ambient pressure decreases *S* by transfer the spray momentum to the ambient gas, and stronger air resistance force is expected with higher ambient pressure. Under different injection pressures, *S* of 30 MPa is larger than that of 10 MPa, and impingement time of 30 MPa is earlier than that of 10 MPa due to higher spray velocity.

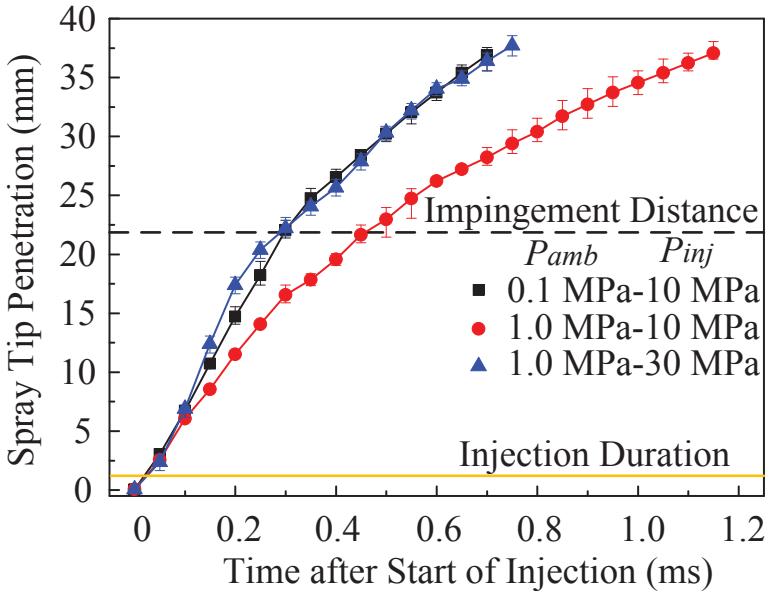

Figure 3.1 Spray tip penetration (*S*).

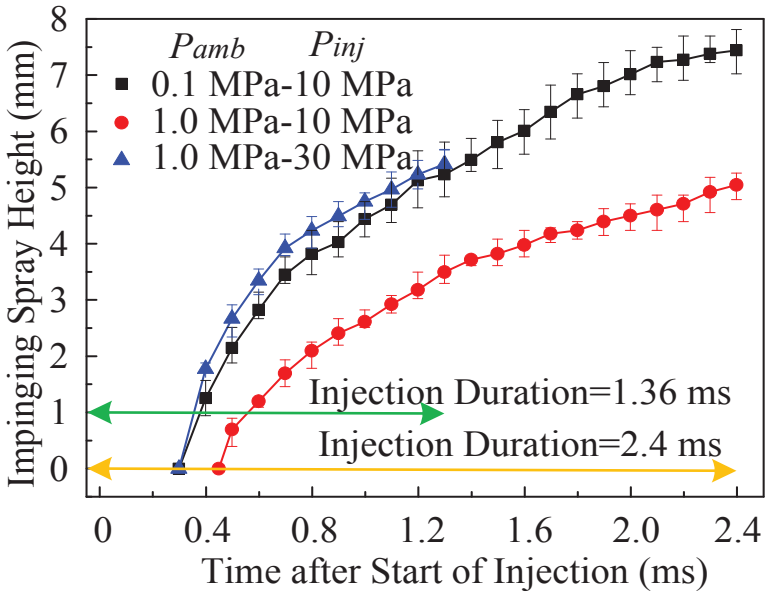

Figure 3.2 Impinging spray height (H_i).

Figure 3.2 presents impinging spray heights under three conditions (the same as spray tip penetration). The horizontal axis is the time after start of injection, and the vertical axis is impinging spray height H_i. In contrast to ambient pressures, H_i of 0.1 MPa is larger than that of 1.0 MPa. Although increasing the pressure can increase the spray angle, resulting more droplets above the wall. Higher ambient pressure increases the density of the ambient atmosphere, resulting in a decrease in the droplets splashing, thus decreasing H_i. In comparison with the injection pressures, H_i of 30 MPa is larger than that of 10 MPa, it can be expected that the increased injection pressure results in much more droplets above the wall than 10 MPa.

3.1.3 Fuel Adhesion Characteristics

Figure 3.3 shows the evolution of the adhered fuel on wall. The pseudocolor represents the fuel adhesion thickness varying from 0 to 2.5 μm. Further, the cross symbol is the impingement point. All cases at different time show similar structures. It is clear that the area and thickness increase with time, and it can be expected that there are still some droplets impinging on the wall. The fuel adhesion thickness is not uniform in the initial stage. The non-uniform tendency is more obvious with time. The thicker fuel adhesion area is located at the upstream. The increased injection and ambient pressure decrease the maximum thickness of the adhesion.

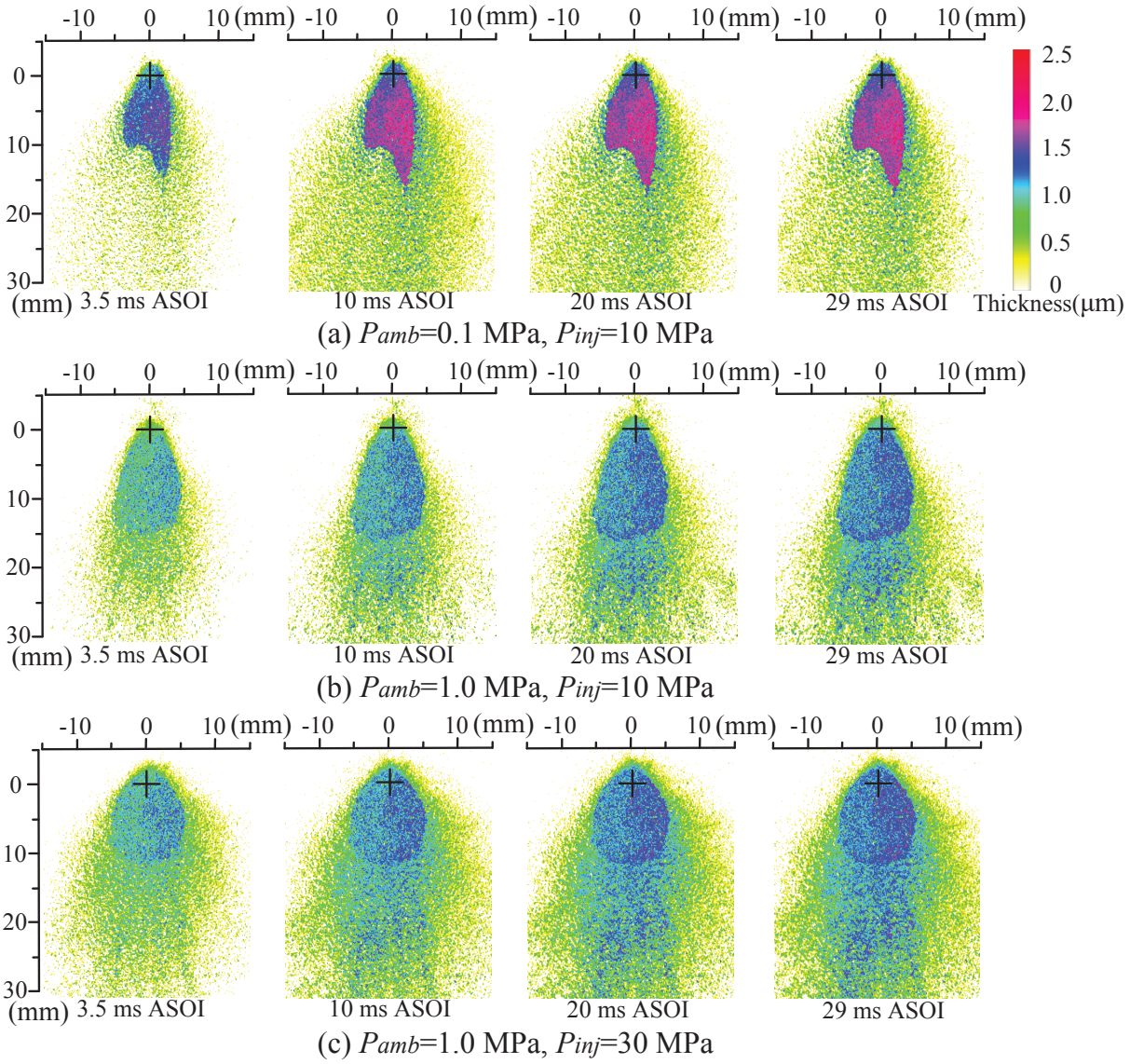

Figure 3.3 Fuel adhesion evolution.

The fuel adhesion mass and area were calculated and depicted in Figure 3.4 and 3.5. The horizontal axis is the time after start of injection, and the vertical axis is fuel adhesion mass and area, respectively. For all conditions, when the spray starts, both the fuel mass and area increase. Comparing with different conditions, it is clear that an increase of the ambient pressure decreases the fuel adhesion mass and area, whereas increasing the injection pressure increases those. This can be argued that the increased ambient pressure coalesces the droplets after impingement, then the bigger droplets are difficult to drop on the wall with the effect of vortex. However, the

increased injection pressure makes the droplets breakup into smaller ones, which causes more droplets dropping on the wall after impingement.

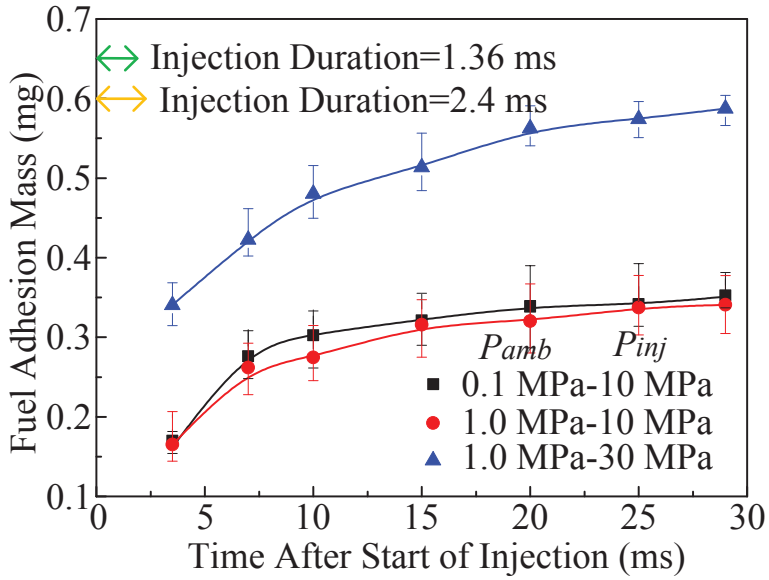

Figure 3.4 Fuel adhesion mass.

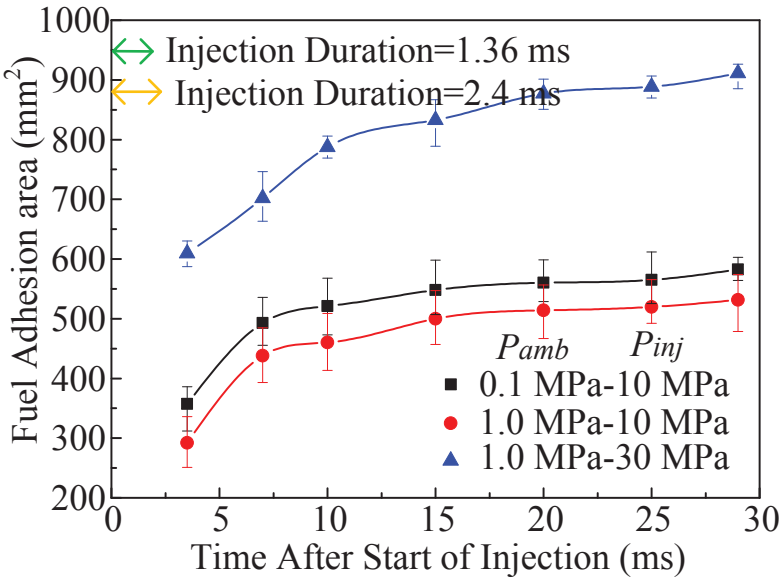

Figure 3.5 Fuel adhesion area.

Time-resolved results of the maximum fuel adhesion thickness under different conditions are presented in Figure 3.6. The horizontal axis is the time after start of injection, and the vertical axis is the fuel adhesion maximum thickness. It can be seen the maximum thickness decrease

with an increase of ambient pressure. Stronger drag force decelerates the droplets greatly. As a result, the droplets drop on wall more easily, and the fuel adhesion becomes thicker. On the contrary, an increase of injection pressure increases the maximum fuel adhesion thickness due to the enhancement of breakup and atomization.

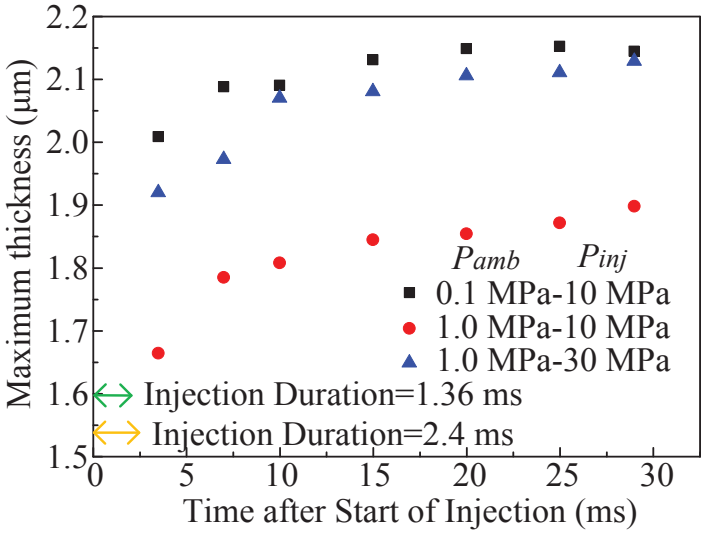

Figure 3.6 Maximum fuel adhesion thickness.

In order to get more details about fuel adhesion thickness, the probability of fuel adhesion thickness is depicted in Figure 3.7. The horizontal axis is fuel adhesion thickness, and the vertical axis is the probability of fuel adhesion thickness. The dotted lines show fuel adhesion thickness of P_{amb} = 0.1 MPa, and the solid lines show that of P_{amb} = 1.0 MPa.

The probability based on fuel adhesion thickness is about the thickness of each pixel, and the probability of fuel adhesion thickness must satisfy the normalization conditions:

$$\sum_{i=0}^{\infty} f_M(h_i) = 1 \tag{3.1}$$

where the sum of fuel adhesion mass in the thickness fraction between h - Δh and h is defined as $M(h)$, $f_M(h)$ is the probability of $M(h)$, and Δh is 0.05 μm.

Firstly, the results at the ambient pressure of 0.1 MPa are examined. There are two peak values at 0.3 μm and 1.7 μm, respectively. Moreover, the thickness range is from 0 to 2.2 μm and injection pressure has less effect on that. Then the results at the ambient pressure of 1.0 MPa are examined. It is interesting to find that only one peak value exists under 1.0 MPa, and the peak

value is larger than that of 0.1 MPa. This indicates that an increase of ambient pressure improves the uniformity of adhesion thickness. Increasing ambient pressure under a certain temperature raises the density of ambient gas, leading to an increase of the momentum transfer between the spray and the ambient gas. As a result, the spray angle increases and the droplet velocity decreases. Consequently, the droplets drop on the wall more evenly, resulting in more uniform fuel adhesion.

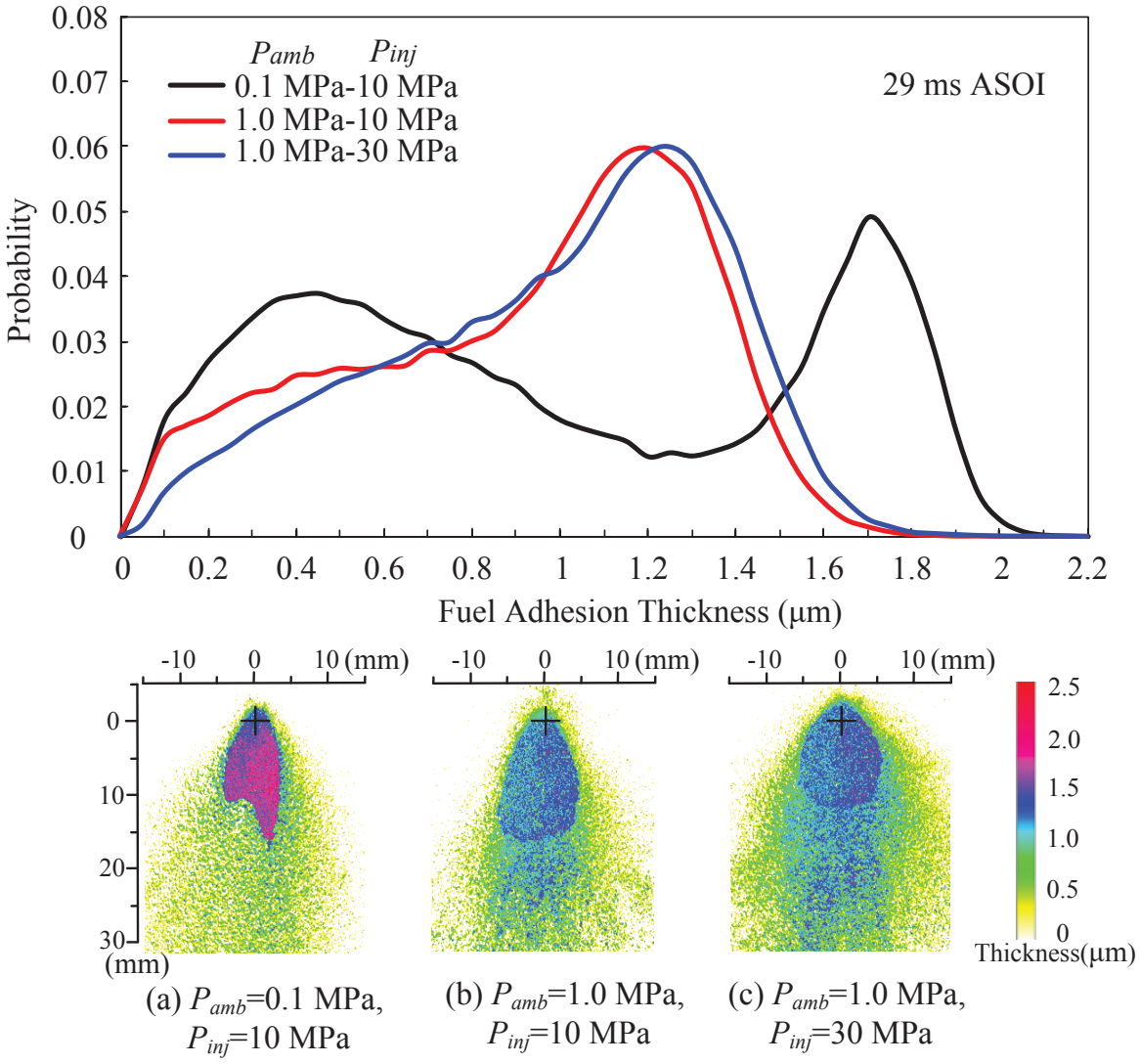

Figure 3.7 Probability of fuel adhesion mass along thickness.

3.2 EFFECT OF SURFACE ROUGHNESS

3.2.1 Experimental Conditions

Table 3.2 Experimental conditions

Injector Conditions	
Injector Type	Mini-Sac, Single-Hole
Hole Type	Straight-Hole without Counterbore
L/D Ratio	4.8
Nozzle Hole Diameter (d)	0.135 mm
Injection Conditions	
Fuel	Toluene
Injection Mass (M_{inj})	3.0 mg
Injection Pressure (P_{inj})	10, 20, 30 MPa
Injection Duration (t_d)	2.4, 1.65, 1.36 ms
Ambient Conditions	
Ambient Gas	Nitrogen
Ambient Pressure (P_{amb})	0.1, 1.0 MPa
Ambient Temperature (T_{amb})	300 K
Ambient Density (ρ_{amb})	1.19, 11.9 kg/m^3
Impingement Conditions	
Impingement Plate	Quartz Glass
Impingement Distance (L_w)	22 mm
Impingement Angle	45 deg
Surface Roughness	Ra2.5, Ra7.7 μm

The experimental conditions, given in Table 1, were determined considering the real operating conditions of passenger car gasoline engines. The injection pressures varied from 10 to 30 MPa and the ambient pressures ranged between 0.1 and 1.0 MPa, which means that the ambient gas density changed between 1.19 and 11.9 kg/m3. The experiments were conducted with nitrogen at room temperature. A mini-sac injector with a nozzle hole of diameter 0.135 mm was used; the nozzle is a conventional straight-hole without a counterbore. The length-to-diameter (L/D) ratio

is 4.8. Toluene was employed as a surrogate fuel for gasoline. The injection mass was kept constant at 3.0 mg under different conditions, resulting in different injection durations of 2.4, 1.65, and 1.36 ms at different injection pressures. The impingement angle was 45 deg and the impingement distance was 22 mm from the nozzle exit to the impingement point of the flat wall along the spray axis. The surface roughness of the new piston used in the engine is approximately Ra1.0, but it may increase to Ra10.0 or more owing to combustion (Maligne and Bruneaux, 2011). To investigate the effect of wall roughness, glass plates with two different surface roughnesses, Ra2.5 and Ra7.7 μm, were chosen. Moreover, the surface roughness was measured by a portable high-performance surface roughness and waviness measuring instrument (Kosaka Laboratory Ltd., SE300), whose resolution is 0.0064 μm.

3.2.2 Spray Impingement Characteristics

3.2.2.1 Spray impingement

To discuss the spray characteristics under different wall roughnesses, the ambient pressure was set at 1.0 MPa and the injection pressure was set at 30 MPa. The spray and adhered fuel adhesion images from 0.15 to 10 ms after start of injection (ASOI) with a wall roughness of Ra2.5 are presented in Figure 3.8. The sprays are shown in false-color images acquired from the Mie scattering experiment, and fuel adhesions are shown in the raw images obtained from the RIM experiment. Owing to the Mie scattering of droplets above the wall, the bright area in the raw images is the fuel spray during injection. The fuel adhesion, spray, and splash edge can be identified by image edge detection due to different intensities of light. However, due to the overlap of spray droplets cloud in the impinging region, the detection of fuel adhesion edge in raw images of RIM is still far from being achieved with accuracy during impingement.

Before impingement, the sprays are asymmetric because of the internal flow of the injector. Wavy edges of the spray were observed that might be attributed to the air resistance force and turbulence in the spray (Wang et al., 2016). During impingement, there are fuel spray above the wall. At 0.6 ms ASOI, the fuel adhesion tip is shorter than the spray tip, indicating that most of the fuel droplets splash above the wall instead of spreading on it. Fuel spray above the wall can also be seen from the bottom-view image. At 1.4 ms ASOI, equivalent to 0.06 ms after end of injection (AEOI), the fuel spray in the fuel adhesion image still can be observed. From 3.5 ms

ASOI, the fuel adhesion is formed on the wall without bright regions, but some droplets still exist in the false color image.

Figure 3.9 shows spray and the adhered fuel images at a wall roughness of Ra7.7. The tendencies of spray and fuel adhesion formation are the same as that at Ra2.5. The radial distance after impingement at Ra7.7 is smaller, and the impinging spray height is larger due to the stronger drag force of the wall. At 3.5 ms ASOI, more droplets are observed in the air above the wall from the false color images. This might be caused by two reasons. First, the stronger drag force decelerates the spray, so that more droplets are left. Second, a higher roughness intensifies the splashing process, resulting in droplets in the air.

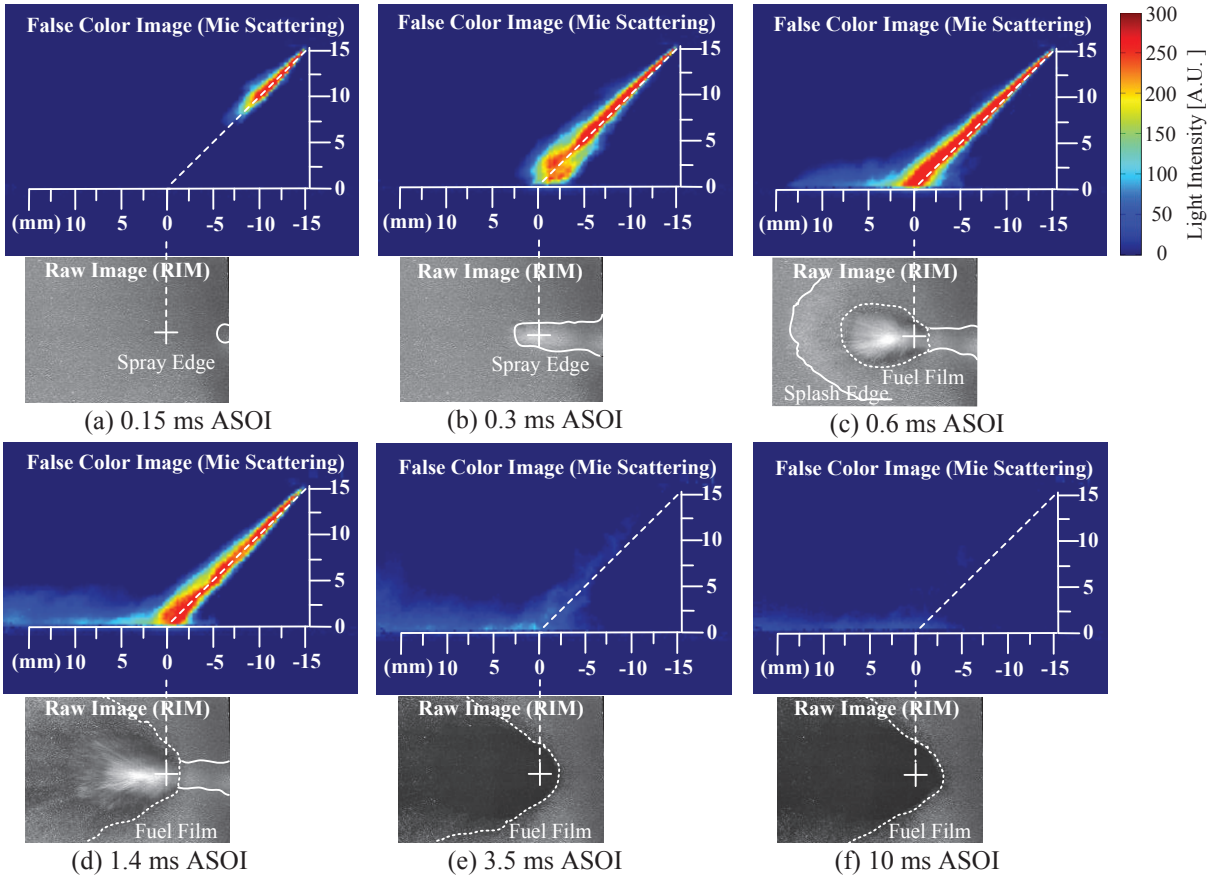

Figure 3.8 Spray impingement and fuel adhesion images on Ra2.5 roughness wall (P_{amb} = 1.0 MPa, P_{inj} = 30 MPa).

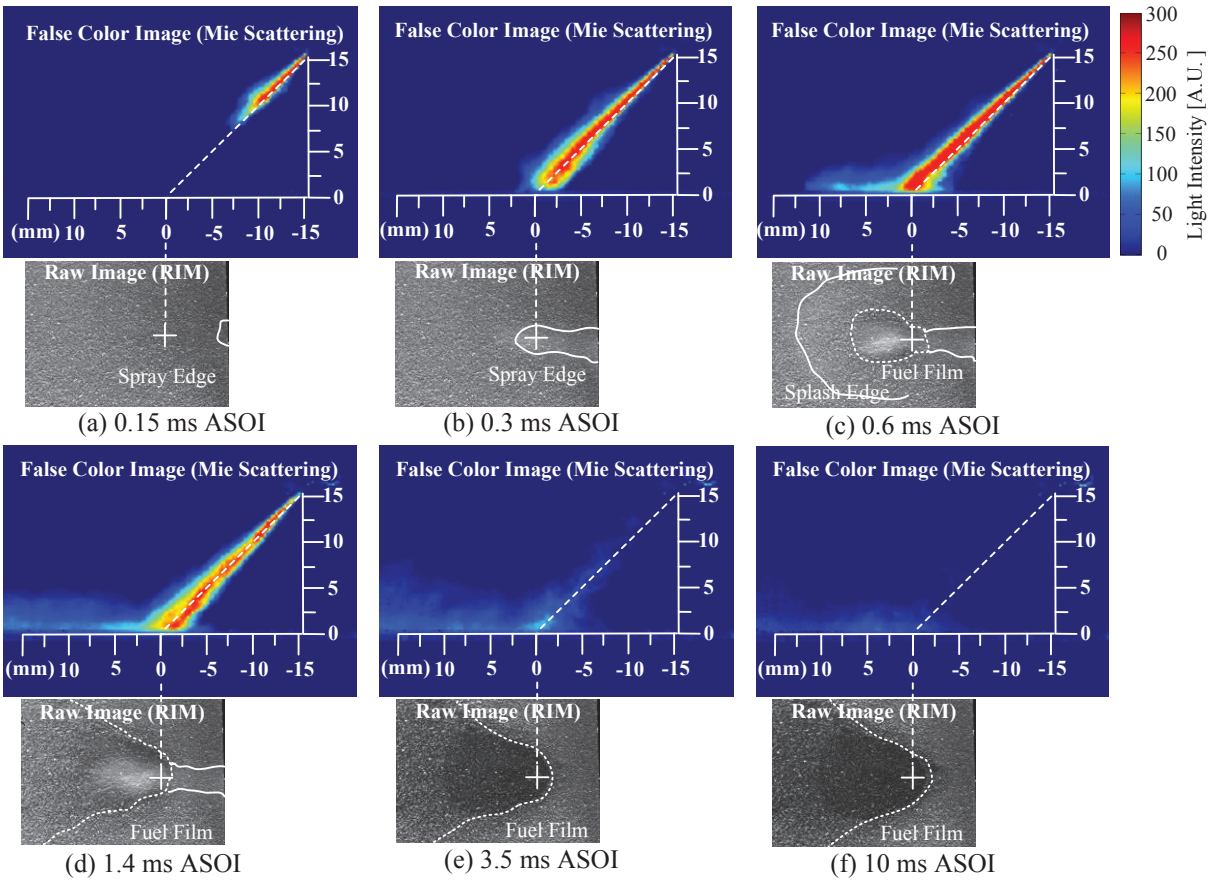

Figure 3.9 Spray impingement and fuel adhesion images on Ra7.7 roughness wall (P_{amb} = 1.0 MPa, P_{inj} = 30 MPa).

3.2.2.2 Spray tip penetration

Figure 3.10 shows spray tip penetrations under three conditions, and the dotted line is the impingement distance. Three conditions were investigated (P_{amb} = 0.1 MPa, P_{inj} = 10 MPa, P_{amb} = 1.0 MPa, P_{inj} = 10 MPa, and P_{amb} = 1.0 MPa, P_{inj} = 30 MPa). Generally, the spray development can be divided into two stages. It increases almost linearly before impingement, and the gradient of S decreases after spray impingement. The splashing due to the wall impingement, drag force from the wall and ambient gas can be regarded as the main reasons for this phenomenon. However, the gradient decreases before impingement when P_{amb} = 1.0 MPa, and the air resistance of high ambient density should be responsible for it (Li et al., 2012). More importantly, after impingement, S of Ra2.5 is larger than that of Ra7.7 under all conditions. Due to stronger drag force on Ra7.7 wall, spray velocity decreases more rapidly. Besides, under different ambient pressures, S of 0.1 MPa is larger than that of 1.0 MPa, and impingement time of 0.1

MPa is earlier than 1.0 MPa that agrees well with other results (Wang et al., 2016). It can be expected that higher ambient pressure decreases S by transferring the spray momentum to the ambient gas, and stronger air resistance force is expected with higher ambient pressure. Under different injection pressures, S of 30 MPa is larger than that of 10 MPa, and impingement time of 30 MPa is earlier than that of 10 MPa due to higher spray velocity.

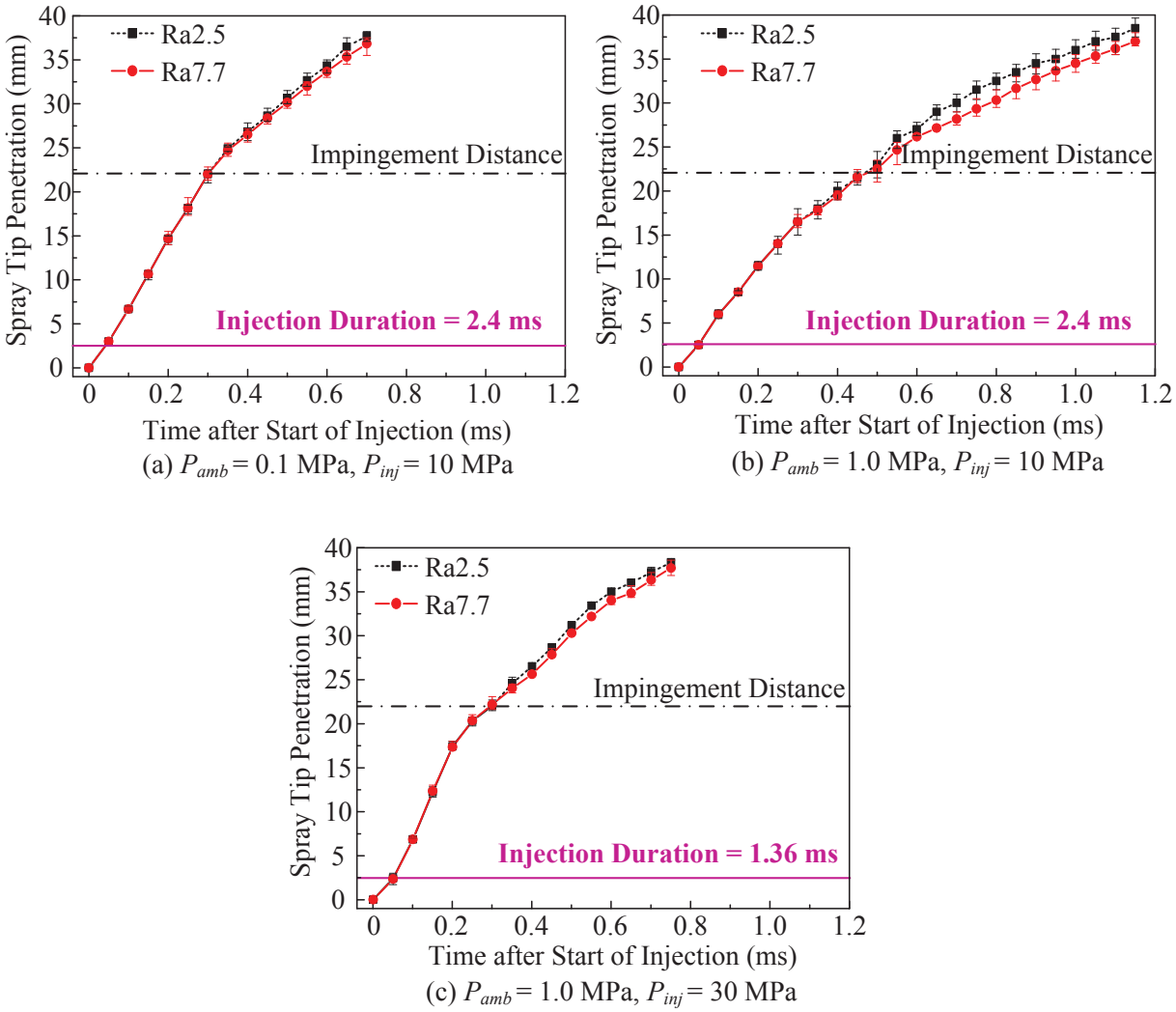

Figure 3.10 Spray tip penetration under different conditions.

3.2.2.3 Impinging spray height

Figure 3.11 presents impinging spray heights under three conditions (the same as spray tip penetration). The horizontal axis is the time after start of injection, and the vertical axis is the impinging spray height H_i.

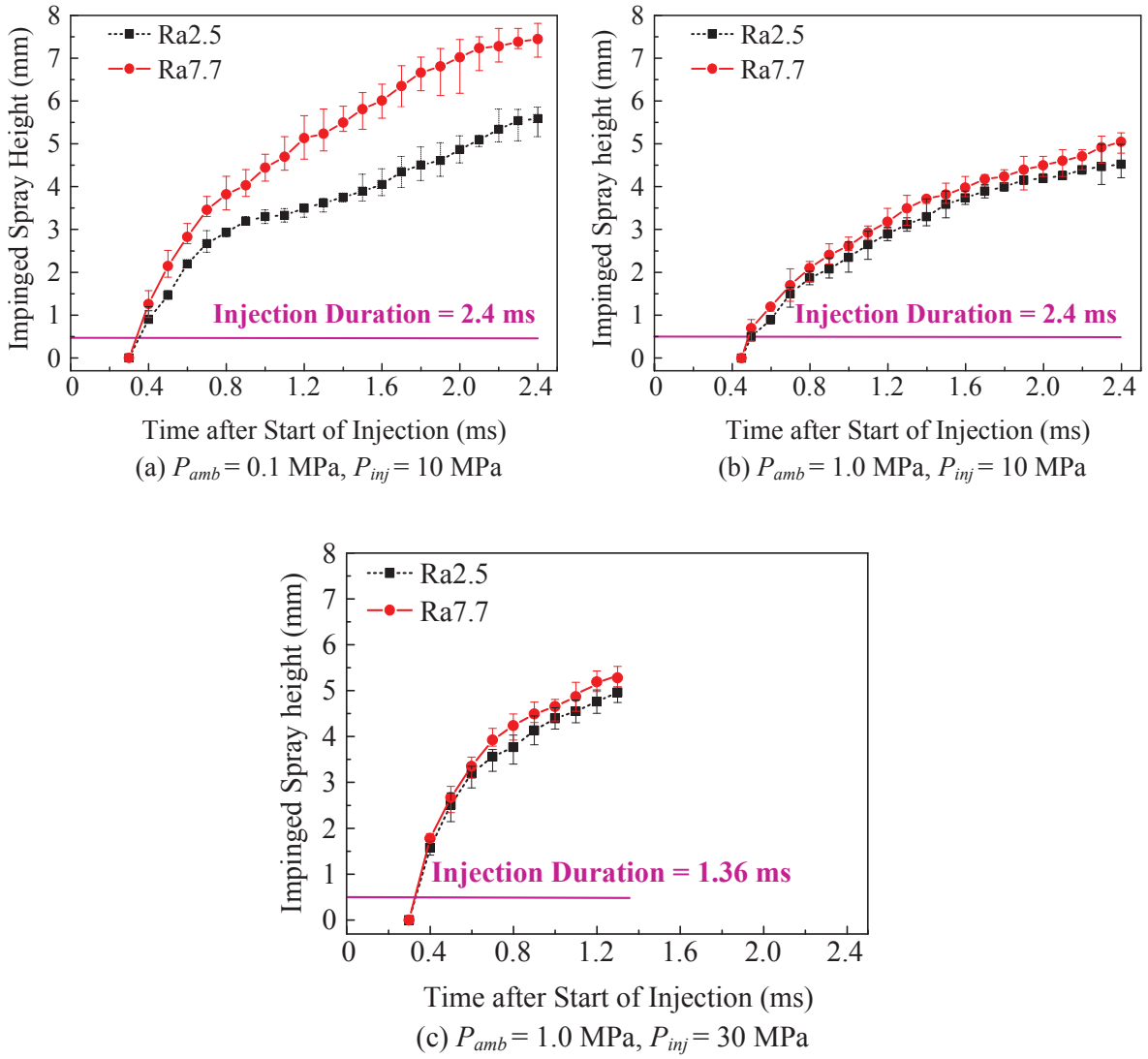

Figure 3.11 Impinging spray height under different conditions.

Under all conditions, H_i of Ra7.7 is larger than that of Ra2.5. Owing to higher wall roughness, the wall has a stronger drag force, so the number of droplets formed from impingement increases, resulting in an increase of H_i. In contrast to ambient pressures, H_i of 0.1 MPa is larger than that of 1.0 MPa. Although increasing the pressure can increase the spray angle (Guan et al., 2015), resulting in more droplets above the wall. Higher ambient pressure increases the density of the ambient atmosphere, resulting in a decrease in the droplet splashing, thus decreasing H_i. In comparison with the injection pressures, H_i of 30 MPa is larger than that of 10 MPa, it can be expected that the increased injection pressure results in much more droplets above the wall than 10 MPa. It is noteworthy that the difference caused by varying the roughness is

larger when ambient pressure is lower. It can be observed that the cases with low ambient pressure show higher sensitivity to the variation of wall roughness due to stronger splashing process.

3.2.3 Fuel Adhesion Characteristics

3.2.3.1 Fuel adhesion evolution

Figure 3.12 shows the evolution of the adhered fuel on walls of different roughnesses under an ambient pressure of 1.0 MPa and injection pressure of 30 MPa. To observe the results clearly, fuel adhesion images undergo 90° clockwise rotation. The fuel adhesions formed on the Ra2.5 and Ra7.7 walls at 3.5, 10, 20, and 29 ms ASOI are shown. The pseudo color represents the fuel adhesion thickness varying from 0 to 2.5 μm. Further, the cross symbol is the impingement point.

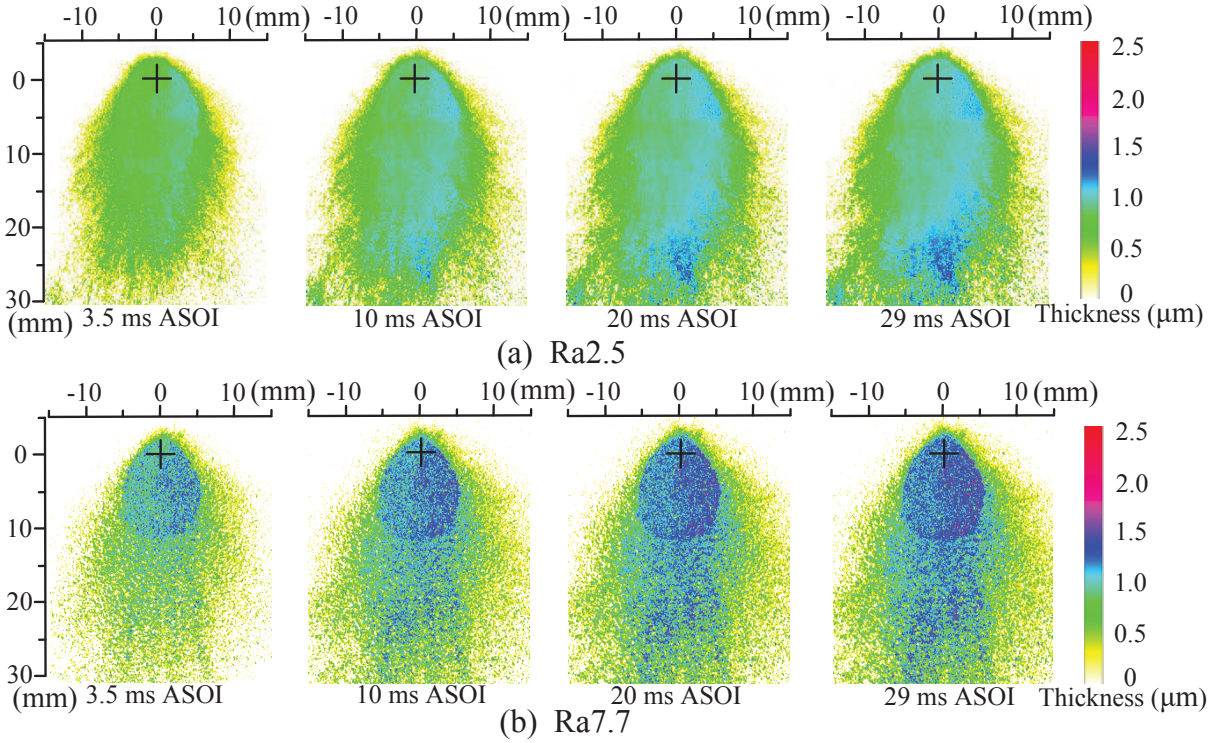

Figure 3.12 Fuel adhesion evolution on different roughness walls (P_{amb} = 1.0 MPa, P_{inj} = 30 MPa).

For Ra2.5, all cases at different time show similar structures. In the initial stage, the thickness is almost uniform; however, from 3.5 ms ASOI fuel adhesion becomes moderately thicker at the downstream. At the bottom region, there is a cluster of droplets caused by secondary breakup of fuel adhesion on the impingement wall surface (Zama et al., 2014). For Ra7.7, fuel adhesion thickness is not uniform in the initial stage. The non-uniform tendency is

more obvious with time. The thicker fuel adhesion area is located at the upstream. For both Ra2.5 and Ra7.7, the fuel adhesion areas are almost symmetric, and they increase with time. The increased area can be expected that there are still some droplets impinging on the wall even after the end of injection that can also be seen from the Mie scattering results in Figure 3.7 and 3.8. The difference of thicker adhesion areas between Ra2.5 and Ra7.7 might be due to the different drag forces of the wall. For Ra2.5, high velocity droplets impinge on the wall then splash and rebound. Some droplets above the wall collide with others and velocity directions change; because of the vortex, they drop on the wall again, and this might result in some thicker area on the downstream. However, when the wall roughness increases, the velocities of the splashing and rebounding droplets decrease considerably (Mundo et al., 1995). After collision, velocity directions of these droplets change and they drop on the wall readily, and this might be responsible for the fuel thicker area on the upstream.

3.2.3.2 Fuel adhesion mass and area

The fuel adhesion mass and area are calculated and depicted in Figure 3.13. The horizontal axis is the time after start of injection. The left vertical axis of the above figure is the fuel adhesion mass, and the right vertical axis is the ratio of fuel adhesion mass to total fuel mass. The left vertical axis of the below figure is fuel adhesion area.

For all conditions, when the spray starts, both the fuel mass and area increase. Finally, the mass and area of the fuel adhesion at Ra7.7 are higher than those at Ra2.5. One possible reason is that when fuel spray impinges on a wall with higher roughness, the splashing velocity of droplets become smaller due to the reduction of the horizontal velocity component (Mundo et al., 1995), resulting in more fuel left on the wall. Comparing with different conditions, when P_{amb} = 0.1 MPa and P_{inj} = 10 MPa, the fuel adhesion mass and area of Ra7.7 are moderately larger than those of Ra2.5, as shown in Figure 3.13 (a). However, such tendency becomes weaker when the ambient pressure is increased to 1.0 MPa, as shown in Figure 3.13 (b). On the contrary, the tendency becomes stronger when the injection pressure is increased to 30MPa, as shown in Figure 3.13 (c). This indicates that increasing the ambient pressure decreases the differences in the fuel mass and area between two kinds of walls, whereas increasing the injection pressure increases the differences. It can be argued that the increased ambient pressure decelerates the droplets after the splashing and rebounding processes for two types of walls that causes more

droplets to promptly drop on the wall. However, the increased injection pressure accelerates the droplets, which causes fewer droplets to drop on the wall after the splashing and rebounding processes. Further, this accelerating effect is more significant for the wall with a smaller roughness. More importantly, both mass and area of the fuel adhesion increase even AEOI for all the conditions, and the droplets in the air impinging on the wall should be the reason for that. The same phenomena can also be seen in (e) and (f) of Figures 3.8 and 3.9.

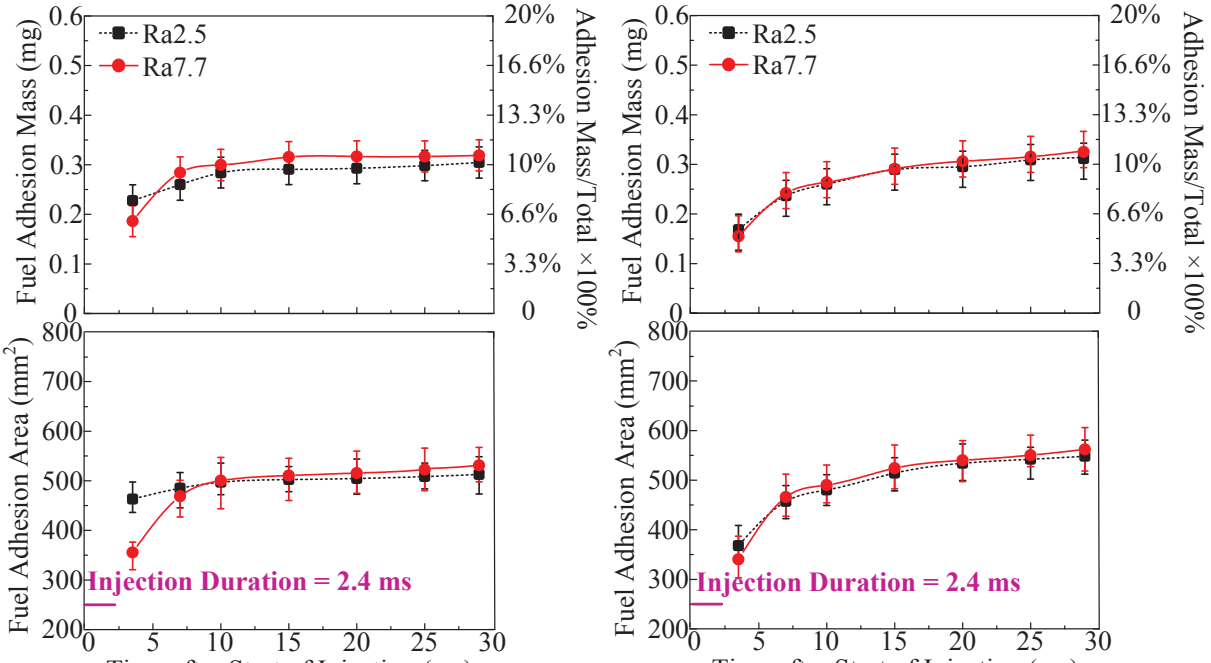

(a) P_{amb} = 0.1 MPa, P_{inj} = 10 MPa

(b) P_{amb} = 1.0 MPa, P_{inj} = 10 MPa

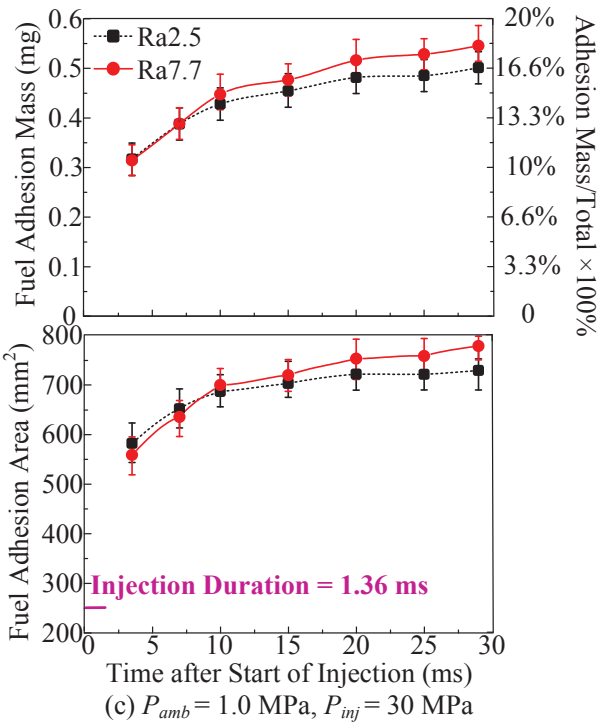

Figure 3.13 Fuel adhesion mass and area under different conditions.

3.2.3.3 Fuel adhesion thickness

Time-resolved results of the maximum fuel adhesion thickness under different conditions are presented in Figure 3.14. The horizontal axis is the time after start of injection, and the vertical axis is the fuel adhesion maximum thickness.

It can be seen that the maximum thickness values of Ra7.7 are above 1.6 μm, whereas those of Ra2.5 are below 1.6 μm. This is due to the effect of wall surface roughness on droplets. Stronger drag force decelerates the droplets substantially. As a result, the droplets drop on the wall readily, and the fuel adhesion becomes thicker. Furthermore, it is remarkable that an increase of ambient pressure decreases the maximum fuel adhesion thickness. One possible reason is that the increased spray angle results in a uniform distribution of droplets on the wall. On the contrary, an increase of injection pressure increases the maximum fuel adhesion thickness due to better dispersion (Wang et al., 2016).

In order to obtain more details about fuel adhesion thickness, the probability of fuel adhesion thickness is depicted in Figure 3.15. The horizontal axis is fuel adhesion thickness, and

the vertical axis is the probability. The dotted lines represent fuel adhesion thickness of Ra2.5, and the solid lines represent that of Ra7.7.

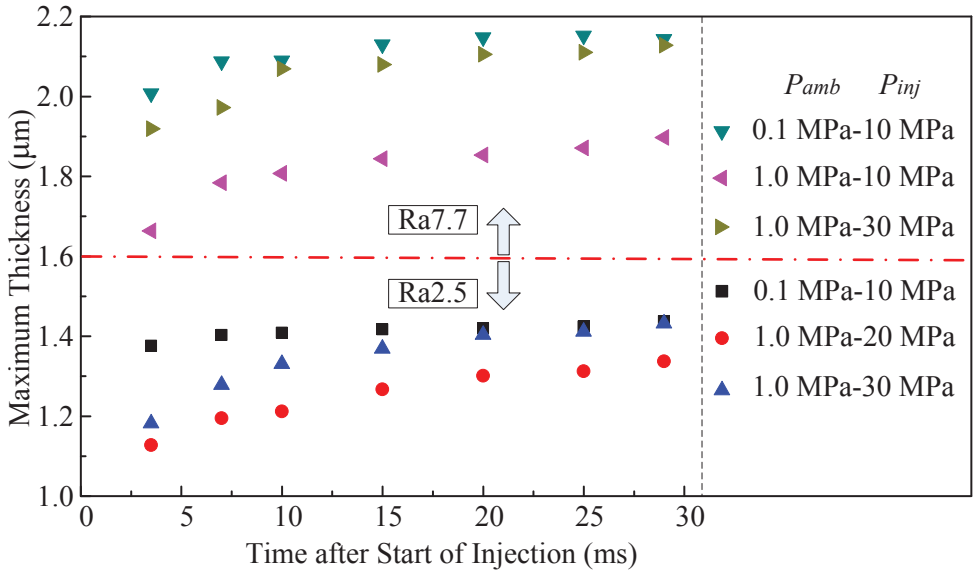

Figure 3.14 Maximum thickness of fuel adhesion under different conditions.

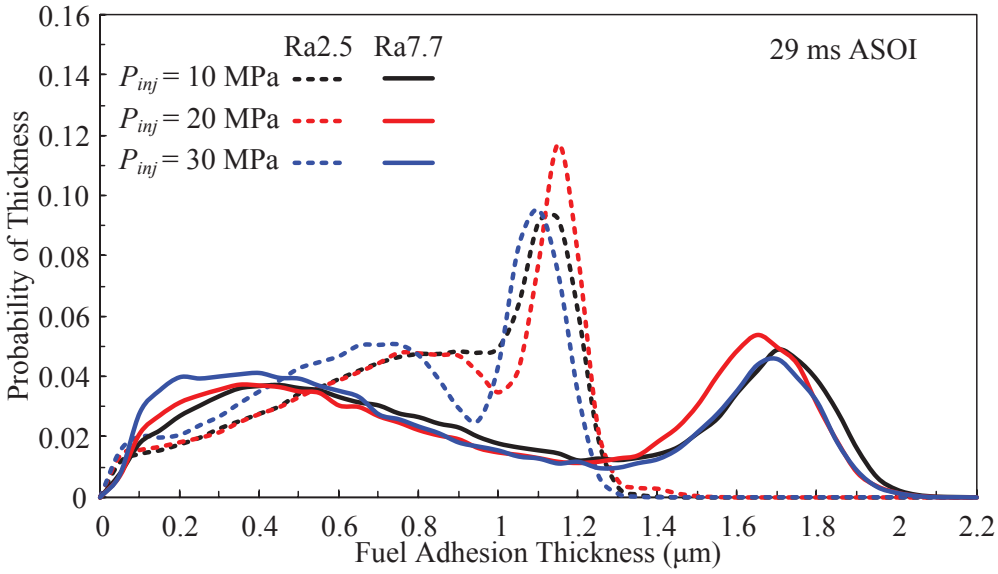

(a) P_{amb} = 0.1 MPa

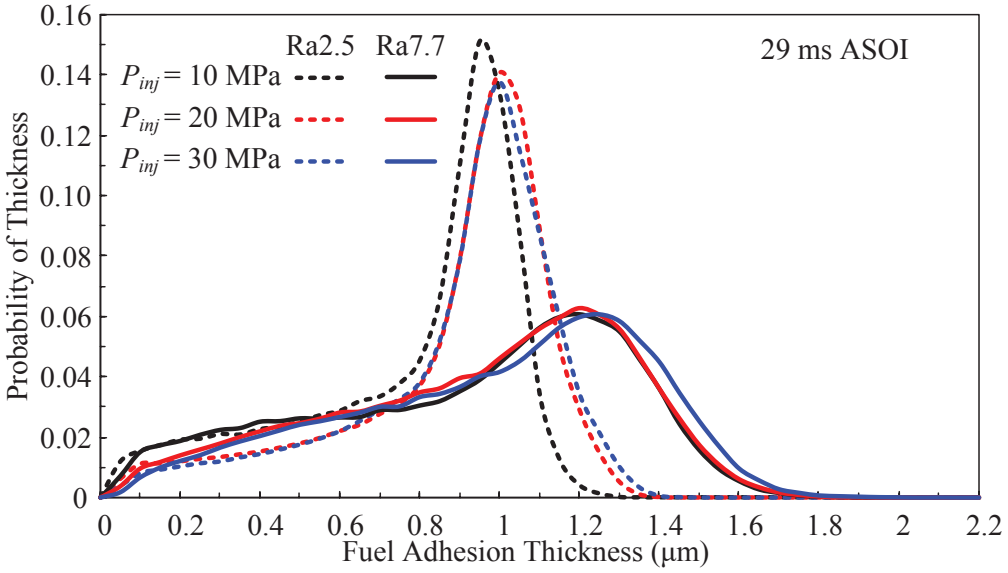

(b) P_{amb} = 1.0 MPa

Figure 3.15 Probability of fuel adhesion thickness (29 ms ASOI).

Firstly, the results at the ambient pressure of 0.1 MPa are examined. For Ra2.5, there are two peak values at 0.7 μm and 1.1 μm, respectively. For Ra7.7, there are also two peak values at 0.3 μm and 1.7 μm. Moreover, the thickness range of Ra7.7 is from 0 to 2.2 μm that is wider than that of Ra2.5. Two peak values of Ra2.5 are considerably bigger than that of Ra7.7. This indicates that the fuel adhesion is uniform for a wall of smaller roughness. One possible reason is that for small roughness of wall, some droplets impinge on the wall, and then spread out readily. Whereas, for the wall with larger roughness, uniform spread is difficult. This result can also be seen in Figure 3.12.

The results at the ambient pressure of 1.0 MPa are then examined. It is interesting to find that only one peak value exists at 1.0 MPa, and the peak value is larger than that of 0.1 MPa. This indicates that an increase in ambient pressure improves the uniformity of adhesion thickness. Increasing ambient pressure under a certain temperature increases the density of ambient gas, leading to an increase in the momentum transfer between the spray and the ambient gas. As a result, the spray angle increases and the droplets velocities decrease (Guan et al., 2015). The increased spray angle leads to better atomization and more fuel impinging on fuel uniformly. Moreover, the droplets with a decelerated velocity impinge on the wall and spread out easily to

form a fuel adhesion. Even the splashing droplets with decelerated velocity can impinge on the wall again readily with the help of vortex, resulting in more uniform fuel adhesion.

To explain the wall roughness effect on fuel adhesion uniformity more clearly, a cumulative distribution function $F(x)$, as shown in Eq. (3.2) is used.

$$F(x) = \sum_{i=0}^{x} f_M(h_i) \tag{3.2}$$

In Figure 3.16, the horizontal axis is fuel adhesion thickness, and the vertical axis is $F(x)$. $F(x)$ increases with fuel adhesion thickness. The dotted lines represent Ra2.5, and the solid lines represent Ra7.7. If the fuel adhesion is completely uniform, the cumulative distribution function $F(x)$ is a straight line perpendicular to the horizontal axis, shown as in a dashed dotted line. If the fuel adhesion is completely non-uniform, the cumulative distribution function $F(x)$ is a straight line with a certain slope to the horizontal axis, shown as in a dashed double-dotted line.

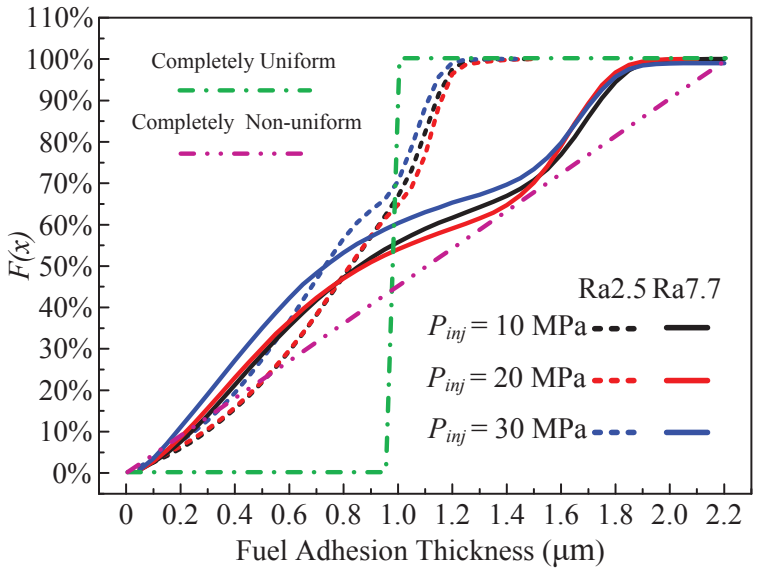

(a) P_{amb} = 0.1 MPa

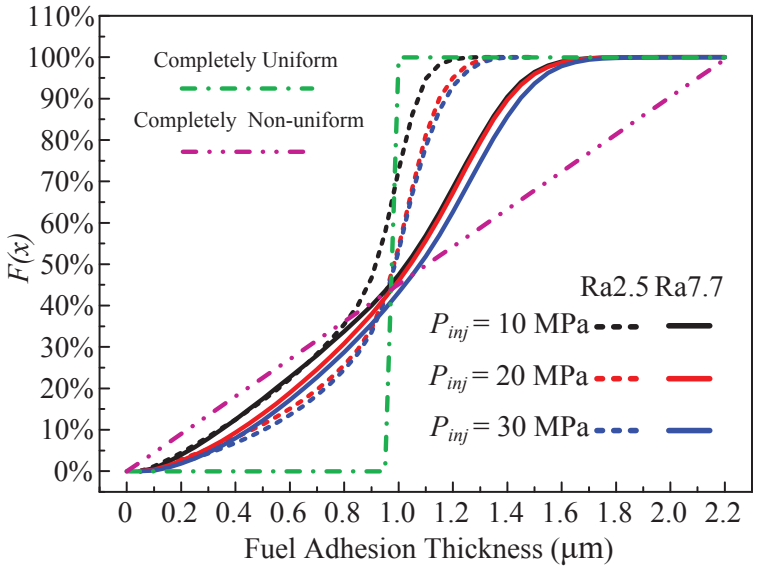

(b) P_{amb} = 1.0 MPa

Figure 3.16 Cumulative distribution function curves (29 ms ASOI).

For the ambient pressure of 0.1 MPa, the curves of Ra2.5 increase readily than that of Ra7.7. The curves of Ra2.5 reach to 100% at about 1.3 μm, whereas the curves of Ra7.7 reach to 100% at about 2.0 μm. Furthermore, the curves of Ra2.5 are closer to the completely uniform curve, whereas the curves of Ra7.7 are closer to the completely non-uniform curve, indicating that the fuel adhesion of Ra2.5 is considerably more uniform than that of Ra7.7. The curves with different injection pressures are similar to each other, indicating that the injection pressure has less effect on the uniformity of fuel adhesion thickness than wall roughness.

For an ambient pressure of 1.0 MPa, the tendencies are similar to those of 0.1 MPa, except that the curves for Ra2.5 under 1.0 MPa are substantially closer to the completely uniform curve and the curves for Ra7.7 under 1.0 MPa are considerably farther from the completely non-uniform curve, which also proves that the ambient pressure promotes uniformity in the fuel adhesion thickness.

Further investigation was conducted to clarify the effect of wall roughness on fuel adhesion thickness along different lines. In Figure 3.17, the coordinate system is defined, and the origin o is determined as the impingement point. The positive *y* axis is along the direction of fuel splash after impingement, and positive x axis is perpendicular to the *y* axis, pointing to the left. Because

fuel adhesion is almost symmetric about $x = 0$ axis, we only discuss the adhesion thickness along $x = 0$ line. For horizontal axis, we divided fuel adhesion by $y = 0$, 10 and 20 mm lines that represent the upstream, midstream, and downstream of the fuel adhesion.

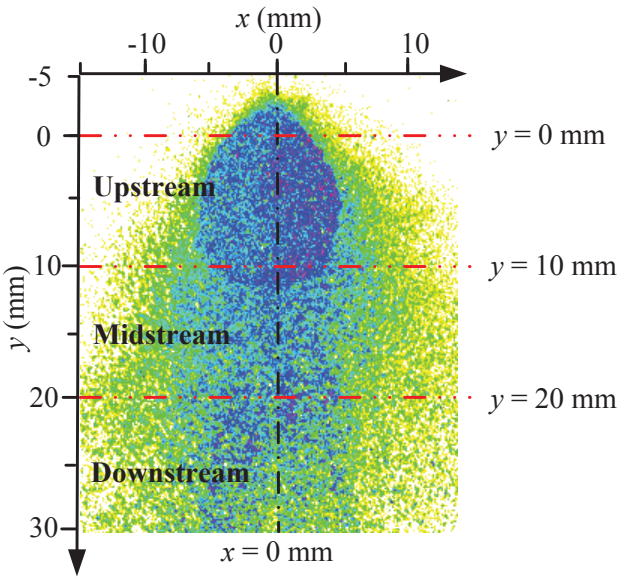

Figure 3.17 Definition of fuel adhesion thickness along different lines.

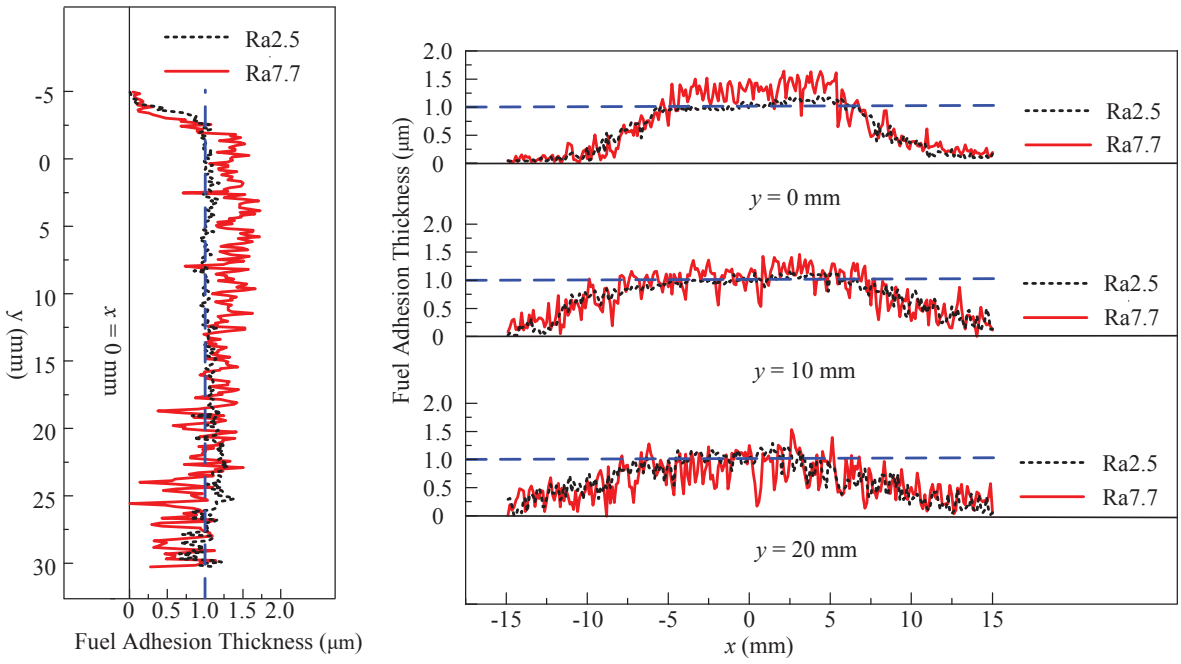

(a) Fuel adhesion thickness along $x = 0$ line (b) Fuel adhesion thickness along $y = 0$, 10 and 20 mm lines

Figure 3.18 Fuel adhesion thickness along different lines (29 ms ASOI, P_{amb} = 1.0 MPa, P_{inj} = 30 MPa).

To express concisely, the fuel adhesion thickness along $x = 0$ line was defined as $x0$. The fuel adhesion thickness along $y = 0$, 10, and 20 lines were defined as $y0$, $y10$, and $y20$, respectively. In the following discussion, the terms of $x0$, $y0$, $y10$ and $y20$ are used to represent the fuel adhesion thickness along these different lines. The experimental condition discussed in this section is at 29 ms ASOI, P_{amb} = 1.0 MPa, and P_{inj} = 30 MPa, as shown in Figure 3.17.

Figure 3.18 (a) shows the fuel adhesion thickness along $x = 0$ line. The horizontal axis is fuel adhesion thickness, and the vertical y axis is from -5 to 30 mm. For Ra2.5, $x0$ increases from -5 to -2.5 mm and remains almost constant from -2.5 to 20 mm; it finally decreases with large fluctuations. For Ra7.7, $x0$ increases from -5 to -2.5 mm and remains almost constant from -2.5 to 10 mm; it finally decreases with considerably larger fluctuations than those of Ra2.5. At the constant value stage, $x0$ of Ra7.7 is larger than that of Ra2.5. The fluctuation of Ra7.7 is significantly remarkable than that of Ra2.5. This indicates that the fuel adhesion is more uniform for the smaller roughness of the wall.

Figure 3.18 (b) shows the fuel adhesion thickness along different y lines. The horizontal x axis is from -15 to 15 mm, and the vertical axis is the fuel adhesion thickness. For Ra2.5, $y0$, $y10$, and $y20$ increase from -15 to -5 mm, then remains almost constant from -5 to 5mm, and finally decreases. At the constant value stage, $y0$ are similar to $y10$, but smaller than $y20$. The fluctuation of $y0$ is similar to that of $y10$, but smaller than that of $y20$. This indicates that, for Ra2.5, fuel adhesion thickness downstream is larger, and the uniformity of fuel adhesion thickness downstream is considerably inferior to that in the upstream and midstream.

For Ra7.7, the tendency is similar to Ra2.5, except that the value at the constant stage is slightly different. At the constant stage, $y0$ of Ra7.7 is larger than that of Ra2.5, whereas $y10$ and $y20$ of Ra7.7 is almost the same as those of Ra2.5. This suggests that, the fuel adhesion thickness of upstream is thicker for larger roughness of the wall. For $y0$, $y10$, and $y20$, the fluctuations of Ra7.7 are significantly remarkable than those of Ra2.5. This indicates that the fuel adhesion is more uniform for smaller roughness of the wall.

3.3 EFFECT OF IMPINGEMENT DISTANCE

3.3.1 Experimental Conditions

The reduction of particulate number (PN) emissions is the major concern of a gasoline DI engine due to the introduction of PN standards in Euro 6 emission regulations. During the catalyst-warm-up operation, the retarded injection timing is used to increase the exhaust gas temperature. Although multiple-injection strategy is used to reduce the wall wetting, the late injection near top dead center (TDC) resulted in an increase in PN emissions. To clarify the spray-wall interactions under the aforementioned engine conditions, the equivalent experimental conditions in the constant volume chamber were determined in Table 3.3.

Table 3.3 Experimental conditions

Injection Conditions	
Fuel	Toluene
Injection Mass (M_{inj})	3.0 mg
Injection Pressure (P_{inj})	10, 20, 30 MPa
Injector Type	Mini-Sac, Single-Hole
Nozzle Hole Diameter (d)	0.135 mm
Injection Duration (t_d)	2.4, 1.65, 1.36 ms
Ambient Conditions	
Ambient Gas	Nitrogen
Pressure (P_{amb})	0.5 MPa
Temperature (T_{amb})	300 K
Density (ρ_{amb})	5.95 kg/m^3
Impingement Conditions	
Impingement Plate	Quartz Glass
Impingement Distance (D_{imp})	28, 40 mm
Impingement Angle (θ_{imp})	45°
Surface Roughness	Ra7.5 μm

The fuel tested in this study was toluene, as a surrogate fuel for gasoline. The injection mass was kept constant at 3.0 mg equivalent to the total injection quantity of the multi-hole injector divided by hole number. The injection pressures changed from 10 to 30 MPa considering the phenomena, resulting in different injection durations of 2.4, 1.65, and 1.35 ms. The ambient density of non-evaporating conditions is kept the same as that of in-cylinder conditions. A mini-sac injector with a single hole (0.135 mm) was used. To determine the effect of impingement distance on fuel adhesion, it ranged between 28 and 40 mm from the nozzle exit to the wall along the spray axis. The impingement angle was 45 deg from the spray axis to the flat wall. The surface roughness of the new piston used in gasoline engine is approximately Ra1.0, but it may increase up to Ra10.0 or more due to deposit accumulation (Luo et al., 2017). Therefore, a circle plate made of quartz glass with surface roughness of Ra7.5 μm was placed under the injector as a flat wall, representing a used piston in the engine. As shown in Figure 3, the diameter of the plate was 50 mm and its thickness was 2 mm. The coordinate system was defined, and the intersection point o of the spray axis and the wall was defined as the impingement point.

3.3.2 Spray Impingement Characteristics

Figure 3.19 shows R_s under three conditions (P_{inj} = 10, 20, and 30 MPa). The horizontal axis is the time after start of injection, and R_s is in the vertical axis. R_s of D_{imp} = 28 mm is larger than that of D_{imp} = 40 mm under all conditions. The ambient pressure (P_{amb} = 0.5 MPa) results in strong interaction between the fuel and nitrogen, decelerating the droplets before impingement. During the spray propagation at the shorter impingement distance, the fuel with higher Weber number diffuses around after impingement on the wall. As a result, R_s of D_{imp} = 28 mm is larger than that of D_{imp} = 40 mm. Moreover, R_s increases with an increase in the injection pressure. It can be expected that the increased injection pressure enhances the kinetic energy of fuel.

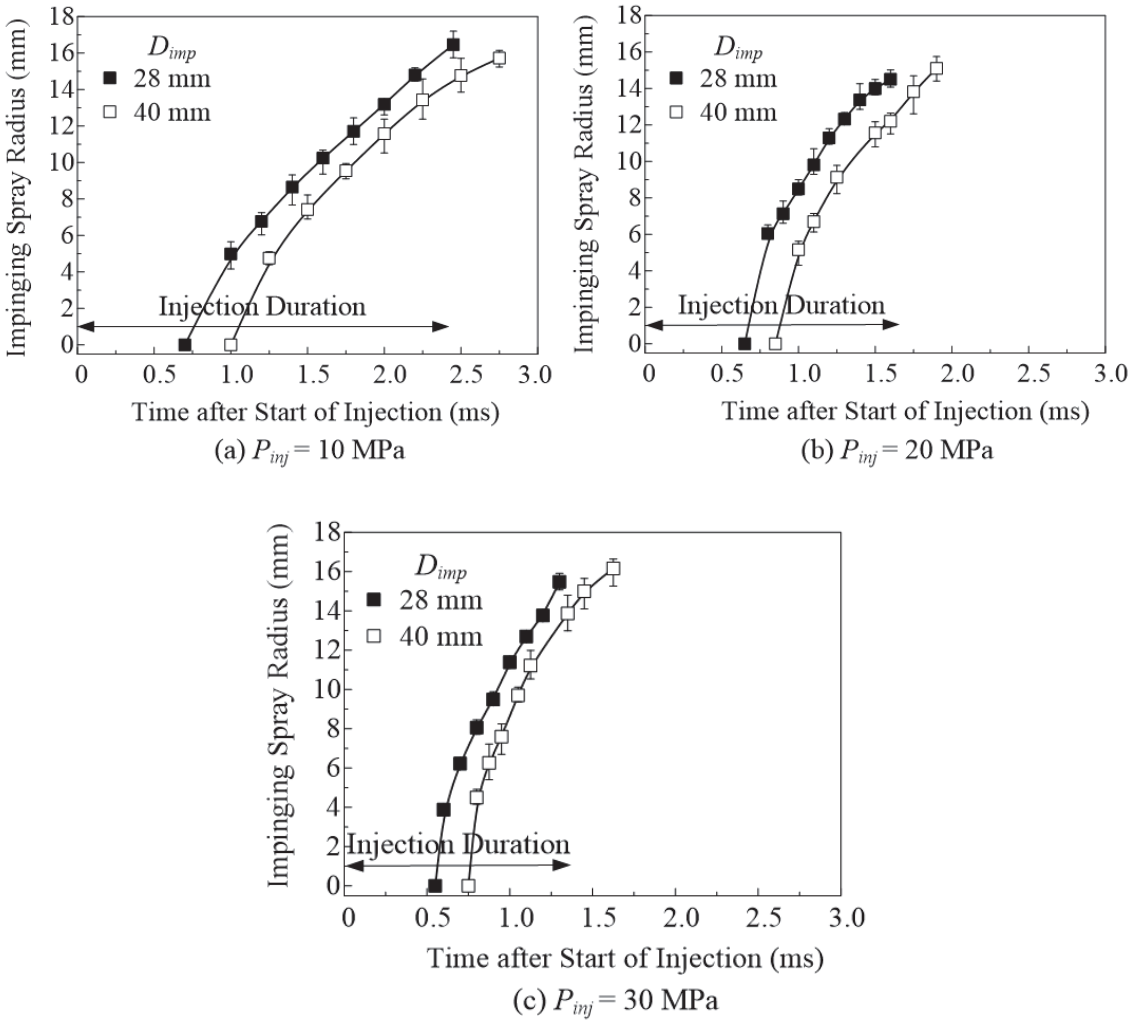

Figure 3.19 Impinging spray radius, R_s (Front view)

Figure 3.20 shows H_v under three conditions (P_{inj} = 10, 20, and 30 MPa). The horizontal axis is the time after start of injection, and H_v is in the vertical axis. H_v of D_{imp} = 28 mm is larger than that of D_{imp} = 40 mm under all conditions. Owing to its shorter impingement distance, the fuel with higher Weber number and momentum impinges on the wall, leading to a decreasing number of droplets depositing on the wall, and an increasing number of splashing droplets (Bai et al., 1995). Therefore, H_v of D_{imp} = 28 mm is larger than that of D_{imp} = 40 mm. In contrast to the different injection pressures, H_v increases more rapidly with an increase in injection pressure. It can be expected that the increased injection pressure enhances the Weber number and the initial kinetic energy of the fuel spray, resulting in faster vortex generation.

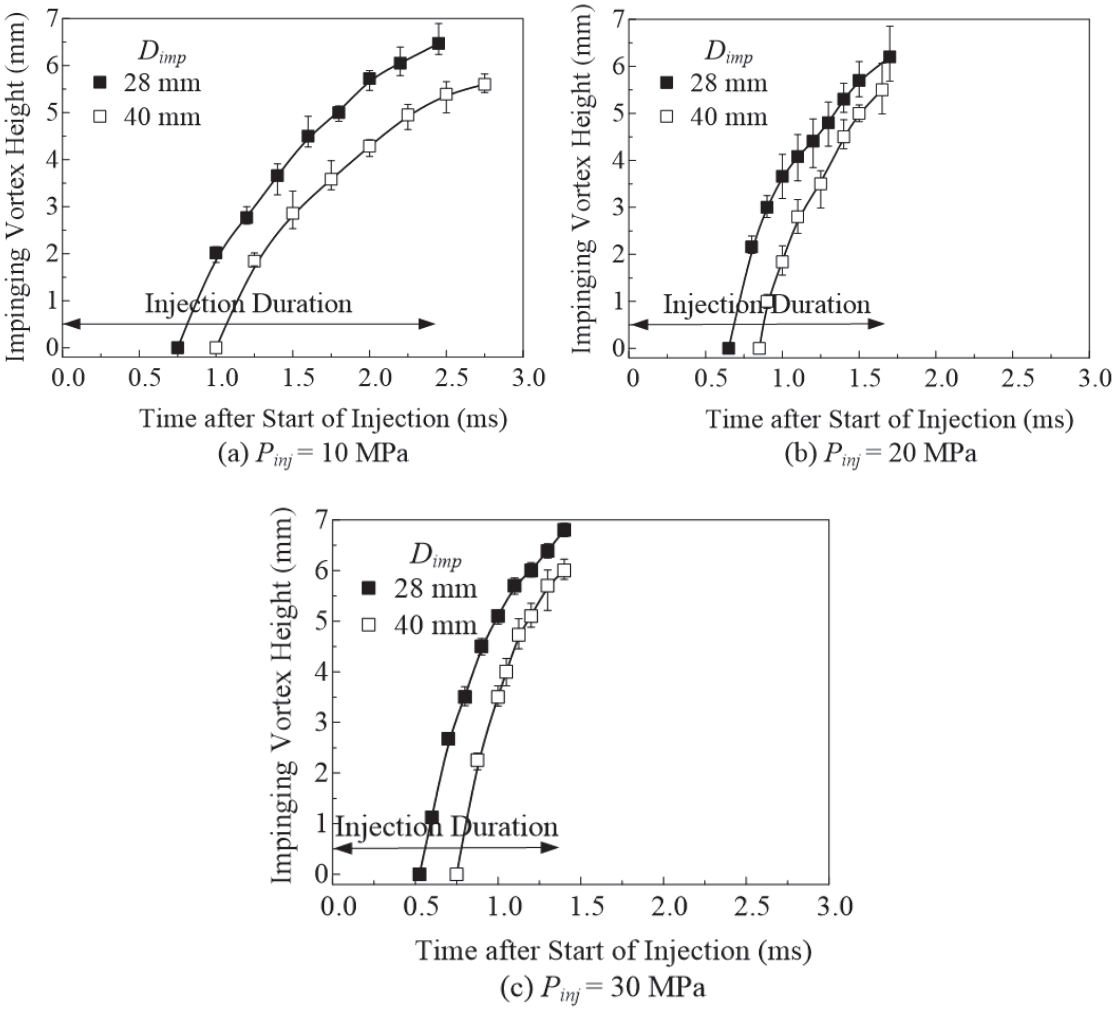

Figure 3.20 Impinging vortex height, H_v (Front view)

Figure 3.21 presents *S,* and the impingement distance is shown by the broken line. Three conditions (P_{inj} = 10, 20, and 30 MPa) were investigated. For all conditions, the spray development can be divided into two stages. It increases almost linearly before impingement, and the gradient of *S* decreases after spray impingement (Luo et al., 2017). The drag force from the wall and ambient gas can be regarded as the main reasons for this phenomenon. It is noteworthy that before impingement, *S* is almost the same under different impingement distances. However, after impingement, *S* of D_{imp} = 40 mm is slightly larger than that of D_{imp} = 28 mm under all conditions. One possible reason is that, after impingement, the fuel disperses and spreads in all directions, with the result that the interaction between the droplets and air is much stronger than before. Moreover, friction from the wall can be regarded as another reason. As a result, *S* increases with the increased impingement distance. Additionally, under different

injection pressures, the *S* of 30 MPa is larger than that of 10 MPa, and the impingement time of 30 MPa is shorter than that of 10 MPa owing to higher Weber number of the spray.

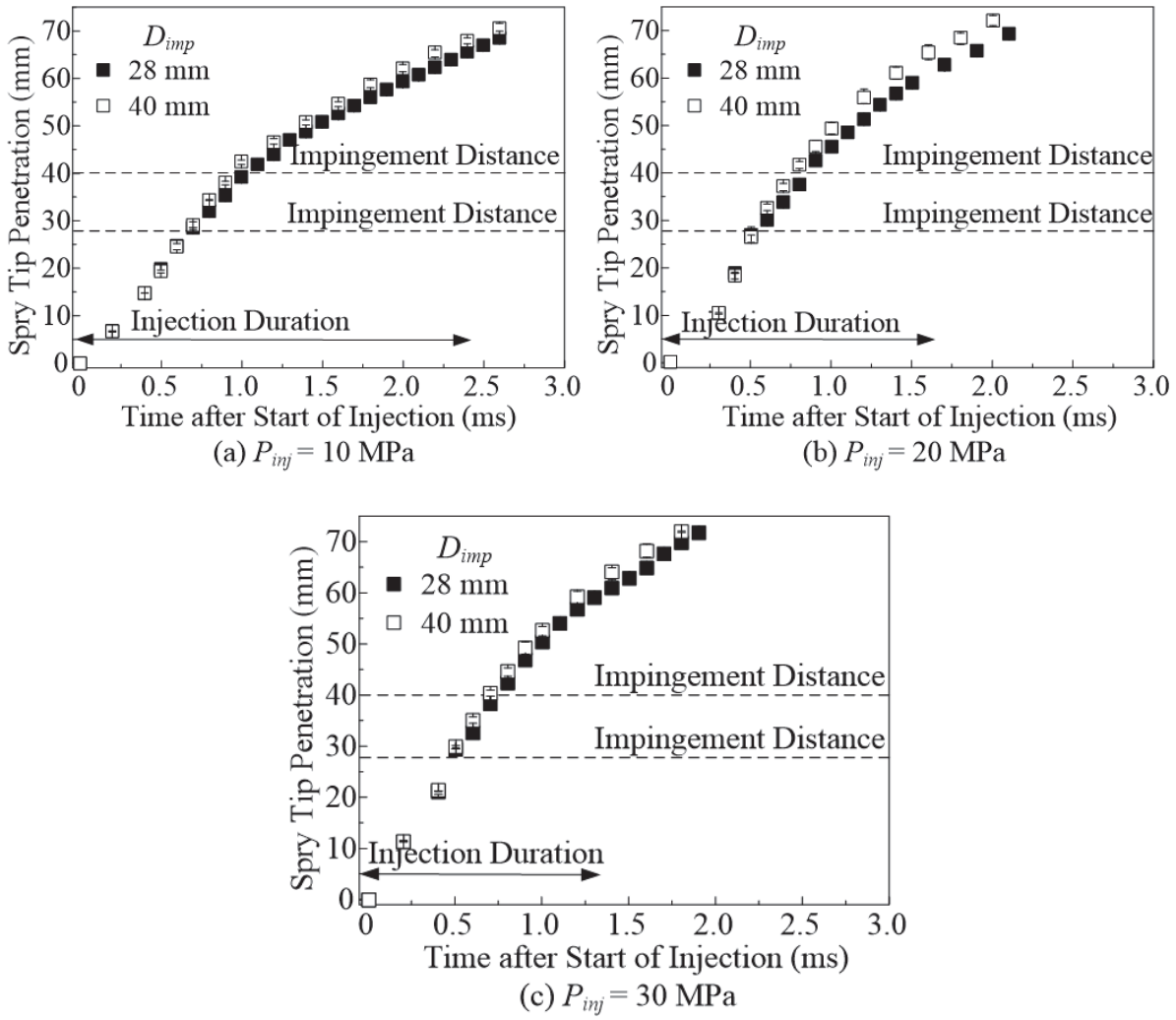

Figure 3.21 Spray tip penetration, *S* (Side view)

Figure 3.22 presents H_i under three conditions (P_{inj} = 10, 20, and 30 MPa). The horizontal axis is the time after start of injection, and H_i is in the vertical axis. It is clear that H_i of D_{imp} = 28 mm is larger than that of D_{imp} = 40 mm under all conditions. This phenomenon can be attributed to the different momentum of the droplets impinging on the wall. The droplets of D_{imp} = 28 mm have higher Weber number when impinging on the wall, and many droplets splash around after impingement, resulting in larger H_i compared with that of D_{imp} = 40 mm. In contrast to different

conditions, H_i increases and the gradient of H_i becomes larger owing to the effect of the enhanced kinetic energy of fuel.

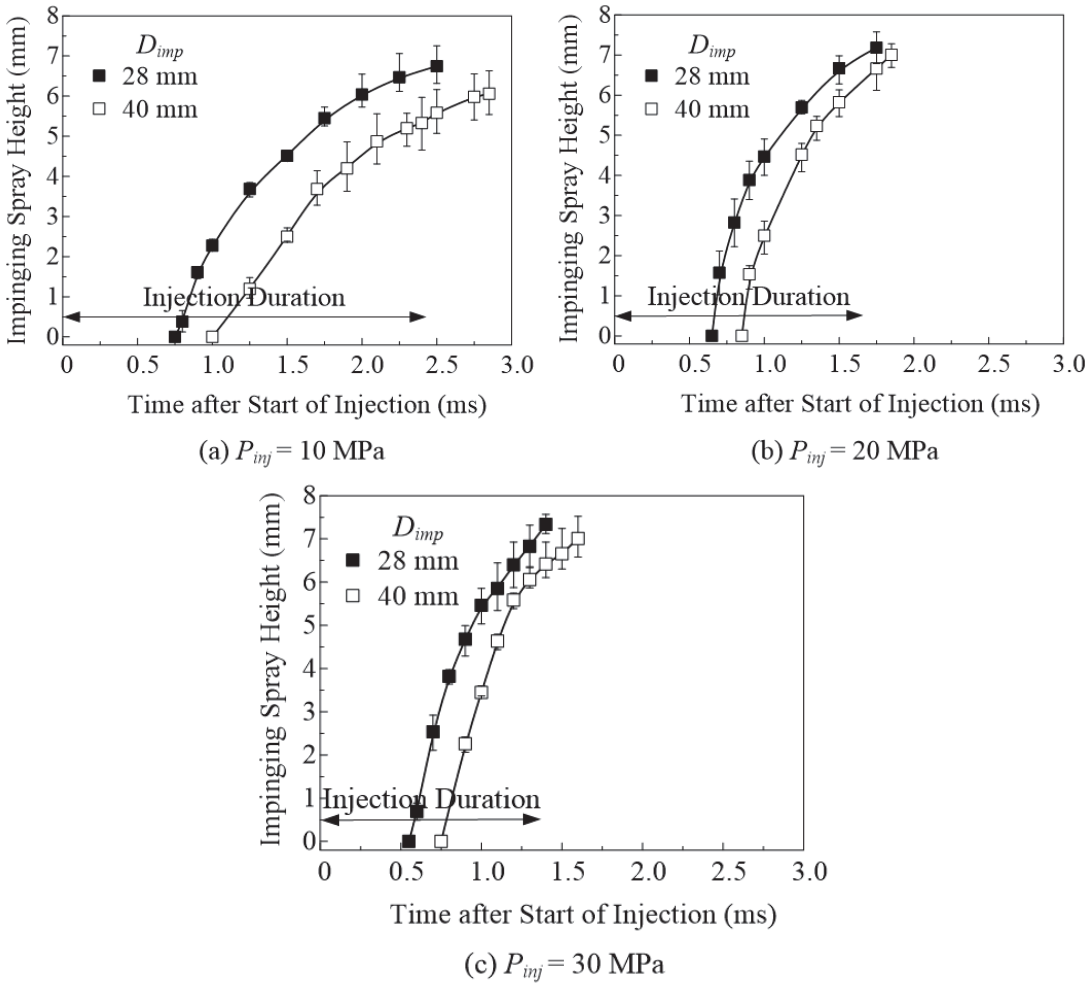

Figure 3.22 Impinging spray radius, R_s (Front view)

3.3.3 Fuel Adhesion Characteristics

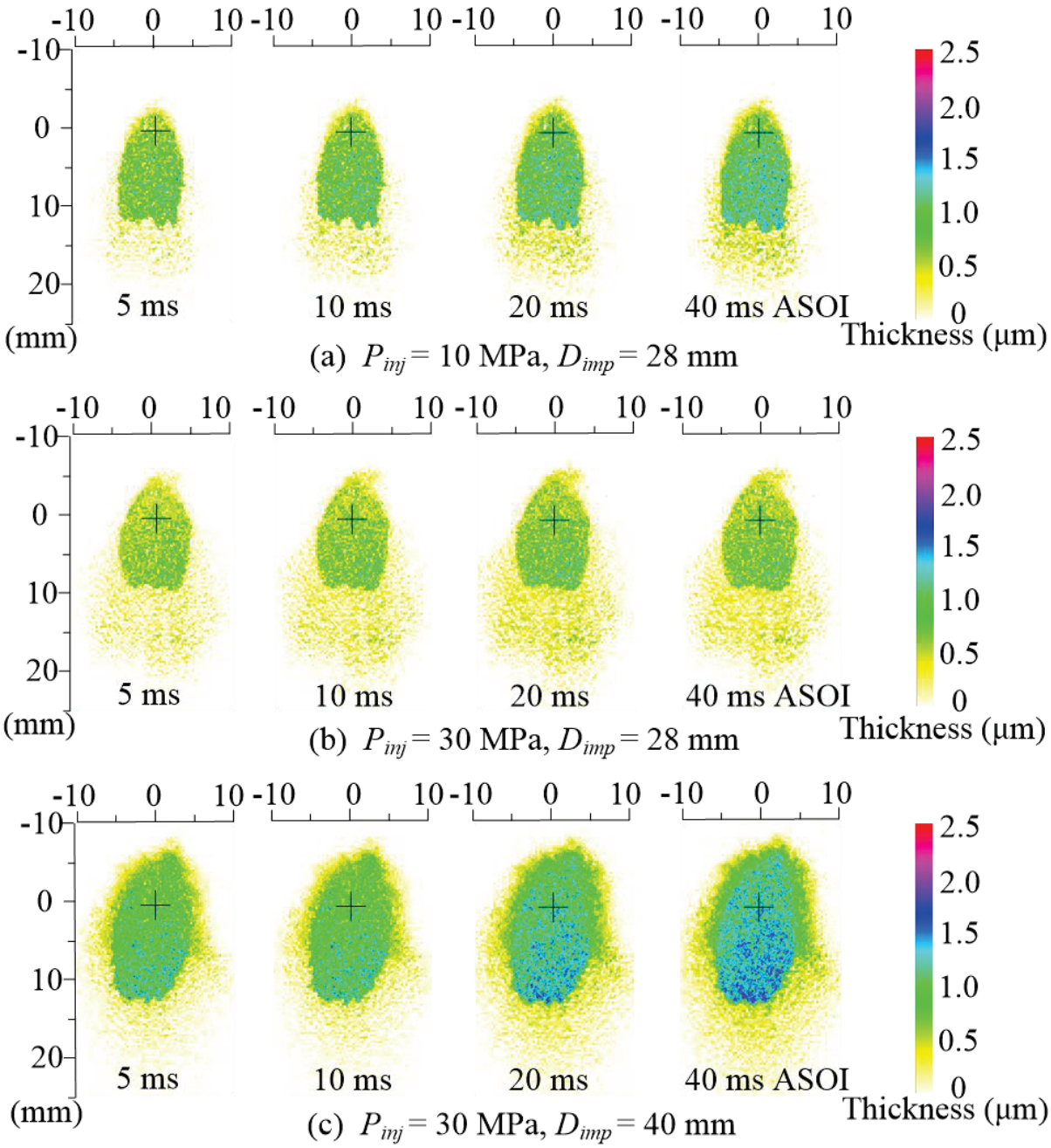

Figure 3.23 Fuel adhesion evolution (Bottom view)

During the spray, some scattered light from the floating droplets above the impingement region. In order to eliminate the stray light error, all results are after the end of injection (EOI) (Luo et al., 2017).

Figure 3.23 shows the evolution of the adhered fuel under different conditions. The fuel adhesions on the wall at 5, 10, 20, and 40 ms ASOI are shown. The pseudocolor represents the adhered fuel thickness, varying from 0 to 2.5 μm, and the impingement point is shown by the cross symbol. Under each condition, all cases at different times show similar structures, and the fuel adhesion areas are almost symmetric. It is evident that the wetted area increases under higher injection pressure, and the better atomization of a high injection pressure should be responsible for this. More importantly, when D_{imp} = 28 mm, the fuel adhesion becomes a little thicker at the upstream, whereas when D_{imp} = 40 mm, the thicker region moves downstream. There may be two reasons for this. One is that there are different impact regimes for droplets impinging on the wall: "stick," "spread," and "splash" (Bai et al., 1995). The increased impingement distance decelerates the droplets owing to the ambient pressure (P_{amb} = 0.5 MPa). Thus, after impingement on the wall, some droplets may change their behavior from "splash" to "spread," or even to "stick", resulting in thicker fuel adhesion of D_{imp} = 40 mm. The second reason may be that even though some droplets splash off the wall, the droplets with low velocity easily drop back on the wall, causing the thicker fuel adhesion to move down.

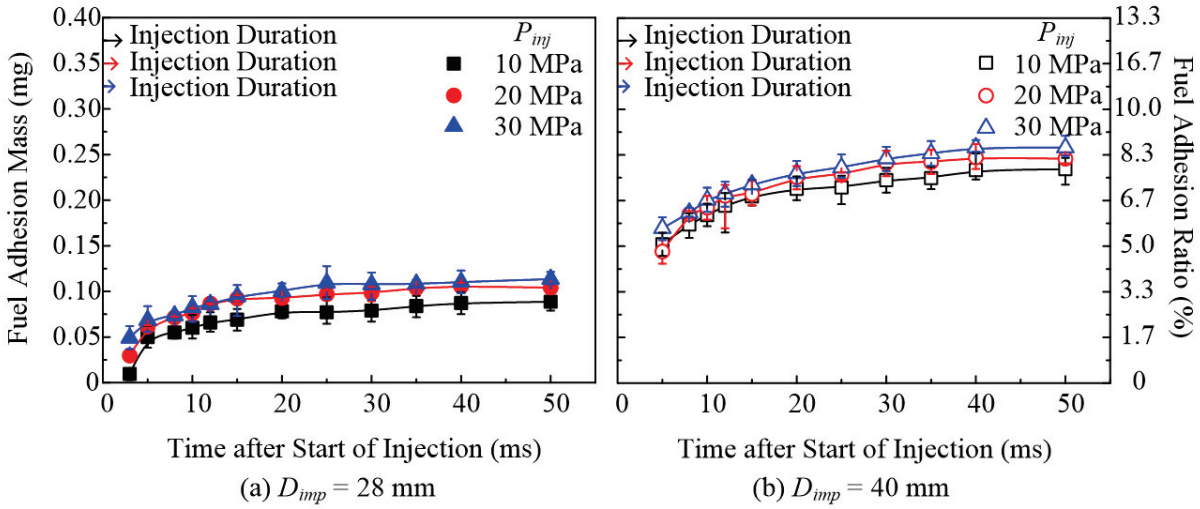

Figure 3.24 Fuel adhesion mass

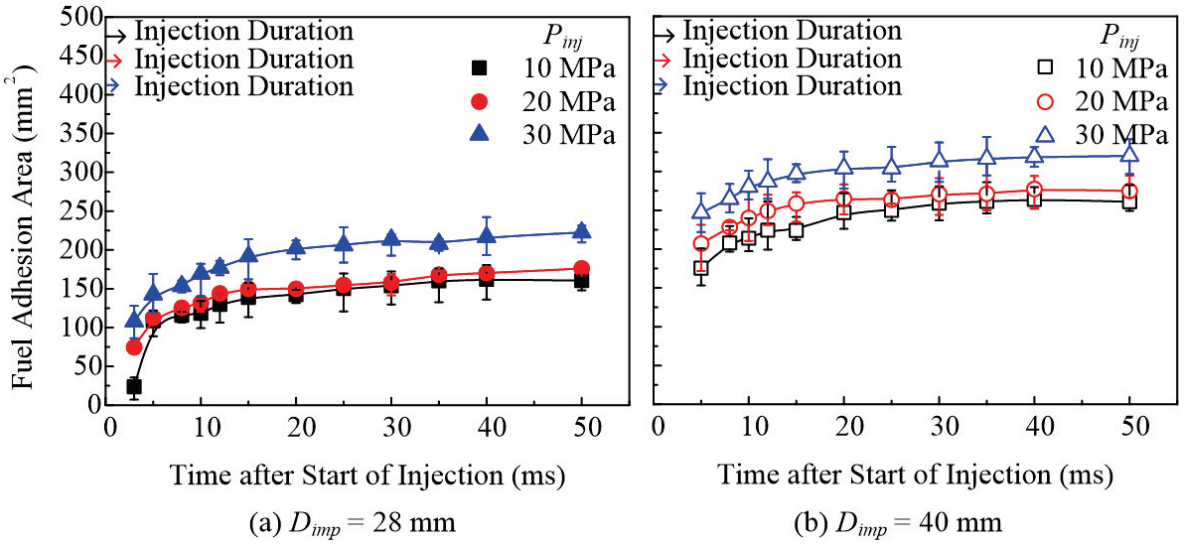

Figure 3.25 Fuel adhesion area

The fuel adhesion mass and area are depicted in Figures 3.24 and 3.25. The adhesion mass ratio is defined as the ratio of adhesion mass to total injection mass. The fuel adhesion mass and area increase with time even after the end of injection because there are still some droplets dropping on the wall. An increase in injection pressure under a certain ambient pressure increases the fuel adhesion mass and area owing to better atomization. Furthermore, both fuel adhesion mass and area increase at a large impingement distance. A decrease in the number of splashing droplets tends to be responsible, which agrees well with the Mie scattering results. Additionally, the bigger spray width and better atomization should be other reasons for this. Park et al. (2004) have already proven that the spray width increases as the spray flows downstream, and the SMD decreases at a large impingement distance. Therefore, the wider spray and better atomization of D_{imp} = 40 mm is formed before impingement, resulting in bigger adhesion area and mass on the wall. The same tendency of the wider fuel adhesion at D_{imp} = 40 mm, can also be observed in the comparison between Figures 3.23 (b) and (c).

Figure 3.26 shows the adhesion mass ratio under different conditions at 40 ms ASOI. For D_{imp} = 28 mm, the adhesion mass ratio increases from 2.9% to 3.7% with an increase in injection pressure. However, by increasing the D_{imp} to 40 mm, the ratio increases from 7.8% to 8.6% at increased injection pressures, and thus, the ratios of D_{imp} = 40 mm are more than twice at D_{imp} = 28 mm.

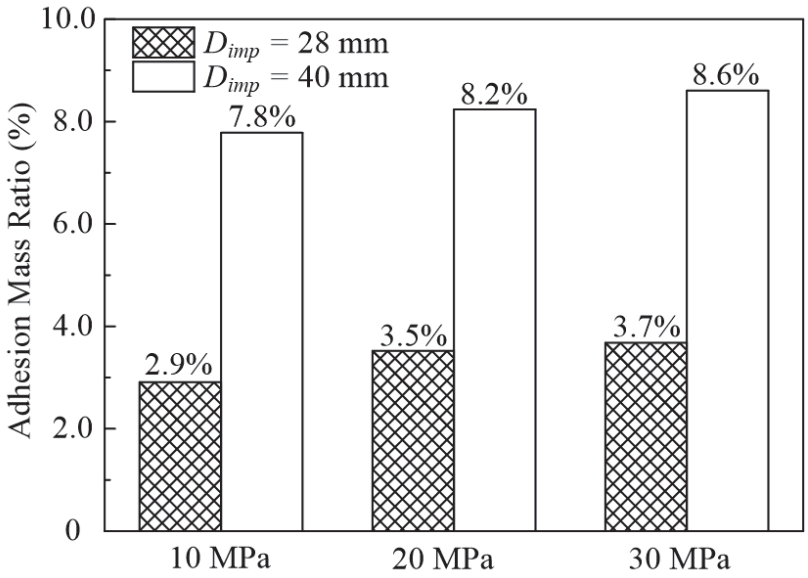

Figure 3.26 Adhesion mass ratio (40 ms ASOI)

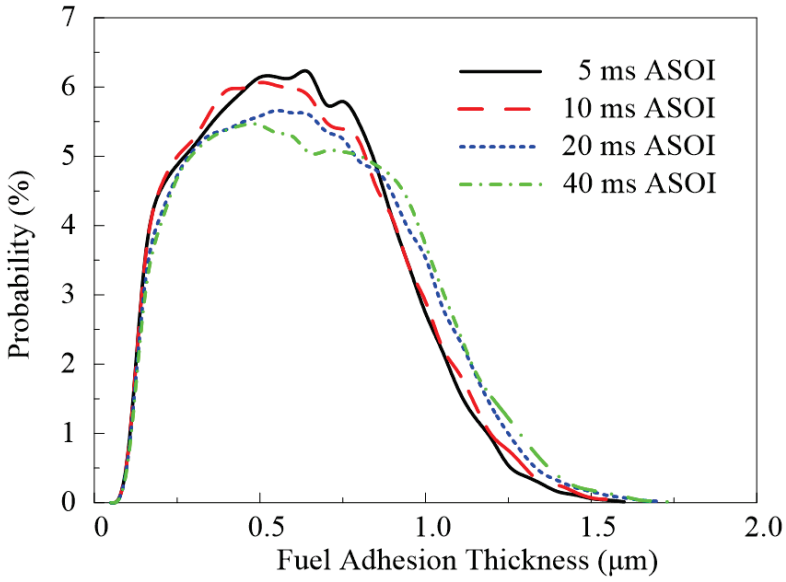

Figure 3.27 Probability of thickness with time (P_{inj} = 30 MPa, D_{imp} = 28 mm)

To further investigate the adhesion thickness, the probability of thickness was determined. As shown in Figure 3.27, the horizontal axis is the fuel adhesion thickness, and the vertical axis is the probability of mass. Figure 3.27 describes the probability of thickness with different times at P_{inj} = 30 MPa and D_{imp} = 28 mm, and the average values of three shots were presented. It is reported that the peak value of the curves decreases, and the curve becomes a little wider with

time, which indicates that the uniformity of adhesion thickness becomes worse with time. And the same observation can be derived from Figure 3.23 (b). One possible explanation could be that some rebounding and splashing droplets fall on the wall.

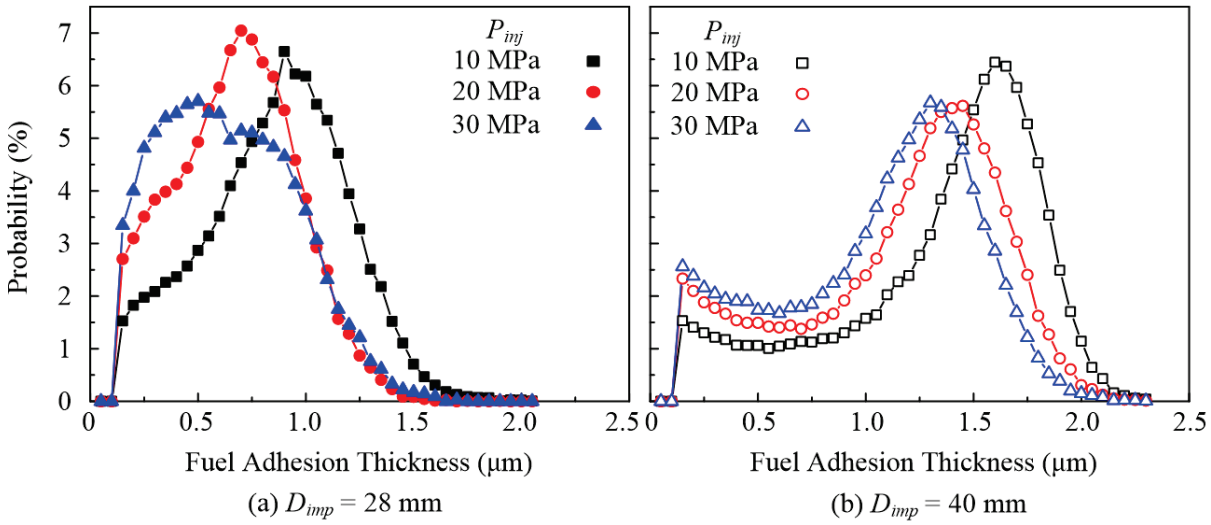

Figure 3.28 Probability of fuel adhesion thickness (40 ms ASOI)

Figure 3.28 illustrates the effects of impingement distance and injection pressure on adhesion thickness, and the average values of three shots were presented. First, the results of D_{imp} = 28 mm are examined. Only one peak value exists and the increased injection pressure causes the curve to shift to the left, leading to thinner fuel adhesion. It can be argued that high injection pressure improves the atomization and dispersion of droplets, resulting in thinner fuel adhesion, and the same conclusion can be drawn from the comparison between Figures 3.23 (a) and (b). Secondly, there are two peak values with D_{imp} = 40 mm, which indicates that an increase in impingement distance deteriorates the uniformity of adhesion thickness. The transition of "splash" to "spread" and "stick" phenomenon could be a possible explanation for this. The same observation can also be noted from the comparison of Figures 3.23 (b) and (c). It is interesting to find that the maximum thickness with D_{imp} = 40 mm is approximately 2.2 μm, and it is larger than that with D_{imp} = 28 mm. The main possible reason is that the number of splashing droplets decreases owing to low velocity at a large impingement distance.

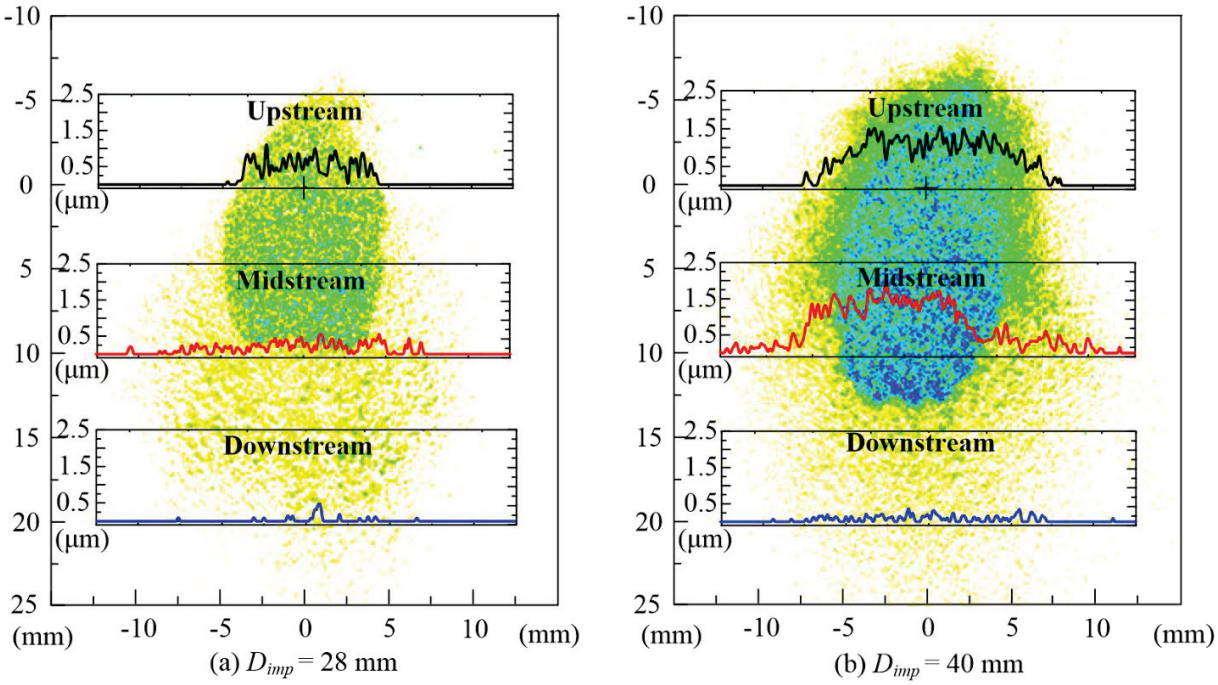

Figure 3.29 Fuel adhesion thickness distribution (40 ms ASOI)

Further investigation was carried out to clarify the effect of impingement distances on the distribution of fuel adhesion thickness (shown in Figure 3.29). The fuel adhesion was divided by y = 0, 10, and 20mm lines that represent the upstream, midstream, and downstream of the fuel adhesion. When D_{imp} = 28 mm, the fuel adhesion thickness decreases from upstream to downstream, and the uniformity of thickness improves from upstream to downstream. However, when D_{imp} = 40 mm, the fuel adhesion thickness increases from upstream to midstream, and then decreases from midstream to downstream. The changed regime of the droplets, from "splash" to "spread" with a large impingement distance is a possible explanation for that distribution pattern. Furthermore, when D_{imp} = 40 mm, the thickness uniformity on upstream is similar to that occurring on midstream, but both uniformities are worse than that located on downstream. In contrast to other impingement distances, the fuel adhesion on upstream and midstream becomes thicker with a large impingement distance, and the uniformity of thickness deteriorates with a large impingement distance. On the contrary, the fuel adhesion on downstream shows a slight change.

3.4 SUMMARY

The characteristics of the fuel spray and fuel adhesion at different pressures, wall roughnesses and impingement distances were investigated experimentally. The spray tip penetration and impinging spray height were acquired, the fuel adhesion evolution was analyzed, and the thickness distribution of fuel adhesion thickness and along different lines were discussed. The conclusion and summary are listed as follows:

1. According to the above discussion, the fuel adhesion mass and area increase with time even after the end of injection. Both ambient and injection pressure favor the atomization of spray. The ambient pressure improves the uniformity of the fuel adhesion, while the injection pressure has little effect on it.

2. The tip of fuel adhesion is shorter than the spray tip because fuel droplets splash above the wall after impingement. Fuel droplets still exist in the air above the wall even after the end of injection. An increase in wall roughness decreases the spray tip penetration and increases the impinging spray height.

3. An increase in wall roughness increases the mass, area and maximum thickness of the fuel adhesion, and it deteriorates the uniformity of the fuel adhesion. The fuel adhesion becomes slightly thicker in downstream for Ra2.5, whereas the thicker area moves upstream for Ra7.7.

4. With a large impingement distance under ambient condition, the velocity of droplets decreases significantly, resulting in more droplets adhering to the wall instead of splashing out of the wall. As a result, R_s, H_v, and H_i decrease with an increase in impingement distance. However, after impingement, owing to the stronger drag force by the ambient gas and friction from the wall, S increases with the increase in impingement distance.

5. At a large impingement distance, the lower velocity, bigger spray width, and better atomization are the main reasons for increased fuel adhesion on the wall after impingement. Under the large impingement distance condition, more fuel adheres on midstream and the thickness uniformity of fuel adhesion becomes worse. Moreover, the maximum thickness of fuel adhesion increases with a large impingement distance.

CHAPTER 4 FUEL ADEHISON FORMATION UNDER EVAPORATION CONDITIONS

4.1 EFFECT OF AMBIENT TEMPERATURE

A series of extensive studies have been conducted on fuel adhesion characteristics under non-evaporation conditions in chapter 3. However, the air temperature in a real engine during operation is quite high, especially when the engine is under high load. Until now, the formation of fuel adhesion on the wall is still ambiguous and requires more research. In order to enhance our understanding, the formation of fuel adhesion and the mechanisms behind it will be investigated under evaporation conditions in this chapter.

4.1.1 Experimental Conditions

The injector parameters and impingement conditions are listed in Table 4.1. A mini-sac injector with a nozzle hole diameter of 0.155 mm was used. The nozzle was a conventional straight-hole type without a counterbore, and the length-to-diameter (L/D) ratio was 4.2. The impingement angle was 45 deg, and the impingement distance of 22 mm from the nozzle exit to the point of impingement along the spray axis was the same as the distance near top dead center (TDC). The surface roughness of the new piston used in gasoline engine is approximately Ra (arithmetical mean deviation of the profile) of 1.0 μm, but it may increase up to Ra10.0 μm or more due to deposit accumulation [Luo et al., 2017; Maligne et al., 2011]. Therefore, the flat wall was made of quartz glass (Sigma Koki, DFSQ1-50CO2) with a surface roughness Ra7.0 μm, measured by a portable high-performance surface roughness and waviness measuring instrument (Kosaka Laboratory Ltd., SE300) with a resolution of 0.0064 μm to represent the rough surface of the piston. As shown in Figure 2.3, the impingement plate with a diameter of 50 mm and a thickness of 2 mm was placed under the injector. The point of intersection (o) of the nozzle center axis and the wall was defined as the impingement point. The direction of spray after impingement is the positive y axis, while the positive z axis is parallel to the injector, and the x axis is defined as the perpendicular direction to the yz plane, pointing out of the figure.

Table 4.1 Injector parameters and impingement conditions

Injector Parameters	
Injector Type	Mini-Sac
Hole Number	1
Hole Type	Straight-Hole without Counterbore
L/D Ratio	4.2
Nozzle Hole Diameter (mm)	0.155
Impingement Conditions	
Impingement Plate	Quartz Glass
Impingement Distance (mm)	22
Impingement Angle (°)	45
Surface Roughness (μm)	Ra 7.0

Table 4.2 Test conditions

	Non-evaporation conditions	Evaporation Conditions
Test Fuel	Toluene	
Fuel Temperature (K)	298	
Injection Mass (mg)	4	
Ambient Gas	Nitrogen	
Injection Pressure (MPa)	30	
Injection Duration (ms)	1.7	
Ambient Density (kg/m^3)	5.95	
Ambient Temperature (K)	298	433
Ambient Pressure (MPa)	0.5	0.73

The test conditions are listed in Table 4.1. Toluene was employed as a substitute for gasoline. The fuel temperature (before injection) was regulated by a cooling system to maintain it at room temperature. The injection mass was 4.0 mg with a pressure of 30 MPa and a duration of 1.7 ms. This experiment was conducted in a constant high-pressure chamber filled with nitrogen gas. Temperature was set to 298 and 433 K in order to determine the effect of ambient temperature on the experiment. Also, the ambient density was kept constant at 5.95 kg/m^3 by adjusting the ambient pressure at 0.5 and 0.73 MPa, accordingly. One thing worth noting that the saturated

temperatures (T_{sat}) at 0.5 and 0.73 MPa are 450 and 472 K, which can be seen that $T_{amb} < T_{sat}$ under both conditions.

4.1.2 Spray Impingement Characteristics

Fuel adhesion during injection has been shown in Figure 4.1, where the impingement point is denoted by the cross symbol. The spray above the impingement wall was well illuminated. It was hard to separate the fuel adhesion from the impinging spray after processing the image by RIM, which was the reason why the fuel adhesion mass and area results were shown after the end of injection (EOI) in the next section to eliminate the stray light error. Furthermore, the fuel adhesion on the wall was divided into regions I and II as shown in Figure 4.1, with more description to be provided in the following section.

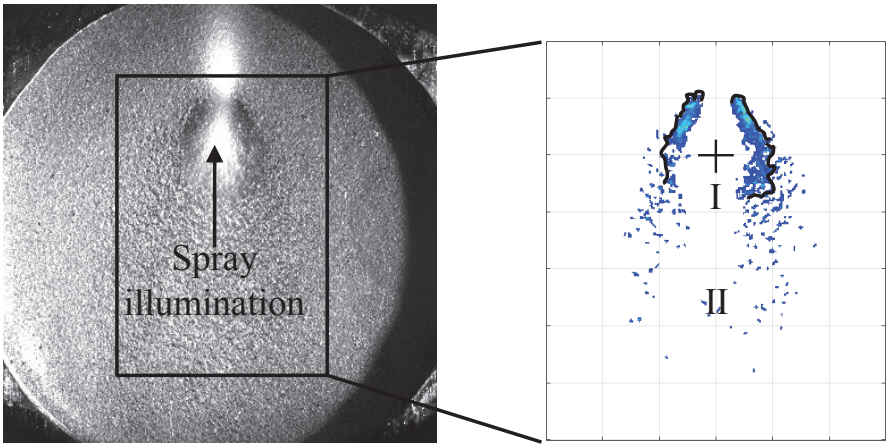

Figure 4.1 Fuel adhesion during injection duration (T_{amb} = 433 K, 1.5 ms ASOI)

4.1.2.1 Spray impingement

To discuss the spray characteristics under different ambient temperatures, the images of spray and adhered fuel at 1.5 ms and 4.0 ms after start of injection (ASOI) under T_{amb} = 298 K are presented in Figure 4.2 (a). The sprays are displayed as binary images acquired from the Mie scattering experiment, and the fuel adhesions are shown in pseudocolor images obtained from the RIM experiment. The varying adhesion thickness from 0 to 2.0 μm was represented by the pseudocolor images with the impingement point denoted by the cross symbol. During injection the fuel adhesion is invalid (left figure) due to the illumination of the droplets above the wall, as explained above. After injection (right figure), the fuel adhesion is complete and thus available.

After impingement, the impinging spray height at 4.0 ms ASOI is a little larger than that at 1.5 ms ASOI as more droplets get accumulated at the downstream. More importantly, the fuel adhesion at impingement region (region I) has greater thickness than that at the other region (region II) and the thickness decreases along *y* axis, although some thick adhesion can be seen in region II. This is due to different mechanisms in the formation of fuel adhesion, which will be explained in more detail in the following section.

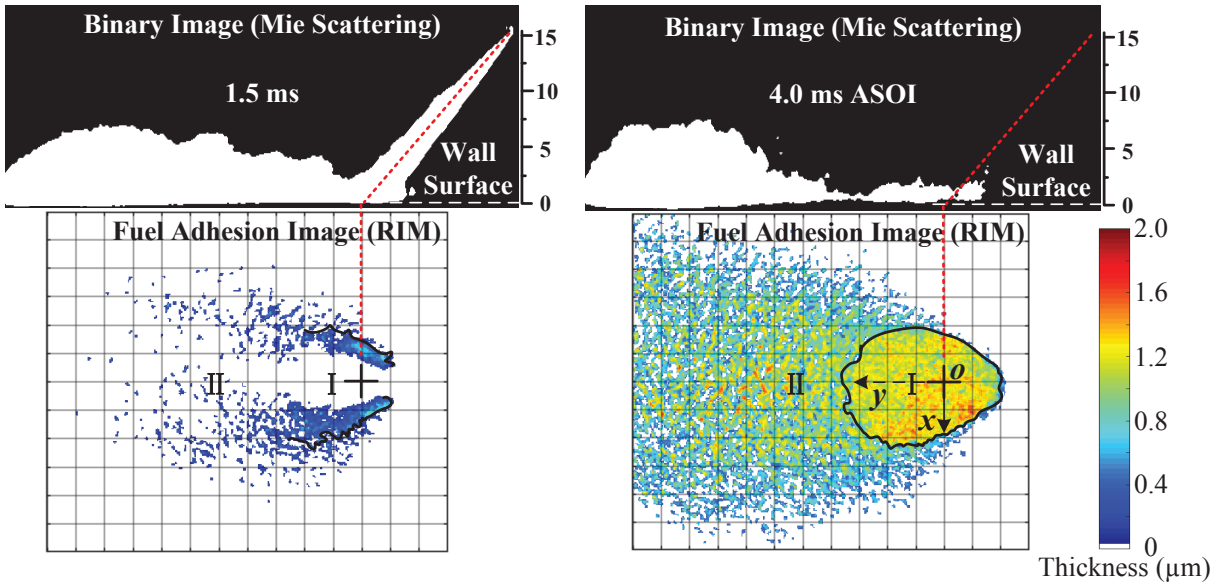

(a) T_{amb}=298 K

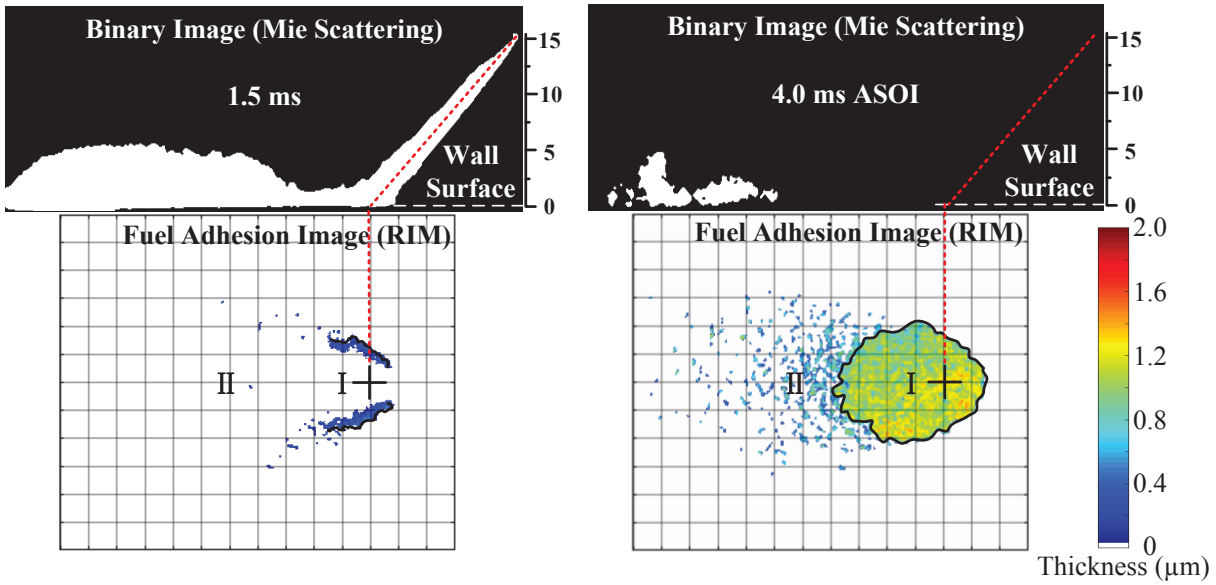

(b) T_{amb}=433 K

Figure 4.2 Spray impingement and fuel adhesion during and after injection

The images of spray and adhered fuel at 1.5 ms and 4.0 ms after start of injection (ASOI) under T_{amb} = 433 K can be seen in Figure 4.2 (b). Under condition of high ambient temperature, the impinging spray height is shorter than that under T_{amb} = 298 K, owing to the evaporation of fuel droplets. This phenomenon is more obvious after injection (at 4.0 ms AOSI). Moreover, the spray area is smaller in contrast to that observed under T_{amb} = 298 K, which can be also explained by the evaporation of droplets during spray. In this case, the fuel adhesion area is smaller when compared to that in Figure 4.2 (a). The possible reasons for it may be summarized as follows: during spray, some droplets evaporate before impingement; and even when some fuel adheres on the wall, it evaporates rapidly under high ambient temperature. By comparing Figure 4.2 (a) and (b), it is evident that evaporation is more significant at the periphery of the fuel adhesion than that observed in region I.

4.1.2.2 Spray tip penetration and impinging spray height

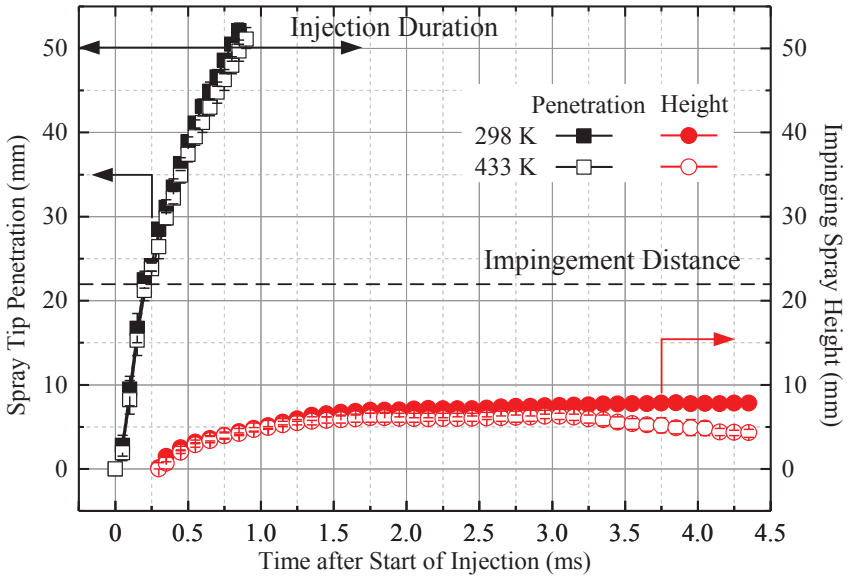

Figure 4.3 Spray tip penetration and impinging spray height

The spray tip penetration S and impinging spray height H_i can be seen in Figure 4.3. The horizontal axis represents time after start of fuel injection, with the left vertical axis being S, and the right vertical axis being H_i. The results under T_{amb} = 298 K and 433 K are plotted using solid and open data. The broken line represents the impingement distance. It can be seen that at the start of injection, S under T_{amb} = 433 K is shorter than that under T_{amb} = 298 K. The evaporation of the atomized droplets is believed to be responsible for this. Furthermore, this tendency

increases slightly after impingement, which can be attributed to the fact that impingement contributes towards the breakup and atomization of droplets (Pei et al., 2017; Luo et al., 2018). Since smaller droplets evaporate under T_{amb} = 433 K, H_i under T_{amb} = 433 K is always shorter than that under T_{amb} = 298 K. It is interesting to find that after EOI, a large difference can be observed between different temperatures. Even after EOI, the incoming fuel droplets are still observed above the wall after impingement as seen in the binary images shown in Figures 4.2. However, under T_{amb} = 433 K, the incoming droplets are not sufficient owing to the evaporation of droplets during propagation. Additionally, the droplets above the wall evaporate quickly. The same conclusion can also be obtained by comparing the images between Figures 4.2 (a) and (b).

4.1.3 Fuel Adhesion Characteristics

4.1.3.1 Evolution of Fuel Adhesion

To illustrate the effect of air temperature on the evolution of fuel adhesion, graphs showing the same at 3, 5, 10, 20, 30 and 50 ms ASOI are arranged in Figure 4.4. The cross symbol represents the impingement point, and the pseudocolor represents the fuel adhesion thickness varying from 0 to 2.0 μm.

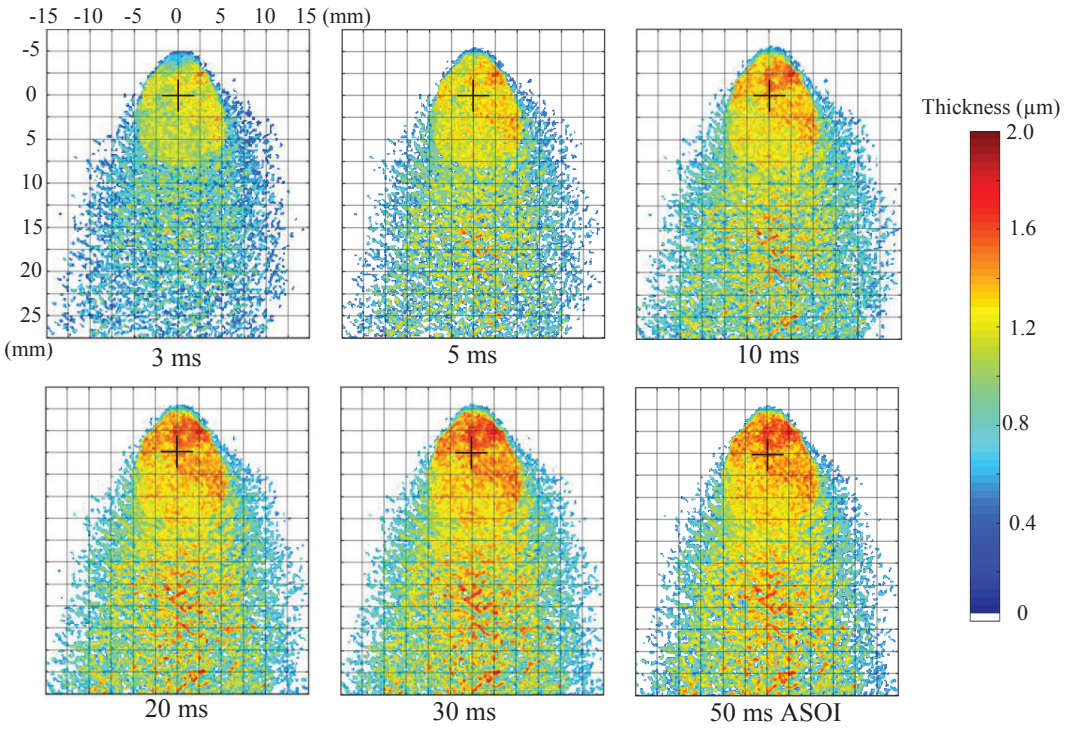

(a) T_{amb} = 298 K

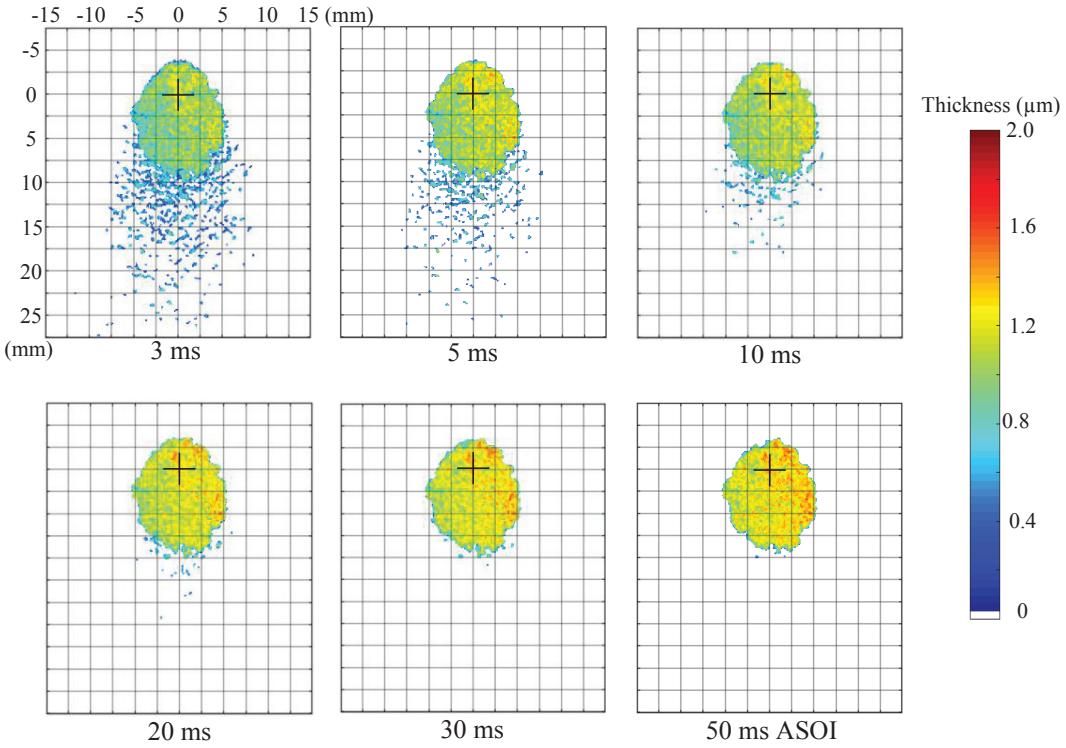

(b) T_{amb} = 433 K

Figure 4.4 Evolution of fuel adhesion on the wall

In Figure 4.4 (a), all the given situations at different times show a similar fuel adhesion structure, except for the thickness. A larger volume of fuel accumulates in the impingement region when compared to the bottom. It is worth noting that the thickness of the fuel adhesion increases with time in both regions due to the secondary breakup of fuel droplets re-deposited on the wall (Luo et al., 2017). Additionally, the adhesion is observed to be much thinner in the periphery of the adhesion. Compared with Figure 4.4 (b), it is evident that the high air temperature accelerates the evaporation of fuel adhesion, resulting in less fuel being depositing on the wall. At the bottom, the fuel adhesion is discontinuous and quite thin. With time, the thin fuel adhesion at the periphery evaporates fast and only the fuel in the impingement region is left on the wall. Hence, it can be concluded that the evaporation of fuel impinged on the wall occurs from the region of low adhesion thickness to high adhesion thickness because of the strong heat transfer (Maligne et al., 2011). Another observation that should be noted is that under temperature of 433 K, the fuel adhesion becomes thicker with time only in the region of impingement region, which is different from condition of 298 K. Additionally, the fuel adhesion

remaining on the wall at 50 ms ASOI is similar to the adhesion above 1 μm at 3, 5, 10, 20 and 30 ms ASOI on the wall. These phenomena will be discussed in detail in the next section on the mechanism of fuel adhesion of. On comparing Figure 4.2 (a) with (b), it can be observed that the uniformity of adhesion thickness at 433 K is much better than that at 298 K, particularly when the comparison is made at 50 ms ASOI recording time. This can also be due to the evaporation of thin fuel adhesion under 433 K.

4.1.3.2 Fuel adhesion mass and area

Figure 4.5 shows the fuel adhesion mass and area, with time after start of injection as the horizontal axis is, fuel adhesion mass and area as the left vertical axis and right vertical axes, respectively. The results under T_{amb} = 298 K and 433 K are plotted using solid and open data.

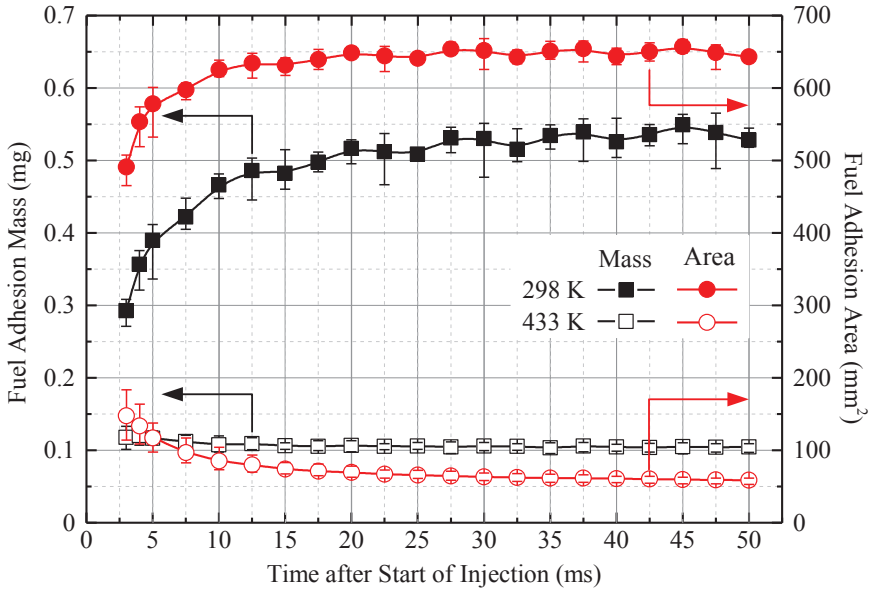

Figure 4.5 Fuel adhesion mass and area on the wall

It reveals that under T_{amb} = 298 K, the fuel adhesion area initially increases with time (from 0 to 20 ms ASOI) owing to some splashing droplets deposited on the periphery of the adhesion. However, then the fuel adhesion area remains almost constant (from 20 to 50 ms ASOI). This is due to the droplets being re-deposited on the original region, thus leading to only an increase in mass but not area. The same observation can also be derived from Figure 4.4 (a). Under T_{amb} = 433 K, the area of fuel adhesion initially decreases sharply with time (from 0 to 20 ms ASOI) and then decreases only slightly (from 20 to 50 ms ASOI). This suggests that the fuel adhesion

evaporates from the thin region (at the bottom), leading to sharp decrease. Nevertheless, from 20 to 50 ms ASOI, only the thick adhesion is left behind.

The fuel adhesion mass increase slightly (from 20 to 50 ms ASOI) under T_{amb} = 298 K as there are still some droplets falling to the wall. But it keeps constant (from 20 to 50 ms ASOI) under T_{amb} = 433 K, owing to the competition between the re-depositing droplets and evaporation of the fuel adhesion on the wall.

4.1.3.3 Fuel adhesion thickness

Figure 4.6 shows the average and maximum thickness of fuel adhesion on the wall. Time after start of injection is the horizontal, and the vertical axis is the thickness of fuel adhesion. The results under T_{amb} = 298 K and 433 K are plotted using solid and open data. Both average and maximum thickness are seen to increase with time, and the maximum thickness is larger than the average thickness under the same conditions. An interesting observation is that the average thickness under T_{amb} = 298 K is smaller than that under T_{amb} = 433 K. One possible explanation for this could be that the fuel on the wall evaporates under T_{amb} = 433 K, and the decrease in the ratio of fuel adhesion area is faster than that of decrease in fuel adhesion mass. The same conclusion can also be drawn from the graphs at 50 ms ASOI in Figure 4.4: under T_{amb} = 298 K, even though the maximum thickness increases to 2.0 μm, there is much thinner fuel adhesion than 0.8 μm; under T_{amb} = 433 K, almost all fuel adhesion thickness is larger than 1.0 μm.

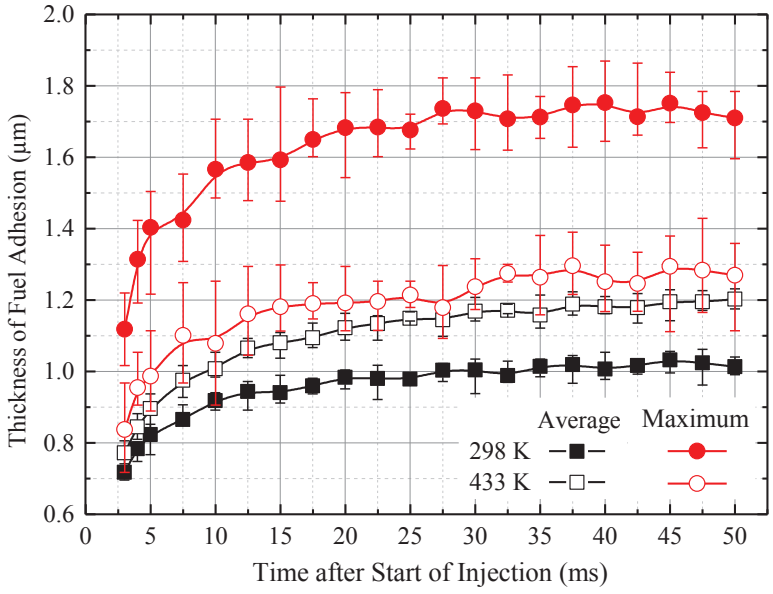

Figure 4.6 Average and maximum thickness of fuel adhesion on the wall

The mass of the adhesion thickness was determined via further study. As shown in Figure 4.7, the horizontal axis is the fuel adhesion thickness and the vertical axis is fuel adhesion mass. The adhesion mass is based on the value of each pixel as shown in the equation below:

$$M(h) = \sum_{i=0}^{\infty} h(i) \tag{4.1}$$

where the sum of fuel adhesion mass in the thickness fraction between $h \pm 0.5\Delta h$ and h is defined as $M(h)$, and Δh is 0.05 μm.

Figure 4.7 describes the fuel adhesion mass varying with thickness at different times, and the results under T_{amb} = 298 K and 433 K plotted using solid and open data. It was reported that the peak value of the curve increases and moves to the right due to the re-depositing droplets. These tendencies are similar under different temperatures, although some differences in shapes are observed. Under T_{amb} = 433 K, the mass of the fuel adhesion at thickness from 0.05–0.8 μm is almost 0 when compared to that under T_{amb} = 298 K. It has also been demonstrated that air with high temperature contributes more towards evaporation of thin fuel adhesion and promotes a more uniform thickness of fuel adhesion, thus resulting in a narrow shape at 433 K, which agrees well with the results in Figure 4.4 (b).

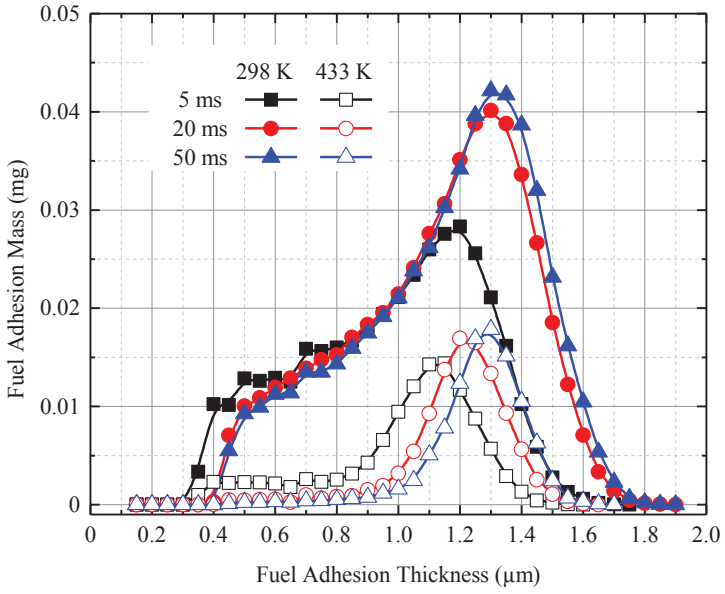

Figure 4.7 Fuel adhesion mass for different thicknesses

This section seeks to clarify the effect of high ambient temperature on the thickness of fuel adhesion along different lines, which were well defined to express them concisely. As shown in Figure 4.8, the coordinate system is established and the origin *o* is defined as the impingement point. As the fuel adhesion is almost symmetric along the *x* axis, its distribution has only been discussed along different *y* lines. The fuel adhesion was divided using $y = -2.5$, 2.5, 7.5, and 12.5 mm at the vertical axis, and the thickness along these lines was defined as $H_{-2.5}$, $H_{2.5}$, $H_{7.5}$, and $H_{12.5}$, respectively. The values of $H_{-2.5}$, $H_{2.5}$, $H_{7.5}$, and $H_{12.5}$ at 5 and 50 ms ASOI under T_{amb} = 298 K and 433 K are depicted in Figure 4.9, respectively. The horizontal axis is from −15 to 15 mm, and the vertical axis denotes fuel adhesion thickness.

The results at 5 ms ASOI are shown in Figure 4.9 (a). The thickness under T_{amb} = 298 K is larger than that under T_{amb} = 433 K due to non-evaporation. In all cases, thickness initially increases, then remains constant, and finally decreases, with the exception of $H_{12.5}$, where it is discontinuous and variable. At the constant value stage, $H_{-2.5}$ and $H_{2.5}$ at 298 K are almost the same as those at 433 K, but $H_{7.5}$ at 298 K is slightly larger than that at 433 K. It is particularly significant that the constant value stages of both 298 K and 433 K are similar, which is defined as region I and the downstream part whose value is variable is defined as region II. The boundary between regions I and II is drawn by detecting the constant value in thickness using our in-house code in the MATLAB software, and the results are shown in Figure 4.8 (a), from which it can be observed that the region I of 298 K is quite similar to that of 433 K, which agrees well with the observation in Figure 4.4 (a).

A similar result was observed in Figure 4.9 (b) regardless of the behavior of $H_{-2.5}$, because at 50 ms ASOI, $H_{-2.5}$ at 433 K evaporates for a quite long time, resulting in its sharp reduction. The regions I and II are shown in Figure 4.8 (b) after applying the same criterion to them. It must also be noted that region I is similar at 5 ms and 50 ms ASOI as well, and the same observation can be seen in Figure 4.4 (b).

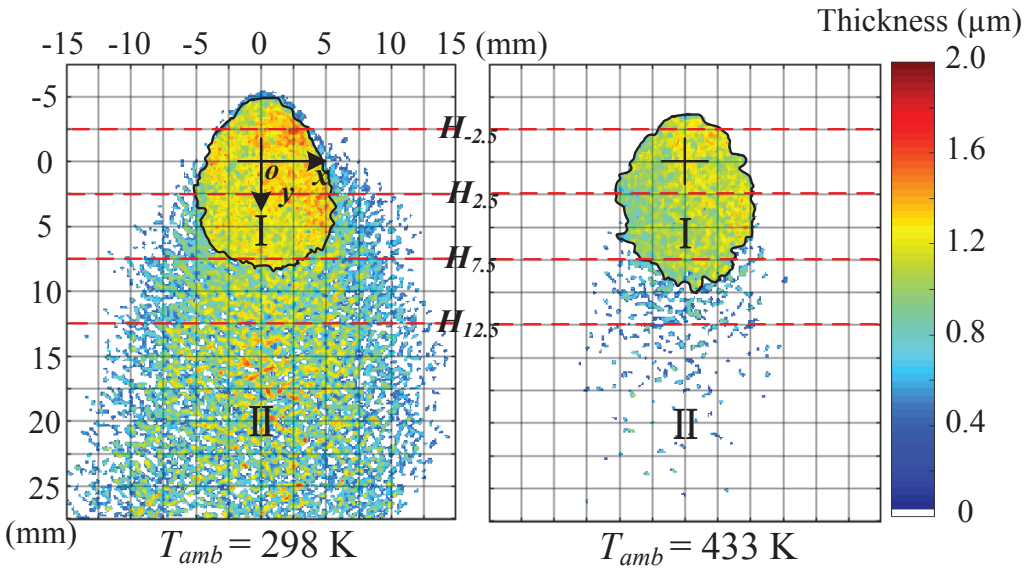

(a) 5 ms ASOI

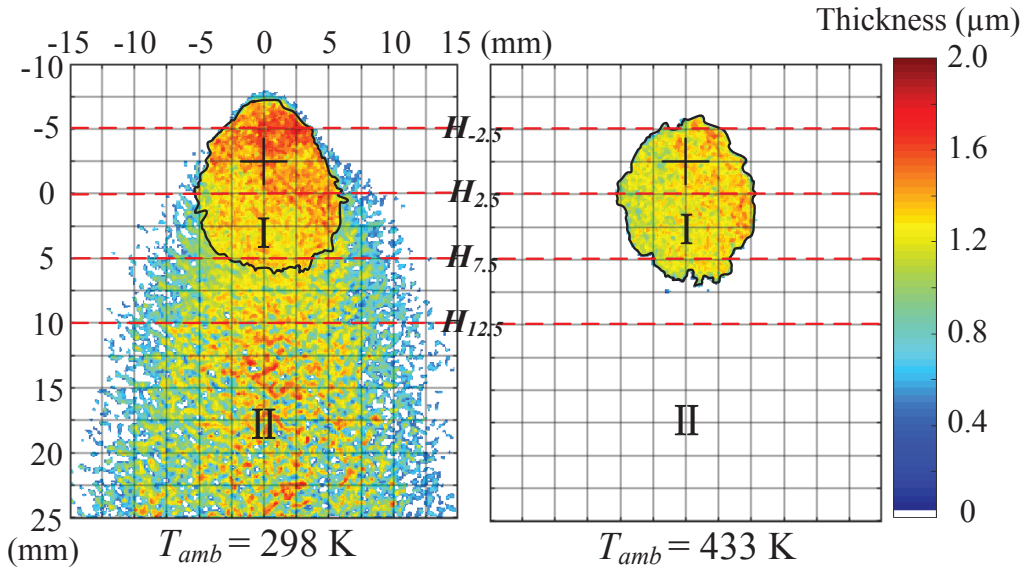

(b) 50 ms ASOI

Figure 4.8 Fuel adhesion under different ambient temperatures

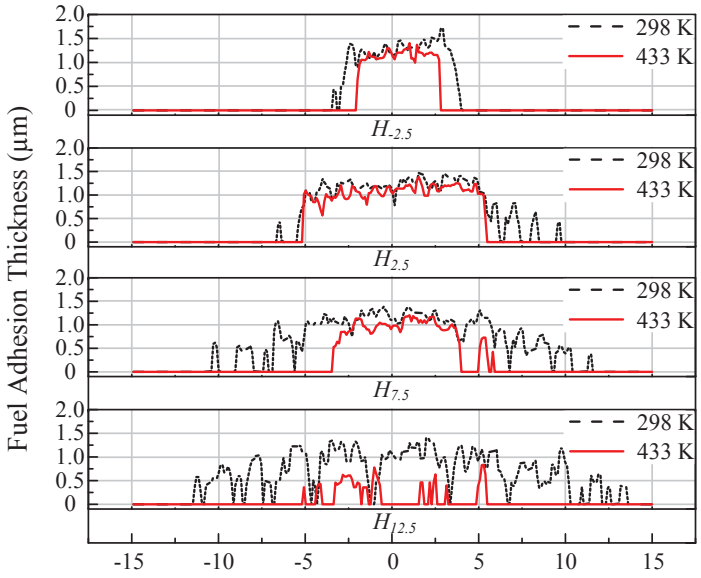

(a) 5 ms ASOI

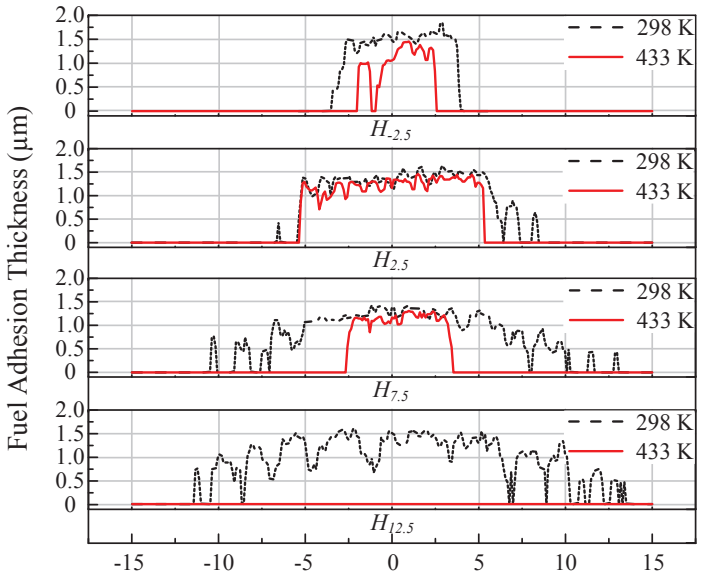

(b) 50 ms ASOI

Figure 4.9 Fuel adhesion thickness along different lines

In order to check the fuel adhesion mass in region I, the variation of mass with thickness at different times is shown in Figure 4.10. The plotted curves of 433 K appear to move to the left when compared to those of 298 K due to evaporation, while maintaining similar shapes, which also demonstrates the same mechanism in formation. Moreover, the curve shifts to the right with

time as some droplets are re-deposited on the wall, and the same observation can also be seen in Figure 4.7.

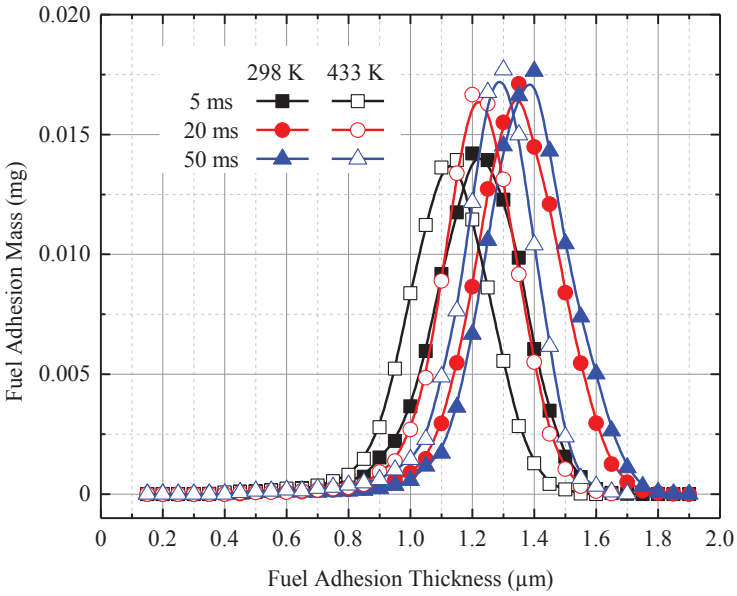

Figure 4.10 Fuel adhesion mass for different thicknesses in region I

In summary, as mentioned above, the fuel adhesion on the wall can be divided into regions I and II in order to study the different mechanisms of fuel adhesion formation as shown in Figure 4.11.

Region I: Primary impingement region. The direct spray impinges on the wall, causing some fuel to stick to it to form the adhesion.

Region II: Secondary impingement region. After impingement on the wall, most of the fuel splashes off it. The splashing droplets are re-deposited on the wall because of coalescence and air force to form the adhesion.

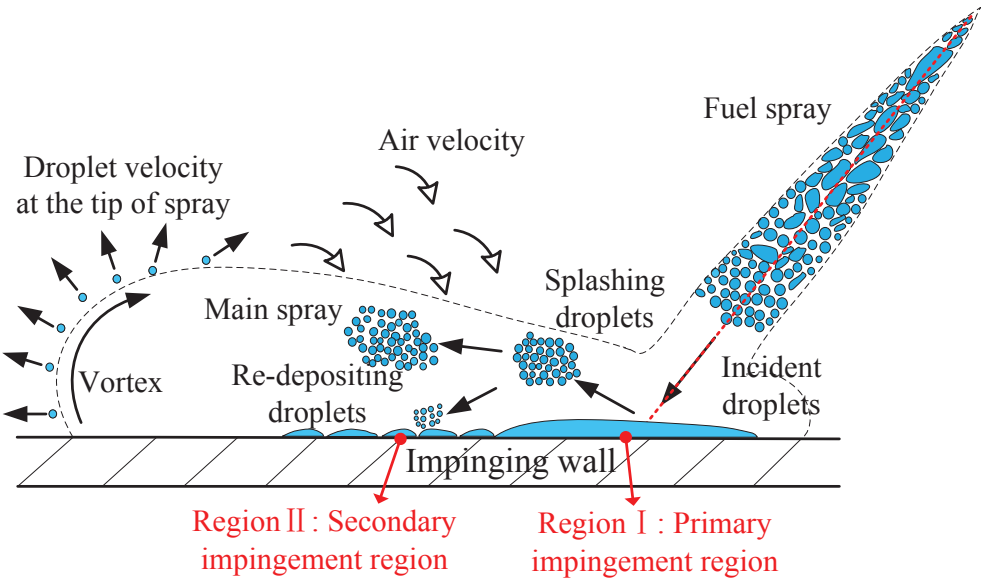

(a) During injection

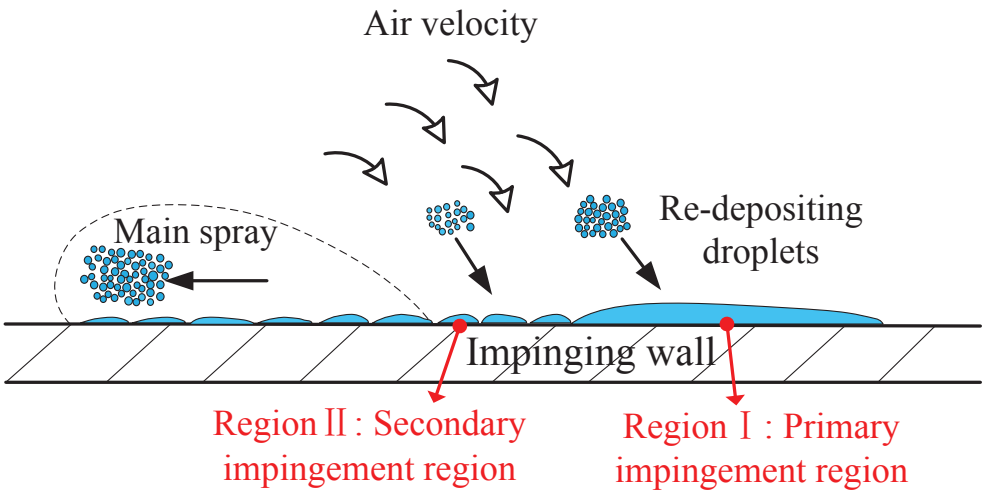

(b) After injection

Figure 4.11 Mechanisms of fuel adhesion formation in different regions

During injection: When the fuel is injected out of the nozzle, it breaks up into ligaments and large droplets. Through the fuel flow along the spray axis, the ligaments and large droplets break up into small ones due to the interaction between the liquid fuel and air. Under T_{amb} = 298 K, after initial impingement on the wall, some of the fuel on the wall forms region I and other fuel droplets splash off the wall. Nevertheless, the splashing droplets may collide and coalesce with others, resulting in a change in velocity and leading to it being re-deposited on the wall to form region II, which agrees with the observations made in Figure 4.2 (a). However, under high temperature condition, the fuel in region II is less owing not only to the decrease in impinging droplets but also the evaporation of the adhered fuel. The same phenomena can be seen in Figs. 4.1 and 4.2 (b).

After injection: Although there is no fuel injected out of the nozzle, some fuel droplets are still in the air or above the wall. Under T_{amb} = 298 K, as the spray moves along the wall, the air velocity changes. Then the air pushes the splashing droplets to re-deposit in regions I and II, which agrees well with the observations in Figure 4.4 (a). However, under T_{amb} = 433 K, the splashed droplets evaporate fast, resulting in few droplets re-depositing in region II. However, as region I is formed via direct spray impingement, it is affected less by the high ambient temperature, with only the periphery adhesion evaporating, resulting in fuel adhesion in region I being almost the same as that under room temperature. The same phenomena can be observed in Figs. 4.2 (b) and 4.4 (b).

As summarized above, the fuel adhesion in region I is formed by the direct spray and it shows little change under different ambient temperature conditions. While the fuel adhesion in region II is formed by the re- depositing droplets, and it is sensitive to the ambient temperature because some splashing droplets evaporate before re-depositing on the wall and some can even re-deposit on the wall to form adhesion, ultimately it evaporates more easily owing to the strong heat transfer. These are the reasons why the fuel adhesion in region I under temperatures of T_{amb} = 298 K and 433 K is similar, but varies greatly in region II, as shown in Figure 4.8.

4.2 EFFECT OF NOZZLE HOLE DIAMETER

Some investigations have been conducted into the spray characteristics resulting different hole diameters. The effect on the spray tip penetration, spray cone angle and spray volume were checked by many researchers. However, the effect of nozzle hole diameter on the fuel adhesion has been seldom reported. In this part, the adhered fuel is tested by different injectors of hole diameter under both non-evaporation and evaporation conditions. Experiments were performed in a constant high-pressure chamber. Specifically, all the results were time-resolved to better understand the impinging spray of a gasoline engine.

4.2.1 Experimental Conditions

In order to investigate the effect of nozzle hole diameter on fuel adhesion. Two types of injector (D13 and D15) were tested, as shown in Figure 4.12. The detailed parameters are listed in Table 4.3. Two mini-sac injectors with a nozzle hole diameter of 0.135 and 0.155 mm were used. The nozzle was a conventional straight-hole type without a counterbore, and the nozzle hole length was kept the same value at 0.65 mm, resulting that the different the length-to-diameter (L/D) ratios are 4.8 and 4.2. The impingement angle was 45° and the impingement distance from the nozzle exit to the point of impingement at the flat wall along the spray axis was 22 mm. The flat wall was made of quartz glass (Sigma Koki, DFSQ1-50CO2) with a surface roughness Ra (arithmetical mean deviation of the profile) of 7.0 μm, measured using a portable high-performance surface roughness and waviness measuring instrument (Kosaka Laboratory Ltd., SE300) with a resolution of 0.0064 μm.

The test conditions are listed in Table 4.4. Toluene was employed as a substitute for gasoline. The fuel temperature (before injection) was regulated by a cooling system to maintain it at room temperature. The injection mass by different injectors were 3.0 and 4.0 mg with a pressure of 20 MPa and durations of 1.65 and 2.1 ms, respectively. This experiment was conducted in a constant high-pressure chamber filled with nitrogen gas. Temperature was set to 298 and 433 K in order to determine the effect of ambient temperature on the experiment. Also, the ambient density was kept constant at 5.95 kg/m^3 by adjusting the ambient pressure at 0.5 and 0.73 MPa, accordingly. One thing worth noting that the saturated temperatures (T_{sat}) at 0.5 and 0.74 MPa are 450 and 472 K, which can be seen that $T_{amb} < T_{sat}$ under both conditions.

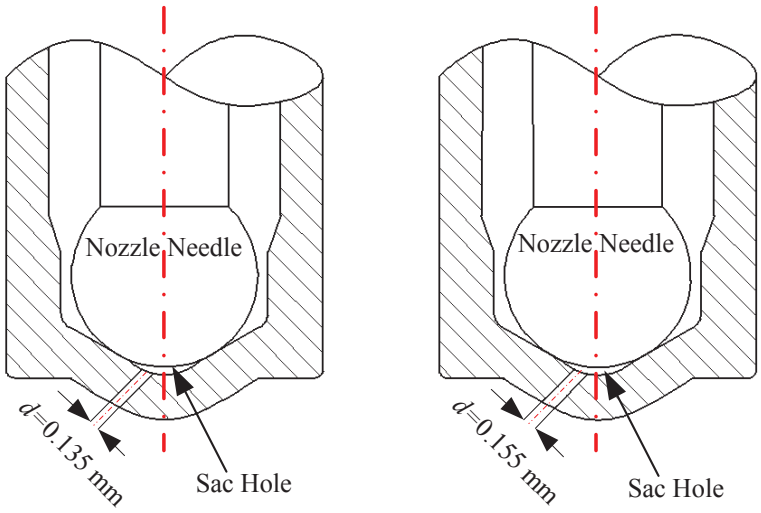

(a) D_{13} (b) D_{15}

Figure 4.12 Specification of the injectors with different nozzle hole diameters

Table 4.3 Injector parameters and impingement conditions

Injector Parameters		
Injector Type	Mini-Sac	
Hole Number	1	
Hole Type	Straight-Hole without Counterbore	
Nozzle Hole Length (mm)	0.65	
L/D Ratio	4.8	4.2
Nozzle Hole Diameter (mm)	0.135	0.155
Impingement Conditions		
Impingement Plate	Quartz Glass	
Impingement Distance (mm)	22	
Impingement Angle (°)	45	
Surface Roughness (μm)	Ra 7.0	

Table 4.4 Injection and ambient conditions

Injection Conditions		
Test Fuel	Toluene	
Fuel Temperature (K)	293	
Injection Pressure (MPa)	20	
Injection Mass (mg)	3	4
Injection Duration (ms)	1.65	2.1
Ambient Conditions		
	Non-evaporation conditions	Evaporation Conditions
Ambient Gas	Nitrogen	
Ambient Density (kg/m^3)	5.95	
Ambient Temperature (K)	298	433
Ambient Pressure (MPa)	0.5	0.74

4.2.2 Fuel Adhesion Characteristics

Figure 4.13 shows the evolution of the adhered fuel of different injectors under non-evaporation condition. The fuel adhesions on the wall at 5, 20, and 50 ms ASOI are shown. The pseudocolor represents the adhered fuel thickness, varying from 0 to 2.0 μm, and the impingement point is shown by the cross symbol. Under each condition, all cases at different times show similar structures, and the fuel adhesion areas are almost symmetric. It is evident that the fuel adhesion is formed at 5 ms, although some differences can be observed at 20 and 50 ms: due to the re-deposition droplets on the wall, the wet area and thickness increase with time. It is interesting to find that the adhesion area of D15 is larger than that of D13. Two reasons should be responsible for this. One is that the injection mass of D15 is larger. Another is that both Zhang et al. (2017) and Algayyim et al. (2018) reported the spray angle increase at the increased hole diameter of nozzle, which leads to the larger fuel adhesion on the wall after impingement. More importantly, the thickness of fuel adhesion on the wall of D13 is around 1.0 μm, which is smaller than that of D15. As we known, the small hole favors the atomization of spray, at a result, the droplet

diameter decreases with small hole diameter. Then the *Re* decreases and *Oh* increases, thus, after impingement on the wall, some droplets may change their behavior from "deposition" to "splashing", resulting in thinner fuel adhesion of D13. Moreover, the fuel adhesion after 5 ms AOSI of D13 changes less compared to that of D15, and the better atomization may be one possible reason for this.

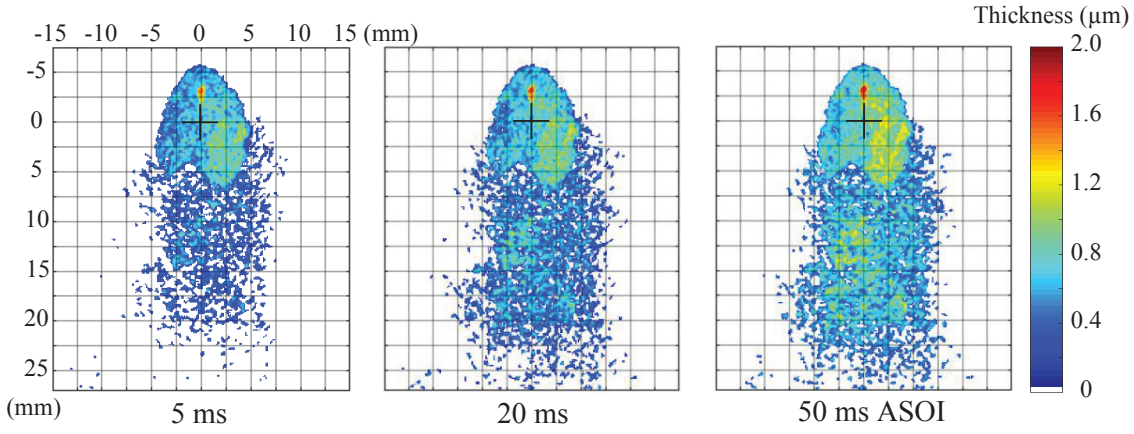

(a) D13

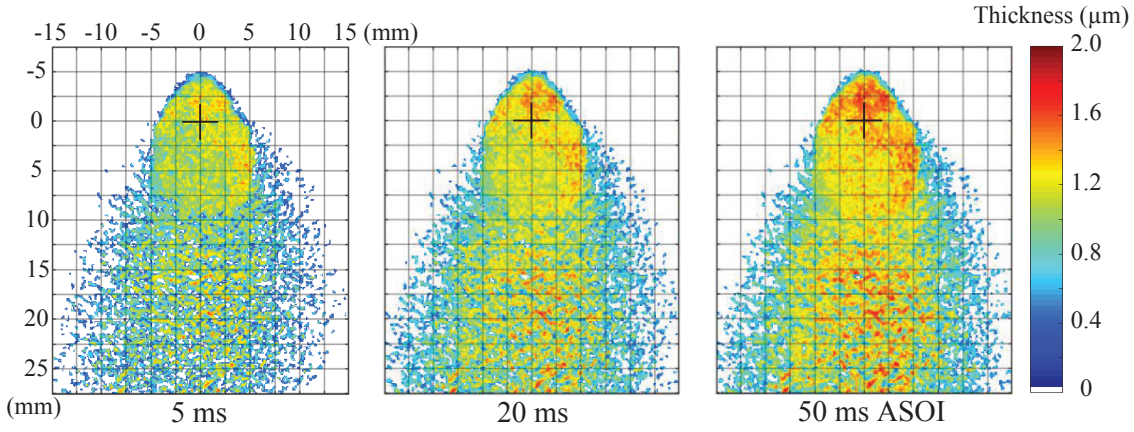

(b) D15

Figure 4.13 Fuel adhesion evolution on the wall injected by the injectors with different nozzle hole diameters (T_{amb} = 298 K)

Figure 4.14 illustrates the evolution of the adhered fuel of different injectors under evaporation condition. The fuel adhesions on the wall at 5, 20, and 50 ms ASOI are shown. The pseudocolor represents the adhered fuel thickness, varying from 0 to 2.0 μm, and the impingement point is shown by the cross symbol. Compared to Figure 4.13, fuel adhesion at all cases become smaller due the droplets evaporation. Owing to the better atomization of D13, the

SMD decreases, which promotes the atomization of liquid phase spray and enhances the resistance of the liquid phase spray penetration, leading to shorter liquid fuel spray penetration, resulting that the adhesion decreases more sharply. Under evaporation condition, small droplets evaporate fast during spray propagation before impingement, leading to shorter liquid phase spray penetration, which agrees well with the observation of Du et al., 2017. It should be noted that the thick fuel region moves from upstream to downstream in contrast to non-evaporation condition. This is attributed to the droplets evaporation before impingement. Furthermore, the fuel adhesion evaporates from the thin part to the thick one, which has been discussed in detail in part 4.1.

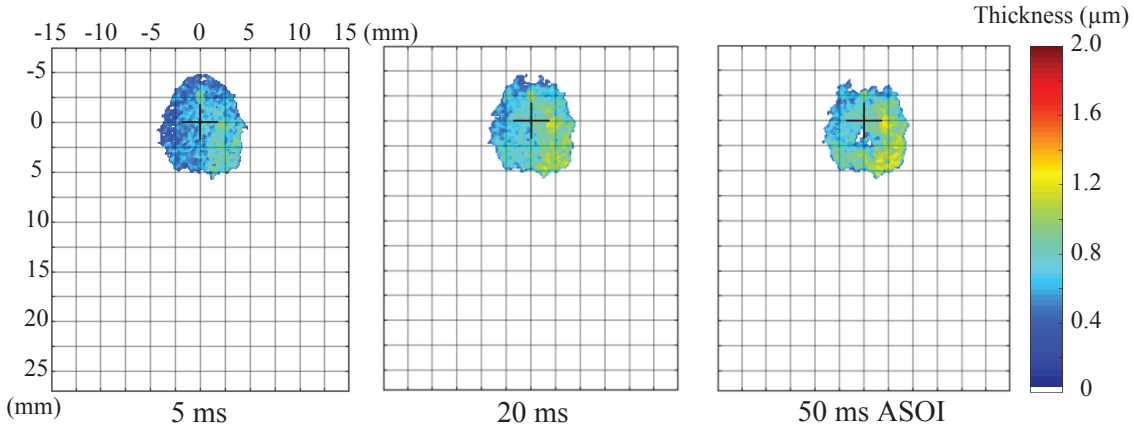

(a) D13

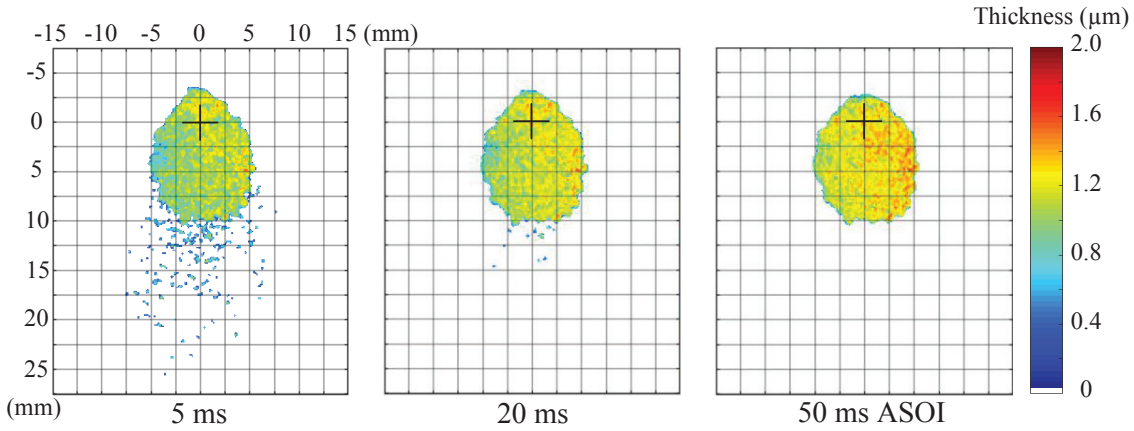

(b) D15

Figure 4.14 Fuel adhesion evolution on the wall injected by the injectors with different nozzle hole diameters (T_{amb} = 433 K)

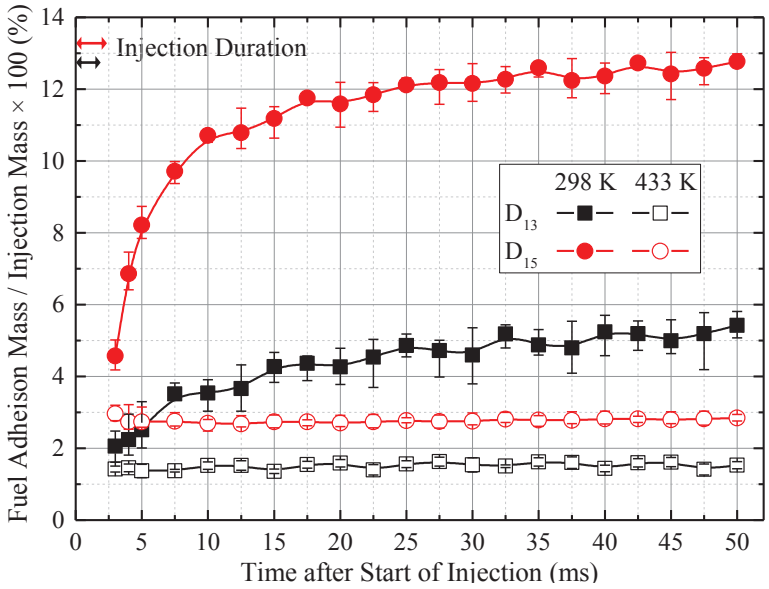

Figure 4.15 Fuel adhesion ratio under different conditions

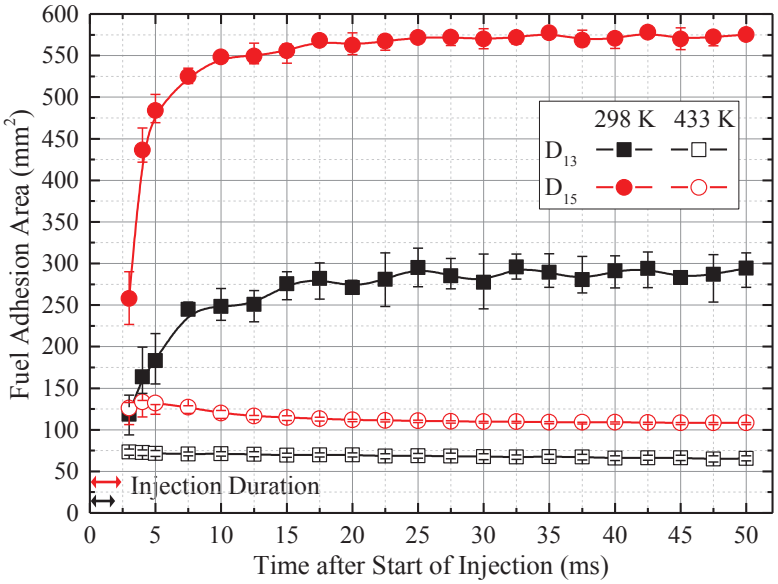

Figure 4.16 Fuel adhesion area under different conditions

The fuel adhesion mass ratios are depicted in Figures 4.15. The adhesion mass ratio is defined as the ratio of adhesion mass to total injection mass. The mass ratio increases with time even after the end of injection because there are still some droplets dropping on the wall. An increase in hole diameter under both non-evaporation and evaporation conditions increases the fuel adhesion mass ratio owing to poor atomization. Moreover, Du et al. [2018] reported that the liquid penetration of the spray by small hole diameter is shorted under both non-evaporation and

evaporation conditions, resulting in less fuel adhering on the wall, which should be another reason for the less ratio of D13. Furthermore, the adhesion mass ratio under 298 K increases significantly from 5 to 15 ms ASOI compared to that under 433 K. The re-depositing droplets on the wall tends to be responsible, which agrees well with the observation results in Figure 4.13. And from 15 to 50 ms ASOI, the fuel mass under 298 K increases slightly due to the re-deposition, however, it keeps almost constant under 433 K owing to the competition between re-deposition and fuel evaporation.

The fuel adhesion areas are depicted in Figures 4.16. The adhesion area increases with time even after the end of injection under 298 K because there are still some droplets dropping on the wall. An increase in hole diameter under both non-evaporation and evaporation conditions increases the fuel adhesion area owing to poor atomization. The same tendency can also be observed in the comparison between Figures 4.13 and 4.14. Furthermore, the adhesion area decreases slightly under 433 K owing to the evaporation.

Figure 4.17 shows the maximum thickness of fuel adhesion on the wall. Time after start of injection is the horizontal, and the vertical axis is the thickness of fuel adhesion. The results under 298 K and 433 K are plotted using solid and open data. The maximum thickness is seen to increase with time, and the results of 298 K is larger than that under 433 K. The fuel evaporation should be responsible for this. It should be noted that the maximum thickness of D13 is smaller than that of D15 due to the better atomization, and the same conclusion can be found in Figure 4.13 and 4.14.

Figure 4.18 shows the average thickness of fuel adhesion on the wall. Time after start of injection is the horizontal, and the vertical axis is the thickness of fuel adhesion. The results under 298 K and 433 K are plotted using solid and open data. An interesting thing is that the average thickness under 298 K is smaller than that under 433 K. One possible explanation for this could be that the fuel on the wall evaporates under 433 K, and the decrease in the ratio of fuel adhesion area is faster than that of decrease in fuel adhesion mass. And the average thickness of D13 is smaller than that of D15 due to the better atomization.

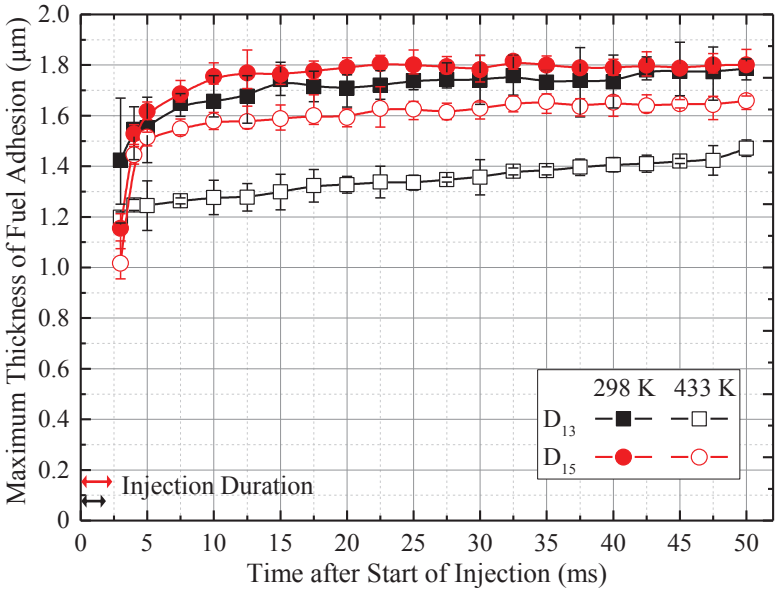

Figure 4.17 Maximum Thickness of Fuel adhesion under different conditions

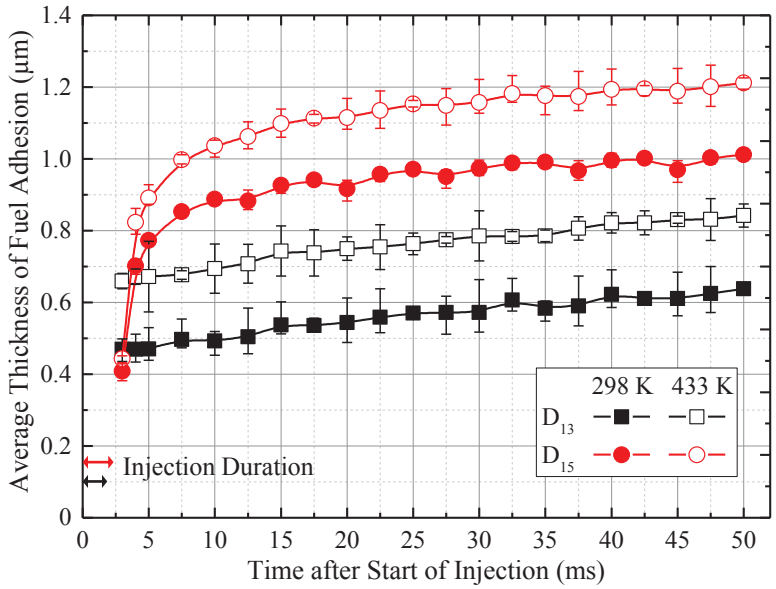

Figure 4.18 Average Thickness of Fuel adhesion under different conditions

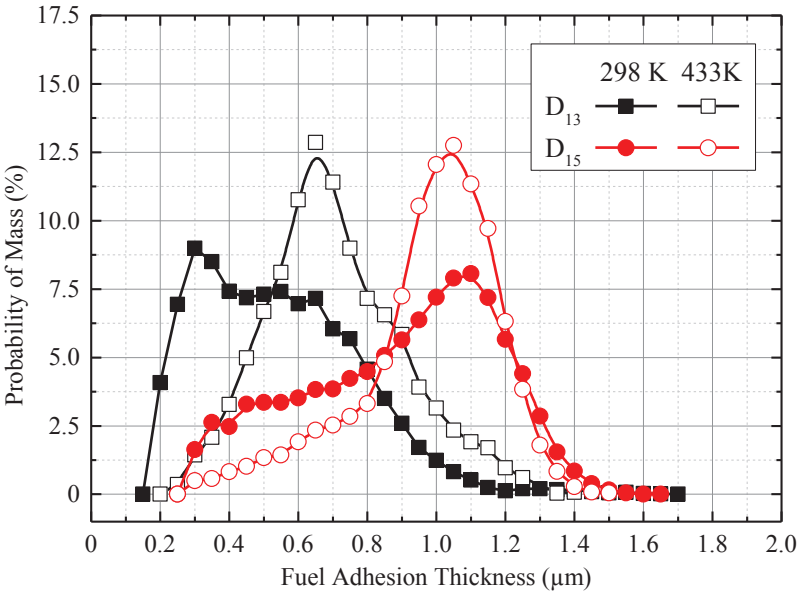

(a) 5 ms ASOI

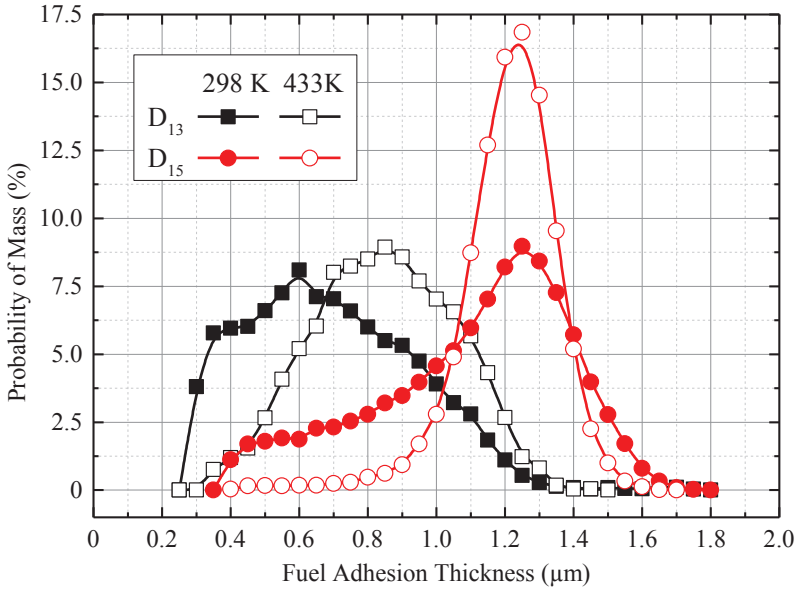

(b) 50 ms ASOI

Figure 4.19 Probability of mass along thickness

To further investigate the adhesion thickness, the probability of thickness was determined. As shown in Figure 4.19, the horizontal axis is the fuel adhesion thickness, and the vertical axis is the probability of mass. The probability of mass is based on the value of each pixel, and the probability must satisfy the normalization conditions as equation (4.1)

Figure 4.19 (a) describes the probability of fuel adhesion mass varying with thickness at 5 ms, and the results under 298 K and 433 K plotted using solid and open data. It reveals that the peak value of the curve increases by increased the ambient temperature. It has been demonstrated that air with high temperature contributes more towards evaporation of thin fuel adhesion, resulting in peak value increasing. Moreover, the curve become a little narrow compared to that under 298 K, indicating that the uniformity of the fuel adhesion is improved. Furthermore, it is clear that the curve of D15 move to right compared to D13. The poor atomization and more fuel adhesion on the wall should be responsible for it. For the probabilities at 50 ms ASOI in Figure 4.19 (b), the curves under 298 K move to right, because that some re-depositing droplets on the wall to increase the adhesion thickness, which agrees well with the results in Figure 4.13 and 4.17. However, under 433 K, owing to the evaporation, the curves become narrow, and peak values increase, leading to better adhesion uniformity.

Further investigation was conducted to clarify the effect of hole diameter on fuel adhesion thickness along different lines. In Figure 4.20, the coordinate system is defined, and the origin *o* is determined as the impingement point. The positive *y* axis is along the direction of fuel splash after impingement, and positive *x* axis is perpendicular to the *y* axis, pointing to the left. Because fuel adhesion is almost symmetric about $x = 0$ axis, we divided fuel film by $y = 0$, 5 and 10mm lines that represent the upstream, midstream, and downstream of the fuel adhesion.

To express concisely, the fuel adhesion thickness $y = 0$, 5, and 10 lines were defined as *y*0, *y5*, and *y*10, respectively. In the following discussion, the terms of *y*0, *y5* and *y10* are used to represent the fuel adheison thickness along these different lines. The experimental condition discussed in this section is at 5 ms ASOI, as shown in Figure 4.20.

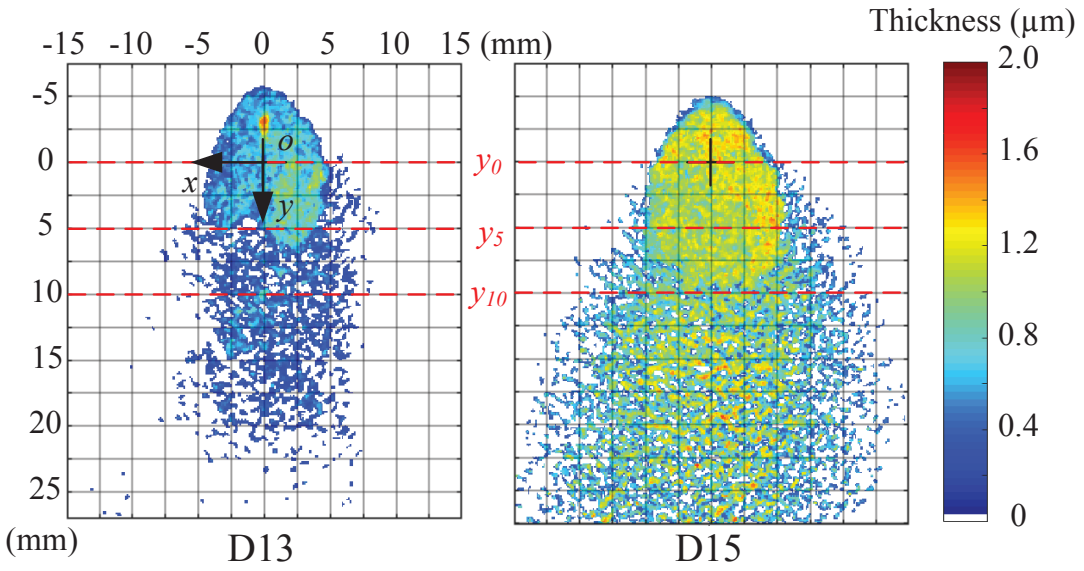

(a) 298 K

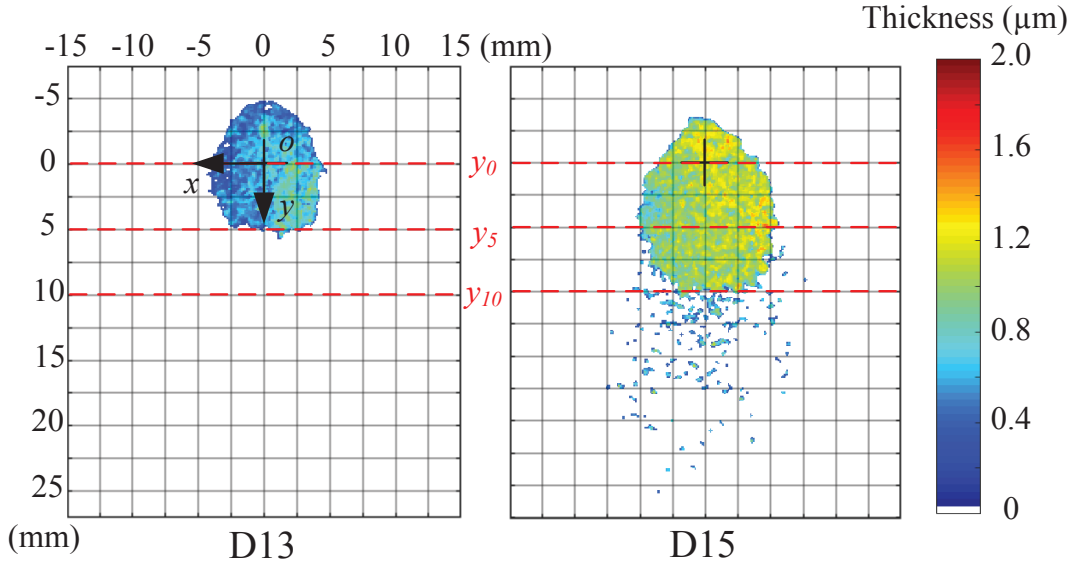

(b) 433 K

Figure 4.20 Definition of fuel adhesion thickness along different lines (5 ms ASOI)

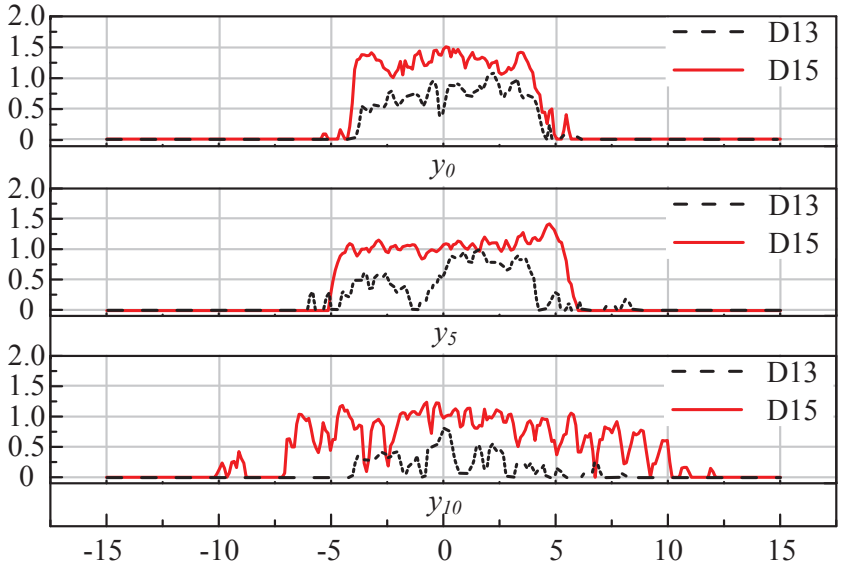

(a) 298 K

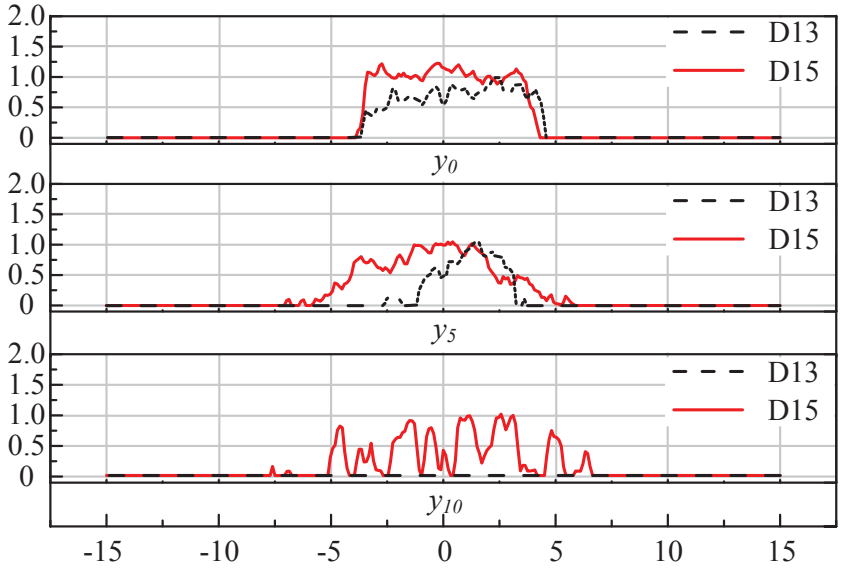

(b) 433 K

Figure 4.21 Fuel adhesion thickness distribution along different lines (5 ms ASOI)

Figure 4.21 (a) shows the fuel adhesion thickness distribution under 298 K. For D13, the fuel adhesion thickness and uniformity of thickness decreases from upstream to downstream. However, for D15, y_0 and y_5 are almost the same, and they are bigger than y_{10}. Moreover, the uniformity of y_0 and y_5 is better than y_{10}. In contrast to different hole diameter, the fuel adhesion

becomes thicker with a large hole diameter, and the uniformity of thickness improves with a large hole diameter. This is attributed to the larger spray angle of D15, more fuel adheres on the wall uniformly. Under 433 K, shown in Figure 4.21 (b), the thickness decreases from upstream to downstream for both D13 and D15. And the uniformity become worse from upstream to downstream. Owing to the fuel evaporation, thickness is smaller than that under 298 K. In contrast to different hole diameter, the fuel adhesion becomes thicker with a large hole diameter, and the uniformity of thickness improves with a large hole diameter.

4.3 SUMMARY

It is widely known that the fuel rich zones in engines are the major contributors towards soot emissions, which is why they must be avoided as much as possible. Unfortunately, it is difficult to predict the occurrence of fuel adhesion, as the mechanism behind it is still not clear. The aim of this chapter was to investigate the fuel adhesion formation under high temperature conditions to understand its mechanism. For this, toluene was injected via a single-hole injector on the wall. Mie scattering and RIM methods were applied to observe the impinging spray structure and fuel adhesion on the wall. The spray tip penetration and impinging spray height were compared, and the evolution of fuel adhesion along with its mass, area, and thickness were studied. The main conclusions are summarized as follows:

1. High ambient temperature has a significant impact on the impinging spray and fuel adhesion on the walls of the engine. A high ambient temperature favors the evaporation of fuel, thus decreasing the penetration of the spray tip and the height of the impinging spray. Moreover, it decreases the mass, area, and maximum thickness of the fuel adhesion owing to the evaporation effect. Also, is increases the average thickness with the decrease in ratio of fuel adhesion area faster than that of fuel adhesion mass.

2. The fuel adhesion continues to increase even after the end of injection, because of droplets being re-deposited on the wall. However, under T_{amb} = 433 K, the adhered fuel evaporates from the periphery to the impingement region even where there are still some droplets being re-deposited on the wall, but the increased adhesion can only be observed in region I. By comparing the evolution of fuel adhesion under different ambient temperatures, it can be concluded that high ambient temperatures lead to more uniform fuel adhesion on the wall.

3. The distribution of adhesion mass and thickness was studied in regions I and II. Similar curves were observed in region I under different ambient temperatures, whereas there was great variation in region II. Based on these results, different mechanisms were described for the formation of fuel adhesion during and after injection. The primary spray impinging on the wall contributed to the formation of fuel adhesion in region I, known as the primary impingement region. The splashing droplets impinging next on the wall contributed to the formation of fuel adhesion in region II, known as the secondary impingement region. Furthermore, high ambient temperatures exert more influence on the fuel adhesion formation in region II when compared to region I.

4. Decreasing the nozzle hole diameter can reduce the fuel adhesion mass, area, average thickness and maximum thickness owing to the better atomization. However, the large hole diameter improves the uniformity of the thickness.

CHAPTER 5 MICROSCOPIC BEHAVIORS OF IMPINGING SPRAY

It is well known that the microscopic characteristics of fuel spray are very important on the atomization and mixture formation. The droplet size and number distributions reveal the quality of spray and atomization, which affects the subsequent combustion and emissions characteristics. In this study, the droplet size was measured with particle image analysis (PIA) technique. Microscopic characteristics of impinging spray were obtained using ultra-high speed imaging. By changing the injection and ambient pressures, the influences of breakup and coalescence on the droplet behavior were investigated. Before impingement, the region near the center of spray has the larger droplets size and lower number density than the edge, which suggests that the spray breakup and atomization was poor in the center region. After impingement, the droplet size decreases along the distance from the wall under low ambient pressure. However, large droplets size appears in the region far from the wall under high ambient pressure, indicating the existence of coalescence effect on the droplets.

5.1 EXPERIMENTAL CONDITIONS

The experimental conditions were given in Table 5.1. Two injection pressures of 10 and 20 MPa, and two ambient pressures of 0.1 and 0.5 MPa, equivalent to the ambient gas densities of 1.19 and 5.95 kg/m^3, were investigated. This experiment was conducted in a constant volume chamber filled with nitrogen gas at room temperature. A mini-sac injector with a nozzle hole diameter of 0.135 mm was used. The nozzle is a conventional straight-hole type without counterbore. The length-to-diameter (L/D) ratio was 4.8. Toluene was employed as a surrogate fuel for gasoline. The injection mass was kept constant at 3.0 mg under different conditions, resulting in different injection pulse widths of 2.4 and 1.65 ms at different injection pressures. The impingement angle was 45° and the impingement distance was 22 mm from the nozzle exit to the impingement point of the flat wall along the spray axis. The flat wall was made of quartz glass (Sigma Koki, DFSQ1-50CO2) with a surface roughness of Ra7.7 μm. Moreover, the surface roughness was measured by a portable high-performance surface roughness and waviness measuring instrument (Kosaka Laboratory Ltd., SE300) with a resolution of 0.0064 μm.

Table 5.1 Experimental conditions.

Injector Conditions	
Injector Type	Mini-Sac, Single-Hole
Hole Type	Straight-Hole without Counterbore
L/D Ratio	4.8
Nozzle Hole Diameter (d)	0.135 mm
Injection Conditions	
Fuel	Toluene
Injection Mass (M_{inj})	3.0 mg
Injection Pressure (P_{inj})	10, 20 MPa
Injection Duration (t_d)	2.4, 1.65 ms
Ambient Conditions	
Ambient Gas	Nitrogen
Ambient Pressure (P_{amb})	0.1, 0.5 MPa
Ambient Temperature (T_{amb})	300 K
Ambient Density (ρ_{amb})	1.19, 5.95 kg/m^3
Impingement Conditions	
Impingement Plate	Quartz Glass
Impingement Distance (L_w)	22 mm
Impingement Angle (θ_{imp})	45°
Surface Roughness	Ra7.7

5.2 MIEROSCOPIC MORPHOLOGY OF IMPINGEMENT ON THE WALL

5.2.1 Before Impingement

Figure 5.1 shows the spray morphology along the spray axis. Four conditions (P_{inj} = 10 MPa, P_{amb} = 0.1 MPa; P_{inj} = 10 MPa, P_{amb} = 0.5 MPa; P_{inj} = 20 MPa, P_{amb} = 0.1 MPa; P_{inj} = 20 MPa, P_{amb} = 0.5 MPa) were investigated.

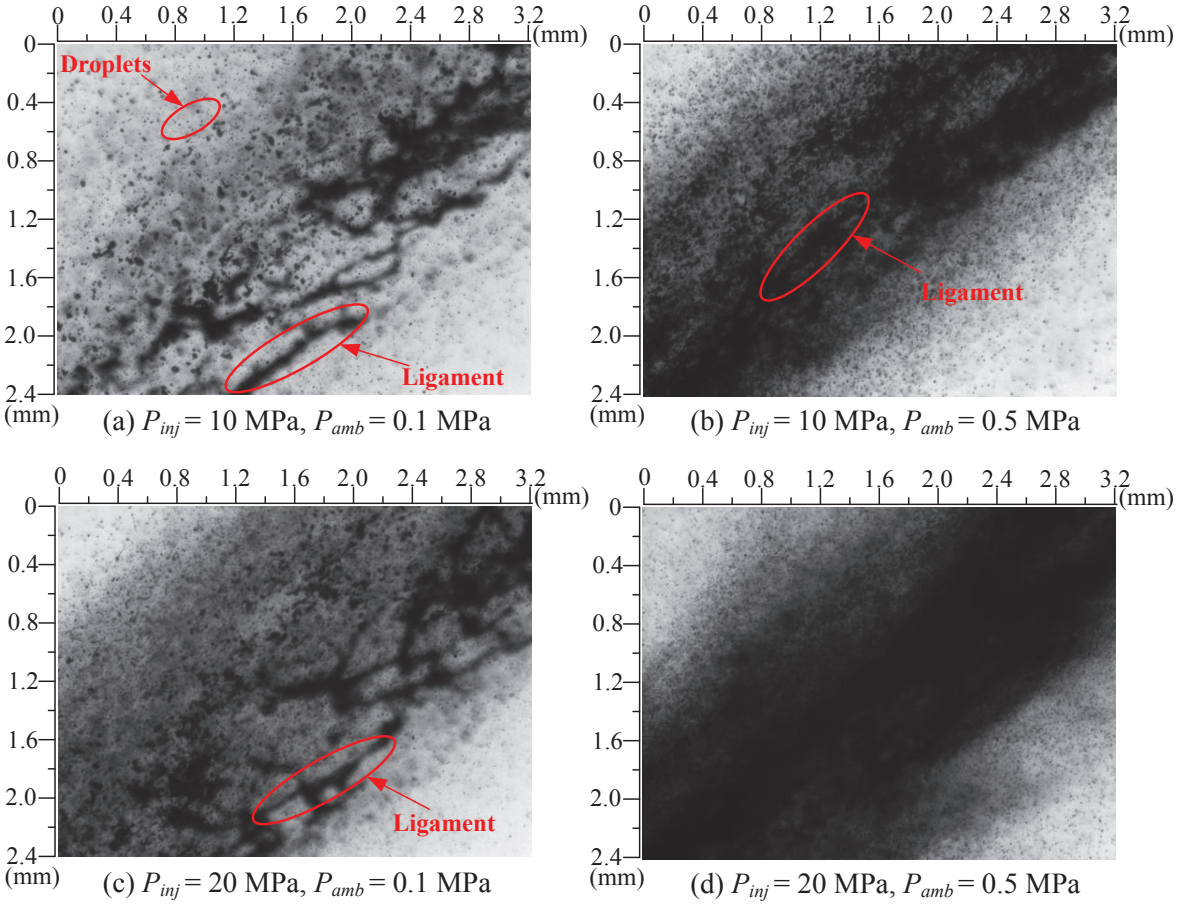

Figure 5.1 Spray morphology at the position of before impingement.

Generally, when the fuel injected out of the nozzle hole, they start to break-up into liquid ligaments and small droplets (Baumgarten et al., 2006). It is clear that the fuel jet developed with heterogeneity in droplet concentration: the core region had high concentration, while the periphery had low one. It can also be found that the spray flow is not symmetric, and that maybe due to the special structure of the needle hole. Shown in Figure 5.1 (a), some relatively large droplets and ligaments are observed at downstream of the spray axis, whereas most of tiny droplets are at upstream. Compared with Figure 5.1 (b), it is evident that with an increase of ambient pressure, droplets become smaller, and droplets density are quite higher, ligaments become shorter and smaller, which suggests that an increase in ambient pressure promotes liquid fuel breakup process, resulting in smaller droplets. The much stronger drag force should be responsible for smaller droplets. An increased ambient pressure increases the gas density in the chamber, resulting stronger interaction between fuel liquid and nitrogen gas. Therefore, droplets and ligaments tend to break up easily. Moreover, the spray width is a little larger than that of

P_{amb} = 0.1 MPa, which is consistent with previous studies (Guan et al., 2015; Feng et al., 2016). Comparing with Figure 5.1 (a) and (c), it can be seen that droplets and ligaments become smaller under high injection pressure. The enhanced kinetic energy leads to better dispersion and atomization should be the reason for it. Additionally, under high injection and ambient pressure, there are many tiny droplets, making the droplets too dense to detect the ligaments, shown in Figure 5.1 (d).

5.2.2 After Impingement

Figure 5.2 shows the spray morphology after impingement. The same four conditions were examined. The solid line represents the surface of the wall.

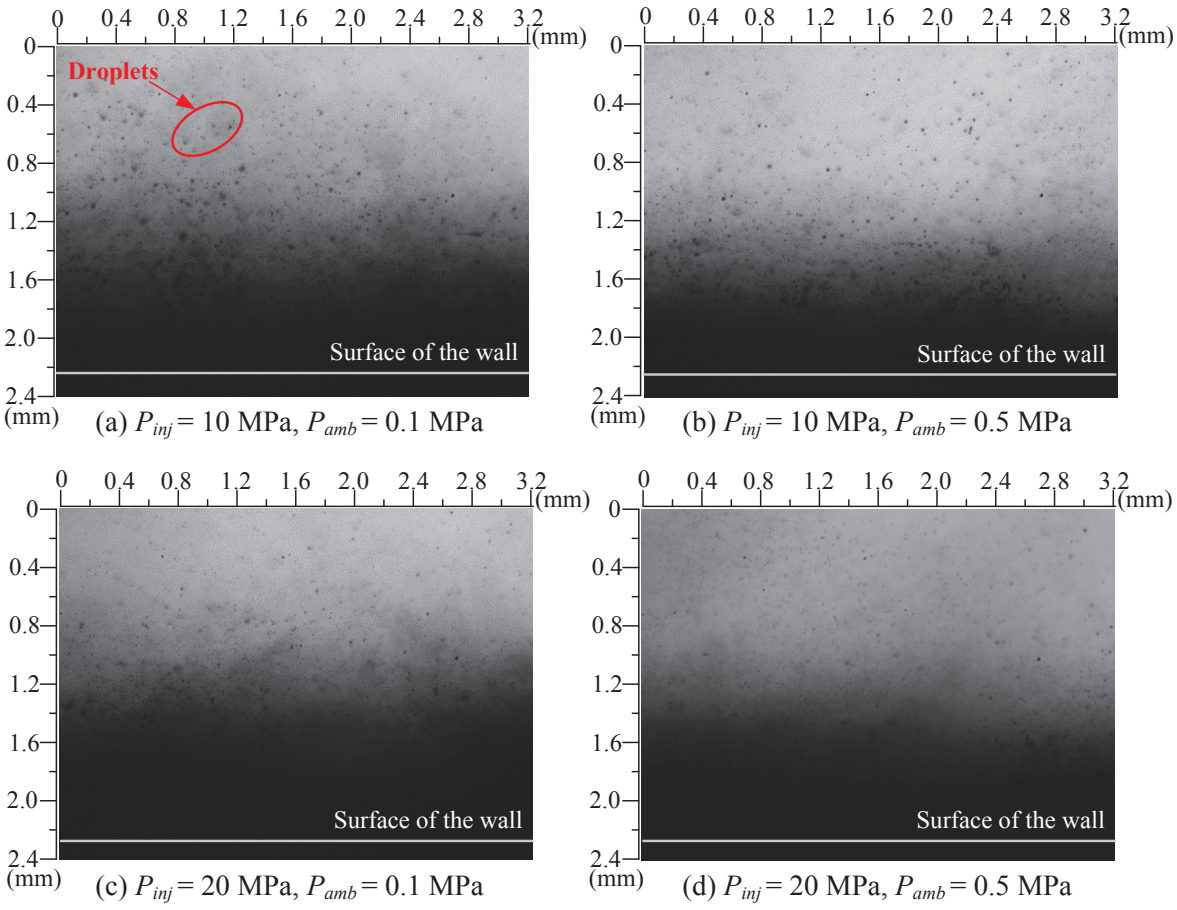

Figure 5.2 Spray morphology at the position of after impingement.

It is interesting to find that only small droplets can be observed in the figures which can be attributed to the impingement favors the process of ligaments breakup into droplets. The regions

of near the wall are very dense as many droplets impinge on the wall and deposit on the wall or splash off wall. The droplets far away from the wall are clear and easy to be distinguished. Some tendencies can also be noticed. Droplets appears smaller with an increase of injection and ambient pressure.

With these observations, it becomes clear that rapid breakup and atomization happens under high injection and ambient pressure condition. However, there is another coalescence effect of high ambient pressure, which will be discussed in the following section. Additionally, wall impingement makes the ligaments disappeared.

5.3 DROPLET SIZE DISTRIBUTION

5.3.1 Before Impingement

Droplets size distribution before impingement is shown in Figure 5.3. Figure (a) describes the small size (0-50 μm) distribution under four conditions (P_{inj} = 10 MPa, P_{amb} = 0.1 MPa; P_{inj} = 10 MPa, P_{amb} = 0.5 MPa; P_{inj} = 20 MPa, P_{amb} = 0.1 MPa; P_{inj} = 20 MPa, P_{amb} = 0.5 MPa). It is reported that curve moves towards to left and peak value of the curve increase with an increase of injection and ambient pressure, indicating better breakup. More importantly, the peak value of high injection pressure condition (P_{inj} = 20 MPa, P_{amb} = 0.1 MPa) is larger than that of high ambient pressure condition (P_{inj} = 10 MPa, P_{amb} = 0.5 MPa). One possible explanation for this could be that there are different mechanism effects of high injection and ambient pressure on the droplets size. Droplets with more momentum under high injection pressure entrain with surrounding gas more easily, facilitating the breakup of fuel jet. However, the elevated ambient pressure leads to strong drag force between air and droplets that shears droplets into small ones. As a result, the inner effect of droplets is more significant than the outer one on breakup phenomenon, especially for small size droplets. Moreover, high ambient pressure may also affect the coalescence of the droplets, which will be discussed in the following sections.

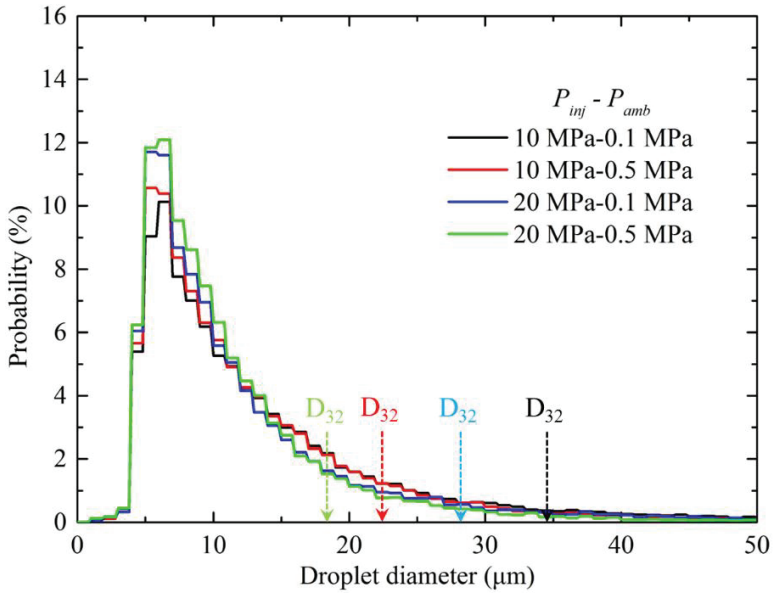

(a) Small size distribution.

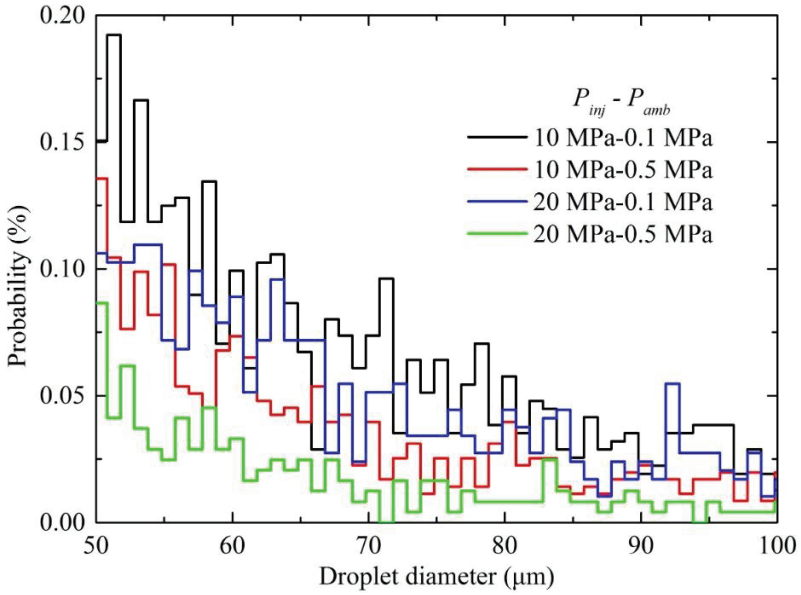

(b) Large size distribution.

Figure 5.3 Droplet size distribution before impingement.

Figure 5.3 (b) shows the large size (50-100 μm) distribution under the same four conditions. The probability of large size droplet decreases with an increase in injection and ambient pressure. It should be noted that the probability of high injection pressure condition (P_{inj} = 20 MPa, P_{amb} = 0.1 MPa) is larger than that of high ambient pressure condition (P_{inj} = 10 MPa, P_{amb} = 0.5 MPa). This can be argued that the elevated ambient pressure has a more positive effect on the breakup

of large size droplets because of air drag force, and the same conclusion can also be observed from Figure 5.1 (b) and (c). Generally, SMD is used to evaluate atomization, defined as follows:

$$\mathrm{SMD} = \frac{\sum N_i d_i^3}{\sum N_i d_i^2} \tag{5.1}$$

As the number of larger size droplet increases under P_{inj} = 20 MPa, P_{amb} = 0.1 MPa, SMD is larger than that under P_{inj} = 10 MPa, P_{amb} = 0.5 MPa.

5.3.2 After Impingement

Droplets size distribution after impingement is shown in Figure 5.4. Figure (a) provides the small size (0-50 μm) distribution under the four conditions. It can be found that curve moves towards to left and peak value of the curve increase in contrast to before impingement, which indicates the impingement facilitates the breakup of small size droplets. One important thing is that the peak value of higher injection pressure condition (P_{inj} = 20 MPa, P_{amb} = 0.1 MPa) is larger than that of higher ambient pressure condition (P_{inj} = 10 MPa, P_{amb} = 0.5 MPa), and even larger than that of higher injection and ambient pressure condition (P_{inj} = 20 MPa, P_{amb} = 0.5 MPa). It can be expected that some small droplets coalesce under higher ambient pressure. After impingement on the wall, droplets splash off the wall. Because of the changed velocity direction, some droplets collide with each other, then they appear to coalesce under high ambient pressure. In addition, the vortex after impingement also helps to enhance the coalescence behavior. It is interesting that after impingement, SMD under higher ambient condition (P_{inj} = 10 MPa, P_{amb} = 0.5 MPa) is larger than high injection pressure condition (P_{inj} = 20 MPa, P_{amb} = 0.1 MPa), and even larger than low injection and ambient pressure condition (P_{inj} = 10 MPa, P_{amb} = 0.1 MPa). High ambient pressure decelerates the droplets, and the coalescence phenomenon after impingement by the help of vortex appears much stronger, especially on droplets of low velocity.

Figure 5.4 (b) provides the large size (50-100 μm) distribution. The probability of large size droplet decreases sharply compared with before impingement, which manifests the impingement also has a positive effect of breakup. Furthermore, the probability under P_{inj} = 10 MPa, P_{amb} = 0.5 MPa is higher than that of P_{inj} = 10 MPa, P_{amb} = 0.1 MPa to some extent, which can also explain the reason SMD under P_{inj} = 10 MPa, P_{amb} = 0.5 MPa is larger than that of P_{inj} = 10 MPa, P_{amb} = 0.1 MPa.

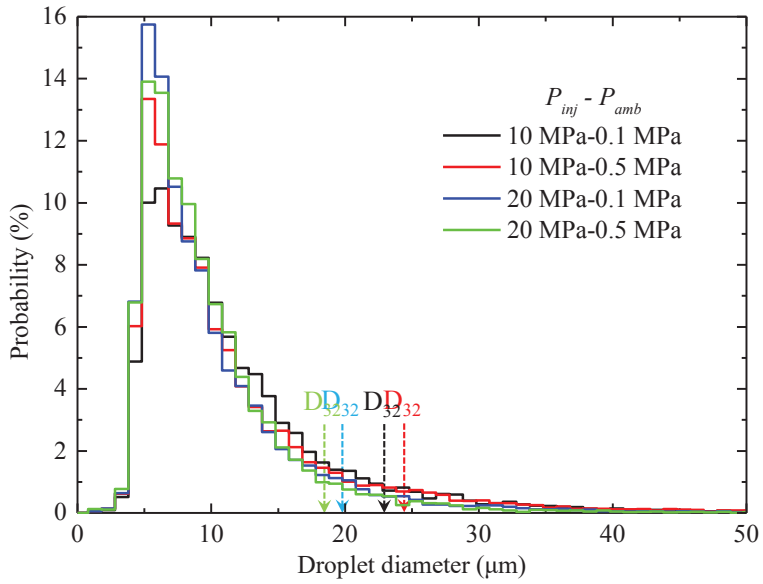

(a) Small size distribution.

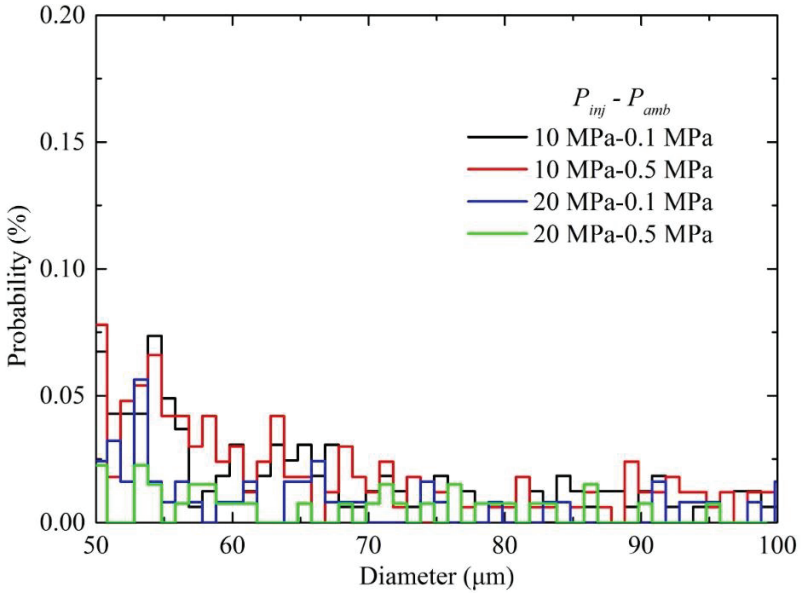

(b) Large size distribution.

Figure 5.4 Droplet size distribution after impingement.

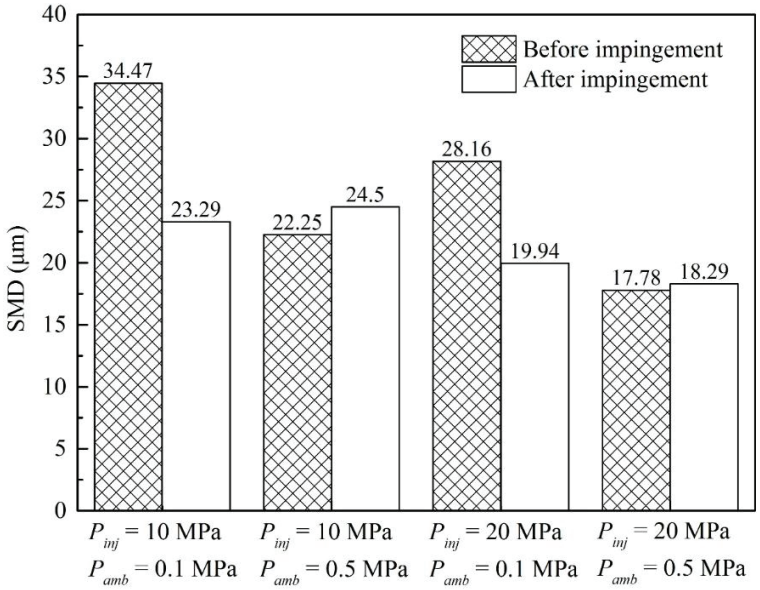

Figure 5.5 SMD before and after impingement.

In order to clarify the atomization characteristic clearly, SMD before and after impingement were depicted in Figure 5.5. Before impingement, SMD under P_{inj} = 10 MPa, P_{amb} = 0.1 MPa is used as reference condition, and both injection and ambient pressure favor the atomization as SMD decreases compared to the reference condition. Further, high ambient pressure has a more positive effect on atomization due to low probability of larger size of droplets. After impingement, SMD under low ambient pressure drops dramatically but SMD under high ambient pressure increases to some extent. More violent coalescence effect on droplets after impingement under high ambient pressure should be the reason for that.

5.4 DROPLET NUMBER DISTRIBUTION

For a better understanding the effect of breakup and coalescence on droplets, spatial distribution of droplets size was analyzed.

5.4.1 Before Impingement

Figure 5.6 shows the definition of radial distance from the axis of spray before impingement. The dashed dotted line represents the axis of the spray. Some regions were divided by every 0.4 mm apart from the spray axis. Droplets number and SMD were examined at each region.

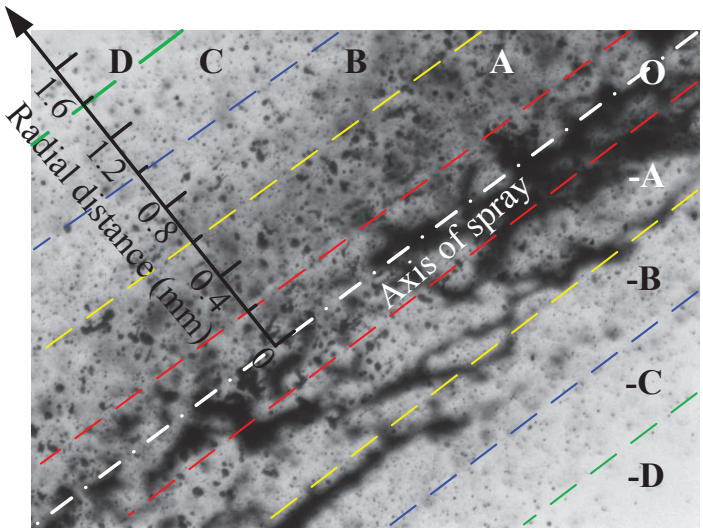

Figure 5.6 Definition of radial distance from the axis of spray before impingement.

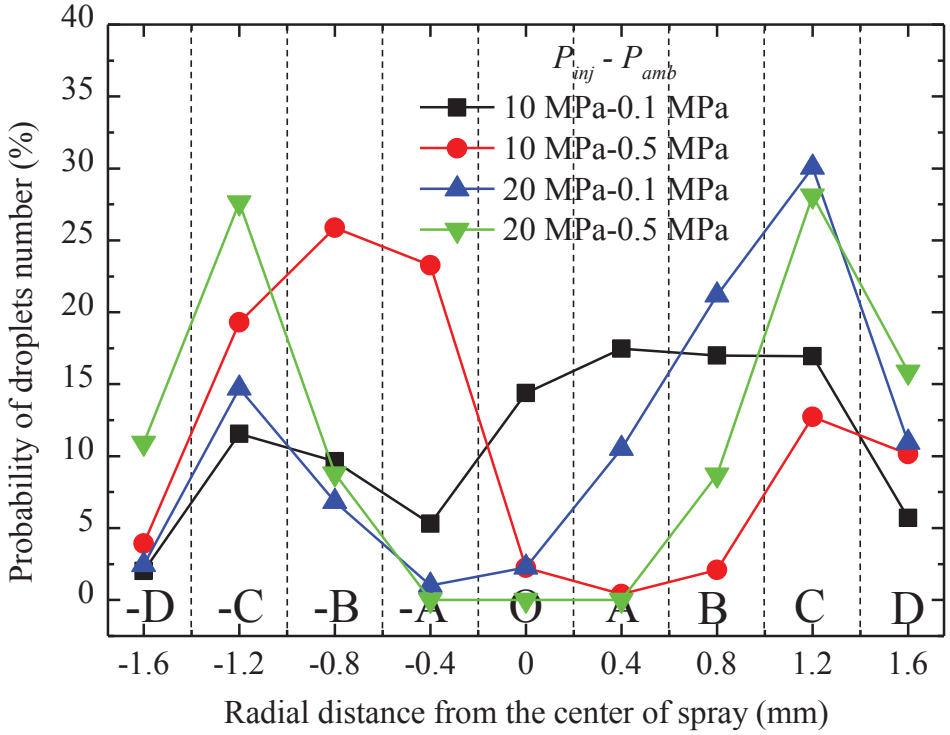

Figure 5.7 Probability of droplet number along the radial distance before impingement.

Figure 5.7 shows the probability of droplets number along radial distance. All cases show similar "M" type curves except for P_{inj} = 20 MPa, P_{amb} = 0.5 MPa condition. As the spray is quite dense under high injection and ambient pressure condition, it is difficult to detect the droplets, therefore the probability in the center region is "0". There are some ligaments and big

drops near the axis of the spray, called the core of spray. Apart from the axis, the number of droplets increases as better breakup and dispersion. Around the periphery, only some tiny droplets can be detected.

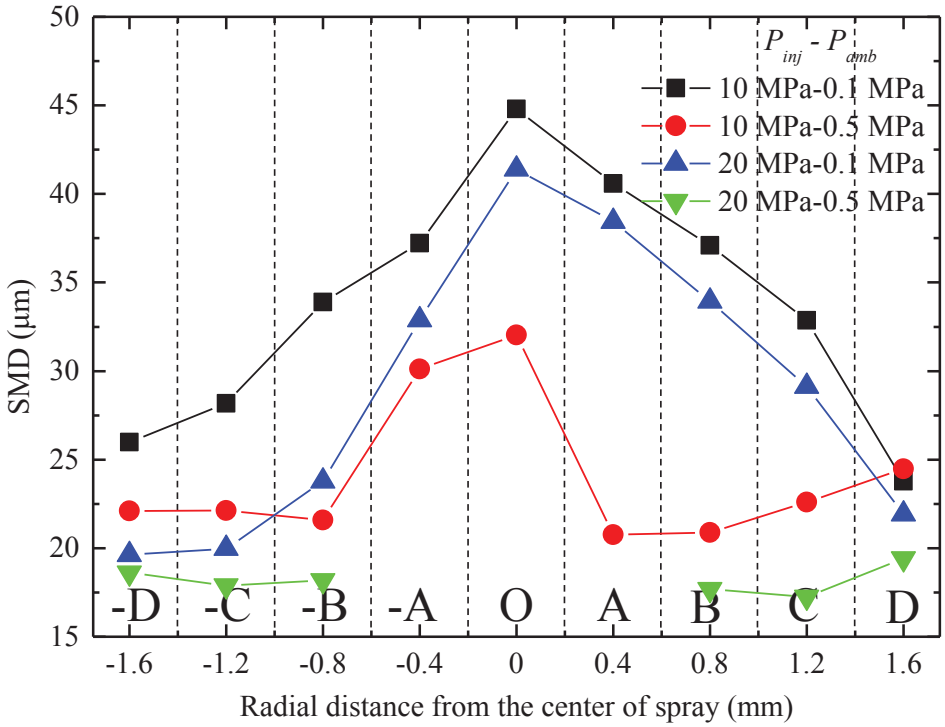

Figure 5.8 SMD distribution along the radial distance before impingement.

Shown in Figure 5.8, it is SMD distribution along the radial distance. It can be found all cases show similar "∧" type curves, although some differences are observed. The main reason for it may be summarized as follows: the droplets on the edge of the spray are affected by shear force between the air and spray envelope, consequently, these droplets may break up into small ones during they progress into the surrounding gas. It can be also concluded that both injection and ambient pressure facilitates the atomization of droplets due to SMD decreasing, compared with square, circle, and up triangle data. This indicates that the spatial distribution of droplets also can provide a good estimation of breakup and atomization process, which agrees well with the observation results in Figure 5.1. One thing should be noted, under P_{amb} = 0.5 MPa, SMD at the periphery is a litter larger and then decreases along the radial distance to the axis to some extent, which suggests the evidence that ambient pressure has the effect of coalescence on small droplets around periphery during the spray. With an increase of ambient pressure, firstly the

enhanced air drag force promotes the breakup of droplets significantly. Secondly, as the increased ambient pressure slows droplets down dramatically, when some droplets collide, they seem easy to coalesce with each other. Additionally, the coalescence effect is more obvious on the droplets of lower velocity, compared with SMD under P_{amb} = 0.1 MPa. This coalescence effect of ambient pressure was also reported by some previous literatures (Payri et al., 1996; Lacoste et al., 2003).

5.4.2 After Impingement

The definition of vertical distance from the wall after impingement is shown in Figure 5.9. As the near-wall region is difficult to analyze, the region within 0.6 mm from the wall is considered unavailable. Data from the region farther than 0.6 mm from the wall, which has almost triple the area of the unavailable region can be obtained for analysis and comparison. Starting from a distance of 0.6 mm from the wall, the available area is subdivided into four regions labeled I–IV in Fig. 13, with the inter-region dividing lines being lines of equal distance from the wall at 0.4 mm intervals. The droplet number and SMD were examined in each region.

Figure 5.10 provides the probability of droplets number along vertical distance. All cases under different conditions show similar “>” type curves. Firstly, the number of droplets increases along the vertical distance, and then decreases at the periphery.

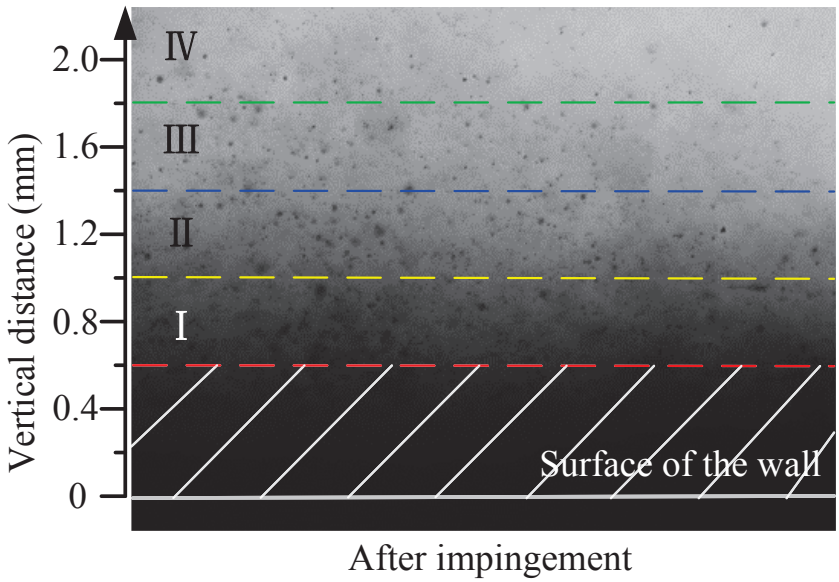

Figure 5.9 Definition of vertical distance from the wall after impingement.

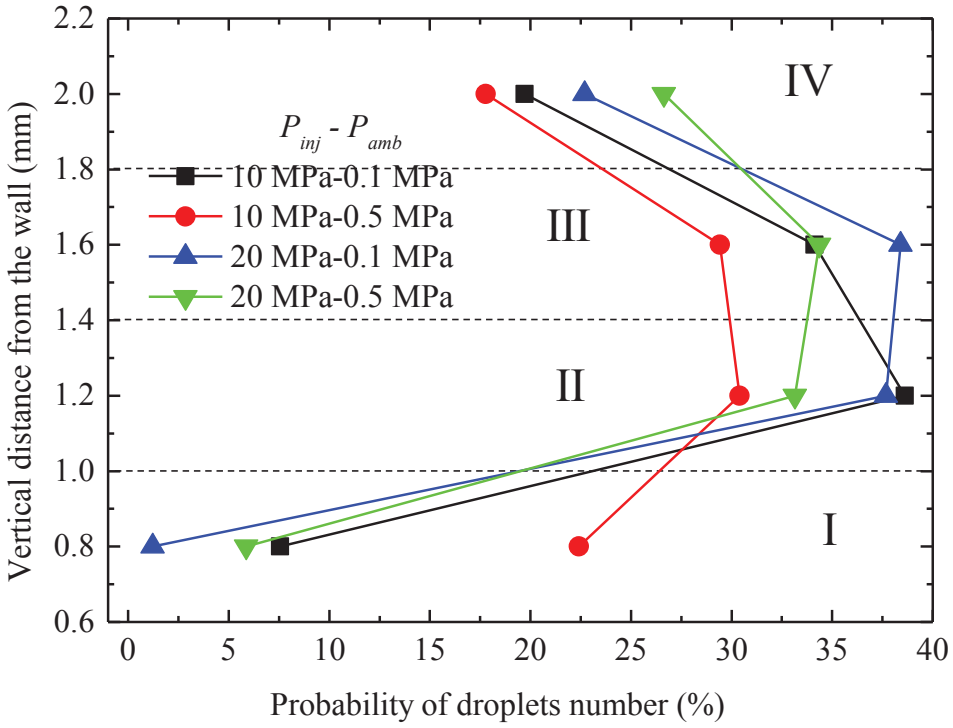

Figure 5.10 Probability of droplet number along the vertical distance after impingement.

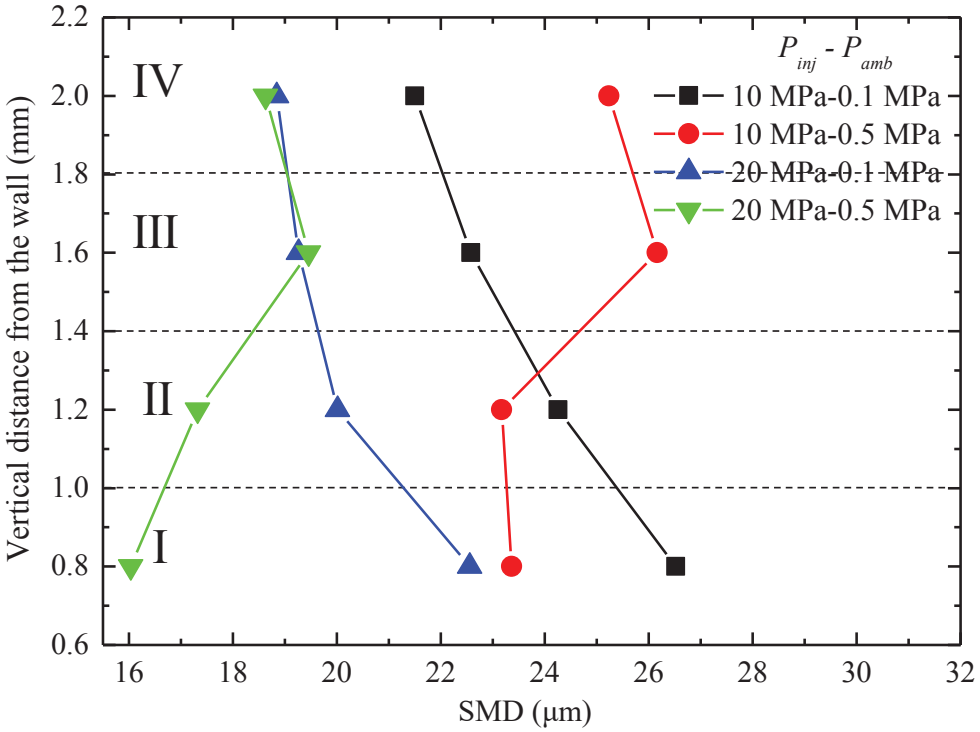

Figure 5.11 Probability of droplet number along the vertical distance after impingement.

Regarding droplets size after impingement, results depicted in Figure 5.11. It illustrates that impingement on the wall make droplets smaller, compared with Figure 5.8. It is worth noting that SMD decreases from the near wall region to periphery under P_{amb} = 0.1 MPa, which can be attribute to better breakup at periphery. However, under P_{amb} = 0.5 MPa, reversal phenomenon can be observed that SMD increase from the near wall region to periphery. This result can also demonstrate that there is coalescence effect on droplets under high ambient pressure. And the coalescence effect is more obvious on the droplets of lower velocity, in contrast to before impingement. As mentioned above, during impinging spray, air drag force decelerates droplets, then the droplets appear to coalesce by the help of vortex and ambient pressure more easily. This is also the reason for slight increase in SMD under high ambient pressure compared between before and after impingement in Figure 5.5.

In summary, Figure 5.12 reveals the schematic of coalescence and breakup model before and after impingement.

Breakup model: where the droplets break up into small one by the interaction of air, or droplets collide with a moderate velocity, and then break up into smaller ones.

Coalescence model: where the droplets collide with a quite slower velocity, and then coalesce into big ones.

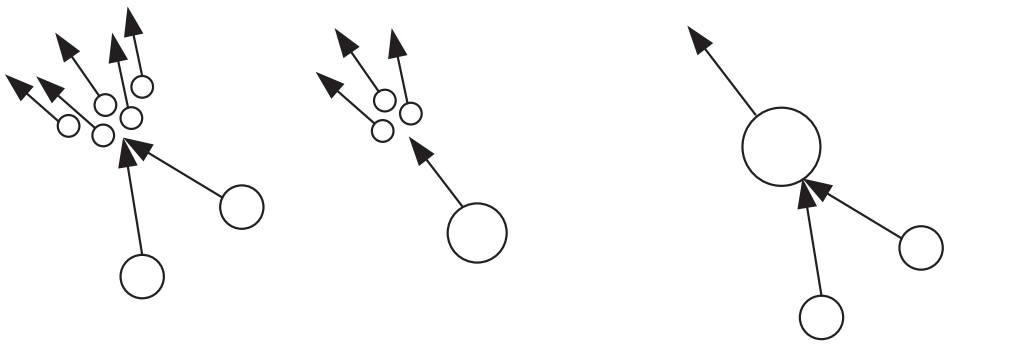

Figure 5.12 Schematic of breakup and coalescence models.

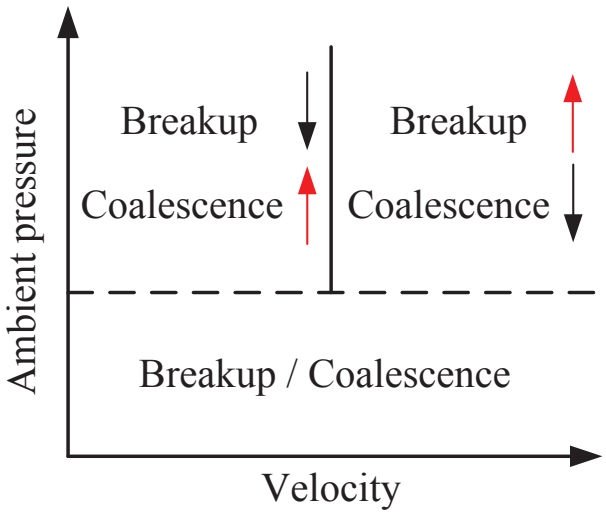

Figure 5.13 Overview of transition conditions at fixed velocity and ambient pressure.

Figure 5.13 illustrates the transition conditions at fixed velocity and ambient pressure conditions. Generally, both breakup and coalescence phenomena exit during the spray. When the ambient pressure is increased, droplets with lower velocity become collide with each other easily and coalesce into larger ones at the periphery of the spray. However, that effect becomes weaker when the velocity of droplets is high. Because the droplets with high momentum can struggle out after collision, resulting in small droplets again. After impingement, as the vortex changing the direction of droplets, droplets are easy to collide with each other, resulting more obvious phenomenon of coalescence, especially on droplets with low velocity.

5.5 COMPARISON OF FUEL ADHESION FORMATION WITH SINGLE DROPLET ANALYSIS

The Ohnesorge number (*Oh*) is a dimensionless number that relates the viscous forces to inertial and surface tension forces (McKinley et al., 2011).

$$Oh = \frac{\mu}{\sqrt{\rho \sigma d_0}} \tag{5.2}$$

Weber number (*We*) and Reynolds number (*Re*) are also used governing droplet impact (Schulz et al., 2016).

$$We = \frac{\rho d_0 v^2}{\sigma} \tag{5.3}$$

$$Re = \frac{\rho v d_0}{\mu} \tag{5.4}$$

In order to evaluate the influence on fuel adhesion mass correctly, the *Re*, *We* and *Oh* were calculated in Figure 5.14 and 5.15 respectively. The spray droplets under ambient pressure 0.1 and 1.0MPa are potted in black and white respectively. Additionally, three exemplary splashing limitations for a wetted wall are shown in Figure 5.14, which are taken from Vander et al., Kuhnk et al., and Kalantari (2004; 2006; 2007). Actually, these three-limitation equations are similar to each other, deposition and splashing regions are located on left and right of the lines. When ambient pressure is 1.0 MPa, the adhered fuel adhesion mass is almost larger than that 0.1 MPa. Although there is some difference, the spray-wall impingement is more complicated because of the effect of vortex. That effect is not obvious when the size of droplet is big (P_{amb}=1.0 MPa and P_{inj}=10 MPa. The different size of droplet can explain the fuel adhesion mass changing. In Figure 5.15, although researchers seldom used the *We-Oh* to separate the spray-wall impingement behavior, it can be make sense that left and right part represent the deposition and splashing region respectively.

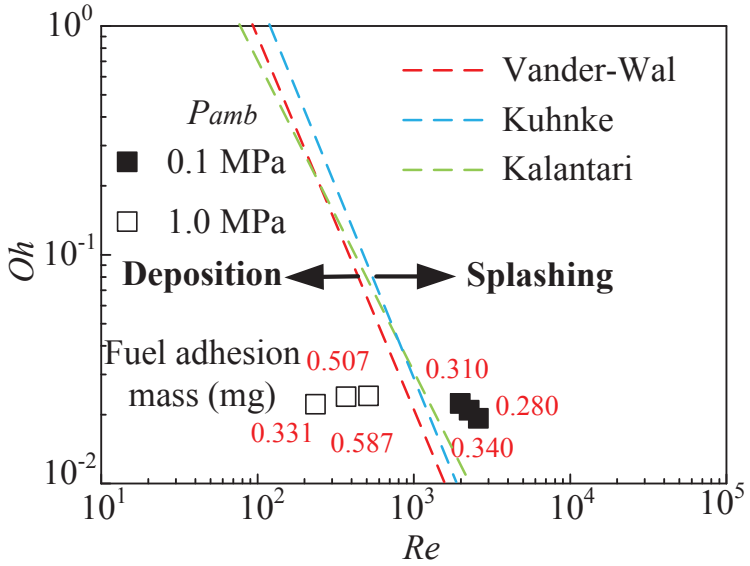

Figure 5.14 *Re* to *Oh* under different conditions

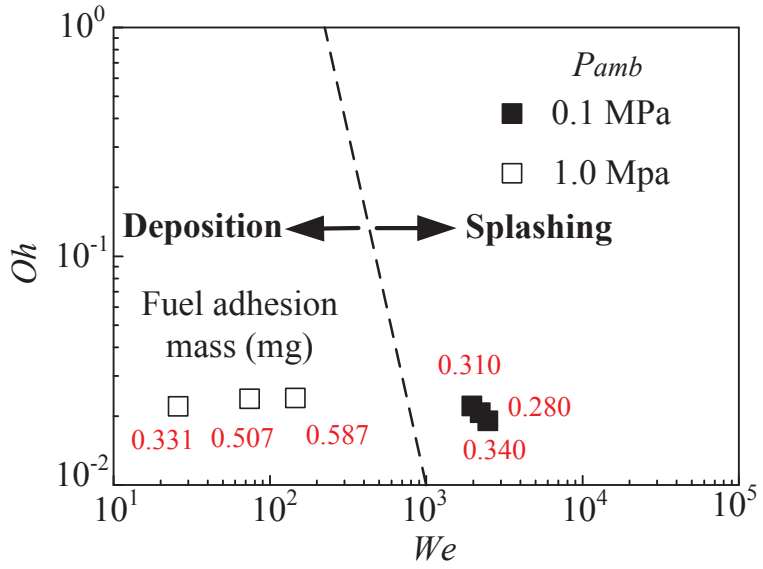

Figure 5.15 *We* to *Oh* under different conditions

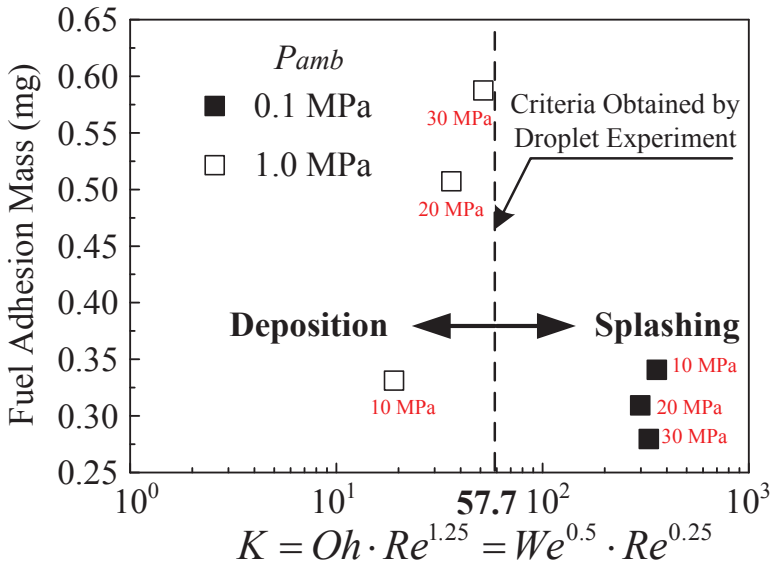

Figure 5.16 Relationship between fuel adhesion mass and *K*

To delineate the so-called impact regimes from each other, researcher used the dimensionless *K* number (*K*) as the splashing threshold parameter (Mundo et al., 1995; Moreira et al., 2010).

$$K = Oh \cdot Re^{1.25} = We^{0.5} \cdot Re^{0.25} \tag{5.5}$$

The empirically found K is integrated in most spray-wall impingement models used in CFD. And Mundo et al. (1995) also found the value of K (57.7) to separate the deposition and splash, which can be seen in Figure 5.16. The spray droplets under ambient pressure 0.1 and 1.0 MPa are potted in black and white respectively. When K is smaller than 57.7, most droplets deposit on the wall, otherwise most droplets splash off the wall, resulting left part fuel adhesion mass is larger than right part. The excluded different point (P_{amb}=1.0 MPa and P_{inj}=10 MPa) is the same as Re and We number, and the reason has been explained above.

5.6 SUMMARY

In this chapter, an experimental study was conducted to investigate the microscopic characteristics of impinging spray under gasoline conditions. PIA was applied to observe the microscopic spray structure, and droplets were detected by refined criteria. The droplet size distributions and SMD were calculated and compared under various injection and ambient pressures. The main conclusions are drawn as follows:

(1) Before impingement, large droplets and ligaments can be observed. Both injection and ambient pressures increase the droplet density by promoting the breakup process. However, under high injection and ambient pressures, the spray droplets are dense, and it is difficult to observe the ligaments and large droplets. Moreover, after impingement, the near-wall region becomes very dense as many droplets accumulate, whereas the droplets far away from the wall are clear and easily observed.

(2) Before impingement, injection pressure has a more positive effect on the distribution of small droplets, and ambient pressure favors the breakup of large droplets. Furthermore, after impingement, the probability of small droplets under P_{inj} = 20 MPa, P_{amb} = 0.1 MPa is higher than that under P_{inj} = 20 MPa, P_{amb} = 0.5 MPa. And the probability of large droplets under P_{inj} = 10 MPa, P_{amb} = 0.5 MPa is higher than that under P_{inj} = 10 MPa, P_{amb} = 0.1 MPa, which demonstrates the coalescence effect of ambient pressure.

(3) Before impingement, the probability distribution of droplet number along the radial distance from the spray axis shows “M”-type curve. And the SMD distribution along the radial distance shows “∧”-type curve. After impingement, the probability distribution of droplet number along the vertical distance shows similar “>”-type curve. The SMD decreases from the near-wall

region to the periphery under P_{amb} = 0.1 MPa, whereas a reversal phenomenon can be observed under P_{amb} = 0.5 MPa.

(4) Both the breakup and coalescence behaviors of droplets occur during the impinging spray. At low velocity, the coalescence phenomenon is more obvious at the periphery of spray under high ambient pressure. However, it weakens at increased droplet velocity.

(5) Key factor governing the spray-wall impingement behavior were found. The adhered fuel mass increase with smaller *Re*, *We*, and *K* numbers

CHAPTER 6 CONCLUSIONS

In the current study, the impinging spray on the wall by single-hole gasoline injector under non-evaporation and evaporation conditions were investigated experimentally. The high-speed video observation method (Mie scattering) and Refractive Index Matching (RIM) were implemented under different engine dynamic operation to visualize the spray and fuel adhesion, respectively. The characteristics of spray morphology such as spray tip penetration, impinging spray height were compared during the injection process and the evolution of fuel adhesion such as mass, area and thickness were analyzed after the injection processes in detail. The effect of injection pressure (10, 20, 30 MPa) and ambient pressure (0.1, 0.5, 1.0 MPa) were paid attention to firstly, and then the surface roughness of the impinging wall (Ra 2.5, Ra7.7), and impingement distances (28 and 40 mm) were selected to acquire a better understanding about the impinging spray under non-evaporation conditions. Furthermore, the effect of ambient temperatures (298 and 433 K) on fuel adhesion was considered, along with the effect of hole diameter (0.135 and 0.155 mm). Moreover, droplets behaviors before and after impingement were discussed deeply by Particle Image Analysis (PIA) equipment. Additionally, the relationship between the fuel adhesion on the wall and the corresponding spray behaviors was investigated under the same conditions of the experiments as well. The main conclusions are summarized in this chapter.

6.1 FINDINGS OF THE CURRENT STUDY

The motivation and significance of this study were introduced, and a review of the previous research in this field was conducted to give more background information of the current study in Chapter1. After that, the experimental approaches applied in this research were introduced in very detail in Chapter 2. The discussion and analysis about the results were in chapter 3-5. The main findings are classified as following.

6.1.1 Non-evaporation Spray Evolution and Fuel Adhesion Formation

The characteristics of fuel spray and adhesion under different pressures, wall roughnesses and impingement distances were investigated experimentally under non-evaporation condition in chapter 3. The values of R_s, H_v, S, and H_i were acquired, and the fuel adhesion evolution was

analyzed. Furthermore, the probabilities of adhesion and thickness distribution were discussed. The major conclusions are as follows:

- The fuel adhesion tip is shorter than the spray tip because fuel droplets splash above the wall after impingement. Fuel droplets still exist in the air above the wall even after the end of injection. Owing to better atomization with high injection pressure, the fuel adhesion on the wall increases. An increase in ambient pressure improves the uniformity of the fuel adhesion.

- An increase in wall roughness decreases the spray tip penetration and increases the impinging spray height. The fuel adhesion mass and area increase with time even after the end of injection. The fuel adhesion becomes slightly thicker in downstream for Ra2.5, whereas the thicker area moves upstream for Ra7.7. An increase in wall roughness increases the mass and area of the fuel adhesion. The ambient pressure decreases the differences between the two types of walls, whereas the injection pressure increases the differences. A higher roughness results in a higher maximum thickness of the fuel adhesion. An increase in roughness deteriorates the uniformity of the fuel adhesion. Wall roughness affects the fuel adhesion thickness along different lines. For $x0$, the adhesion thickness for Ra7.7 is higher than that for Ra2.5 at the constant value stage, and the thickness uniformity for Ra7.7 is considerably inferior to that for Ra2.5. For y lines, the adhesion thickness for Ra7.7 is higher than that for Ra2.5 in the upstream region, and the thickness uniformity for Ra7.7 is poor compared to that for Ra2.5.

- With a large impingement distance under ambient condition, the velocity of droplets decreases significantly, resulting in more droplets adhering to the wall instead of splashing out of the wall. As a result, R_s, H_v, and H_i decrease with an increase in impingement distance. However, after impingement, owing to the stronger drag force by the ambient gas and friction from the wall, S increases with the increase in impingement distance. Both the high injection pressure and large impingement distance increase the fuel adhesion mass and area, but the mechanisms are different. Owing to better atomization with high injection pressure, the fuel adhesion on the wall increases. At a large impingement distance, the lower velocity, bigger spray width, and better atomization are the main reasons for increased fuel adhesion on the wall after impingement. Under the large impingement distance condition, more fuel adheres on midstream and the thickness uniformity of fuel adhesion becomes worse.

Moreover, the maximum thickness of fuel adhesion increases with a large impingement distance.

6.1.2 Evaporating Spray Evolution and Fuel Adhesion Formation

The aim of this study in chapter 4 was to investigate the effect of high temperature on fuel adhesion under gasoline engine conditions to understand its mechanism. For this, toluene was injected via a single-hole injector on the wall. Mie scattering and RIM methods were applied to observe the impinging spray structure and fuel adhesion on the wall. The spray tip penetration and impinging spray height were compared, and the evolution of fuel adhesion along with its mass, area, and thickness were studied. Finally, the mechanisms of fuel adhesion formation were established in regions I and II. Moreover, due to the importance in the design of the injector hole diameter, especially for the characteristics of atomization, the effect of hole diameter the fuel adhesion was checked. RIM experiment was done to measure the fuel adhesion under different hole diameters of gasoline injector. The main conclusions of this study are summarized as follows:

- High ambient temperature has a significant impact on the impinging spray and fuel adhesion on the walls of the engine. A high ambient temperature favors the evaporation of fuel, thus decreasing the spray tip penetration and impinging spray height of liquid phase. Moreover, it decreases the mass, area, and maximum thickness of the fuel adhesion owing to the evaporation effect. Also, it increases the average thickness owing to the decrease in ratio of fuel adhesion area being faster than that of fuel adhesion mass. The fuel adhesion continues to increase even after the end of injection, because of droplets being re-deposited on the wall. However, under T_{amb} = 433 K, the adhered fuel evaporates from the periphery of the impingement region even where there are still some droplets being re-deposited on the wall, but the increased adhesion can only be observed in region I. By comparing the evolution of fuel adhesion under different ambient temperatures, it can be concluded that high ambient temperatures lead to more uniform fuel adhesion on the wall.
- The distributions of adhesion mass were studied in regions I and II. Similar curves were observed in region I under different ambient temperatures, whereas there was great variation in region II. Based on these results, different mechanisms were described for the formation of fuel adhesion during and after injection. The primary spray impinging on the wall

contributed to the formation of fuel adhesion in region I, known as the primary impingement region. The splashing droplets impinging next on the wall contributed to the formation of fuel adhesion in region II, known as the secondary impingement region. Furthermore, high ambient temperature exerts more influence on the fuel adhesion formation in region II when compared to region I.

- Decreasing the nozzle hole diameter can reduce the fuel adhesion mass, area, average thickness and maximum thickness owing to the better atomization. However, the large hole diameter improves the uniformity of the thickness under both non-evaporation and evaporation conditions.

6.1.3 Microscopic Spray Behaviors

The microscopic characteristics of impinging spray under gasoline conditions were studied in chapter 5. PIA was applied to observe the microscopic spray structure, and droplets were detected by refined criteria. The droplet size distributions and SMD were calculated and compared under various injection and ambient pressures. Furthermore, the correlation between droplets behaviors and fuel adhesion on the wall was discussed in this chapter, too. The main conclusions of this study are drawn as follows:

- Before impingement, large droplets and ligaments can be observed. Both injection and ambient pressures increase the droplet density by promoting the breakup process. However, under high injection and ambient pressures, the spray droplets are dense, and it is difficult to observe the ligaments and large droplets. Moreover, after impingement, the near-wall region becomes very dense as many droplets accumulate, whereas the droplets far away from the wall are clear and easily observed. Before impingement, injection pressure has a more positive effect on the distribution of small droplets, and ambient pressure favors the breakup of large droplets. Furthermore, after impingement, the probability of small droplets under P_{inj} = 20 MPa, P_{amb} = 0.1 MPa is higher than that under P_{inj} = 20 MPa, P_{amb} = 0.5 MPa. And the probability of large droplets under P_{inj} = 10 MPa, P_{amb} = 0.5 MPa is higher than that under P_{inj} = 10 MPa, P_{amb} = 0.1 MPa, which demonstrates the coalescence effect of ambient pressure.
- Before impingement, the probability distribution of droplet number along the radial distance from the spray axis shows “M”-type curve. And the SMD distribution along the radial

distance shows "∧"-type curve. After impingement, the probability distribution of droplet number along the vertical distance shows similar ">"-type curve. The SMD decreases from the near-wall region to the periphery under P_{amb} = 0.1 MPa, whereas a reversal phenomenon can be observed under P_{amb} = 0.5 MPa. Both the breakup and coalescence behaviors of droplets occur during the impinging spray. At low velocity, the coalescence phenomenon is more obvious at the periphery of spray under high ambient pressure. However, it weakens at increased droplet velocity.

- Key factor governing the spray-wall impingement behavior were found. The adhered fuel adhesion mass increase with smaller *Re*, *We*, and *K* numbers. Although combination with the fuel adhesion mass and droplets behavior has been done to find some partial conclusion, the gasoline spray-wall is totally complicated and need more investigation have to be taken to identify the fuel adhesion formation and impingement process.

6.2 RECOMMENDATIONS FOR FUTURE WORKS

There is much more effort, which can be made in the following study of this field.

For example, the sprays and fuel adhesions in the current study are all injected by the single-hole injector, hence the spray evolutions and adhesions by the multiple-hole injector should also be measured in the further. The application of 2D cavity and even real engine may release more practical situations.

There are no combustion conditions in the current investigation. The detail mechanism of impinging spray combustion characteristics needs to be further explored. As a result, the nozzle spray combustion processes under the corresponding conditions should be evaluated in detail in the further.

Although the ambient physical condition implemented in the current study are aiming to reproduce the real engine operation environment, the turbulent, tumble, and squish flow inside the combustion chamber all play significant roles in the mixture formation and combustion process. Therefore, it is recommended to correlate the fuel adhesion formation with combustion characteristics of impinging spray in optical engine as well.

The effect of most basic and important parameters (injection pressure, ambient pressure, ambient temperature, wall roughness and hole diameter) on spray evolution and fuel adhesion are investigated in the current experimental study. However, some more crucial factors, such as the wall temperature and injection strategy should also be taken into the consideration when conduction the fuel spray and fuel adhesion formation study under the practical gasoline conditions.

The model for impinging spray should be considered in the CFD to increase the accuracy of simulation results in the future.

ACKNOWLEDGEMENT

I would like to express my sincere gratitude to my supervisor, Professor Keiya NISHIDA, for his invaluable guidance and constant encouragement throughout the years of my PhD study. He has been a source of inspiration and motivation for my research. Without his guidance and support, this research could not be completed properly.

I am also greatly acknowledged Professor Yukihiko MATSUMURA, Associate Professor Youichi OGATA and Associate Professor Shuhei INOUE. They gave me so much positive help on the research, the accumulation of the knowledge and my life, and I have learnt lot from them. In addition, I would like to express my heartfelt thanks to Dr. Kim for his technical in reviewing my research.

My great appreciation also goes to other members of our gasoline spray group throughout the research, Mr. Uchitomi, Mr. Watanabe, and Mr. Ichikawa for their help in setting up and collecting data of this work. I also show my appreciation to Mazda Motor Corporation, not only for the finical support, but also technological support. Especially I would like to thank Dr. Zhang from Mazda for his dedicated supports, insightful comments and guidance in my study.

Then I want greatly thank Mr. Si, Mr. Yang and Mr. Rizal, who came to the group with me together. We studied together and helped each other for research and living. Moreover, I would also like to thank all the past and present members of Fluid Engineering and Spray/Simulation Technology Laboratory, in Department of Mechanical Systems Engineering, Hiroshima University, for their enthusiastic help to both of my life and study.

Finally, my thanks would go to my beloved family for their loving considerations and great confidence on me all through these years. Last but not the least, I owe special thanks to my wife, Dr. Yu, for being supportive and patient throughout the years, for her love and encouragement.

LIST OF PUBLICATIONS

International Journals

1. **Hongliang Luo***, Shintaro Uchitomi, Keiya Nishida, Youichi Ogata, Wu Zhang, Tatsuya Fujikawa. Experimental Investigation on Fuel Film Formation of Spray Impingement on Flat Walls with Different Surface Roughness. Atomization and Sprays, 27(7): 611–628, 2017. (SCI, IF=1.235) DOI: 10.1615/AtomizSpr.2017019706
2. **Hongliang Luo**, Keiya Nishida*, Shintaro Uchitomi, Youichi Ogata, Wu Zhang, Tatsuya Fujikawa. Microscopic behavior of spray droplets under flat-wall impinging condition. Fuel, 219: 467-476,2018. (SCI, IF=4.908) https://doi.org/10.1016/j.fuel.2018.01.059
3. **Hongliang Luo***, Keiya Nishida, Shintaro Uchitomi, Youichi Ogata, Wu Zhang, Tatsuya Fujikawa. Effect of Spray Impinging Distance on Piston Top Fuel Adhesion in Direct Injection Gasoline Engines. International Journal of Engine Research,2018 (Online First). (SCI, IF=2.775) https://doi.org/10.1177/1468087418774175
4. **Hongliang Luo***, Keiya Nishida, Shintaro Uchitomi, Youichi Ogata, Wu Zhang, Tatsuya Fujikawa. Effect of Temperature on Fuel Adhesion under Spray-Wall impingement Condition. Fuel, 234:56-65,2018. (SCI, IF=4.908) https://doi.org/10.1016/j.fuel.2018.07.021

International Conferences

1. **Hongliang Luo**, Shintaro Uchitomi, Keiya Nishida, Youichi Ogata, Wu Zhang, Tatsuya Fujikawa. Fuel Adhesion Characteristics of Flat Wall-Impinging Spray under DISI Engine Conditions. 29th Annual Conference on Liquid Atomization and Spray Systems-Americas (ILASS-Americas 2017), 15-18, May, 2017, Atlanta, GA.
2. **Hongliang Luo**, Shintaro Uchitomi, Keiya Nishida, Youichi Ogata, Wu Zhang, Tatsuya Fujikawa. Effect of Impingement Distance on Fuel Adhesion of Hole-Nozzle Spray under Various Injection Pressures. The 9th International Conference on Modeling and Diagnostics for Advanced Engine Systems (COMODIA 2017), 25-28, Jul, 2017, Okayama, Japan.
3. **Hongliang Luo**, Keiya Nishida, Shintaro Uchitomi, Youichi Ogata. Fuel Adhesion Characteristics of Flat-Wall Impinging Spray under Gasoline Engine Conditions. The International Conference on Advances in Construction Machinery and Vehicle Engineering (ICACMVE 2017), 14-16, Sep, 2017, Qinhuangdao, China.

4. **Hongliang Luo**, Shintaro Uchitomi, Keiya Nishida, Youichi Ogata. Fuel Adhesion Characteristics by Spray Impingement on the Flat Wall. The 1st International Symposium on Fuels and Energy, 10-12, Jul, 2017, Hiroshima, Japan.
5. **Hongliang Luo**, Keiya Nishida, Youichi Ogata. Characteristics of gasoline fuel adhesion on the impingement wall. KAUST Research Conference: Combustion in Extreme Conditions, 5-8, Mar, 2018, King Abdullah University of Science and Technology, Sandi Arabia.
6. Shintaro Uchitomi, **Hongliang Luo**, Keiya Nishida, Youichi Ogata. Adhesion Characteristics of Fuel Spray Impinging on Flat Wall under High-Temperature and High-Pressure Ambient Condition. 18th Annual Conference on Liquid Atomization and Spray Systems-Asia (ILASS–Asia 2017), 18-21, Oct, 2017, Jeju Island, Korea.
7. Keiichi Katayama, Gnanasekaran KishorKumar, **Hongliang Luo**, Keiya Nishida, Yoichi Ogata. Spark-Ignited Combustion Characteristics of Gasoline Spray Injected by Hole-Type Nozzle for Direct Injection Engine. 18th Annual Conference on Liquid Atomization and Spray Systems-Asia (ILASS-Asia 2016), 7-9, Nov, 2016 Chennai, India.

REFERENCES

1. **Akop MZ, Zama Y, Furuhata T, & Arai M.** Experimental investigations on adhered fuel and impinging diesel spray normal to a wall. Atomization and Sprays 2013; 23(3): 211-231. DOI: 10.1615/AtomizSpr.2013007447

2. **Akop M Z, Zama Y, Furuhata T, et al.** Characteristics of adhesion of diesel fuel on impingement disk wall. Part 1: effect of impingement area and inclination angle of disk[J]. Atomization and Sprays, 2013, 23(8): 725-744. DOI: 10.1615/AtomizSpr.2013008113.

3. **Akop M Z, Zama Y, Furuhata T, et al.** Characteristics of adhesion diesel fuel on an impingement disk wall Part 2: Droplet Weber number and adhered fuel mass[J]. Atomization and Sprays, 2014, 24(8): 651-671. DOI: 10.1615/AtomizSpr.2014008445.

4. **Akop MZ, Zama Y, Furuhata T, & Arai M**. Characteristics of adhesion diesel fuel on an impingement disk wall. Part 3: Ambient pressure effect. Atomization and Sprays 2014; 24(7): 625-650. DOI: 10.1615/AtomizSpr.2014010224

5. **Alkidas AC.** Combustion advancements in gasoline engines. Energy Conversion and Management 2007; 48(11): 2751-2761. https://doi.org/10.1016/j.enconman.2007.07.027

6. **Algayyim SJM, Wandel AP & Yusaf T.** The impact of injector hole diameter on spray behaviour for butanol-diesel blends. Energies 2018; 11(5): 1298. doi:10.3390/en11051298

7. **Alger T, Huang Y, Hall M, & Matthew RD.** Liquid film evaporation off the piston of a direct injection gasoline engine. SAE Technical Paper 2001-01-1204; 2001. https://doi.org/10.4271/2001-01-1204.

8. **Allocca L, Lazzaro M, Meccariello G, Montanaro A.** Schlieren visualization of a GDI spray impacting on a heated wall: Non-vaporizing and vaporizing evolutions. Energy 2016; 108: 93-98. https://doi.org/10.1016/j.energy.2015.09.107

9. **Anon VA.** Bosch Motronic MED7 Gasoline Direct Injection. Volkswagen Self-Study Program, 253, 2002.

10. **Andreassi L, Ubertini S, & Allocca L.** Experimental and numerical analysis of high pressure diesel spray–wall interaction. International journal of multiphase flow 2007; 33(7): 742-765. https://doi.org/10.1016/j.ijmultiphaseflow.2007.01.003

11. **Andresen P, Meijer G, Schlüter H, Voges H, Koch A, Hentschel W, Oppermann W, and Rothe E.** Fluorescence Imaging inside an Internal Combustion Engine using Tuable Excimer Lasers. Applied optics 1990; 26: 2392-2404.https://doi.org/10.1364/AO.29.002392

12. **Arcoumanis C, Cutter P, & Whitelaw DS.** Heat transfer processes in diesel engines. Chemical Engineering Research and Design 1998; 76(2): 124-132. https://doi.org/10.1205/026387698524695

13. **Arcoumanis C, & Chang JC.** Heat transfer between a heated plate and an impinging transient diesel spray. Experiments in Fluids 1993; 16(2): 105-119.https://doi.org/10.1007/BF00944912

14. **Bai CX, Rusche H, & Gosman AD.** Modeling of gasoline spray impingement. Atomization and Sprays 2002; 12(1-3): 1-27. DOI: 10.1615/AtomizSpr.v12. i123.10

15. **Bai C, & Gosman AD.** Development of methodology for spray impingement simulation. JOURNAL OF ENGINES 1995; 104(3): 550-568. http://www.jstor.org/stable/44633238

16. **Baumgarten C.** Mixture Formation in Internal Combustion Engines, Springer Verlag, Germany, 2006.

17. **Bruneaux G.** Liquid and Vapor Spray Structure in High-Pressure Common Rail Diesel Injection. Atomization and Sprays 2001; 11(5): 533-556. DOI: 10.1615/AtomizSpr.v11.i5.40

18. **Berg T, Deppe J, Michaelis D, Voges H, Wissel S.** Comparison of particle size and velocity investigations in sprays carried out by means of different measurement techniques. ICLASS'06, Kyoto, Japan, 2006.

19. **Cathcart G, & Railton D.** Improving robustness of spray guided DI combustion systems: the air-assisted approach. JSAE paper 5360, 2001.

20. **Cen C, Wu H, Lee CF, Liu F, & Li Y.** Experimental investigation on the characteristic of jet break-up for butanol droplet impacting onto a heated surface in the film boiling

regime. International Journal of Heat and Mass Transfer 2018; 123: 129-136. https://doi.org/10.1016/j.ijheatmasstransfer.2018.02.059

21. **Crua C, Heikal MR, & Gold MR.** Microscopic imaging of the initial stage of diesel spray formation. Fuel 2015; 157: 140-150. https://doi.org/10.1016/j.fuel.2015.04.041

22. **Cheng YS, Deng K, and Li T.** Measurement and simulation of wall-wetted fuel film thickness. Int. J. Thermal Sci. 2010; 49(4): 733–739. https://doi.org/10.1016/j.ijthermalsci.2009.10.006.

23. **Ding CP, Sjöberg M, Vuilleumier D, Reuss DL, He X, Böhm B.** Fuel film thickness measurements using refractive index matching in a stratified-charge SI engine operated on E30 and alkylate fuels. Experiments in Fluids 2018; 59(3): 59. https://doi.org/10.1007/s0034

24. **Dillon ME, Wang G, and Huey RB.** Global metabolic impacts of recent climate warming. Nature 2010; 467: 704-706. doi:10.1038/nature09407

25. **Drake MC, Fansler TD, and Rosalik ME.** Quantitative high-speed imaging of piston fuel films in direct-injection engines using a refractive-index-matching technique. The 15th Annual Conference on Liquid Atomization and Spray Systems, Madison, WI, 15-17 May 2002,1-8.

26. **Drake MC, Fansler TD, Solomon AS, et al.** Piston fuel films as a source of smoke and hydrocarbon emissions from a wall-controlled spark-ignited direct-injection engine. SAE Technical Paper 2003-01-0547, 2003. https://doi.org/10.4271/2003-01-0547.

27. **Drake MC and Haworth DC.** Advanced gasoline engine development using optical diagnostics and numerical modeling. Proceedings of the Combustion Institute 2007; 31(1): 99-124. https://doi.org/10.1016/j.proci.2006.08.120

28. **Du W, Lou J, & Liu F.** Effects of Nozzle Hole Diameter on Diesel Sprays in Constant Injection Mass Condition. SAE Technical Pape 2017-01-2300, 2017. https://doi.org/10.4271/2017-01-2300

29. **Du W, Zhang Q, Bao W, & Lou J.** Effects of injection pressure on spray structure after wall impingement. Applied Thermal Engineering 2018; 129: 1212-1218. https://doi.org/10.1016/j.applthermaleng.2017.10.083

30. **Feng Z, Zhan C, Tang C, Yang K, Huang Z.** Experimental investigation on spray and atomization characteristics of diesel/gasoline/ethanol blends in high pressure common rail injection system. Energy 2016,112: 549-561. https://doi.org/10.1016/j.energy.2016.06.131.

31. **Florian S, Jürgen S, Frank B, et al.** The influence of spray parameters on the formation of fuel wall films. 27th Annual Conference on Liquid Atomization and Spray Systems, Brighton, UK, September, 2016, pp. 1-8.

32. **Fujimoto H, Hori T, Senda J, Nakagawa H, Kamata S, Katsuta K.** Visualization of Micro Structure in a Diesel Spray by Use of Photography with High Spatial Resolution. SAE Technical Paper 2008-01-2465, 2008. https://doi.org/10.4271/2008-01-2465.

33. **Guan L, Tang C, Yang K, Mo J, Huang Z.** Effect of di-n-butyl ether blending with soybean-biodiesel on spray and atomization characteristics in a common-rail fuel injection system. Fuel 2015; 140: 116-125. https://doi.org/10.1016/j.fuel.2014.09.104.

34. **Gulder OL, Smallwood GJ, and Snelling DR.** Diesel Spray Structure Investigation by Laser Diffraction and Sheet Illumination. SAE Technical Paper 920577; 1992. http://www.jstor.org/stable/44611272

35. **Guo H, Ma X, Li Y, Liang S, Wang Z, Xu H, Wang J.** Effect of flash boiling on microscopic and macroscopic spray characteristics in optical GDI engine. Fuel 2017; 190: 79-89. https://doi.org/10.1016/j.fuel.2016.11.043.

36. **Guo M, Kishi R, Shi B, Ogata Y, and Nishida K.** Effects of cross-flow on fuel spray injected by hole type injector for direct-injection gasoline engine. Atomization and Sprays 2015: 25(1): 81-98. DOI: 10.1615/AtomizSpr.2014011375

37. **Guo M, Shimasaki N, Nishida K, Ogata Y, Wada Y.** Experimental study on fuel spray characteristics under atmospheric and pressurized cross-flow conditions. Fuel 2016; 184:846-855. https://doi.org/10.1016/j.fuel.2016.07.083

38. **Gold M, Stokes J, Morgan R, Heikal M, Sercey GD, Begg S.** Air-fuel mixing in a homogeneous charge DI gasoline engine. SAE Technical Paper 2001-01-0968; 2001. https://doi.org/10.4271/2001-01-0968.

39. **Haworth DC.** A review of turbulent combustion modeling for multidimensional in-cylinder. SAE Technical Paper 2005-01-0993, 2005. https://doi.org/10.4271/2005-01-0993

40. **Henkel S, Beyrau F, Hardalupas Y, Taylor A.** Novel method for the measurement of liquid film thickness during fuel spray impingement on surfaces, Optics express 2016; 24(3): 2542-2561. https://doi.org/10.1364/OE.24.002542.

41. **He X, Ratcliff MA, Zigler BT.** Effects of gasoline direct injection engine operating parameters on particle number emissions. Energy & Fuels 2012; 26(4): 2014-2027. DOI: 10.1021/ef201917p.

42. **Heil B, Weining HK, Karl G, Panten D, & Wunderlich K.** Verbrauch und Emissionen—Reduzierungskonzepte beim Ottomotor. MTZ-Motortechnische Zeitschrift 2001; 62(11): 900-915.

43. **Hitomi M.** Our direction for ICE- efficient contribution to environment. The 9th International Conference on Modeling and Diagnostics for Advanced Engine Systems (COMODIA 2017), Jul, 25-28, Okayama, Japan.

44. **Hiroyasu H, & Arai M.** Structures of fuel sprays in diesel engines. SAE Technical Paper 1050-1061; 1990. http://www.jstor.org/stable/44548562

45. **Hodges JT, Baritaud TA, & Heinze TA.** Planar Liquid and Gas Fuel and Droplet Size Visualization in a Dl Diesel Engine. SAE transactions 1991; 100(3): 1284-1302.http://www.jstor.org/stable/44554479

46. **JATO Dynamics.** Global car sales up by 2.4 % in 2017 due to soaring demand in Europe, Asia-Pacific and Latin America. Feb. 20, 2018, London, UK.

47. **Jing D, Zhang F, Li Y, Xu H, & Shuai S.** Experimental investigation on the macroscopic and microscopic spray characteristics of dieseline fuel. Fuel 2017; 199: 478-487. https://doi.org/10.1016/j.fuel.2017.02.055Get rights and content

48. **Joshi A.** Progress and Outlook on Gasoline Vehicle Aftertreatment Systems. Johnson Matthey Technology Review 2017; 61(4): 311-325. doi:10.1595/205651317x696306

49. **Kalantari D, Tropea C.** Spray impact onto flat and rigid walls: Empirical characterization and modelling. International Journal of Multiphase Flow 2007; 33(5): 525-544. https://doi.org/10.1016/j.ijmultiphaseflow.2006.09.008

50. **Kashdan JT, Shrimpton JS, Whybrew A.** A digital image analysis technique for quantitative characterisation of high-speed sprays. Opt Laser Eng 2007; 45(1): 106–15. https://doi.org/10.1016/j.optlaseng.2006.03.006.

51. **Kim Y, Kim M, Yeom J, and Min K.** LIEF Measurement and Calculation Analysis of Evaporation Spray. THIESEL 2002 Conference on Thermo- and Fluid Dynamic Process in Diesel Engines, Valencia, Spain, 2002.

52. **Kim SJ, Kim YN, & Lee JH.** Analysis of the in-cylinder flow, mixture formation and combustion processes in a spray-guided GDI engine. SAE Technical Paper 2008-01-0142, 2008. https://doi.org/10.4271/2008-01-0142

53. **Kosaka H, Won YH, and Kamimoto T.** A Study of the Structure of Diesel Sprays Using 2-D Imaging Techniques. SAE Technical Paper 920107; 1992. http://www.jstor.org/stable/44611207

54. **Ko K, Huh J, & Arai M.** Diesel Spray Impingement Behavior and Adhering Fuel on a Recessed Wall. SAE Technical Paper 2003-01-1834; 2003. https://doi.org/10.4271/2003-01-1834

55. **Kume T, Iwamoto Y, Iida K, Murakami M, Akishino K, & Ando H.** Combustion control technologies for direct injection SI engine. SAE technical paper 960600, 1996. DOI: https://doi.org/10.4271/960600

56. **Kuhnke D.** Spray/wall interaction modelling by dimensionless data analysis. Shaker, 2004.

57. **Lacoste J, Crua C, Heikal M, Kennaird D, Gold M.** PDA characterisation of dense diesel sprays using a common-rail injection system. SAE Technical Paper 2003-01-3085, 2003. https://doi.org/10.4271/2003-01-3085

58. **Lacis AA, Hansen JE, Russell GL, Oinas V, and Jonas J.** The role of long-lived greenhouse gases as principal LW control knob that governs the global surface temperature for past and future climate change. Tellus B: Chemical and Physical Meteorology 2013, 65:19734. https://doi.org/10.3402/tellusb.v65i0.19734

59. **Lai MC, Zheng Y, Shost M, Xie X, Matsumoto A, Wang J, Zhang X, Moon S, Gao J, Fezzaa K, Zigan L, Schmitz I, Wensing M, Leipertz A.** Characterization of Internal flow and Spray of Multihole DI Gasoline Spray using X-ray Imaging and CFD. SAE Technical Paper 2011-01-1881; 2011. https://doi.org/10.4271/2011-01-1881

60. **Lahane S, & Subramanian KA.** Impact of nozzle holes configuration on fuel spray, wall impingement and NOx emission of a diesel engine for biodiesel–diesel blend (B20). Applied Thermal Engineering 2014; 64(1-2): 307-314. https://doi.org/10.1016/j.applthermaleng.2013.12.048

61. **Lee S, Sungwook P.** Experimental study on spray break-up and atomization processes from GDI injector using high injection pressure up to 30MPa. International Journal of Heat and Fluid Flow 2014; 45: 14-22. https://doi.org/10.1016/j.ijheatfluidflow.2013.11.005.

62. **Li Y.** Experimental study on spray and combustion characteristics of diesel-like fuels, PhD, University of Birmingham, 2012.

63. **Liu H, Chen B, Feng L, Wang Y, Yi W, & Yao M.** Study on Fuel Distribution of Wall-Impinging Diesel Spray under Different Wall Temperatures by Laser-Induced Exciplex Fluorescence (LIEF). Energies 2018; 11(5): 1249. doi:10.3390/en11051249

64. **Liu Y, Pei Y, Peng Z, Qin J, Zhang Y, Ren Y, Zhang M.** Spray development and droplet characteristics of high temperature single-hole gasoline spray. Fuel 2017; 191: 97-105. https://doi.org/10.1016/j.fuel.2016.11.068.

65. **Luo HL, Uchitomi S, Nishida K, Ogata Y, Zhang W, Fujikawa T.** Experimental Investigation on Fuel Film Formation of Spray Impingement on Flat Walls with Different Surface Roughness. Atomization and Sprays 2017; 27(7): 611–628. DOI: 10.1615/AtomizSpr.2017019706.

66. **Luo H, Shintaro U, Nishida K, et al.** Fuel Adhesion Characteristics of Flat Wall-Impinging Spray under DISI Engine Conditions. In: The 29th Annual Conference on Liquid Atomization and Spray Systems-Americas, Atlanta, GA, 15-18 May 2017, 1-13.

67. **Luo HL, Nishida K, Uchitomi S, Ogata Y, Zhang W, Fujikawa T.** Microscopic behavior of spray droplets under flat-wall impinging condition. FUEL 2018; 219: 467-476. https://doi.org/10.1016/j.fuel.2018.01.059.

68. **Luo HL, Uchitomi S, Nishida K, Ogata Y, Zhang W, Fujikawa T.** Effect of Impingement Distance on Fuel Adhesion of Hole-Nozzle Spray under Various Injection Pressures. COMODIA 2017, Okayama, Japan, 25-28 Jul. 2017, 1-10. https://doi.org/10.1299/jmsesdm.2017.9.C104.

69. **Luo HL, Nishida K, Uchitomi S, Ogata Y, Zhang W, Fujikawa T.** Effect of Spray Impinging Distance on Piston Top Fuel Adhesion in Direct Injection Gasoline Engines. International Journal of Engine Research 2018. (Online First). https://doi.org/10.1177/1468087418774175.

70. **Maligne D and Bruneaux G.** Time-resolved fuel film thickness measurement for direct injection SI engines using refractive index matching. SAE Technical Paper 2011-01-1215, 2011. https://doi.org/10.4271/2011-01-1215.

71. **Maly RR.** State of the art and future needs in SI engine combustion. Symposium (International) on Combustion 1994; 25(1): 111-124. https://doi.org/10.1016/S0082-0784(06)80635-1

72. **Manin J, Bardi M, Pickett LM, Dahms RN, Oefelein JC.** Microscopic investigation of the atomization and mixing processes of diesel sprays injected into high pressure and temperature environments. Fuel 2014; 134: 531-543. https://doi.org/10.1016/j.fuel.2014.05.060.

73. **Maria van der Hoeven.** Energy and Climate Change - World Energy Outlook Special Report, International Energy Agency 2015.

74. **McKinley GH, and Michael R.** Wolfgang von ohnesorge. Physics of Fluids 2011, 23(12): 127101. https://doi.org/10.1063/1.3663616

75. **Moreira ALN, Moita AS, & Panao MR.** Advances and challenges in explaining fuel spray impingement: How much of single droplet impact research is useful?. Progress in energy and combustion science 2010; 36(5): 554-580. https://doi.org/10.1016/j.pecs.2010.01.002

76. **Montanaro A, Malaguti S, Alfuso S.** Wall impingement process of a multi-hole GDI spray: Experimental and numerical investigation. SAE Technical Paper 2012-01-1266; 2012. https://doi.org/10.4271/2012-01-1266.

77. **Montanaro A, Allocca L, Costa M, Sorge U.** Assessment of a 3D CFD model for GDI spray impact against wall through experiments based on different optical techniques. International Journal of Multiphase Flow 2016; 84: 204-216. https://doi.org/10.1016/j.ijmultiphaseflow.2016.05.007

78. **Mundo CHR, Sommerfeld M, Tropea C.** Droplet-wall collisions: experimental studies of the deformation and breakup process. International journal of multiphase flow 1995; 21(2): 151-173. https://doi.org/10.1016/0301-9322(94)00069-V

79. **Naber JD, Siebers DL.** Effects of gas density and vaporization on penetration and dispersion of diesel sprays. SAE Technical Paper 960037; 1996. https://doi.org/10.4271/960034

80. **Oh H, Bae C, & Min K.** Spray and combustion characteristics of ethanol blended gasoline in a spray guided DISI engine under lean stratified operation. SAE International Journal of Engines 2010; 3(2010-01-2152): 213-222. https://doi.org/10.4271/2010-01-2152

81. **Okamoto S, Kawashima H, Ishima T, Nakama K.** Analysis of the fuel adhering to a model engine cylinder by using time series LIF methods. The 12th Triennial Int. Conf. on Liquid Atomization and Spray Systems, Heidelberg, Germany, 2–6 Sep. 2012, 1-8.

82. **Panao MRO, & Moreira ALN.** Heat transfer correlation for intermittent spray impingement: a dynamic approach. International Journal of Thermal Sciences 2009; 48(10): 1853-1862. https://doi.org/10.1016/j.ijthermalsci.2009.02.018

83. **Park SW, and Lee CS.** Macroscopic and microscopic characteristics of a fuel spray impinged on the wall. Experiments in fluids 2004; 37 (5): 745-762. https://doi.org/10.1007/s00348-004-0866-3

84. **Park C, Kim S, Kim H, & Moriyoshi Y.** Stratified lean combustion characteristics of a spray-guided combustion system in a gasoline direct injection engine. Energy 2012; 41(1): 401-407. https://doi.org/10.1016/j.energy.2012.02.060

85. **Pastor JV, Payri R, Garcia-Oliver JM, & Briceno FJ.** Analysis of transient liquid and vapor phase penetration for diesel sprays under variable injection conditions. Atomization and Sprays 2011; 21(6): 503-520. DOI: 10.1615/AtomizSpr.2011003721

86. **Payri F, Desantes J M, Arregle J.** Characterization of DI Diesel sprays in high density conditions. SAE Technical Paper 960774, 1996. https://doi.org/10.4271/960774

87. **Pei Y, Qin J, Li X, Zhang D, Wang K, Liu Y.** Experimental investigation on free and impingement spray fueled with methanol, ethanol, isooctane, TRF and gasoline. Fuel 2017; 208: 174-183. https://doi.org/10.1016/j.fuel.2017.07.011.

88. **Peery KM.** The Heintz straticharge engine: modifications I through V. Department of Mechanical Engineering, Stanford University, 1975.

89. **Piazzullo D, Costa M, Allocca L, Montanaro A, Rocco V.** A 3D CFD Simulation of GDI Sprays Accounting for Heat Transfer Effects on Wallfilm Formation. SAE International Journal of Engines 2017; 10: 2166-2175. https://doi.org/10.4271/2017-24-0041.

90. **Pickett LM, Kook S, and Williams TC.** Visualization of Diesel Spray Penetration, Cool-Flame, Ignition, High-Temperature Combustion, and Soot Formation Using High-Speed Imaging. SAE Technical Paper 2009-01-0658; 2009. https://doi.org/10.4271/2009-01-0658

91. **Pizziol B, Costa M, Panão MO, & Silva A.** Multiple impinging jet air-assisted atomization. Experimental Thermal and Fluid Science 2018; 96: 303-310. https://doi.org/10.1016/j.expthermflusci.2018.03.019

92. **Preussner C, Doring C, Fehler S, Kampmann S.** GDI: interaction between mixture preparation, combustion system and injector performance. SAE Technical Paper, 980498; 1998. https://doi.org/10.4271/980498

93. **Romain N.** Introduction to engine fueling systems. Car engineer,05-22-2013.

94. **Siebers DL.** Liquid-phase Fuel Penetration in Diesel Sprays, SAE Technical Paper 980809; 1998. https://doi.org/10.4271/980809

95. **Schulz F, Schmidt J, Kufferath A, & Samenfink W.** Gasoline wall films and spray/wall interaction analyzed by infrared thermography. SAE International Journal of Engines 2014; 7: 1165-1177. https://doi.org/10.4271/2014-01-1446

96. **Schulz F, Schmidt J, and Beyrau F.** Development of a sensitive experimental set-up for LIF fuel wall film measurements in a pressure vessel. Experiments in Fluids 2015; 56(5): 1-16. https://doi.org/10.1007/s00348-015-1971-1.

97. **Schulz F, Samenfink W, Schmidt J, et al.** Systematic LIF fuel wall film investigation. Fuel 2016; 172: 284–292. https://doi.org/10.1016/j.fuel.2016.01.017.

98. **Schulz F and Beyrau F.** The influence of flash-boiling on spray-targeting and fuel film formation. Fuel 2017; 208: 587-594. https://doi.org/10.1016/j.fuel.2017.07.047.

99. **Senda J.** Experimental studies on the behavior of a small droplet impinging upon a hot surface. ICLASS-82, 397, 1982.

100.**Senda J, Takeuchi K and Sato Y.** Atomization of Spray Droplet Impinging upon a Hot Surface. Internal Combustion Engine (Nainen kikan)(in Japanese with English summary), (Sankai-dou) 1982; 21-268:9-18.

101.**Senda J, Yamada K, Fujimoto H and Miki H**. The Heat - Transfer Characteristics of a Small Droplet Impinging upon a Hot Surface. JSME Int. Journal 1988; Series II, 3(1):105-111. https://doi.org/10.1299/jsmeb1988.31.1105

102.**Senda J, Kobayashi M, Iwashita S, & Fujimoto H.** Modeling of diesel spray impingement on a flat wall. SAE transactions 1994; 103(3):1918-1931. http://www.jstor.org/stable/44632927

103.**Senda J, Kanda T, Al-Roub M, Farrell PV, Fukami T, & Fujimoto H.** Modeling spray impingement considering fuel film formation on the wall. SAE Technical Paper 970047；1997. https://doi.org/10.4271/970047.

104.**Senda J, Ohnishi M, Takahashi T, Fujimoto H, Utsunomiya A, Wakatabe M.** Measurement and modeling on wall wetted fuel film profile and mixture preparation in intake port of SI engine. SAE Technical Paper 1999-01-0798, 1999. https://doi.org/10.4271/1999-01-0798.

105.**Spicher U, Kölmel A, Kubach H, & Töpfer G.** Combustion in spark ignition engines with direct injection. SAE Technical Paper 2000-01-0649, 2000. DOI: https://doi.org/10.4271/2000-01-0649

106.**Suresh M, Prakash H, & Durga PB.** Operation and developments of DISI engines—a review. Int RJ Latest Trends Eng Technol (IJLTET) 2015; 5(4): 31-37.

107.**Tanaka D, Uchida R, Noda T, Kolbeck A, Henkel S, Hardalupas Y, Taylor A, Aradi, A.** Effects of fuel properties associated with in-cylinder behavior on particulate number from a direct injection gasoline engine. SAE Technical Paper, 2017-01-1002; 2017. https://www.sae.org/publications/technical-papers/content/2017-01-1002/

108.**Vander WRL, Berger GM, Mozes SD.** The splash/non-splash boundary upon a dry surface and thin fluid film. Experiments in fluids 2006; 40(1): 53-59. https://doi.org/10.1007/s00348-005-0045-1

109. **Wang D, & Fan LS.** Particle characterization and behavior relevant to fluidized bed combustion and gasification systems. In Fluidized bed technologies for near-zero emission combustion and gasification 2013; 42-76. https://doi.org/10.1533/9780857098801.1.42

110. **Wang Z, Xu H, Jiang C, Wyszynski ML.** Experimental study on microscopic and macroscopic characteristics of diesel spray with split injection. Fuel 2016; 174: 140-152. https://doi.org/10.1016/j.fuel.2016.01.083.

111. **Wakuri Y, Fujii M, Amitani T, Rsuneya R**. Studies on the penetration of fuel spray of diesel engine. Trans. JSME 1957, 25: 820-826

112. **Yang B and Ghandhi J.** Measurement of diesel spray impingement and fuel film characteristics using refractive index matching method. SAE Technical Paper 2007-01-0485, 2007. https://doi.org/10.4271/2007-01-0485.

113. **Yeh C, Kamimoto T, Kosaka H, and Kobori S.** Quantitative Measurement of 2-D Fuel Vapor Concentration in a Transient Spray via Laser-Induced Fluorescence Technique. SAE Technical Paper 941953; 1994. http://www.jstor.org/stable/44612413

114. **Yu H, Liang X, Shu G, Wang Y, and Zhang H.** Experimental investigation on spray-wall impingement characteristics of n-butanol/diesel blended fuels. Fuel 2016; 182: 248-258. https://doi.org/10.1016/j.fuel.2016.05.115

115. **Yu H, Liang X, Shu G, Sun X, Zhang, H.** Experimental investigation on wall film ratio of diesel, butanol/diesel, DME/diesel and gasoline/diesel blended fuels during the spray wall impingement process. Fuel Processing Technology 2017; 156: 9-18. https://doi.org/10.1016/j.fuproc.2016.09.029.

116. **Yu J, Vuorinen V, Hillamo H, Sarjovaara T, Kaario O, Larmi M.** An experimental investigation on the flow structure and mixture formation of low pressure ratio wall-impinging jets by a natural gas injector. Journal of Natural Gas Science and Engineering 2012; 9: 1-10. https://doi.org/10.1016/j.jngse.2012.05.003

117. **Zhang T, Dong B, Chen X, Qiu Z, Jiang R & Li W.** Spray characteristics of pressure-swirl nozzles at different nozzle diameters. Applied Thermal Engineering 2017; 121: 984-991. https://doi.org/10.1016/j.applthermaleng.2017.04.089

118. **Zhang Y, Jia M, Liu H, Xie M, Wang T, and Zhou L.** Development of a new spray/wall interaction model for diesel spray under PCCI-engine relevant conditions. Atomization and Sprays 2014; 24(1): 41-80. DOI: 10.1615/AtomizSpr.2013008287

119. **Zhang Y, Jia M, Duan H, Wang P, Wang J, Liu H, & Xie M.** Numerical and experimental study of spray impingement and liquid film separation during the spray/wall interaction at expanding corners. International Journal of Multiphase Flow 2018. https://doi.org/10.1016/j.ijmultiphaseflow.2018.05.016

120. **Zhao F, Lai MC, Harrington DL.** Automotive spark-ignited direct-injection gasoline engines. Progress in energy and combustion science 1999; 25(5): 437-562. https://doi.org/10.1016/S0360-1285(99)00004-0

121. **Zhao H, and Ladommatos N.** Engine Combustion Instrumentation and Diagnostics. Warrendale PA, USA, Society of Automotive Engineers,2001.

122. **Zhao L, Torelli R, Zhu X, Scarcelli R, Som S, Schmidt H, Naber J, Lee S.** An Experimental and Numerical Study of Diesel Spray Impingement on a Flat Plate. SAE Int. J. Fuels Lubr. 2017; 10(2): 407-422. doi:10.4271/2017-01-0854

123. **Zheng Y, Xie X, Lai MC, et al.** Measurement and simulation of DI spray impingements and film characteristics. The 12th Triennial Int. Conf. on Liquid Atomization and Spray Systems, Heidelberg, Germany, 2–6 Sep. 2012, 1-8.

124. **Zhou ZF, Murad SHM, Tian JM, Camm J, & Stone R.** Experimental investigation on heat transfer of n-pentane spray impingement on piston surface. Applied Thermal Engineering 2018; 138: 197-206. https://doi.org/10.1016/j.applthermaleng.2018.04.059

125. **Zama Y, Odawara Y, and Furuhata T.** Experimental study on velocity distribution of post-impingement diesel spray on a wall, Part 2: Effect of ambient gas density and injection pressure on flow pattern. Atomization and Sprays 2014, 24(8): 723-746.